A Novel Hybrid Numerical Renormalization Group Approach to Non-Equilibrium Dynamics and Spectral Functions

Dissertation
zur Erlangung des Doktorgrades
der Naturwissenschaften
der Fakultät Physik an der
Technischen Universität Dortmund

vorgelegt von

Jan Oliver Böker

geboren in Schwelm

Lehrstuhl für Theoretische Physik 2
Fakultät Physik
Otto-Hahn-Str. 4
D-44227 Dortmund
Technische Universität Dortmund

-September 2021-

Erster Gutachter	Prof. Dr. Frithjof B. Anders
Zweiter Gutachter	Prof. Dr. Jan von Delft
Kontakt zum Autor	jan.boeker@tu-dortmund.de

Contents

Abstract

We present an approach for quantum impurity systems (QISs) that extends the numerical renormalization group (NRG) to an open quantum system (OQS) formulation. The continuous conduction band is divided into an arbitrary Wilson chain and a set of reservoirs without affecting the local bath hybridization function. One reservoir is coupled to each chain site and is treated by the Bloch-Redfield formalism (BRF), which includes the Born-Markov approximation (BMA).

This open chain formalism (OCF) yields true thermalization in local time-dependent non-equilibrium expectation values (TD-NEVs), as well as finite lifetime in local equilibrium spectral functions (ESFs). It reproduces the $t \to \infty$ steady-state predicted by the NRG and the correct relaxation rates in the resonant level model (RLM). By enlarging the Wilson chain, the accuracy of the BMA, especially with respect to short-time dynamics, is increased. The formation of Hubbard-peaks and the Kondo-resonance are reproduced for the single impurity Anderson model (SIAM).

The BMA in second order results in the persistence of finite-size oscillations to some degree, which can be damped by the well-established procedure of z-averaging. We find the BRF to be inadequate for interacting models, if the local Coulomb repulsion exceeds the conduction bandwidth, and discuss several options to improve the OCF for this parameter regime.

Since the motivation for this thesis is of pure methodological nature, we restrict to the most simple quantum impurity models (QIMs) to benchmark our algorithm. However, the OCF is as versatilely applicable to more complex models as the pure NRG. Consequently, our approach can be adapted to e.g. multi-impurity models, as well as simulate local transport properties in and out of equilibrium.

Kurzfassung

Wir präsentieren einen Ansatz zur Behandlung von Quantenstörstellensystemen, der die numerische Renormierungsgruppe (NRG) zu einem offenen-Quantensystem-Formalismus erweitert. Das kontinuierliche Leitungsband wird in eine beliebige Wilsonkette und einen Satz von Reservoirs aufgeteilt, ohne die lokale Badhybridisierungsfunktion zu beeinflussen. An jedes Kettenglied wird jeweils ein Reservoir über den Bloch-Redfield Formalismus (BRF) angekoppelt, der eine Born-Markov-Näherung (BMN) impliziert.

Dieser offene-Wilsonketten-Formalismus (OWF) garantiert eine echte Thermalisierung für lokale nicht-Gleichgewichtsdynamik, sowie eine endliche Lebenszeit für lokale Gleichgewichtsspektralfunktionen. Der Ansatz reproduziert die von der NRG vorhergesagten Gleichgewichtswerte für $t \to \infty$ und die korrekten Relaxationsraten für das Resonanzlevel-Modell. Durch Verlängerung der Wilsonkette wird die Genauigkeit der BMN, speziell für die Kurzzeitdynamik, erhöht. Die Formierung der Hubbardhügel und der Kondoresonanz können für das Einzelstörstellen-Anderson-Modell reproduziert werden.

Die BMN in zweiter Ordnung ist nicht in der Lage, die Oszillationen, die durch die Banddiskretisierung im Kontext der NRG entstehen, vollständig zu dämpfen, kann jedoch durch die wohlbekannte z-Mittelung konstruktiv ergänzt werden. Es stellt sich heraus, dass der BRF nicht effizient ist für wechselwirkende Systeme, in denen die lokale Wechselwirkung die Bandbreite übersteigt. Hierzu diskutieren wir mehrere alternative Optionen.

Die Motivation zu dieser Arbeit ist rein methodologischer Natur, weshalb wir uns auf die einfachsten Quantenstörstellenmodelle beschränken. Der OWF ist allerdings ebenso vielfältig einsetzbar wie die NRG selbst, und damit anwendbar auf z.B. Multi-Störstellenmodelle oder lokalen Gleichgewichts- und Nicht-Gleichgewichts-Transport.

Publication List

During the course of the work for this thesis the following article has been published.

Jan O. Böker, Frithjof B. Anders. "Restoring the continuum limit in the time-dependent numerical renormalization group approach". In: *Physical Review B* 102.7 (Aug. 2020), p. 075149. DOI: `https://doi.org/10.1103/PhysRevB.102.075149`.

Table of Abbrevations

AKM	anisotropic Kondo model
AMEA	auxiliary master equation approach
ASB	Anders-Schiller basis
BA	Born approximation
BMA	Born-Markov approximation
BRF	Bloch-Redfield formalism
BRT	Bloch-Redfield tensor
CFE	continued fraction expansion
CWC	closed Wilson chain
DDM	diagonal part of the density matrix
DMRG	density matrix renormalization group
DOF	degrees of freedom
DOS	density of states
EDOF	environment degrees of freedom
ESF	equilibrium spectral function
FDM	full density matrix
FIFP	frozen impurity fixed point
FLOA	factorized local operator approximation
FOFP	free orbital fixed point
GF	Green's function
IRLM	interacting resonant level model
LMFP	local moment fixed point
LOA	local operator approximation
MA	Markov approximation
MSA	Markov and secular approximation
NRG	numerical renormalization group
ODDM	off-diagonal part of the density matrix
OCF	open chain formalism
OQS	open quantum system
OWC	open Wilson chain
QD	quantum dot

QIM	quantum impurity model
QIS	quantum impurity system
RG	renormalization group
RGF	reservoir Green's function
RLM	resonant level model
SAM	symmetrical Anderson model
SCFP	strong coupling fixed point
SIAM	single impurity Anderson model
SSA	single shell approximation
STM	scanning tunnelling microscopy
TD-EGF	time-dependent retarded equilibrium Green's function
TD-NEV	time-dependent non-equilibrium expectation value
TD-NRG	time-dependent numerical renormalization group
VFFP	valence fluctuation fixed point

1. Introduction

Solid state physics is a materials science, that is intended to explain macroscopic behavior of crystalline solids, such as the conductivity of heat or electric current, by understanding their properties on a microscopic, i.e. atomic level. On this scale, it is often indispensable to consider quantum mechanical effects. A typical sample used in experiments contains a particle number of the order of 10^{23}. It is clearly impossible to solve such a system, when considering all quantum mechanical particle interactions. This is why physicists reduce the complexity of the problem by concentrating on single weakly or non-interacting electrons. However, this method fails to describe materials, in which strong correlation effects play a dominant role. These materials show unusual, and often technologically useful, electronic and magnetic properties such as superconductivity [1, 2], Mott insulation [3, 4] or heavy fermion behavior [5, 6].

One example of a strong correlation effect was discovered in the 1930's in a gold sample contaminated with iron atoms [7]. At very low temperatures of a few Kelvin, the sample displayed an increase of electrical resistivity upon further lowering the temperature, which contradicted the traditional perspective at that time. In the 1960's Jun Kondo was able to explain the resistivity minimum by an interaction between the magnetic moment of the iron impurities and the conduction band electron spins of the gold atoms [8]. This so-called Kondo effect is not restricted to magnetic impurities diluted in a host metal, but can also be observed in quantum dots (QDs) [9]. These are artificial atoms that confine a localized charge in all space dimensions. The localized spin of an electron can be used as a qubit and can be manipulated by coherent laser pulses, which builds the foundation of quantum computing [10, 11, 12].

The basis of theoretically describing a QIS, such as the above mentioned localized iron impurities coupled to the itinerant gold electrons, is the reduction of the complex many-body interactions to an effective QIM. The SIAM [13, 14, 15] is a basic QIM, which is capable of describing the Kondo effect and is connected to the Kondo model by a Schrieffer-Wolff transformation [16]. It contains a single orbital hybridized with a non-interacting band of conduction electrons. By the introduction of a local Coulomb repulsion between electrons of opposite spin, the SIAM is able to explain the formation of a local magnetic moment and ultimately the Kondo effect itself. From the SIAM one can derive even simpler models as the (interacting) RLM [17, 18].

A variety of methods has been applied to approximately solve QIMs in an analytical and numerical manner[1]. A major challenge to those approaches is the applicability over a wide range of energies, spanning from the width of the conduction band to the exponentially small temperatures, at which the Kondo effect emerges. One of the most successful approaches is the renormalization group (RG) [20, 21], which provides an effective low-energy Hamiltonian by iteratively integrating out high-energy modes and thus renormalizing the energy scales of the system. From the RG, Kenneth Wilson developed the NRG in the 1970's [22], with which he was able to solve the Kondo model. The NRG is based upon a logarithmic discretization of the conduction band energy spectrum. These discrete modes are iteratively coupled to the impurity to form a so-called Wilson chain. The logarithmically decreasing coupling parameters embed an energy hierarchy that reveals the RG character of this method and allows for a truncation of high-energy states of the system. This truncation is the numerical aspect of the NRG and allows to significantly increase the system size.

Since its development, the NRG has successfully been applied to calculate local equilibrium and non-equilibrium quantities of QIMs [23, 24, 25]. The drawback of this method are finite-size effects due to the band discretization [26, 27, 28], which inevitably neglects modes from the energy continuum. In TD-NEVs, this translates to back-reflections of charge along the Wilson chain [29, 30], due to the decreasing chain parameters, as well as reflection at the end of the chain, which ultimately leads to revival effects of charge at the impurity and prohibits a thermalization of the system [31]. In ESFs the discretization of the band continuum prohibits a finite lifetime of local excitations, which is a practical obstacle for the depiction of the spectrum [32].

Throughout the years, several attempts have been made to improve the finite-size effects of the NRG. One of the basic concepts to restore the continuum is z-averaging proposed by Oliveira *et al* [33]. Here the results are averaged over several Wilson chains, which differ by a shift of the discretization of the conduction band. Thus finite-size oscillations in equilibrium [26] and non-equilibrium [29] quantities can be reduced. However, a thermalization to the correct steady-state is not achieved. For spectral functions it is customary to artificially broaden the spectrum with a Gaussian [34] or a Lorentzian [32]. This renders satisfactory results for low-energies, but over-

---

[1] A detailed overview can be found in Ref. [19], Chap. 1.

broadens the spectrum at higher energies. Furthermore, in the SIAM the ESF can be slightly optimized by a correction of the self-energy [35]. However, a natural intrinsic broadening is still not provided.

Güttge *et al* proposed a hybrid NRG+DMRG approach [36]. Here an effective tight-binding chain is coupled to the end of a Wilson chain. The Wilson chain is treated with the NRG, while in the tight-binding chain a truncation of high-energy states is not possible. Thus, a density matrix renormalization group (DMRG) [37] is required, which is more versatile, since it discards those states, which have a small contribution to the ground state instead, and is thus applicable for arbitrary tight-binding chains. A drawback of the DMRG is the fact, that it is basically restricted to ground state, i.e. temperature $T = 0$ calculations. The NRG+DMRG approach has been shown to produce accurate results for the interacting resonant level model (IRLM) [36], but provides neither a true thermalization for longer times, nor a finite lifetime.

In this thesis we propose an OCF by hybridizing the NRG with a BRF [38, 39, 40]. To be precise, a Wilson chain with reservoirs coupled to each chain site is constructed by a continued fraction expansion (CFE) [41]. This open Wilson chain (OWC) resembles the exact continuum of the conduction band. The reservoir-chain coupling is performed by a BRF, which is a coupling in second order of the hybridization strength. This formalism includes dissipation, since the reservoirs absorb surplus charge and can thus reduce back-reflections. Furthermore, the BRF includes a true thermalization to the steady-state predicted by the NRG, as well as natural broadening of the local excitations. In the limit of a small discretization parameter and a long Wilson chain, the system becomes exact in the sense, that the reservoirs resemble a small perturbation to the Wilson chain, which is approximately exact in second order.

Above we have introduced the reservoirs as a correction to the Wilson chain to restore the full continuum. However, the opposite perspective is possible as well. At the foundation of the BRF lies the BMA, which assumes the hybridization between the local system (impurity) and the bath (conduction band) to be the smallest energy scale of the total QIS. By extracting modes from the bath and coupling them to the impurity, the local system is expanded and the remaining bath modes are re-coupled from the impurity to the single chain sites. From that perspective, the Wilson chain acts as a buffer zone [42, 43, 44] and the system becomes exact, if the energy levels of this buffer zone are sufficiently dense, which is in accordance with the criterion above. Typical approaches use an equidistant energy spacing, while we use a logarithmic spacing due to the Wilson chain energy hierarchy.

Dorda *et al* [45, 46] have used the auxiliary master equation approach (AMEA) as an OQS approach, that is to some degree similar to our OCF formalism. In contrast, an arbitrary system with few degrees of freedom (DOF) instead of a Wilson chain is chosen as an auxiliary buffer zone between the impurity and the reservoirs. The coupling is treated with a standard Lindblad formalism [47, 48], where all Lindblad, as well as buffer zone, parameters are fitted to resemble the exact bath hybridization function for the local Green's function as accurately as possible. The group is able to reproduce the SIAM spectral function well in both equilibrium and non-equilibrium. In contrast, we rigorously derive the OWC parameters to obtain an exactly defined system. This gives a physical justification of our method, which goes beyond the argument of rendering adequate results. The NRG allows us to efficiently calculate large systems, where the Bloch-Redfield tensor (BRT) can be solved exactly by including the secular approximation. Furthermore, the BRF is more complex than the Lindblad formalism, which is the reason, why the group could not reproduce the SIAM results for a single chain system with the AMEA.

This thesis is organized as follows: In Chap. 2 we introduce the relevant QIMs of this thesis and review their most important features. In Chap. 3 the NRG is derived in the canonical way and is adapted to the calculation of TD-NEVs and ESFs. Also the finite-size properties of the Wilson chain are discussed, which are the motivation for our OCF. The BRF is reviewed in Chap. 4 and the implications of the BMA are illustrated for the atomic RLM and SIAM, respectively. In Chap. 5 we present the CFE, which is then used to extend the system Hamiltonian by a Wilson chain and thus to construct an OWC. Exemplarily for the RLM, we illustrate how the BMA is improved by the Wilson chain or how the OQS formulation of the BRF introduces true relaxation and broadening to the Wilson chain. The OCF is adapted to the NRG in Chap. 6, by introducing several approximations for a truncation of high-energy states in the OWC that do not corrupt the fundamental properties[2] of the time-dependent density matrix. In Chap. 7 the OCF is tested for interacting QIMs, i.e. the IRLM and the SIAM, respectively. Especially, we extend the investigations of Chap. 4 with respect to the suitability of the formalism for all energy ranges of the local Coulomb repulsion in relation to the bandwidth of the conduction band. Finally, in Chap. 8 we conclude the findings of the thesis and propose ideas regarding a further application and extension of the OCF.

Throughout this thesis we presume $\hbar = 1$ and $k_\mathrm{B} = 1$. Consequently, frequencies

---

[2] i.e. positive semi-definiteness, hermiticity and the conservation of the trace for all times

and temperatures are interpreted as energies and time is an effective inverse energy. We will denote D as the bandwidth of the conduction band for the sake of convenience, although, strictly speaking, it is the half bandwidth. The Fermi-energy ϵ_{F} is defined as zero in this thesis and the hybridization Γ will be our favored energy scale, since it is invariant under poor man's scaling.

2. Quantum Impurity Models

In the middle of the last century researchers began to discover that impurities in metal alloys can have interesting impacts on physical properties of the host material. Since those days, theorists developed several models to describe impurities on a quantum level, i.e. QIMs, as well as versatile methods to solve those models analytically and numerically. Impurities can influence transport properties of the host material. One of the most important impurity effects is the modification of electrical resistivity at low temperatures, which was discovered in 1934 [7]. This effect was explained by Jun Kondo in 1964 [8], although it took another 10 years to find a satisfying theoretical treatment of the Kondo effect, until Wilson developed the NRG [22]. Nowadays, several experimental realizations of the Kondo effect are possible (see Sec. 2.6), spanning from magnetic adatoms on non-magnetic surfaces to localized electrons serving as QDs.

In a QIM, the impurity is described as a small subsystem with a finite number of DOF. An example could be a single energy level in the outer orbital of a $3d$ or $4f$ atom. An electron can be localized in this orbital, but in comparison to the other electrons of the atom, it is confined less strongly and can thus hybridize with the environment of the impurity. Furthermore, if the spin of this level is not compensated by another electron of the atom, an effective magnetic moment is generated, which makes the impurity magnetic. The distribution of impurities in a real material can be assumed to be random. In this thesis we concentrate on simple metals as the host material, which are characterized by a broad conduction band of s or p states. We approximate those (itinerant) conduction electrons as non-interacting particles moving within a periodic potential. For that reason, it is convenient to express the conduction band by the one-particle Hamiltonian

$$H_{\mathrm{B}} = \sum_{\mathbf{k},\sigma} \epsilon_{\mathbf{k}} c^{\dagger}_{\mathbf{k},\sigma} c_{\mathbf{k},\sigma}, \tag{1.0.1}$$

with $c^{(\dagger)}_{\mathbf{k},\sigma}$ annihilating (creating) a free conduction electron of wave-vector $\mathbf{k}$ and spin σ with an associated energy $\epsilon_{\mathbf{k}}$. The free electron gas H_{B} is mathematically simple and thus many physical properties are trivially known, which simplifies calculations. Without loss of generality, we define the absolute conduction band excitation energies as limited by an upper bound D, called bandwidth. Due to the large number of free electrons at $\mathcal{O}(10^{23})$, the band can be treated as a continuous spectrum.

Charge transfer between the impurity (local system) and the band is mediated by a hybridization $V_{\mathbf{k}}$ via the term

$$H_{\mathrm{SB}} = \sum_{\mathbf{k},\sigma} V_{\mathbf{k}} (d^{\dagger}_{\sigma} c_{\mathbf{k},\sigma} + c^{\dagger}_{\mathbf{k},\sigma} d_{\sigma}), \tag{1.0.2}$$

with a local operator $d^{(\dagger)}_{\sigma}$ and a conduction band operator $c^{(\dagger)}_{\mathbf{k},\sigma}$. The normalization factor of $1/\sqrt{N}$ is absorbed in the definition of $V_{\mathbf{k}}$, where N is the total number of conduction band electrons and goes to infinity for a continuous band. The spectral coupling function is given as

$$\Gamma(\omega) = \pi \sum_{\mathbf{k}} V^2_{\mathbf{k}} \delta(\omega - \epsilon_{\mathbf{k}}). \tag{1.0.3}$$

We can define

$$V c_{0,\sigma} = \sum_{\mathbf{k}} V_{\mathbf{k}} c_{\mathbf{k},\sigma} \tag{1.0.4}$$

with $c^{(\dagger)}_{0,\sigma}$ annihilating (creating) a Wannier state localized at the impurity. V is the $\mathbf{k}$-independent hybridization, defined by $V^2 = \sum_{\mathbf{k}} V^2_{\mathbf{k}}$, which follows from the normalization of the band operators. If the bandwidth D is the dominant energy scale of the system, we can assume the wideband limit $D \gg \Gamma$. Furthermore we approximate the conduction band density of states (DOS) as a flat band

$$\rho_0(\omega) = \frac{1}{2D} \Theta(|D| - \omega). \tag{1.0.5}$$

The spectral coupling function (1.0.3) then reduces to

$$\Gamma(\omega) = \Gamma \Theta(|D| - \omega), \tag{1.0.6}$$

where $\Gamma = \pi V^2 \rho_0(\epsilon_{\mathrm{F}} = 0) = \frac{\pi V^2}{2D}$ can serve as the energy scale of the system. The flat-band assumption is thus valid, since we are not interested in the influence of an energy dependent coupling function $\Gamma(\omega)$ onto the local dynamics.

If the local impurity potential is strong enough, i.e. $\Gamma \gg D$, a bound state with an itinerant electron below the conduction band can likely occur, meaning that its wave-function falls off fast with the distance to the impurity. If the potential is not sufficiently attractive, still a so-called virtual bound state is possible. Here the free electron is localized for a finite time in the vicinity of the impurity, and the wave-function has a narrow peak at the impurity site, called virtual bound state resonance. However, this state is not a real bound state, since the wave-function becomes a Bloch state far from the impurity.

2.1. Kondo Effect

In 1934, de Haas *et al* found that impure gold wires have a resistivity minimum at low temperatures [7]. To this point, resistivity was believed to entirely stem from electron-phonon and electron-electron scattering, which would predict it to monotonously decrease with temperature [49], plus a residual contribution of the impurities, which results in a constant resistivity for $T \to 0$. The resistivity minimum was later found to be contributed to magnetic impurities in a non-magnetic metal. In 1964, Jun Kondo was able to theoretically describe the origin of the resistivity minimum on the basis of the s-d model (see Sec. 2.2). He realized that at low temperatures the effective interaction between the localized impurity electron spin and the conduction band electrons is increased. In this case higher order perturbation terms are important to electron scattering. Kondo calculated second order terms, i.e. two-step electron scattering, which yield a contribution $\propto -c_{\mathrm{imp}} J \ln T$ to the resistivity, with J being the Heisenberg exchange coupling, c_{imp} the concentration of impurities and T being the temperature. This finding explained the resistivity minimum for $J > 0$ (anti-ferromagnetic case), but implied a divergence for $T \to 0$. In contrast, real materials exhibit a resistivity plateau below a certain temperature, called Kondo temperature T_{K}. It was shown, that including higher order terms did not help and that any perturbative approach breaks down below T_{K}.

Understanding the origin of the resistivity plateau while simultaneously including the phenomenon of the resistivity minimum is called the "Kondo problem". It turned out, that the cause of this plateau lies in the fact, that the local spin is screened more and more by itinerant electrons, when the temperature is lowered [22], i.e. the impurity spin forms a quasi-particle together with a free electron state of opposite spin [50]. This special fragile state can only be formed, if the thermal energy is sufficiently low to not let kinetic processes break up the bond. The increase in resistivity, observed in real materials by lowering the temperature below T_{K}, is attributed to the so-called Kondo resonance. It is expressed as a peak in the local impurity density of states around the Fermi level.

In 1974, Kenneth Wilson developed the NRG (see Chap. 3), which is a non-perturbative approach, capable of solving the Kondo problem.

2.2. Kondo Model

Experimental data [51] suggested that the depth of the resistivity minimum was proportional to the concentration c_{imp} of magnetic impurities in the sample. Based upon that finding, Jun Kondo realized that the minimum can be attributed to independent impurities. For that reason, he used the s-d exchange model to explain the resistance behavior at low temperatures. This model describes the local magnetic moment in the d-shell of a single impurity coupled to s-like electrons of the conduction band via a spin-spin Heisenberg interaction. In the context of the Kondo effect this model is also called the "Kondo model". The isotropic version of the s-d model is given by

$$H_{\mathrm{sd}} = H_{\mathrm{B}} + J\mathbf{S}_{\mathrm{imp}} \cdot \mathbf{S}. \tag{2.2.1}$$

Here the first term is the conduction band part of Eq. (1.0.1). The second term accounts for an effective Heisenberg interaction J between the local impurity spin $\mathbf{S}_{\mathrm{imp}}$ and the total conduction electron spin

$$\mathbf{S} = \frac{1}{2N} \sum_{\mathbf{k},\mathbf{k}'} \sum_{\sigma,\sigma'} c^{\dagger}_{\mathbf{k},\sigma} \boldsymbol{\sigma}_{\sigma\sigma'} c_{\mathbf{k}',\sigma'}. \tag{2.2.2}$$

$\boldsymbol{\sigma}$ is a vector comprising the three Pauli matrices, and $\uparrow$ ($\downarrow$) accounts for the first (second) index of those matrices. For an anti-ferromagnetic interaction ($J > 0$) the conduction band electron spins align anti-parallelly to the impurity spin. This enables spin-flip scattering processes between two degenerate states. With Eq. (2.2.1) Kondo perturbatively calculated contributions to the resistivity ρ by considering all possible scattering processes $\langle \mathbf{k}', \sigma' | \, T \, | \mathbf{k}, \sigma \rangle$ [8][1]. The second order term in J yielded the already known potential scattering contribution R_{imp}, which is constant in the temperature T.

---

[1] T is the T-matrix, which is a sum of terms that include H_{sd}, as well as the retarded Green's function of the free electrons in increasing order. The state $|\mathbf{k}, \sigma\rangle$ refers to the wave vector $\mathbf{k}$ and the spin component σ of a conduction band electron. For details see [6].

By going to third order in J, spin-flip terms need to be considered, leading to

$$\rho(T) = R_{\mathrm{imp}} \left(1 - 4J\rho_0(\epsilon_{\mathrm{F}}) \ln\left(\frac{k_{\mathrm{B}}T}{D}\right) + ...\right). \tag{2.2.3}$$

The logarithmic term arises from conduction band spins scattering at the local moment, and is present in analog calculations for quantities like the local magnetization or entropy as well [6]. Kondo showed [8], that (2.2.3) is already in good agreement with experimental data of dilute Fe in Au for low temperatures. However, in the limit $T \to 0$ the resistivity diverges to infinity, which is unphysical. Kondo's perturbative calculations are no longer valid below a certain temperature, i.e. the Kondo temperature T_{K}. Finding a theory for the physical behavior of magnetic alloys in this regime is referred to as the "Kondo problem".

2.3. Kondo Problem

Following Kondo's publication in 1964, many researchers were inspired to solve the Kondo problem. As it turned out, higher order terms could not cancel the divergence. Abrikosov [52] improved Kondo's theory to find second order terms proportional to $\left(1 + 2J\rho_0(\epsilon_{\mathrm{F}}) \ln\left(\frac{k_{\mathrm{B}}T}{D}\right)\right)^{-1}$. He was able to resolve the divergence for $T \to 0$, but in the anti-ferromagnetic case $J > 0$, he obtained a singularity at

$$T_{\mathrm{K}} = \frac{D}{k_{\mathrm{B}}} e^{-1/(2J\rho_0)}, \tag{2.3.4}$$

which is here identified as the Kondo temperature. In quantum-field theories, such a logarithmic singularity is called an infra-red problem.

A fruitful approach was developed by Anderson [53], referred to as "poor man's scaling". He realized, that the divergence is generated by terms of the type $\ln(\epsilon/D)$. If the system was renormalized in a way, that D is reduced, the occurrence of the divergence could be successively shifted to smaller energies ϵ. A smaller bandwidth D corresponds to the highest bath excitations being eliminated. Anderson chose a more general version of (2.2.1), i.e. the anisotropic Kondo model (AKM)

$$H_{\mathrm{AKM}} = H_{\mathrm{B}} + J_z S^z_{\mathrm{imp}} S^z + \frac{1}{2} J_\perp \left(S^+_{\mathrm{imp}} S^- + S^-_{\mathrm{imp}} S^+\right), \tag{2.3.5}$$

with anisotropic coupling parameters $J_\perp$ and J_z. Here J_z determines, whether the coupling is ferromagnetic or anti-ferromagnetic and $J_\perp \geq 0$. Anderson applied a perturbative RG procedure, yielding an effective low-energy model with renormalized coupling parameters. In lowest order these parameters satisfy the simple flow equations

$$\frac{dJ_\perp}{d\ln D} = -2\rho_0 J_\perp J_z, \qquad \frac{dJ_z}{d\ln D} = -2\rho_0 J_\perp^2. \tag{2.3.6}$$

It is convenient to plot the solutions of Eq. 2.3.6 in a diagram with J_z on the horizontal and $J_\perp$ on the vertical axis. The flow for decreasing D is then depicted as arrows. Depending on the initial values for the coupling parameters, different fixed points of the flow can be reached by lowering D. For $J_z < -J_\perp$ we reach a ferromagnetic fixed point with $J_\perp = 0$. Here spin-flip processes are suppressed, leading to the formation of a stable local magnetic moment. For that reason it is called the local moment fixed point (LMFP). In all other cases, the couplings diverge to positive infinity, which is the strong coupling fixed point (SCFP). The line $|J_\perp| = -J_z$ represents a transition of the Kosterlitz-Thouless type.

In the isotropic case, for weak coupling $\rho_0 J \ll 1$ and for a constant DOS of the conduction band, the Kondo temperature (2.3.4) is found to be constant under the flow of D. By applying the poor man's scaling in third order, one obtains an improved version of (2.3.4) as

$$T_\mathrm{K} = \frac{D}{k_\mathrm{B}}\sqrt{2\rho_0 D}e^{-1/(2J\rho_0)}. \tag{2.3.7}$$

With poor man's scaling the Kondo problem can be solved in higher order perturbations due to the down-scaling of D. The ferromagnetic case is exactly solvable this way. However, in the physically more relevant anti-ferromagnetic case, the coupling diverges when lowering D, as mentioned above. For that reason, a perturbative treatment is no longer possible and calculations are restricted to $D \approx \max\{k_\mathrm{B}T, k_\mathrm{B}T_\mathrm{K}\}$.

Numerous attempts have been made in the 60's and early 70's to tackle the Kondo problem perturbatively, however, all approaches failed for anti-ferromagnetic coupling between the local moment and the conduction band. In 1974, K. G. Wilson [22] was able to solve the Kondo problem for the s-d model by applying a logarithmic discretization to the conduction band. The relevant energies of the Kondo problem span from the bandwidth D to small temperatures $k_\mathrm{B}T \ll D$, leading to the divergence of $\ln(\frac{k_\mathrm{B}T}{D})$ (see Eq. (2.2.3)). Wilson discretized this energy spectrum in a way, that the natural logarithmic function is divided into a finite number of identical terms. Hence each energy scale contributes equally to the expression. Upon that idea, Wilson developed the NRG approach to the Kondo problem, which is non-perturbative and thus avoids the infra-red divergencies. In 1980, Wilson's numerical results were later confirmed by analytical calculations [54, 55] using the Bethe-ansatz technique [56]. As the NRG is the foundation of our OQS approach, it is discussed in detail in Chap. 3.

2.4. Single Impurity Anderson Model

Anderson introduced the SIAM Hamiltonian

$$H_{\mathrm{SIAM}} = H_{\mathrm{S}} + H_{\mathrm{SB}} + H_{\mathrm{B}} \tag{2.4.8}$$

$$H_{\mathrm{S}} = \epsilon_d \sum_{\sigma} d_{\sigma}^{\dagger} d_{\sigma} + U d_{\uparrow}^{\dagger} d_{\uparrow} d_{\downarrow}^{\dagger} d_{\downarrow}. \tag{2.4.9}$$

to explain the formation of local magnetic moments in a metallic environment. This model comprises a free electron bath H_{B} of Eq. (1.0.1), coupled via the hybridization term H_{SB} of Eq. (1.0.2) to the local impurity H_{S}. This impurity has an energy level ϵ_{d} and an on-site Coulomb repulsion U, if the impurity site is doubly occupied. In that sense, the SIAM can be interpreted as an atomic Hubbard model [57]. For the $3d$ electrons of transition metals, as well as the $4f$ electrons of rare earth elements, the Coulomb interaction is on the order of several eV according to theoretical estimates [58] and experimental results.

In contrast to the Kondo model, the SIAM does not only include spin-flip terms, but also allows for charge fluctuations. The interaction term is a product of four operators and thus makes the model non-trivial. Originally, the four operators were approximated by a Hartree-Fock term [13], which is bilinear in the operators and includes local expectation values. This allows for an analytical treatment, but inhibits the formation of the local magnetic moment and thus destroys the Kondo effect.

Obviously, the trivial limits of the model are the free orbital regime $V_{\mathbf{k}} = 0$ and the non-interacting case $U = 0$. Let us first consider the former case. Here the local impurity state decouples from the conduction band and can have the following three occupation states: (i) an empty impurity with energy $E_0 = \epsilon_{\mathrm{F}} = 0$, (ii) a singly occupied impurity with $E_{\sigma} = \epsilon_{\mathrm{d}}$ and (iii) the doubly occupied state with $E_2 = 2\epsilon_{\mathrm{d}} + U$. Case (ii), where the impurity is occupied with one electron, represents a local magnetic moment of spin $\pm 1/2$. If E_{σ} lies below the Fermi energy ϵ_{F} and $E_2 - E_{\sigma} > \epsilon_{\mathrm{F}}$, then case (ii) is thermally favored and so a local moment is formed in this atomic limit.

Now, by including a small hybridization $V_{\mathbf{k}}$, the SIAM Hamiltonian (2.4.9) can be shown by a Schrieffer-Wolff transformation [16] to be identical to the Kondo Hamiltonian (2.2.1) in lowest order in $V_{\mathbf{k}}$. Here we use the identities $S^+ = d_\uparrow^\dagger d_\downarrow$, $S^- = d_\downarrow^\dagger d_\uparrow$ and $S^z = \frac{1}{2}(n_{\mathrm{d},\uparrow} - n_{\mathrm{d},\downarrow})$ of local operators with $n_{\mathrm{d},\sigma} = d_\sigma^\dagger d_\sigma$. In the symmetrical case $\epsilon_\mathrm{d} = -U/2$, the effective exchange coupling between the localized spin and the conduction electrons is

$$J = \frac{4V^2}{U} = \frac{4\Gamma}{\pi\rho_0 U}, \tag{2.4.10}$$

which is always ≥ 0, i.e. the coupling is anti-ferromagnetic, and thus the spins are favored to be aligned anti-parallelly.

The case $k_\mathrm{B}T \ll U < D$ and $V = 0$ (i.e. $J = 0$ in the s-d model) corresponds to the LMFP, where the impurity is magnetic and is decoupled from the conduction band. If then $U/T \to 0$, the free orbital fixed point (FOFP) is reached, where all local states are degenerate. This fixed point is not included in the Kondo model. If, on the other hand, $V \to \infty$ (i.e. $J \to \infty$) for finite U, we obtain the SCFP, where the impurity is so strongly coupled to the operator $c_{0,\sigma}$ of Eq. (1.0.4), that this subsystem effectively decouples from the remaining band excitations. More details on the fixed point regimes of the SIAM can be found in Sec. 3.6.

Poor man's scaling can be applied to the SIAM as well. A reduction of the bandwidth leads to a renormalization of the parameters ϵ_d, U and V, respectively [59]. The hybridization Γ is a scaling invariant and can thus serve as a general energy scale. When D reaches the order of the other parameters, perturbation theory begins to break down, i.e. no further renormalization is possible. If D is the smallest system energy, real charge fluctuations between the impurity and the conduction band are prohibited. However, virtual fluctuations are possible and can be taken into account by transforming to the s-d model.

If, starting from the local moment regime, the parameters ϵ_d and U are varied so that either $|E_0 - \epsilon_\mathrm{F}|$ or $|E_2 - \epsilon_\mathrm{F}|$ approaches the hybridization Γ, the impurity is no longer singly occupied, i.e. local charge fluctuations have a relevant impact. This is called the "intermediate valence regime", which is the regime of interest for certain rare earth compounds, where the f-levels lie near the Fermi level [6]. Here Γ is not the smallest energy scale, i.e. $V_{\mathbf{k}}$ cannot be treated as a perturbation parameter, and thus Eq. (2.4.9) can no longer be approximated by the s-d model.

The SIAM is the most simple model for describing magnetic impurities in metals. However, in some materials other aspects, such as orbital degeneracy, Hund's rule couplings, spin orbit interactions and local environment effects need to be considered [60, 61, 62]. This would lead to more complicated impurity Hamiltonians H_{imp} with higher dimensionality. Other possible extensions are a multi-impurity Anderson model or coupling between impurities [63].

In the context of the NRG, different QIMs can relatively flexibly be incorporated into the algorithm. Since the main focus of this thesis is to extend the NRG to an OQS approach (see Chap. 4), we restrict our investigations to the most simple models and leave more sophisticated examples to later applications.

2.5. Interacting Resonant Level Model

In 1970, Anderson and Yuval showed, that at low temperatures the s-d model (2.2.1) can, for a particular coupling $J_z = J_{\mathrm{T}}$ (the Toulouse limit [53]), be interpreted as a much simpler model, called RLM [64]. Here the energy scale Γ needs to be replaced by the Kondo temperature T_{K}. This effect is represented as the Kondo resonance in the local spectral function of the Kondo model. The Hamiltonian of the RLM is similar to the SIAM (2.4.9), but the spin DOF is omitted and thus the Coulomb repulsion is dropped. Vigman and Finkel'shtein [65] later proposed a generalization of the RLM, which is referred to as the interacting resonant level model (IRLM) in the literature, by adding a Coulomb interaction U between the impurity and the conduction band electrons. The IRLM is the minimal model for describing valence-fluctuating systems. Both the RLM and the IRLM describe a phase-shifted Fermi liquid [66, 67]. In the interacting case, the RLM Hamiltonian is extended by

$$H_U = U(d^\dagger d - \langle d^\dagger d\rangle_0)(c_0^\dagger c_0 - \langle c_0^\dagger c_0\rangle_0). \tag{2.5.11}$$

Here $\langle d^\dagger d\rangle_0 = \langle c_0^\dagger c_0\rangle_0 = \frac{1}{2}$ are the ground state expectation values at $\epsilon_{\mathrm{d}} = 0$ for half filling. This way, $\epsilon_{\mathrm{d}} = 0$ is the resonance point of the system. By implementing a perturbation theory for small U, a treatment for the Kondo problem for low temperatures was found without the need for a renormalization. In the non-interacting case, the spectral function is represented by a Lorentzian shaped resonance around the impurity level ϵ_{d} with a width of Γ (see App. A.1). By introducing $U > 0$, this energy scale is renormalized to the effective value Γ_{eff}, which is comparable to the Kondo temperature T_{K}. The low-energy fixed point of the IRLM is equivalent to its non-interacting counterpart for the renormalized hybridization $\Gamma \rightarrow \Gamma_{\mathrm{eff}}$ [68].

The additional DOF of the IRLM allows one to map a general AKM onto this spinless model [65, 18], since both models have similarities with respect to, for example, the partition function and the susceptibility. Here we can substitute the transverse coupling by $J_\perp = 2V$ and the longitudinal coupling by $J_z = \sqrt{2}U + (2 - \sqrt{2})/\rho_0$ [67]. Consequently, for a special $U < 0$ a Kosterlitz-Thouless type transition can be reached. Lowering U from here on lets one enter the ferromagnetic case, while by increasing U Fermi-liquid behavior is observed. A mapping of the AKM onto a spinless model can be advantageous for numerical reasons.

Foundational work regarding the IRLM has been done by Vigman [65], as well as Schlottmann [68, 18]. Camacho *et al* [69] investigated the IRLM in equilibrium, while Güttge *et al* [30, 36], as well as Nghiem *et al* [70] applied it to non-equilibrium dynamics in single-band systems. There also exist numerous applications to two band systems [71, 72, 66, 73, 74, 75].

2.6. Experimental Realization of the Kondo Effect

In the following we present two possibilities to detect the Kondo effect in a real experiment. The explanations are inspired by Ref. [76] and the reader is referred to this source for further information, as well as Ref. [77].

Quantum Dots

Nano-scale lithography enables the building of devices that allow for realizing the Kondo effect with scalable parameters. QDs are examples for such devices, which represent artificially localized electrons coupled to a lead of free electrons. The magnetic moments occur due to the very small capacitance C. Here the free electrons are represented as a two-dimensional electron gas, located at the interface of two semiconducting layers. By applying a gate voltage V_g, electrodes on the surface are negatively charged to confine the electron gas between them. A special configuration of those electrodes lets one separate a relatively small number of electrons of the gas to form a QD. Varying V_g allows to influence the size of the QD and thus the orbital levels. By placing contacts with a voltage V in the electron gas, a controllable current I is induced, that can be directed through the QD. Depending on the direction of the current, one part of the gas serves as the "source" for the QD, while the other one is called the "drain". Here the local energy level ϵ_d of the impurity, the hybridization Γ_S

(Γ_{D}) to the conduction band electrons of the source (drain), as well as the bias voltage are tunable. External parameters like the temperature T and a magnetic field B are variable as well [78]. In order for the QD to be magnetic, it needs to comprise an odd number of electrons, with the highest energy level being occupied by one spin-$\frac{1}{2}$ electron.

By varying the gate voltage V_{g} and measuring the conductance dI/dV for different T, the Kondo effect can be observed. When sweeping V_{g}, several dips of the conductance appear, which can be explained by the "Coulomb blockade". To understand this effect, consider that an itinerant electron, entering the QD from the source, needs to overcome the Coulomb-repulsion $U \propto \frac{e^2}{2C}$ of the locally confined electrons. Thus, when the Fermi-energy lies well below U, a Coulomb blockade is formed, where further transitions to the QD are inhibited. For lower temperatures this effect is enhanced. By varying V_{g}, the local energy level ϵ_{d} can be tuned in such a way, that either the highest occupied or the lowest unoccupied state of the QD lies around the Fermi-level, which supports the conductance of electrons. For temperatures $T \leq T_{\mathrm{K}}$ the Kondo-effect emerges [79]. In a three-dimensional material with magnetic impurities, we expect the conductivity to decrease (i.e. the resistivity to increase) with further lowering temperature, since the increased interaction leads to stronger electron scattering. This can be observed in QDs with an even number of electrons. However, in a voltage gate regime, where the number of electrons in the QD is odd (i.e. the QD possesses a net spin), the interaction helps to overcome the Coulomb blockade and thus increases the conductance. This can be explained by the Kondo resonance.

Scanning Tunnelling Microscopy

Above we have discussed the Kondo effect for an artificial magnetic impurity. However, the anomalous conductivity behavior was first discovered in an impure metal. To examine the effect in those metals, the scanning tunnelling microscopy (STM) can be used. This technique is capable of imaging surfaces with atomic resolution, as well as even physically moving atoms. Here a non-magnetic metal with magnetic impurities (adatoms) on its surface serves as the sample. The STM spectroscopy uses a conducting tip to measure the conductance (which is proportional to the local density of states) at different points of identical distance to the sample. At each point, the bias voltage V between the sample and the tip is varied to obtain conductance curves. If the sample temperature is well below T_{K}, the Kondo resonance can be observed as a dip of the conductance around $V \approx 0$, if the tip is located in proximity to an impurity. The dip can be explained by increased electron scattering off of the impurity or the screening cloud of free electrons. For experimental measures of the Kondo effect with STM see e.g. Ref. [80, 81, 82].

3. Numerical Renormalization Group

In the previous chapter we gave an overview of different QIMs and their applications. Here we focus on the NRG as a powerful method to solve these models. One major challenge for theoretical models when dealing with QISs is the fact, that the environment typically comprises a wide range of excitation energies. Any suitable model thus needs to include the high-energy bandwidth as well as arbitrarily low energies at the same time. When treating such a system perturbatively, the coupling to those low energies often causes so-called "infra-red divergences" [6], which poses a limit to the accessible energy range. Unfortunately, the inclusion of exponentially small energies is essential for the Kondo problem discussed in Sec. 2.3. Consequently, a non-perturbative approach is required, that is able to describe a small impurity coupled to a broad continuum of energies. The RG [53] allows to bridge between distant energy scales by performing a series of renormalization steps. The NRG developed by Wilson [22] is a specific numerical implementation of this approach that is entirely non-perturbative. It is based upon a logarithmic discretization of the conduction band with a discretization parameter Λ. The advantage of the discretization is a separation of the energy scales of the system, allowing to neglect certain high-energy states, whose contributions are thermally suppressed. This truncation of states significantly reduces the Hilbert space of the system, enabling a numerical treatment. When applying truncation to the calculation of time-dependent operators, one needs to pay special attention not to neglect essential information or to "over-count" certain states. This can be ensured by using the Anders-Schiller basis (ASB), which will be addressed in detail in Sec. 3.7. In the case of an OQS approach to the NRG, the correct handling of the truncation is rather complicated and hence we devoted the entire chapter 6 to it.

When applied correctly, the truncation of high-energy states does not significantly impair the results (see Sec. 3.3). However, the discretization itself has major consequences, as it turns the QIS into a closed system, which lacks true dissipation and a finite lifetime of impurity excitations. This will be explained in Sec. 3.8 to 3.10. Several canonical methods for compensating the discretization errors are introduced. In contrast, the main objective of this thesis is to establish a new method for recovering the continuum and thus correcting the most relevant discretization errors by introducing true dissipation to the system. This will be addressed in detail in the subsequent sections.

The presentations of the NRG follow the review by Bulla *et al* [25] and include the references [22, 14, 15, 26].

3.1. Discretization of the Bath Continuum

As a basis for our considerations we start with the Hamiltonian

$$H = H_{\text{imp}} + H_{\text{bath}} + H_{\text{imp-bath}} \tag{3.1.1}$$

of a general QIS, where

$$H_{\text{bath}} = \sum_{k\nu} \epsilon_k c^{\dagger}_{k\nu} c_{k\nu} \tag{3.1.2}$$

describes a continuum of energies ϵ_k within the bandwidth D, while

$$H_{\text{imp-bath}} = \sum_{k\nu} V_k \left(d_\nu c^{\dagger}_{k\nu} + d^{\dagger}_\nu c_{k\nu} \right) \tag{3.1.3}$$

is the coupling term between the impurity site and each bath excitation with hybridization V_k. Here $d_\nu^{(\dagger)}$ annihilates (creates) an impurity excitation while $c_{k\nu}^{(\dagger)}$ annihilates (creates) the k-th bath mode. The general flavor index ν can e.g. denote the spin of the particles, will be dropped from here on and can be recovered at the end. Note that the Hamiltonians H_{bath} and $H_{\text{imp-bath}}$ are basically identical to the definitions (1.0.1) and (1.0.2), respectively. We choose a different notation here, that is in accordance with typical NRG notation. The notation of Chap. 2 will be recovered in Chap. 4, since in the context of the BRF a different partitioning of the total QIS is required. In contrast to Chap. 2, we restrict to the absolute wave-vectors $k = \|\mathbf{k}\|$ from now on, which implies s-wave like conduction band states. The impurity Hamiltonian H_{imp} can be customized to specific QIMs. We concentrate on fermionic operators only, even though the NRG formalism can be adapted to bosonic models or combinations of both as well (see spin-boson model [83] or Bose-Fermi Kondo model [84]).

The impurity Greens function for a simple single orbital QIS is given by

$$G_{d,d^\dagger}(z) = \left(z - \epsilon_\mathrm{d} - \Sigma(z) - \Delta(z)\right)^{-1}, \tag{3.1.4}$$

with ϵ_d being the impurity level energy. The model specifications made in H_imp enter the self-energy $\Sigma(z)$, while all bath information is aggregated in the so-called spectral coupling function (or hybridization function)

$$\Gamma(\omega) = \lim_{\delta\to 0^+} \mathfrak{Im}\Delta(\omega - i\delta) = \pi \sum_k V_k^2 \delta(\omega - \epsilon_k) \tag{3.1.5}$$

with

$$\Delta(z) = \sum_k \frac{|V_k|^2}{z - \epsilon_k}. \tag{3.1.6}$$

Consequently, all transformations of the total Hamiltonian that keep $\Gamma(\omega)$ unchanged do not influence the impurity dynamics and are thus equivalent. We assume that the support of $\Gamma(\omega)$ lies within the interval $[-D, D]$. The Hamiltonian (3.1.1) can be expressed as the continuous version

$$H = H_\mathrm{imp} + \int_{-D}^{D} d\epsilon g(\epsilon) a_\epsilon^\dagger a_\epsilon + \int_{-D}^{D} d\epsilon h(\epsilon) \left(d a_\epsilon^\dagger + d^\dagger a_\epsilon\right) \tag{3.1.7}$$

by mapping the conduction band onto a one-dimensional energy representation of s-wave symmetry[1]. Here $g(\epsilon)$ is the dispersion, while $h(\epsilon)$ denotes the hybridization. The s-wave conduction band operators $a_\epsilon^{(\dagger)}$ satisfy the standard fermionic commutation relations. It has been shown [85] that the functions $g(\epsilon)$ and $h(\epsilon)$ can be directly related to the hybridization function $\Gamma(\omega)$. This means that for a given $\Gamma(\omega)$ one function can be chosen relatively freely, while the other one is then determined [25].

The continuous conduction band is logarithmically discretized, as shown in Fig. 3.1. The parameter $\Lambda > 1$ defines intervals with discretization points $x_n = \pm\Lambda^{-n}, n = 0, 1, 2, ...$ and a width of $d_n = (1 - \Lambda^{-1})\Lambda^{-n}$. This logarithmic discretization is the optimal choice for infra-red problems, such as the Kondo problem, since each interval equally contributes to a logarithmically diverging integral $\int d\epsilon\epsilon^{-1}$. The number of intervals needed to reach a specific energy scale is determined by the choice of Λ.

---

[1] i.e. the diagonal free electron part of the Hamiltonian is turned into a semi-infinite tight-binding chain by a Lanczos algorithm

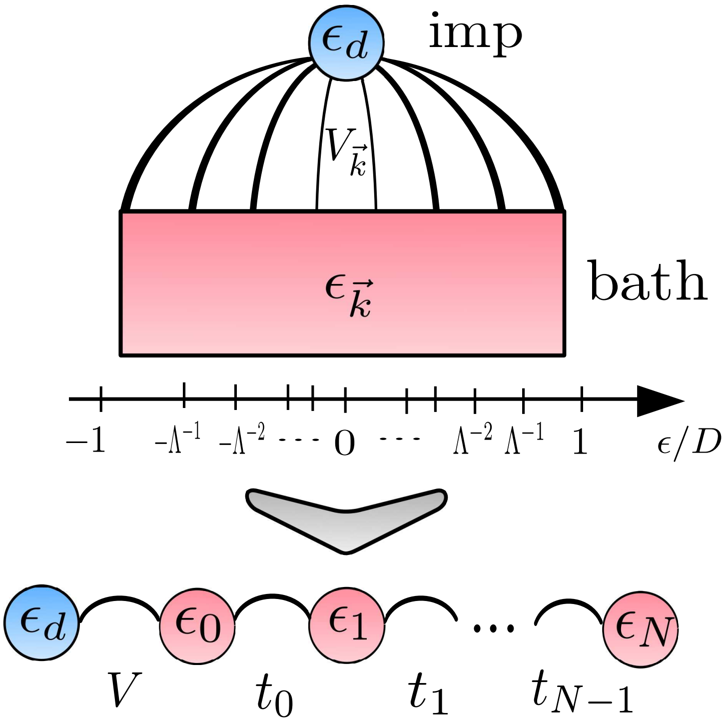

Figure 3.1.: Illustration of the bath discretization and the construction of the Wilson chain. On the top, the system of Eq. (3.1.1) is depicted for the RLM with a local energy level ϵ_d. The bath modes are characterized by the wavevector $\vec{k}$. Beneath the bath, the conduction band spectrum is plotted on an energy axis, discretized with the parameter Λ. At the bottom, the Wilson chain is depicted, which is constructed from the QIS, where each chain site corresponds to a single mode extracted from each discretized interval.

The continuous operators are expressed in a Fourier expansion

$$a_\epsilon = \sum_{n=0}^{\infty} \sum_{p=-\infty}^{\infty} a^+_{np} \Psi^+_{np}(\epsilon) + a^-_{np} \Psi^-_{np}(\epsilon) \tag{3.1.8}$$

on each interval n with

$$\Psi^\pm_{np}(\epsilon) = \begin{cases} e^{2\pi i p \epsilon / d_n} / \sqrt{d_n} & , \Lambda^{-(n+1)} \leq \epsilon < \Lambda^n \\ 0 & \text{else.} \end{cases} \tag{3.1.9}$$

This shifts the ϵ-dependence of the operators to exponential functions. If we define the hybridization function to be section-wise constant on each interval, i.e.

$$h(\epsilon) = h_n^{\pm},\ x_{n+1} < \pm\epsilon < x_n, \tag{3.1.10}$$

only the $p = 0$ modes survive the integration in (3.1.7) which means that only the $p = 0$ modes directly couple to the impurity. It is important to note, that a sectionwise constant hybridization function $h(\epsilon)$ does not imply any restrictions on $\Gamma(\epsilon)$, since all remaining ϵ-dependence can be shifted into the dispersion $g(\epsilon)$.

If the expansion (3.1.8) is applied to the conduction electron part, the $p \neq 0$ do not vanish automatically. In fact, neglecting those terms is the discretization of the bath, which is the essential part of the NRG. This step is justified by the fact, that only the $p = 0$ modes directly couple to the impurity while the coupling between different p-modes is $\propto (1 - \Lambda^{-1})$. Thus the approximation becomes exact in the limit $\Lambda \to 1^+$. The neglection of the $p \neq 0$ modes has proven in numerous cases to be a well-justified approximation [22]. However, in more complex cases like spectral functions or non-equilibrium dynamics this discretization largely impacts the results. This point will be addressed in the second half of this chapter.

So far, the Hamiltonian is expanded in the operators $a_{n0}^{\pm}$. The part $H_{\text{imp-bath}}$ in (3.1.1) can be reinterpreted as the coupling of the impurity site to an operator f_0 defined by $V f_0^{(\dagger)} = \sum_k V_k c_k^{(\dagger)}$. The operator f_0 corresponds to the conduction band spin $\mathbf{S}$ the impurity couples to in real-space in the Kondo model (cf. Sec. 2.2). Constructing a new set of mutually orthogonal operators $f_{n\sigma}^{(\dagger)}$ from the $a_{n0}^{\pm}$ operators by a standard tri-diagonalization procedure, namely the Housholder algorithm, that uses $f_{0\sigma}^{(\dagger)}$ as a reference point, leads to a conduction band in the form of a tight-binding chain with the zeroth site coupled to the impurity. In particular we obtain

$$H_{N_\text{C}} = H_\text{imp} + V\left(d^\dagger f_0 + d f_0^\dagger\right) + \sum_{n=0}^{N_\text{C}} \epsilon_n f_n^\dagger f_n + \sum_{n=0}^{N_\text{C}-1} t_n \left(f_n^\dagger f_{n+1} + f_n f_{n+1}^\dagger\right) \tag{3.1.11}$$

with N_C being the chain length. In the exact case, we have a semi-infinite chain with $N_\text{C} \to \infty$. Equation (3.1.11) is called Wilson chain and its parameters are the on-site energies ϵ_n and the hopping matrix elements t_n. While the initial values ϵ_0 and t_0 can be calculated analytically, the remaining chain parameters are defined by a recursion relation (cf. Appendix A of Ref. [83]). If we presume a general hybridization function, the recursion relations can only be solved numerically. However, for a constant and symmetric hybridization function $\Gamma(\omega)$ on the interval $[-D, D]$, we have $\epsilon_n = 0$ for all

n, and [22]

$$t_n = S \frac{1-\Lambda^{-n-1}}{\sqrt{1-\Lambda^{-2n-1}}\sqrt{1-\Lambda^{-2n-3}}} \Lambda^{-n/2} \tag{3.1.12}$$

with

$$S = \frac{D}{2}(1+\Lambda^{-1}) \tag{3.1.13}$$

for the hopping elements[2]. In the limit of large n this reduces to

$$t_n \to S\Lambda^{-n/2}. \tag{3.1.14}$$

In this section we have transformed the general QIM of Eq. (3.1.1) into the one-dimensional representation (3.1.11) with logarithmically decreasing hopping parameters t_n. Obviously, the Wilson chain is not exact, since the $p \neq 0$ terms have been neglected. However, the chain model does have a physical meaning in the three-dimensional case. Each chain site can be interpreted as a shell of conduction band states which is located concentrically around the impurity. The zeroth Wilson chain site represents the shell with the maximum of its wave-function closest to the impurity and is coupled to the next closest shell, and so on [22, 6].

In a practical application the length N_C of the Wilson chain needs to be chosen finitely. Besides the neglect of the $p \neq 0$ modes, this adds a second approximation to the model. To assess the effect of a finite N_C, consider a semi-infinite chain and choose an arbitrary chain site n. By artificially switching off the hopping parameter t_n, the first n chain sites are decoupled from the semi-infinite rest chain. In this context, t_n can be seen as a perturbation parameter. If the n-th chain site is far remote from the impurity, t_n is small and the quality of the approximation is high. In second order the contribution of t_n is $O(\beta_{N_\mathrm{C}}/\Lambda)$ (see Ref. [14], Appendix F) with β_{N_C} being an effective inverse temperature of the Wilson chain that grows by N_C and Λ (see Eq. (3.5.28)). Thus the chain length N_C defines the accuracy of the procedure.

---

[2] For details on the calculation see Ref. [85]. Here a pseudo-gap system $\Gamma(\omega) \propto |\omega|^r$ is considered. By setting $r = 0$ a constant hybridization is obtained.

3.2. Renormalization Approach

In the previous section we have described the mapping of a general QIM to a semi-infinite chain, whose hopping terms exponentially decrease with the distance to the impurity. For this model an iterative RG procedure can be set up by defining (3.1.11) as a Wilson chain of length N_C. The chain of length $N_\mathrm{C}+1$ can then be constructed by adding the $N_\mathrm{C}+1$-th chain site with the coupling t_{N_C}, which represents the lowest energy scale of the new system. We define

$$\bar{H}_{N_\mathrm{C}+1} = \frac{\Lambda^{N_\mathrm{C}/2}}{S} H_{N_\mathrm{C}+1} \tag{3.2.15}$$

so that the eigenenergies of $\bar{H}_{N_\mathrm{C}+1}$ are $\sim \mathcal{O}(1)$. The recursion relation

$$\bar{H}_{N_\mathrm{C}+1} = \sqrt{\Lambda}\bar{H}_{N_\mathrm{C}} + \bar{t}_{N_\mathrm{C}} \left(f^\dagger_{N_\mathrm{C}} f_{N_\mathrm{C}+1} + f_{N_\mathrm{C}} f^\dagger_{N_\mathrm{C}+1} \right). \tag{3.2.16}$$

can be understood as an RG transformation step $\bar{H}_{N_\mathrm{C}+1} = \mathrm{RG}[\bar{H}_{N_\mathrm{C}}]$. For more details on the RG see e.g. Ref. [6]. Note, that the on-site energies are $\epsilon_n = 0$, assuming a symmetrical DOS. On each iteration step the Hamiltonian is inflated by a factor of $\sqrt{\Lambda}$, and a new site is coupled to the end of the chain. Consequently, the starting point of this NRG procedure is

$$\bar{H}_{N_\mathrm{C}=0} = \frac{\Lambda^{-1/2}}{S} H_0, \tag{3.2.17}$$

which corresponds to a two-site system of the impurity and the zeroth conduction electron site.

We defined the dimensionless hopping parameters

$$\bar{t}_n = t_n \Lambda^{n/2}/S, \tag{3.2.18}$$

which converge to 1 for large n. For a bosonic bath we have $t_n \propto \Lambda^{-n}$ and so a similar scaling can be defined [86].

From Eq. (3.2.15) it follows, that the total scale of a Wilson chain of length N_C is given by

$$\omega_{N_\mathrm{C}} = S\Lambda^{-(N_\mathrm{C}-1)/2}, \tag{3.2.19}$$

which we refer to as the "NRG scale".

We can define the many-particle energies $E_r^{N_\mathrm{C}}$

$$\bar{H}_{N_\mathrm{C}} \left| r; N_\mathrm{C} \right\rangle = E_r^{N_\mathrm{C}} \left| r; N_\mathrm{C} \right\rangle, r = 1, ..., N_\mathrm{S} \tag{3.2.20}$$

with the eigenstates $\left| r; N_\mathrm{C} \right\rangle$ and N_S being the dimension (number of states) of $\bar{H}_{N_\mathrm{C}}$. The assumption that the energies $E_r^{N_\mathrm{C}}$ resemble the exact eigenspectrum of the Wilson chain of length N_C is referred to as the standard "NRG approximation" [22]. The RG flow can be characterized by this chain length dependent energy spectrum.

We want to point out the versatility of the NRG as an impurity solver. In the iterative scheme of the NRG method additional flavors, e.g. the spin or a channel DOF, can easily be included. Fruthermore, the recursion relation (3.2.16) is independent of the starting point H_0. Thus, the impurity Hamiltonian H_imp may be chosen freely and so the NRG can be adapted to different QIMs. In the context of a numerical realization the free electron part can be implemented as a basis class while for each impurity model a new class can be derived from it, inheriting its properties. Any addition to the program can in turn be derived from this class. In fact, for this thesis we have used an existing NRG code, that exploits this efficient architecture.

3.3. Truncation Scheme

In the RG procedure described above the Fock space dimension grows by a factor of d for each added chain site. In the case of the SIAM we have $d = 4$, since the spin is included as a DOF for each particle. This exponential growth quickly sets a limit to the application of the method. Here Wilson's idea of discarding a fraction of $\frac{d-1}{d}$ of the eigenstates by each iteration comes into play. By this truncation of states the Fock space dimension is kept constant for all iterations. To be precise, the Wilson chain is iteratively enlarged by additional chain sites until a certain number N_S of states is reached. Now the Hilbert space of the system is truncated by discarding the respective number of high-energy states on each consecutive iteration. This seemingly drastic approximation is justified by the exponentially decreasing hopping parameters t_n. With each added chain site the total eigenspectum of the Wilson chain undergoes a correction of the order of t_n. If N_C is large, the relative correction of the high energies is negligible. Consequently, the eigenspectrum of a short Wilson chain adequately defines the high-energy states while long chains are required to correctly calculate the low-energy states.

The discretization parameter Λ defines how many iterations are required to reach a certain low-energy scale. By choosing a large Λ the effective energy scale is significantly decreased by each NRG iteration. Consequently, low-energies are reached fast and, at the same time, the number N_S of states kept on each iteration can be chosen to be small. However, the prize one pays are discretization artifacts, such as unphysical oscillations in non-equilibrium dynamics. To combat this effect, z-averaging can be applied, which will be described in Sec. 3.10.

The truncation scheme used in this thesis is implemented as follows. The Hamiltonian is constructed iteratively without truncation until a Fock space dimension $\geq N_\mathrm{S}$ is reached. Now all higher energies are discarded until we are left with N_S states, which will be kept and used to build the new Hamiltonian. The iteration of the first truncation is defined as $n = n_\mathrm{min}$. From here on a fraction of $\frac{d-1}{d}$ states is discarded on each iteration to keep the Fock space constant in dimension. In Fig. 3.3 the quality of different values for N_S is examined for the non-equilibrium case.

In addition to the rescaling of the Hamiltonian and the truncation of high-energy states, on each iteration step n the eigenenergies are shifted by an offset $\Delta E_n = -E_0^n$, with E_0^n being the ground state energy of iteration n. Consequently, the ground state energy is zero at each iteration and the total offset grows with each step. This ensures that in the Boltzmann term $e^{-\beta E_i}$ no divergences occur due to negative energies, which could pose a problem to the natural limitation of computer data types. Furthermore, the offset in combination with the rescaling by $\sqrt{\Lambda}$ on each iteration and the truncation of high energies keeps the eigenspectrum within a constant window of $[0, \mathcal{O}(1)]$.

3.4. Explicit Algorithm

Here we give an overview over the basic application of the NRG method and discuss how the successive enlargement of the Wilson chain is executed in practice.

The first step is to identify the symmetries of the system by finding operators, which commute with the Hamiltonian. These symmetries cause the Hamiltonian to be a block-diagonal matrix, with each block labeled by a distinct set of quantum numbers defined by those operators. In the SIAM the particle number operator

$$Q_{N_\mathrm{C}} = \sum_{n=0}^{N_\mathrm{C}} \left(\sum_\sigma f_{n\sigma}^\dagger f_{n\sigma} - 1 \right) \tag{3.4.21}$$

and the z-component

$$S^z_{N_\mathrm{C}} = \frac{1}{2}\sum_{n=0}^{N_\mathrm{C}}\sum_{\sigma}\sigma f^\dagger_{n\sigma} f_{n\sigma} \tag{3.4.22}$$

of the total spin fulfill these criteria. Each Hamiltonian $\overline{H}_{N_\mathrm{C}}$ is thus divided into independent blocks with quantum numbers defined by the eigenvalues of the corresponding operators $(Q_{N_\mathrm{C}}, S^z_{N_\mathrm{C}})$ to the eigenstate $|r; N_\mathrm{C}\rangle$ defined by Eq. (3.2.20).

Let $|k;n\rangle$ denote a kept eigenstate of the NRG iteration n. To each of those kept states we can construct $d = 4$ states of the new basis as

$$\begin{aligned}|k,0;n+1\rangle &= |k;n\rangle\\ |k,\sigma;n+1\rangle &= f^\dagger_{n+1\sigma}\,|k;n\rangle\\ |k,2;n+1\rangle &= f^\dagger_{n+1\uparrow}f^\dagger_{n+1\downarrow}\,|k;n\rangle\,,\end{aligned} \tag{3.4.23}$$

where the order of the chain operators in the last line is convention. From here on we define $\alpha \in \{0, \sigma, 2\}$ as the general DOF for the new site.

Suppose we know the quantum numbers of the state $|k;n\rangle$, then the quantum numbers of the new four states are defined as well. Now we can use Eq.(3.2.16) to calculate the new Hamiltonian in the new basis as

$$\begin{aligned}&\langle k,\alpha;n+1|\,\bar{H}_{n+1}\,|k',\alpha';n+1\rangle = \sqrt{\Lambda}E^n_k\delta_{kk'}\delta_{\alpha,\alpha'}\\ &+\bar{t}_n\sum_\sigma \langle k,\alpha;n+1|\left(f^\dagger_{n\sigma}f_{n+1\sigma} + f_{n\sigma}f^\dagger_{n+1\sigma}\right)|k',\alpha';n+1\rangle\,.\end{aligned} \tag{3.4.24}$$

For symmetry reasons we are left with the calculation of

$$\langle k,\alpha;n+1|\,f^\dagger_{n\sigma}f_{n+1\sigma}\,|k',\alpha';n+1\rangle = \langle k,\alpha;n+1|\,f^\dagger_{n\sigma}\,|k',\alpha;n+1\rangle\,\delta_{\alpha'-\sigma,\alpha}. \tag{3.4.25}$$

The operator $f_{n+1\sigma}$ acts on the $n+1$-th chain site and thus reduces α' by σ. Since $f^\dagger_{n\sigma}$ is diagonal in the DOF of chain site $n+1$, we obtain the restriction $\alpha'-\sigma = \alpha$. To calculate the remaining term $\langle k,\alpha;n+1|\,f^\dagger_{n\sigma}\,|k',\alpha;n+1\rangle$, we require the transformation

$$|r;n\rangle = \sum_{s\alpha} P_{r,s}[\alpha]\,|s,\alpha;n-1\rangle \tag{3.4.26}$$

with

$$P_{r,s}[\alpha] = \langle s, \alpha; n-1 | r; n \rangle \,, \tag{3.4.27}$$

which is calculated on the previous NRG iteration and then stored[3]. The Hamiltonian (3.4.24) can now be diagonalized to obtain the new eigenbasis $|r; n+1\rangle$, which is then divided into kept and discarded states.

3.5. Thermodynamic Expectation Values

To calculate thermodynamic quantities, a temperature of the system needs to be defined. Due to the properties of the Boltzmann distribution, we can define a narrow temperature window, within which the NRG calculations of a finite chain are valid. The upper limit of this window is determined by the number N_{S} of kept states, while the lower limit is given by the NRG scale $\omega_{N_{\mathrm{C}}}$ (see Eq. (3.2.19)). By choosing a specific finite chain length N_{C}, we accept the neglect of the following chain sites, which would generate an increasingly small energy correction $\Delta E_{N_{\mathrm{C}}}$ to the eigenspectrum. For these corrections to be negligible, i.e. $e^{-\beta_{N_{\mathrm{C}}}(E+\Delta E_{N_{\mathrm{C}}})} \approx e^{-\beta_{N_{\mathrm{C}}}E}$, the temperature has to be chosen such that $T_{N_{\mathrm{C}}} \gg \Delta E_{N_{\mathrm{C}}}$, so the lower limit is given by the NRG scale. A truncation of the high-energy states, on the other hand, implies, that states down to a certain energy $E_{\max}$ are negligible, i.e. $e^{-\beta_{N_{\mathrm{C}}}E_{\max}} \approx 0$. This is fulfilled for $T_{N_{\mathrm{C}}} \ll E_{\max}$. In practical applications we define the system temperature as

$$T_{N_{\mathrm{C}}} = \omega_{N_{\mathrm{C}}}/\bar{\beta} = \bar{\beta}^{-1}\frac{D}{2}(1+\Lambda^{-1})\Lambda^{-(N_{\mathrm{C}}-1)/2}. \tag{3.5.28}$$

with $\bar{\beta} \in [0.5, 1]$ [25]. When referring to a temperature of the finite chain, always the definition (3.5.28) is used. The temperature decreases when increasing N_{C} or Λ, respectively. This corresponds to reaching a better resolution of the smallest energies. With the system temperature defined, thermodynamic impurity quantities can be calculated, where in the most simple examples only the eigenspectrum enters. Equilibrium expectation values of local system operators O_{S}, like the occupation operator $n_{\mathrm{d}} = d^{\dagger}d$ of the impurity, require the knowledge of specific matrix elements. Assuming

---

[3] The conventional way of calculating the matrix elements (3.4.25) is to define an operator O_{α}, that creates a particle with quantum number α on the $n+1$-th site [87]. The fermionic operators are than commuted to bundle all operators that act on the site $n+1$, which influences the sign of the total expression. This composite operator can be defined by a simple chart, while the remaining part is calculated on the iteration n.

that we diagonalized a Wilson chain of length N_C, with N_S being the number of kept low-energy states, the expectation value of the local operator is given by

$$\langle O_\mathrm{S}\rangle = \frac{1}{Z_{N_\mathrm{C}}}\sum_{r=1}^{d\times N_\mathrm{S}} e^{-\beta_{N_\mathrm{C}}E_r^{N_\mathrm{C}}}\,\langle r;N_\mathrm{C}|\,O_\mathrm{S}\,|r;N_\mathrm{C}\rangle\,, \tag{3.5.29}$$

where Z_{N_C} is the partition sum and the index r sums over all low-energy eigenstates left at the last NRG-iteration. In (3.5.29) we omit the high-energy states of iterations $< N_\mathrm{C}$, since their contribution is suppress by the Boltzmann factor. To evaluate the expression, the matrix elements $\langle r;N_\mathrm{C}|\,O_\mathrm{S}\,|r;N_\mathrm{C}\rangle$ are required, which can be obtained by a successive application of the unitary transformation (3.4.26).

3.6. Energy Flow and Fixed Points

A fixed point in the RG procedure is a Hamiltonian $\overline{H}$ which is not altered by the RG step, i.e. $\overline{H} = \mathrm{RG}[\overline{H}]$. In the context of the NRG, a fixed point is reached, if the eigenspectrum of the Wilson chain is not changed by adding two additional sites. Two sites are required here, since the Wilson chain exhibits an even-odd behavior with respect to its length. This effect is typical for fermionic finite-size systems. The reason for the even-odd behaviour in the SIAM lies in the fact, that for an even chain length N_C there is on average an even number of electrons in the system, which can build pairs to form the ground state, called singlet state. Those singlets have a spin of zero, since the spins of two fermions compensate each other. Chains with odd length posses an additional spin doublet. Particle-hole symmetric even chains have an eigenspectrum which is half positive, half negative. In the ground state, the negative half will be fully occupied with two electrons each. For odd chain lengths we have an additional zero eigenvalue.

A flow diagram in the context of the NRG is defined as the eigenspectrum $E_r^{N_\mathrm{C}}$ plotted against the chain length N_C. As explained in Sec. 3.5, a higher chain length corresponds to a lower effective temperature of the Wilson chain. Sections of the flow diagram, in which the eigenspectrum is constant under a small variation of N_C, correspond to an approach to a fixed point. In between those sections we have crossover regimes, where the system transitions from one approximate fixed point to another. The choice of local parameters has an impact on the length of those constant sections and thus on the position of the crossover regimes.

Let us discuss the fixed points of the SIAM as an example. The argumentation here follows the work of Krishna-murthy *et al* [14, 15]. As a first step, we choose the local parameters, i.e. the impurity energy ϵ_d, the Coulomb repulsion U (see Sec. 2.4 for details) and the external magnetic field B. Since the magnetic field is not included in the above mentioned literature, we set $B = 0$. The local parameters define the energy required to occupy the impurity states $|0\rangle, |\sigma\rangle$ and $|2\rangle$, respectively. A higher energy relates to a lower probability for the state to be occupied. A large U decreases the probability for double occupation. A large and positive ϵ_d favors the empty state, while a negative ϵ_d leads to single occupation. If the external magnetic field is chosen $B \neq 0$, we introduce a discrimination of the single spin states to the system.

Depending on the occupation of the impurity we distinguish five different fixed points. In the FOFP all four states are degenerate and thus equally occupied. The frozen impurity fixed point (FIFP) allows only for the empty state, while the LMFP comprises only singly occupied states. The valence fluctuation fixed point (VFFP) prohibits the doubly occupied state and the SCFP effectively decouples the impurity and the zeroth Wilson chain site from the rest of the chain. The LMFP can be reached by choosing U large and $\epsilon_\mathrm{d} < 0$. Thus the singly occupied state represents a local magnetic moment with two degenerate spin states. The FIFP and the VFFP are only accessible in the asymmetric case $\epsilon_\mathrm{d} \neq -U/2$. The former can be obtained, if ϵ_d is the dominant energy, so an occupation of the impurity is energetically prohibited. The latter is reached, if U is dominant and $\epsilon_\mathrm{d} \to 0$, so the empty and the singly occupied state are degenerate, while the doubly occupied state is prohibited. In the FOFP all impurity states are degenerate, which can only be realized if T is the dominant energy and thus all states are equally thermally accessible. Finally, the SCFP implies that the hybridization $\Gamma \propto \sqrt{V}$ between the impurity and the zeroth bath mode is dominant. In this case, those two sites effectively decouple from the remaining bath.

A flow diagram starts at high T and then successively lowers the temperature (i.e. N_C is increased). Depending on the relative value of the particular parameters in comparison to T, different fixed points are approached. In the case of the symmetrical Anderson model (SAM) we start with the FOFP and transition to the LMFP, before finally reaching the SCFP. This fixed point is stable[4]. The temperature regime at which the crossover from the LMFP to the SCFP happens is defined as the Kondo-temperature T_K (see Sec. 2.1). If $U \ll \Gamma$, the LMFP is skipped and the system directly transitions from the FOFP to the SCFP.

---

[4] For more details, e.g. on the Fermi-liquid behavior at very low temperatures, see Ref. [6].

3.7. Complete Basis Set

To calculate local dynamical properties, such as the single-particle Green's function or non-equilibrium expectation values, a restriction to the basis of the last NRG iteration (as in Eq. (3.5.29)) is not sufficient. In fact, we need to define a complete basis set and a corresponding reduced density matrix for each NRG iteration, which will be elaborated on in this section.

So far, we have interpreted the NRG formalism as an iterative enlargement of a Wilson chain and, by that, as an iterative enlargement of the Fock space as well (if no truncation of states is applied). However, for the purpose of evaluating dynamical expectation values of physical operators, a different point of view proves to be advantageous. Consider to start at a full Wilson chain of length N_C, but with all hopping terms t_n set to zero. Thus, the Fock space of the system is of dimension d^{N_C} times the impurity DOF. By applying the NRG algorithm of iteration n (starting with $n = 0$), the hopping element t_n is switched on. At this point, each eigenvalue and eigenstate of the system is degenerate by a factor of $d^{N_\mathrm{C}-n}$. This factor is defined by the number of DOF of the residual chain (which is called the "environment"). The d DOF of the n-th site are labeled by α_n. Thus, an eigenstate of the iteration n can be written as $|r, e_n; n\rangle$ with $e_n = \{\alpha_{n+1}, ..., \alpha_{N_\mathrm{C}}\}$ being the entire environment.

Up to iteration $n = n_\mathrm{min}$ the eigenbasis of the Hamiltonian H_n still comprises a complete basis of the full Fock space of the chain of length N_C, since the environment e_{n_min} provides the degeneracy. To keep the dimension of the problem numerically manageable, the eigenstates are divided into the low-energy kept states $|k, e_{n_\mathrm{min}}; n_\mathrm{min}\rangle$ and the high-energy discarded states $|l, e_{n_\mathrm{min}}; n_\mathrm{min}\rangle$. The labeling of the indices distinctly defines a state as "kept" k or "discarded" l. Only the kept states $|k, \alpha_{n_\mathrm{min}}, e_{n_\mathrm{min}+1}; n_\mathrm{min}\rangle$ are used to span the new subspace. However, together with the discarded states they still form a complete basis. To maintain this completeness after the next iteration we have to combine the discarded states $|l, e_{n_\mathrm{min}}; n_\mathrm{min}\rangle$ of iteration n_min with those discarded states $|l, e_{n_\mathrm{min}+1}; n_\mathrm{min} + 1\rangle$ of the next iteration as well as the kept states $|k, e_{n_\mathrm{min}+1}; n_\mathrm{min} + 1\rangle$. This leads to a completeness relation

$$\mathbf{1}_m = \sum_{n=n_\mathrm{min}}^{m} \sum_{l,e} |l, e; n\rangle \langle l, e; n| + \sum_{k,e} |k, e; m\rangle \langle k, e; m| \, . \tag{3.7.30}$$

for a chain upto the iteration m. Note that from here on we will use the general environment index e, if no further specification is required. By performing the entire

NRG algorithm up to $m = N_\mathrm{C}$ and defining all eigenstates of the last iteration as discarded, one can identify a complete basis

$$\mathbf{1}_{N_\mathrm{C}} = \sum_{n=n_\mathrm{min}}^{N_\mathrm{C}} \sum_{l,e} \left|l,e;n\right\rangle \left\langle l,e;n\right| , \tag{3.7.31}$$

also known as the ASB [23], as a sum over all states discarded in the NRG algorithm. By subtracting both equations, one can express the kept states

$$\sum_{k,e} \left|k,e;m\right\rangle \left\langle k,e;m\right| = \sum_{n=m+1}^{N_\mathrm{C}} \sum_{l,e} \left|l,e;n\right\rangle \left\langle l,e;n\right| \tag{3.7.32}$$

as a sum of all following discarded states. Note that to exploit the complete basis set, information on the discarded states needs to be memorized on each NRG iteration.

Let us now consider the trace of a product of two arbitrary Wilson chain operators A and B, which is a generalized form of calculating expectation values. We use definition (3.7.31) to define an ASB for the evaluation of the trace and insert $\mathbf{1}_n$ between the two operators to obtain

$$\begin{aligned}
\mathrm{Tr}\{AB\} &= X + Y \\
X &= \sum_{n=n_\mathrm{min}}^{N_\mathrm{C}} \sum_{l,e} \sum_{n'=n_\mathrm{min}}^{n-1} \sum_{l',e'} \left\langle l,e;n\right| A \left|l',e';n'\right\rangle \left\langle l',e';n'\right| B \left|l,e;n\right\rangle \\
Y &= \sum_{n=n_\mathrm{min}}^{N_\mathrm{C}} \sum_{l,e} \sum_{r,e'} \left\langle l,e;n\right| A \left|r,e';n\right\rangle \left\langle r,e';n\right| B \left|l,e;n\right\rangle .
\end{aligned} \tag{3.7.33}$$

The sum over the indices r includes kept and discarded states, while l and l' only include discarded states. In Y only one NRG iteration n enters, while in X matrix elements enter, that couple two different iterations n and n'. These matrix elements are complicated to calculate, wherefore we rewrite it in the form

$$\begin{aligned}
X &= \sum_{n'=n_\mathrm{min}}^{N_\mathrm{C}} \sum_{l,e} \sum_{n=n'+1}^{N_\mathrm{C}} \sum_{l',e'} \left\langle l,e;n\right| A \left|l',e';n'\right\rangle \left\langle l',e';n'\right| B \left|l,e;n\right\rangle \\
&= \sum_{n'=n_\mathrm{min}}^{N_\mathrm{C}} \sum_{k,e} \sum_{l',e'} \left\langle k,e;n\right| A \left|l',e';n\right\rangle \left\langle l',e';n\right| B \left|k,e;n\right\rangle
\end{aligned} \tag{3.7.34}$$

by using (3.7.32). We arrive at

$$\mathrm{Tr}\{AB\} = \sum_{n=n_{\min}}^{N_C} \sum_{r,s \notin k,k'} \sum_{e,e'} \langle r,e;n| A |s,e';n\rangle \langle s,e';n| B |r,e;n\rangle . \tag{3.7.35}$$

which is a sum over equal shell contributions only [29]. Here the indices r and s can either be kept or discarded but the kept-kept combination is excluded from the summation. Let us now assume that A is a local operator, i.e. it only acts on DOF of the NRG iterations $n \leq n_{\min}$ (as an example consider the non-equilibrium expectation value of the impurity occupation number. Here $A = n_\mathrm{d}$ and B is the time-dependent density matrix). Such a local operator is diagonal in the environment DOF e, meaning that Eq. (3.7.35) can be written as

$$\mathrm{Tr}\{AB\} = \sum_{n=n_{\min}}^{N_C} \sum_{r,s \notin k,k'} A_{r,s}(n) B^{\mathrm{red}}_{s,r}(n). \tag{3.7.36}$$

Here the reduced operator

$$B^{\mathrm{red}}_{s,r}(n) = \sum_{e} \langle s,e;n| B |r,e;n\rangle \tag{3.7.37}$$

has been introduced. Let us assume that the operator B is time-dependent, then Eq. (3.7.37) yields

$$\begin{aligned}\sum_{e} \langle s,e;n| B(t) |r,e;n\rangle &= \sum_{e} \langle s,e;n| e^{-iHt} B(0) e^{iHt} |r,e;n\rangle \\ &\approx e^{i(E^n_r - E^n_s)t} B^{\mathrm{red}}_{s,r}(n).\end{aligned} \tag{3.7.38}$$

Here $B(0)$ is defined by the initial Hamiltonian H^{i}. Furthermore, we have used the NRG approximation of Sec. 3.2, which assumes that the eigenenergies E^n_r of NRG iteration n represent the exact spectrum of the Wilson chain, as well as a "full Hamiltonian approximation", that assumes that the discretized Wilson chain Hamiltonian H_{N_C} represents the full Hamiltonian H. In fact, no other approximation has entered the expression so far, since complete basis sets have been used. The full Hamiltonian approximation is well justified in certain regimes, but induces finite-size effects in dynamic properties, since the Wilson chain is a closed system that lacks true dissipation. These effects are well understood and will be discussed in Sec. 3.8 to 3.10 in more detail.

3.8. Spectral Function

Let us proceed to the calculation of impurity spectral functions with the NRG. The single-particle retarded Green's function (GF) is defined by

$$G_{A,B}(t) = -i\Theta(t)\mathrm{Tr}\{\rho[A(t), B]_\varsigma\} = -i\Theta(t)\mathrm{Tr}\{A\chi(t)\} \tag{3.8.39}$$

with $[A, B]_\varsigma = AB - \varsigma BA$ and $\varsigma = 1$ for bosonic operators A, B and $\varsigma = -1$ for fermionic operators. The time-dependency is included in the operator $A(t) = e^{iHt}Ae^{-iHt}$ in the first step. By defining

$$\chi = [B, \rho]_\varsigma. \tag{3.8.40}$$

we can shift the time-dependency to $\chi(t) = e^{-iHt}\chi e^{iHt}$. By choosing $A = d_\sigma$ and $B = d_\sigma^\dagger$ as fermionic impurity operators, we obtain the local GF. The spin-index σ will be omitted from here on. Equation (3.7.36) can easily be adapted to this case as

$$\begin{aligned} G_\mathrm{d}(t) &= -i\Theta(t) \sum_{n=n_\mathrm{min}}^{N_C} \sum_{r,s \notin k,k'} d_{r,s}(n)\chi^\mathrm{red}_{s,r}(n;t) \\ &\approx -i\Theta(t) \sum_{n=n_\mathrm{min}}^{N_C} \sum_{r,s \notin k,k'} d_{r,s}(n)\chi^\mathrm{red}_{s,r}(n)e^{i(E^n_r - E^n_s)t}, \end{aligned} \tag{3.8.41}$$

where in the last step the NRG and full Hamiltonian approximations have been applied. The calculation of the matrix elements $d_{r,s}(n) = \langle r;n|\, d\, |s;n\rangle$ follows the procedure explained in Sec. 3.5. The reduced operator

$$\chi^\mathrm{red}_{s,r}(n) = \sum_e \langle s, e; n|\, [d^\dagger, \rho]_\varsigma \,|r, e; n\rangle \tag{3.8.42}$$

requires knowledge of the equilibrium density matrix ρ. We use the ASB to obtain the full density matrix (FDM) [88]

$$\rho = \frac{1}{Z}e^{-\beta H} = \frac{1}{Z}\sum_{m=n_\mathrm{min}}^{N_\mathrm{C}} d^{N_\mathrm{C}-m} \sum_l e^{-\beta E^m_l}\, |l;m\rangle \,\langle l;m|\,. \tag{3.8.43}$$

Here the factor $d^{N_\mathrm{C}-m}$ stems from the summation over the environment DOF e for all iterations $> m$. Instead of $\mathbf{1}_{N_\mathrm{C}}$, one could use $\mathbf{1}_n$ here to make sure, that $m \leq n$, which limits the number of summation terms in (3.8.41). Also, the fact that all discarded states are orthogonal to each other combined with (3.7.32) yields

$$\langle k,e;n|l,e';n'\rangle = 0,\ n \geq n', \tag{3.8.44}$$

which excludes numerous terms in (3.8.41). The overlap elements can be obtained by successively applying the unitary transformation (3.4.26) to reduce n down to n'. It is possible to approximate the density matrix in the spirit of the NRG by the last iteration

$$\rho \approx \frac{1}{Z_{N_\mathrm{C}}} \sum_l e^{-\beta E_l^{N_\mathrm{C}}} \left|l;N_\mathrm{C}\right\rangle \left\langle l;N_\mathrm{C}\right|, \tag{3.8.45}$$

which simplifies the calculation but is only valid if Λ is chosen large enough. It is obligatory to inversely run through all NRG iterations in order to calculate the reduced operator $\chi^{\mathrm{red}}(n)$, or rather the reduced density matrix $\rho^{\mathrm{red}}(n)$, from the respective iteration $n+1$. For an application of the NRG to spectral functions see [24, 88]. In [89] the time-dependent spectral function is covered, which will not be discussed here.

From (3.8.41) the single-particle equilibrium spectral function can be calculated by performing the half-sided Fourier transform

$$G_\mathrm{d}(z) = \int_0^\infty dt e^{izt} G_\mathrm{d}(t) \tag{3.8.46}$$

and then taking the imaginary part to obtain

$$\begin{aligned} A_\mathrm{d}(\omega) =& -\frac{1}{\pi}\mathfrak{Im} G_\mathrm{d}(z=\omega+i0^+) \\ =& \frac{1}{\pi}\sum_{n=n_\mathrm{min}}^{N_C} \sum_{r,s\notin k,k'} d_{r,s}(n)\chi^{\mathrm{red}}_{s,r}(n)\delta\Big(\omega-(E_r^n-E_s^n)\Big). \end{aligned} \tag{3.8.47}$$

The spectral function $A_\mathrm{d}(\omega)$ is expressed as a sum of delta-distributions. First of all, since only ASBs have been employed, the sum rule

$$\sum_{n=n_\mathrm{min}}^{N_C} \sum_{r,s\notin k,k'} d_{r,s}(n)\chi^{\mathrm{red}}_{s,r}(n) = \mathrm{Tr}\{\rho[d,d^\dagger]_s\} \tag{3.8.48}$$

is still fulfilled (see appendix A of Ref. [24]). Secondly, the Wilson chain is a closed system, so its time-evolution is purely unitary and thus its excitations lack a natural finite lifetime. In our OQS approach we solve this problem by introducing true dissipation to the system (see Chap. 4 and 5). In the closed system case, the delta-distributions of Eq. (3.8.47) need to be broadened artificially to display a continuous spectrum. Typically, a logarithmic Gaussian of the form

$$\delta(\omega-\omega_n)\rightarrow\frac{e^{-b^2/4}}{\sqrt{\pi}b\omega_n}\exp\left(-\left(\frac{\ln(\omega/\omega_n)}{b}\right)^2\right)\tag{3.8.49}$$

is chosen [34]. This ensures that excitations with positive energies ω_n have no weight in the negative half $\omega<0$ and vice versa. Also, the logarithmic function allows for a higher resolution of smaller energies. For the smallest energies $\omega_n\approx 0$, a Lorentzian broadening

$$\delta(\omega-\omega_n)\rightarrow\frac{1}{\pi}\frac{b}{(\omega-\omega_n)^2+b^2}\tag{3.8.50}$$

needs to be chosen [32]. Both broadening functions are normalized and thus they maintain the sum-rule (3.8.48).

Let us turn to the SIAM (cf. Sec. 2.4) as a standard model for the application of the NRG to spectral functions. The local one-particle GF for complex frequencies z can be defined as

$$G_\sigma(z)=\langle\langle d_\sigma,d_\sigma^\dagger\rangle\rangle(z)=(z-\epsilon_d-\Sigma_\sigma(z))^{-1}\tag{3.8.51}$$

via its one-particle self-energy $\Sigma_\sigma(z)=\Delta(z)+\Sigma_\sigma^U(z)$ as in Eq. (3.1.4). The hybridization $\Delta(z)$ is trivially known. The non-trivial extension to the spectral function is the introduction of the local Coulomb repulsion U, expressed in the correction

$$\Sigma_\sigma^U(z)=U\frac{F_\sigma(z)}{G_\sigma(z)}.\tag{3.8.52}$$

The term

$$F_\sigma(z)=\langle\langle d_\sigma d_{\bar\sigma}^\dagger d_{\bar\sigma},d_\sigma^\dagger\rangle\rangle(z)\tag{3.8.53}$$

defines another GF for a composite impurity operator with $\bar\sigma=-\sigma$. Now two possible ways for calculating the GF emerge. The first one is to directly calculate $G_\sigma(z)$ from Eq. (3.8.41), which is referred to as the raw Green's function. The second way is to calculate $F_\sigma(z)$ and $G_\sigma(z)$ via (3.8.41) and then build the self-energy (3.8.52) from those two quantities, which then gives the final GF (3.8.51). This way is superior to the

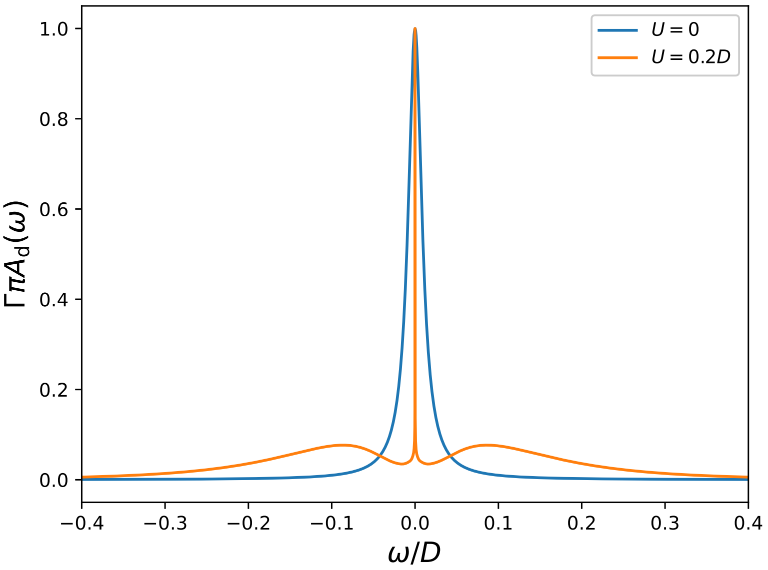

Figure 3.2.: The local spectral function $A_\mathrm{d}(\omega)$ for the SIAM in the particle-hole symmetric case $\epsilon_\mathrm{d} = -U/2$ for $T \to 0$. The NRG parameters are $N_\mathrm{C} = 30, \Lambda = 3, D = 100\Gamma, N_\mathrm{S} = 500$ and an artificial broadening of $b = 0.8$ has been chosen.

raw GF, since a quotient of two numerical functions $F_\sigma(z)$ and $G_\sigma(z)$ is relatively stable with respect to numerical errors (for more details see Ref. [35]). When calculating the self-energy by simply inverting Eq. (3.8.51), numerical errors of the method add up to cause an unphysical case, where

$$\mathfrak{Im}\Sigma_\sigma^U(z) \leq 0 \tag{3.8.54}$$

is not always fulfilled. This could be tackled by increasing the artificial broadening b of the delta-peaks to avoid unphysical oscillations, which in turn washes out information from the spectrum. The effect of the self-energy correction (3.8.52) is to smooth out the curve for small energies, while peaks at high energies are more pronounced. In the SIAM this relates to the Kondo-resonance and the Hubbard-peaks, respectively. The calculation of $F_\sigma(z)$ in the NRG is straightforward by setting $A = d_\sigma d_{\bar{\sigma}}^\dagger d_{\bar{\sigma}}$ and $B = d_\sigma^\dagger$ in Eq. (3.8.39).

In Fig. 3.2 we plot the spectral function of the SAM. In the non-interacting case $U = 0$ one obtains a simple Lorentzian of width Γ, which can be derived analytically (see App. A.1). On the other hand, the interacting case $U > 0$ reveals non-trivial physical properties. For $\omega \approx 0$ (SCFP) we observe the so-called Kondo-peak (or Abrikosov-Suhl resonance), which can be attributed to spin fluctuations. For the particle-hole symmetric case, the value $A_{\mathrm{d}}(0) = 1/\pi\Gamma$ is given by the Friedel sum rule. At the Kondo temperature $\omega \approx T_{\mathrm{K}}$ the system transitions into the LMFP and the spectral function drops to almost zero. From here on, the spectral function grows again to form the so-called Hubbard satellites around $\omega = \epsilon_{\mathrm{d}}$ and $\omega = \epsilon_{\mathrm{d}} + U$, respectively, which are generated by charge fluctuations. For higher temperature the FOFP is reached and the spectral function approaches zero at $\omega \to \pm\infty$.

The spectral function of the SAM is a typical medium for benchmarking the NRG approach. Due to the truncation, the Kondo-peak is underrated by a few percent in the raw GF. Furthermore, unphysical oscillations occur, which can be damped by the self-energy correction (3.8.52). The artificial broadening according to Eq. (3.8.49) tends to give too much weight to higher ω and by that over-broadens the Hubbard satellites.

3.9. Non-Equilibrium Dynamics

Besides spectral functions the non-equilibrium dynamics of a local system operator O_{S} can be calculated in a similar way, but faces different challenges due to the discretization of the bath. We obtain the time-dependent expectation value

$$O_{\mathrm{S}}(t) = \mathrm{Tr}\{\rho(t) O_{\mathrm{S}}\} = \sum_{n=n_{\min}}^{N_C} \sum_{r,s \notin k,k'} O_{r,s}(n) \rho^{\mathrm{red}}_{s,r}(n) e^{i(E^n_r - E^n_s)t} \tag{3.9.55}$$

from Eq. (3.7.36) by choosing $A = O_{\mathrm{S}}$ and $B = \rho$. Equation (3.9.55) is the "fundamental TD-NRG equation", and the tool used for its calculation with the NRG is called time-dependent numerical renormalization group (TD-NRG) [29, 23]. The calculation of the reduced density matrix

$$\rho^{\mathrm{red}}_{s,r}(n) = \sum_e \langle s, e; n| \, \rho^{\mathrm{i}} \, |r, e; n\rangle \tag{3.9.56}$$

turns out to be more complicated than in the case of spectral functions. Suppose we consider non-equilibrium dynamics as the transition from an initial to a final state at

$t = 0$ induced by the time-dependent Hamiltonian

$$H(t) = H^{\mathrm{i}}\Theta(-t) + H^{\mathrm{f}}\Theta(t). \tag{3.9.57}$$

Typical time-dependent parameters can be the impurity parameters, as well as the hybridization V between the impurity and the Wilson chain. The initial FDM at $t = 0$ is then defined as

$$\rho^{\mathrm{i}} = \frac{1}{Z^{\mathrm{i}}} e^{-\beta H^{\mathrm{i}}} = \frac{1}{Z^{\mathrm{i}}} \sum_{\nu=n_{\mathrm{min}}}^{N_{\mathrm{C}}} \sum_{\lambda,\epsilon} e^{-\beta E_{\lambda}^{\nu}} \left|\lambda, \epsilon; \nu\right\rangle \left\langle\lambda, \epsilon; \nu\right|, \tag{3.9.58}$$

which describes a system prepared with the initial parameters of H^{i} at $t \to -\infty$. This system is thus assumed to be well thermalized at $t = 0$. In order to distinguish the eigenstates of H^{i} from those of H^{f}, we use the corresponding Greek letters instead of the Latin ones for the initial basis states. The unitary time-evolution of the time-dependent density matrix

$$\rho(t) = e^{-iH^{\mathrm{f}}t} \rho^{\mathrm{i}} e^{iH^{\mathrm{f}}t} \tag{3.9.59}$$

is determined by the final Hamiltonian. For that reason, Eq. (3.9.55) is expressed in the eigenstates of H^{f} and we are assigned to calculate overlap elements $\langle s, e; n|\lambda, \epsilon; \nu\rangle$ of initial and final basis states of different NRG iterations $n \neq \nu$ to obtain the reduced density matrix (3.9.56). We define a complete initial basis set of

$$\mathbf{1}_n^{\mathrm{i}} = \mathbf{1}_n^{+} + \mathbf{1}_n^{-} = \sum_{\varrho,\epsilon} \left|\varrho, \epsilon; n\right\rangle \left\langle\varrho, \epsilon; n\right| + \sum_{\nu=n_{\mathrm{min}}}^{n-1} \sum_{\lambda',\epsilon} \left|\lambda', \epsilon; \nu\right\rangle \left\langle\lambda', \epsilon; \nu\right|, \tag{3.9.60}$$

where λ' denotes discarded states at iteration $\nu < n$ and ϱ denotes kept and discarded states at iteration $\nu = n$, and insert it into Eq. (3.9.56) to obtain

$$\rho_{s,r}^{\mathrm{red}}(n) = \frac{1}{Z^{\mathrm{i}}} \sum_{e} \sum_{\nu=n_{\mathrm{min}}}^{N_{\mathrm{C}}} \sum_{\lambda,\epsilon} e^{-\beta E_{\lambda}^{\nu}} \left\langle s, e; n\right| \left(\mathbf{1}_n^{+} + \mathbf{1}_n^{-}\right) \left|\lambda, \epsilon; \nu\right\rangle \left\langle\lambda, \epsilon; \nu\right| \left(\mathbf{1}_n^{+} + \mathbf{1}_n^{-}\right) \left|r, e; n\right\rangle. \tag{3.9.61}$$

By neglecting the $\mathbf{1}_n^{-}$ term, the reduced density matrix is referred to as $\rho_{s,r}^{++}(n)$ in the literature [23]. This assumption is exact, if ρ^{i} can be restricted to the last NRG iteration, as in Eq. (3.8.45). We then obtain

$$\langle l, e; n| \mathbf{1}_n^+ |\lambda; N_\mathrm{C}\rangle = \sum_\kappa S^n_{l,\kappa} \langle \kappa, e; n|\lambda; N_\mathrm{C}\rangle \tag{3.9.62}$$

for $n < N_\mathrm{C}$ and

$$\langle l; n| \mathbf{1}_n^+ |\lambda; N_\mathrm{C}\rangle = S^{N_\mathrm{C}}_{l,\lambda} \tag{3.9.63}$$

for $n = N_\mathrm{C}$. The overlap matrix elements

$$S^n_{r,\varrho} = \langle r; n|\varrho; n\rangle \tag{3.9.64}$$

can be calculated straightforwardly by running two independent NRG algorithms for H^i and H^f each, and combining all eigenstates at each iteration n. The elements $\langle \kappa, e; n|\lambda; N_\mathrm{C}\rangle$ can be obtained as described in Sec. 3.8. Thus, after completing the NRG runs, we start with $\rho^\mathrm{red}_{\varsigma,\varrho}(N_\mathrm{C})$ in the initial eigenbasis and successively calculate its contributions for different NRG-iterations $n < N_\mathrm{C}$ by applying Eq. (3.4.26). Each $\rho^\mathrm{red}_{\varsigma,\varrho}(n)$ is then turned into the final eigenbasis by

$$\rho^\mathrm{red}_{s,r}(n) = \sum_{\kappa,\kappa'} S^n_{s,\kappa} S^n_{r,\kappa'} \rho^\mathrm{red}_{\kappa,\kappa'}(n), \tag{3.9.65}$$

where only kept indices κ of the initial basis enter.

Let us discuss the limitations of the approximation of Eq. (3.8.45). As already mentioned, the quality of the NRG can always be improved by increasing the chain length N_C and thus reducing finite-size effects. However, the effective temperature of the system is defined by N_C (see Eq. (3.5.28)). Thus, to calculate systems with large N_C and finite temperature at the same time, $\bar\beta$ needs to be decreased. However, this impairs the approximation (3.8.45), since now energies of iterations $n < N_\mathrm{C}$ have a significant contribution as well. In that case we need to include all iterations and calculate all parts $\rho^{++}_{s,r}(n)$, $\rho^{+-}_{s,r}(n)$, $\rho^{-+}_{s,r}(n)$ and $\rho^{--}_{s,r}(n)$, respectively. In fact, it can be shown, that $\rho^{+-}_{s,r}(n) = \rho^{-+}_{s,r}(n) = 0$ and that the terms $\rho^{++}_{s,r}(n)$ and $\rho^{--}_{s,r}(n)$ can be calculated efficiently for the FDM by a recursive procedure, starting at $n = N_\mathrm{C}$ [90]. However, in this thesis we restrict to the approximation (3.8.45) and thus we need to chose $\bar\beta \approx 1$.

In Fig. 3.3 we display the convergence behavior of the non-equilibrium impurity occupation for the chain length N_C (panel (a) and (b)) and for the number N_S of kept

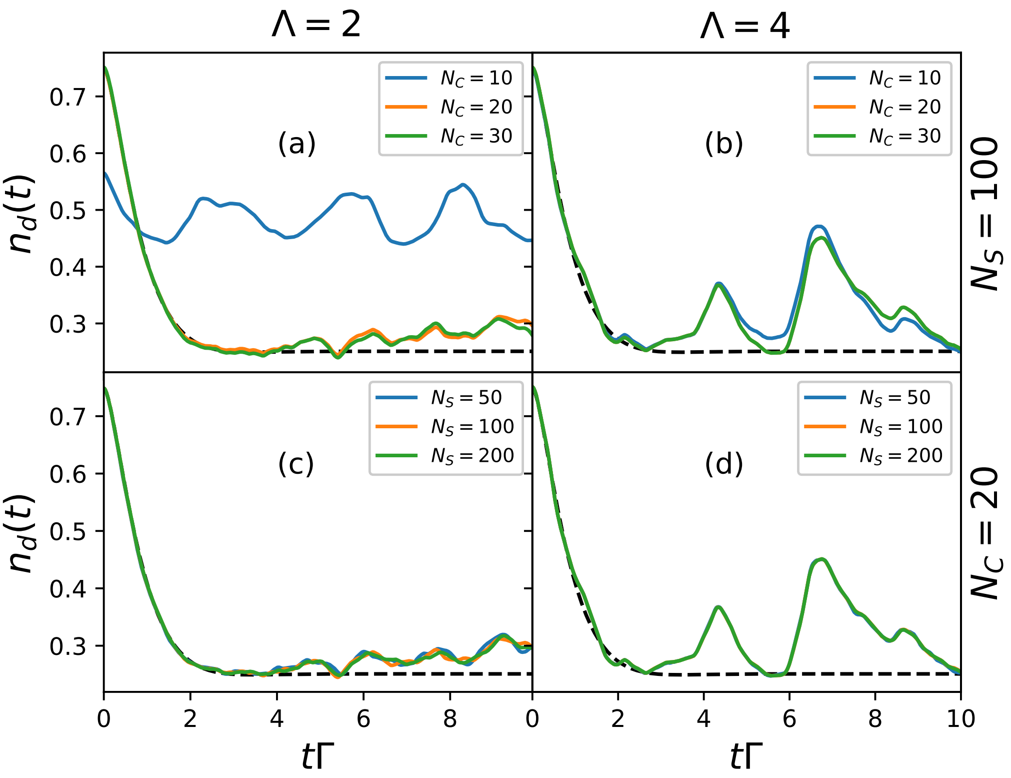

Figure 3.3.: The impurity occupation number for the RLM. We have chosen $D = 100\Gamma, \epsilon_{\mathrm{d}}^{\mathrm{f}} = -\epsilon_{\mathrm{d}}^{\mathrm{i}} = \Gamma$ and the remaining NRG parameters according to the labeling with $\bar{\beta} = 1$. The analytical solution of App. A.2 for $T \to 0$ is added as a black dashed line.

states (panel (c) and (d)) with respect to the discretization parameter Λ. We use the RLM as the most simple benchmark model here. As expected, the curves converge faster, if Λ is chosen to be large. In that sense, a large discretization parameter is superior, since less chain sites and less kept states are required to obtain a convergence to the exact discretized result, at least for short times. However, the drawback of a large Λ is displayed as well, since it increases the amplitude of unphysical oscillations. This discretization effect will be investigated in Sec. 3.10 in more detail. Note that the chain length N_{C} influences the effective temperature of the Wilson chain and thus the equilibrium values, most prominently in the blue curve of panel (a), since here $T \approx \Gamma$. Furthermore it is worth mentioning, that the NRG works astonishingly well even for a small number of kept states N_{S} compared to the total system dimension. This is seen in TD-NRG calculations [23], as well as for equilibrium spectral functions [24].

In Fig. 3.4 we display the revival effect. With increasing chain length N_{C} the

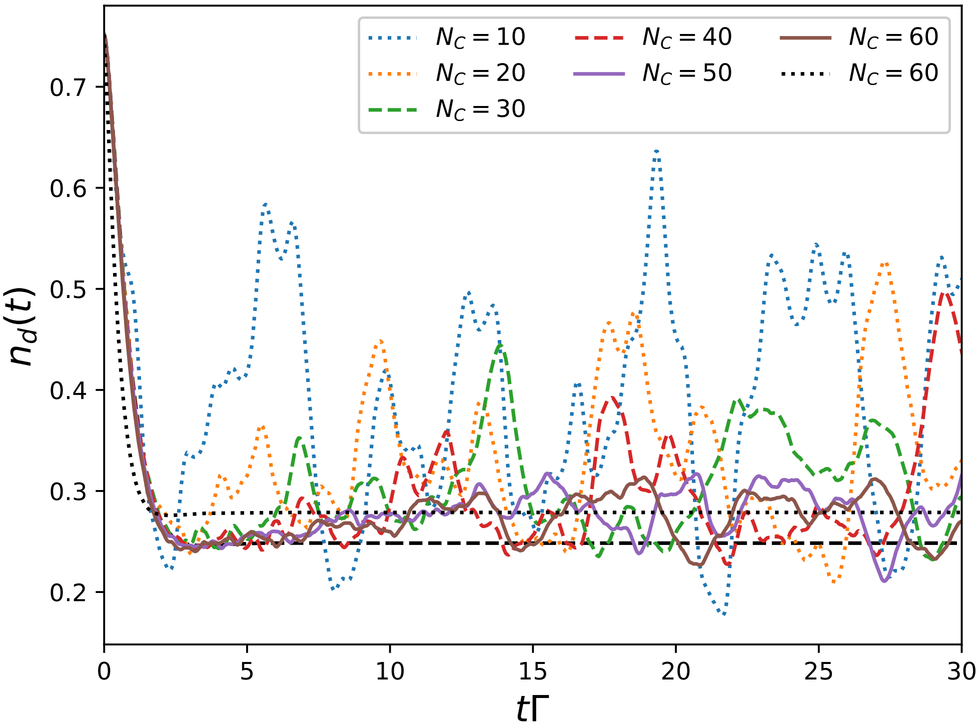

Figure 3.4.: The impurity occupation number for the RLM. We have chosen $D = 100\Gamma, \epsilon_{\mathrm{d}}^{\mathrm{f}} = -\epsilon_{\mathrm{d}}^{\mathrm{i}} = \Gamma, N_{\mathrm{S}} = 100$ and $\bar{\beta} = 1$. The chain length N_{C} is varied and the discretization parameter is adjusted to meet the temperature $T = 10^{-3}\Gamma$ for all curves. The analytical solution of App. A.2 is added as a black dashed line and a version of the purple curve that is artificially damped with $\alpha_n = \omega_n$ is added as a black dotted line.

occurrence of finite-size oscillations is delayed and so the time point, at which the numerical solution significantly deviates from the analytical one, is shifted to the right. At the same time, Λ is decreased, which damps the unphysical oscillations discussed above [30].

Independently of the choice of parameters, the TD-NRG is not able to allow for true thermalization, since the chain length N_{C} is still finite and charge reflections at the end of the chain are inevitable. A simple solution to imitate an OQS is to damp the oscillating terms of the off-diagonal part of the density matrix (ODDM) by a factor of $e^{-\alpha_n t}$ (see the black dotted line in Fig. 3.4), where the damping factor α_n is chosen in accordance with the NRG scale ω_n (see Ref. [23]). This damping relates to an artificial broadening of the respective energy modes. The system now thermalizes for $t \to \infty$ to a steady-state predicted by the diagonal ensemble [91], which is obtained by averaging Eq. (3.9.55) over $t \in [0, \tau]$ and then letting $\tau \to \infty$. This is effectively identical to setting $r = s$. However, this steady-state value is not equal to the Boltzmann distribution, and thus the correct steady-state within the NRG approximation is not reached. This is fixed by the OWC approach that we propose in Chap. 5.

3.10. Discretization Artifacts

When investigating QIMs that exceed the most simple case of the RLM, often flavor DOF (e.g. spin or multi-channel) need to be included. This increases the factor d, by which the Fock space of the Wilson chain is augmented at each NRG iteration. If the number N_S of kept states is limited due to practical reasons, the discretization parameter Λ needs to be increased to justify the truncation of high-energy states. The numerical cost can thus be reduced by $1/\ln(\Lambda)$. However, increasing the discretization takes one further away from the continuum limit $\Lambda \to 1^+$. As a direct consequence of the discretization, the hybridization function $\Gamma(\omega)$ is systematically underestimated. Therefore, the correction factor A_Λ is typically used to increase the coupling V and thus to accelerate the convergence to the continuum limit [14, 27]. For a constant hybridization the analytical correction [14]

$$A_\Lambda = \frac{1}{2}\frac{\Lambda+1}{\Lambda-1}\ln(\Lambda) \tag{3.10.66}$$

is included in all our NRG calculations.

A pronounced consequence of the choice of higher Λ are so-called discretization artifacts [26]. These are expressed as unphysical oscillations around the exact solutions with an amplitude that grows rapidly with Λ. We can significantly suppress these oscillations by simply averaging over several identical configurations of the NRG with slightly varied discretization. This is nowadays referred to as z-averaging [33]. Here we average over N_z Wilson chains, each discretized differently. To be precise, the discretization scheme is altered by choosing

$$\Lambda^{-z} < \epsilon \leq 1, \ (0 < z \leq 1) \tag{3.10.67}$$

as the first discrete interval of the bath instead of $\Lambda^{-1} < \epsilon \leq 1$ (cf. Sec. 3.1). The subsequent discretization points x_n are still scaled by a factor of $\frac{x_n}{x_{n+1}} = \Lambda$ and thus the renormalization scheme of the NRG is not affected by the introduction of z. In fact, if the influence of z was extended to the relation of the discretization points, i.e. $\frac{x_n}{x_{n+1}} = \Lambda^z$, z would merely cause a rescaling of the parameter $\Lambda \to \Lambda^z$. Instead, by solely varying the entry point of the discretization scheme, the sliding parameter z simply yields a logarithmic translation of x_n while not affecting the renormalization. In contrast to Eq. (3.1.12), the chain parameters ϵ_n and t_n need to be calculated numerically, even for a constant density of states. Only for $z = 1$ the standard scheme is recovered.

For this thesis, a z-averaging is implemented as follows. The program is performed N_z times where $z_k = k/N_z, k = \{1, ..., N_z\}$ is chosen. After completion the results are simply averaged. The bare minimum for the z-averaging is $z_1 = 0.25$ and $z_2 = 0.75$, which already significantly damps finite-size effects [26].

The procedure has already been applied to non-equilibrium dynamics [29, 23, 92, 93]. Here we can see, that the tolerance of non-equilibrium dynamics to a large discretization parameter Λ is lower than that of equilibrium properties. Wilson has early pointed out [22], that all values $\Lambda \leq 3$ reflect the continuum adequately in the latter case. However, the effect of the finite-size oscillations in the non-equilibrium case is significantly larger in a comparable range of Λ [23]. Here a z-averaging is of high importance even for $\Lambda \leq 3$.

In Fig. 3.5 the effect of z-averaging is displayed for different values of N_z. Obviously, for $t\Gamma > 6$ the TD-NRG curves perform oscillations around the curve, which can be obtained by an artificial relaxation of the ODDM (dotted curve). These oscillations are damped for increasing N_z, so that the undamped curves converge to the damped ones for shorter times. However, as discussed at the end of Sec. 3.9, the correct steady-state (indicated by the black dashed line of the analytical solution) is not reached in any of both cases.

It has been shown by Güttge *et al* [30], that the source of the discretization artifacts are back-reflections of charge at each chain site due to the discontinuous transitions between the discrete excitations. If one considers a tight-binding chain of finite length, after the local quench at $t = 0$ all charge is transported through the chain and simultaneously reaches the end of the chain. It is then reflected back and reaches the impurity again after a certain time. This revival time is influenced by the chain length. In a Wilson chain with $\Lambda > 1$, the hopping elements decrease logarithmically with the chain site n, leading to back-reflections at each site. Approximately only the fraction of $4/(\Lambda + 1)^2$ is transported from site n to $n + 2$ [19]. In contrast, the charge, that reaches the last chain site and is reflected here, is relatively small in a Wilson chain.

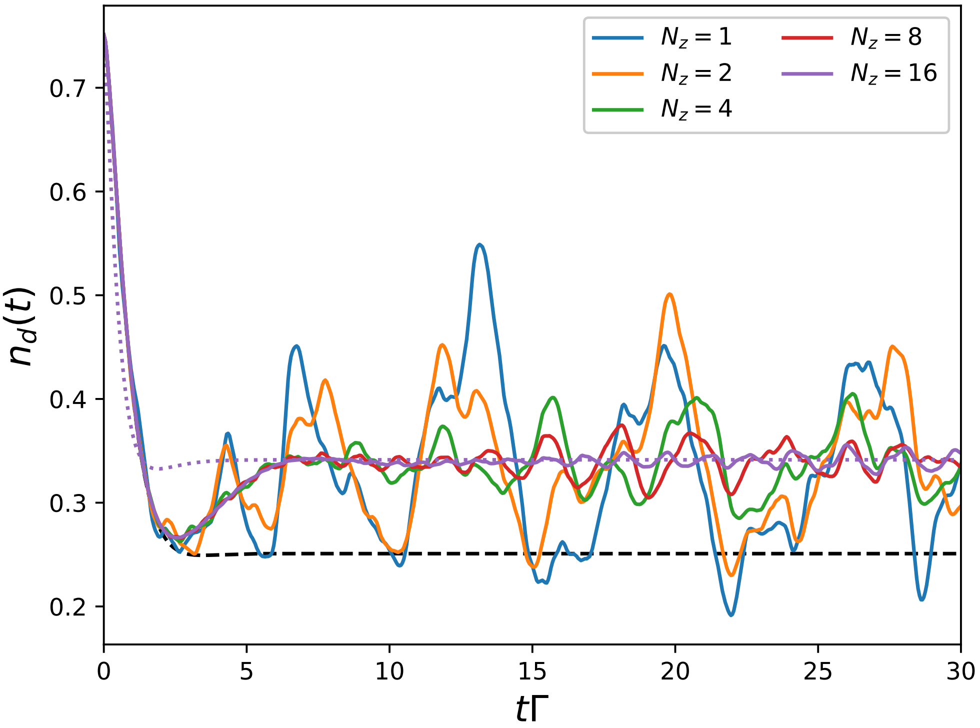

Figure 3.5.: The real-time impurity occupation for the RLM. We have chosen $D = 100\Gamma, \epsilon_{\mathrm{d}}^{\mathrm{f}} = -\epsilon_{\mathrm{d}}^{\mathrm{i}} = \Gamma, N_{\mathrm{S}} = 100, N_{\mathrm{C}} = 20, \Lambda = 4$ with $\bar{\beta} = 1$. The z-averaging is performed with different values for N_z. An artificial damping with $\alpha_n = \omega_n$ is supplemented as a purple dotted line for $N_z = 16$. The analytical solution of App. A.2 is added as a black dashed line.

Also, the charge velocity is proportional to the hopping parameters and is therefore decreased throughout the chain for $\Lambda > 1$. In that way, the Wilson chain allows for a temporary thermalization as well as an increased revival-time at the cost of finite-size oscillations.

3.11. Hybrid-NRG Approach

Above we have mentioned several ways to combat the finite-size effects in the Wilson chain. The z-averaging can, to a certain degree, smooth the oscillations induced by back-reflections at each chain site, but is not capable of reproducing the exact solution of the continuum. An artificial damping with a fixed damping factor allows for a true thermalization for $t \to \infty$, but damps finite-size oscillations in an uncontrolled manner and reaches the same incorrect steady-state as z-averaging. The best results can be obtained by reducing the discretization parameter significantly to around $\Lambda = 1.05$ [19], which practically entirely prevents back-reflections of charge. The chain length is required to be increased accordingly to obtain a sufficient energy resolution. Also, the revival time is increased by increasing the chain length, since it takes longer for the charge to flow along the chain. The required chain length is around $N_\mathrm{C} = 500$ to well reproduce the continuum solution, which is infeasible in the context of most NRG applications.

A more efficient approach to that is the double Wilson chain [36]. Here a relatively short Wilson chain ($N_\mathrm{C} \approx 30$, $\Lambda \approx 1.8$) is followed by an effective tight-binding chain ($N_\mathrm{C} \approx 100$, $\Lambda \approx 1.05$), coupled to the end of the first chain. This double Wilson chain is capable of reproducing the results of the Wilson chain mentioned above ($N_\mathrm{C} = 500$, $\Lambda = 1.05$) with significantly less computational cost. The idea of the double Wilson chain is to rapidly reduce the effective bandwidth of the system with a relatively large Λ, but keep this chain short, in order to avoid back-reflections. From a classical standpoint, these reflections first occur at site n, where the hopping parameter t_n is below the hybridization V. When constructed with the lowered effective bandwidth, the second Wilson chain requires less chain sites to obtain the same energy resolution as the pure Wilson chain.

Even in this shorter Wilson chain, truncation of eigenstates is inevitable. However, for $\Lambda \approx 1.05$ a truncation of high-energy states is effectively impossible. An elegant solution to that is the hybrid NRG-DMRG approach [36]. Here a Wilson chain of length M and a discretization $\Lambda \approx 1.8$ is constructed and the TD-NEV is calculated with the TD-NRG. In contrast to the approach presented in Sec. 3.9, the states at iteration M are divided into a kept and a discarded part and from the kept low-energy sector a time-dependent correction term to the TD-NEV is generated. The kept sector is treated as an effective low-energy impurity, which is couple to a tight-binding chain. This way, the discretization error in the low-energy regime of the system is significantly reduced. Due to the missing energy-hierarchy, the tight-binding chain is treated with a time-dependent DMRG approach to allow truncation.

Although the NRG-DMRG approach significantly reduces the finite-size oscillations in non-equilibrium dynamics, it has several drawbacks. Firstly, due to the application of the DMRG, this hybrid approach is restricted to temperature $T = 0$. Secondly, at a certain chain length the revival-time effectively cannot be increased further, since even for a small Λ back-reflections dominate local dynamics before the reflections from the end of the chain reach the impurity. The approach yields excellent results up to times $t = 100/\Gamma$, but does not reach a true thermalized steady-state. Thirdly, the approach does not include a finite-lifetime for local excitations, and so it is not suitable for the calculation of spectral functions.

In this thesis we propose a different hybrid-NRG approach. Here we construct reservoirs, that recover the continuum limit and couple one single reservoir to each site of the Wilson chain. This way, surplus charge is absorbed into the reservoirs and back-reflections are reduced. Also, the low-energy reservoir at the end of the chain prevents the revival-effect and thus allows for true relaxation. To couple the reservoirs to the Wilson chain we will choose the BRF. Since this is a perturbative approach in second order, we expect some reflections to persist on intermediate time scales. However, in the BRF, the correct steady-state (in the limit of the NRG) is always guaranteed. This formalism generates relaxation rates, which translate to natural broadening parameters and thus it is suitable for ESF as well. Here we consequently expect the broadening induced by the BRF to be too narrow and finite-size oscillations to occur. The BRF will be explained in detail in Chap. 4, while its application to the Wilson chain for the RLM is covered in Chap. 5 and to the NRG in Chap. 6, respectively. Finally, in Chap. 7 the OCF is tested for non-trivial interacting QIMs.

4. Bloch-Redfield Formalism

In the previous chapter the NRG has been discussed as a powerful tool to calculate QISs. The formalism is made for accessing a wide range of energies, spanning from the entire width of the band to the exponentially small Kondo temperature. To meet this requirement, the band is discretized logarithmically and only a finite number of excitations from the infinite environment of the QIS is taken into account. This is due to the fact, that the NRG is effectively a closed system formalism, meaning that each system DOF is considered explicitly. The restriction to a finite - and thereby closed - system is thus of pure practical nature.

Closed systems are by nature conservative, meaning that quantum numbers such as charge or spin are constant due to an absent interaction with an environment. Dissipation of impurity quantities is limited to the size of the closed system and a true relaxation is impossible. Here lies the strength of OQS formalisms. If one is solely interested in the properties of the impurity, an explicit formulation of single environment modes is not necessary. Instead, the continuum is basically treated in a statistical way, which is perfectly sufficient to introduce true dissipation and thermalization into QISs. Needless to say, those OQS formalisms are not exact either. To be precise, several indispensable approximations restrict the system to certain parameter regimes, and thereby make small energies inaccessible, which are essential to the Kondo problem. From this standpoint, a hybrid approach between a closed system impurity solver like the NRG and an OQS formalism appears to be a promising attempt to combine the strength of both worlds. This connection is made in Chap. 5 and 6, where we discuss the construction of an OWC. In Chap. 4, however, the focus lies solely on a didactic introduction to the OQS formalism of our choice, namely the BRF. In the following sections this formalism is explained in the way it is presented in typical literature and its limitations are discussed in detail. Related links are provided at certain points, if further information to the respective topic is desired.

4.1. Open Quantum System

In the theory of OQSs a microscopic quantum mechanical system of finite DOF interacts with a large system in the thermodynamic limit, called the environment or bath. The strength of the theory lies in the fact that if one is interested in the characteristics of the microscopic system only, one does not have to deal with an infinite amount of bath DOF. Instead, the knowledge of macroscopic bath quantities, like e.g. the temperature or the DOS, is sufficient to obtain detailed insight into the microscopic system (simply called "system" from here on). Unlike the unitary time evolution of time-independent Hamiltonians, the theory of OQSs is able to include phenomena like dissipation and fluctuation. The evolution of the density matrix is typically described by a Lindblad or Bloch-Redfield equation. This equation has countless applications in condensed matter [94], quantum optics [95], quantum information [96] and decoherence [97]. An interesting work in the context of this thesis has been published by Schwarz *et al* [98] who use the Lindblad equation to describe transport phenomena.

In many instances, a quantum mechanical system of finite DOF is treated as isolated, we called it a "closed" system. Neglecting the explicit interactions with the rest of the universe is often crucial for a quantitative treatment of a problem. In reality, however, no isolated systems exist, as an interaction with the environment is unavoidable. Therefore, an approach is required which includes dissipative terms without having to deal with the potentially infinite environment DOF. Dissipation is defined as the transformation of directed (usable) kinetic energy into an undirected form. This is realized by a relatively small, well-defined system which transfers energy to a large environment. This energy is then irreversibly lost, which is often associated with an increase in entropy. In classical mechanics friction is a typical mechanism that transforms kinetic into thermal energy which then dissolves into the environment. The latter is often so large, that its temperature is effectively not affected by the small system. Dissipation can thus be seen as an irreversible energy flow that breaks time-reversal symmetry.

To describe dissipation, i.e. the change in local parameters like energy or particle number, a mathematical formulation of the interaction with an infinitely large environment is required. For that purpose the microscopic system is described by reduced operators that contain the relevant environment information, while only living in the local Hilbert space. Two approaches that meet these requirements are the Lindblad formalism and the BRF. Here the evolution of the reduced density matrix is described by a von-Neumann equation, which is a quantized version of the Liouville equation. The BMA is applied, which assumes that the environment is large in relation to the local system and that the system-bath coupling is weak. Due to the additional dissipation terms in the equation of motion the effect of an open system can be described, including a relaxation into a true thermalized state. The BMA turns the von-Neumann equation into a simple master equation in the context of a linear response theory. Therefore, the solutions of these equations contain exponential decay terms of the form $e^{-\gamma t}$. The coefficients γ can be seen as friction parameters that mediate the process of dissipation into the environment, where $\gamma = 0$ accounts for the thermalized steady-state of the system. The parameters of the Lindblad master equation are more general, while the parameters of the BRF are directly derived from bath properties. For more details on the differences of the Lindblad and the BRF see e.g. Ref. [99, 100].

The Lindblad formalism guarantees the fundamental properties of the density matrix, meaning positivity, hermiticity and the conservation of the trace. In this chapter we show that our formalism does not violate these properties. The conservation of the trace in the context of OWC is discussed in detail in Chap. 6. For an alternative introduction to the Lindblad or Bloch-Redfield equation and discussion of the approximations see [39, 101, 40].

The foundation of the formalism described in the subsequent section basically follows Ref. [40]. We restrict our considerations to a fermionic environment. A comparable approach to bosonic systems can be found in Ref. [102].

4.2. Density Matrix of an Open Quantum System

The subject of our study is a small localized system S with a finite number of levels that interchanges energy with a large environment or bath B. For that purpose we begin with a QIS Hamiltonian in the general form

$$H = H_{\mathrm{S}} + H_{\mathrm{B}} + H_{\mathrm{SB}}, \tag{4.2.1}$$

where H_{S} and H_{B} are Hamiltonians for S and B, respectively, and H_{SB} is an interaction Hamiltonian. The reservoir is only of indirect interest and its properties only need to be specified in general terms. In our case, the general temperature and the energy DOS need to be defined. To calculate the time-evolution of the density matrix the quantum mechanical Liouville equation, i.e. the von-Neumann equation

$$\dot{\rho}(t) = i\,[\rho(t), H] \tag{4.2.2}$$

is used. We transform it into the interaction picture using $H_0 = H_\mathrm{S} + H_\mathrm{B}$

$$\rho^\mathrm{I}(t) = e^{iH_0 t}\rho(t)e^{-iH_0 t}. \tag{4.2.3}$$

Since the coupling between the system and the bath is considered to be weak, the oscillations generated by $e^{iH_0 t}$ are relatively fast. Taking the time-derivative of (4.2.3) and using (4.2.2) leads to

$$\dot{\rho}^\mathrm{I}(t) = i\left[\rho^\mathrm{I}(t), H^\mathrm{I}_\mathrm{SB}(t)\right], \tag{4.2.4}$$

introducing the time-dependent hybridization term

$$H^\mathrm{I}_\mathrm{SB}(t) = e^{iH_0 t}H_\mathrm{SB}e^{-iH_0 t} \tag{4.2.5}$$

in the interaction picture. Integrating (4.2.4) for $t \geq 0$ and plugging the obtained $\rho^\mathrm{I}(t)$ back into this equation yields

$$\begin{aligned}
\dot{\rho}^\mathrm{I}(t) &= iR_1(t) - R_2(t),\\
R_1(t) &= [\rho^\mathrm{I}(0), H^\mathrm{I}_\mathrm{SB}(t)],\\
R_2(t) &= \int_0^t dt' \big[\left[\rho^\mathrm{I}(t'), H^\mathrm{I}_\mathrm{SB}(t')\right], H^\mathrm{I}_\mathrm{SB}(t)\big].
\end{aligned} \tag{4.2.6}$$

Even though the coupling term H_SB explicitly appears only in first and second order, this equation is still exact, since higher orders of H_SB are embedded in the time-dependent density matrix $\rho^\mathrm{I}(t)$.

The strength of the BRF for OQSs lies in the fact that if one is interested in the local system S there is no need to worry about the composite system $\mathrm{S} \otimes \mathrm{B}$ in detail. If $\hat{O}_\mathrm{S}$ is such a desired operator in the Hilbert space of S, we can calculate its average in the bath DOF if we have knowledge of the local contribution of $\rho(t)$ alone. This local part is called the reduced density matrix $\rho_\mathrm{S}(t)$ and is defined as

$$\rho_\mathrm{S}(t) = \mathrm{Tr}_\mathrm{B}\big\{\rho(t)\big\} \tag{4.2.7}$$

by tracing out the bath environment degrees of freedom (EDOF). The expectation value of a local operator can be written as

$$\langle \hat{O}_{\mathrm{S}}(t)\rangle = \mathrm{Tr}_{\mathrm{S}\otimes\mathrm{B}}\Big\{\hat{O}_{\mathrm{S}}\rho(t)\Big\} = \mathrm{Tr}_{\mathrm{S}}\Big\{\hat{O}_{\mathrm{S}}\rho_{\mathrm{S}}(t)\Big\}\,. \tag{4.2.8}$$

By using $\rho_{\mathrm{S}}(t)$ we can consider the influence of the environment, and at the same time express the expectation value of local operators in the local space only. Our objective is thus to derive an equation for the reduced density matrix. For that purpose, we take the trace over the bath DOF on both sides in Eq. (4.2.6). We assume that the compound system is in thermal equilibrium, and that system and bath are decoupled for times $t \leq 0$, meaning that no correlations between S and B exist. The initial density matrix

$$\rho^{\mathrm{I}}(0) = \rho_{\mathrm{S}}^{\mathrm{I}}(0)\rho_{\mathrm{B}} \tag{4.2.9}$$

then factorizes into a separate system and bath part. This assumption already eliminates the first term of Eq. (4.2.6), namely

$$\mathrm{Tr}_{\mathrm{B}}\Big\{R_1(t)\Big\} = \mathrm{Tr}_{\mathrm{B}}\Big\{[\rho_{\mathrm{S}}^{\mathrm{I}}(0)\rho_{\mathrm{B}}, H_{\mathrm{SB}}^{\mathrm{I}}(t)]\Big\} = [\rho_{\mathrm{S}}^{\mathrm{I}}(0), e^{iH_{\mathrm{S}}t}\langle H_{\mathrm{SB}}\rangle_{\mathrm{B}}e^{-iH_{\mathrm{S}}t}] \tag{4.2.10}$$

by employing the cyclicality of the trace and $e^{iH_0t} = e^{iH_{\mathrm{S}}t}e^{iH_{\mathrm{B}}t}$, since H_{S} and H_{B} commute. Note that we have defined

$$\rho_{\mathrm{S}}^{\mathrm{I}}(t) = \mathrm{Tr}_{\mathrm{B}}\big\{\rho^{\mathrm{I}}(t)\big\} = e^{iH_{\mathrm{S}}t}\rho_{\mathrm{S}}(t)e^{-iH_{\mathrm{S}}t} \tag{4.2.11}$$

with the cyclicality of the trace in Eq. (4.2.3). Since we assume that in the interaction Hamiltonian H_{SB} bath operators only occur in linear form, $\langle H_{\mathrm{SB}}\rangle_{\mathrm{B}}$ vanishes and likewise does $\mathrm{Tr}_{\mathrm{B}}\Big\{R_1(t)\Big\}$. The second order term $R_2(t)$ remains and encodes the influence of the bath B onto the system S. Thus, the von-Neumann equation becomes

$$\dot{\rho}_{\mathrm{S}}^{\mathrm{I}}(t) = -\mathrm{Tr}_{\mathrm{B}}\Big\{R_2(t)\Big\}\,. \tag{4.2.12}$$

At a first glance, this integro-differential equation resembles a typical Picard-Lindelöf problem by defining

$$\dot{\rho}^{\mathrm{I}}(t) = -R_2(t) \equiv f(t, \rho^{\mathrm{I}}(t)). \tag{4.2.13}$$

The solution can then be obtained by

$$\rho^{\mathrm{I}}_{[l+1]}(t) = \rho^{\mathrm{I}}(0) + \int_0^t ds f(s, \rho^{\mathrm{I}}_{[l]}(s)), \tag{4.2.14}$$

with the initial value $\rho^{\mathrm{I}}_{[0]}(t) \equiv \rho^{\mathrm{I}}(0)$. The time-dependent operator $\rho^{\mathrm{I}}_{[l]}(t)$ is calculated iteratively until the desired convergence at $l = \bar{l}$ is reached. However, since $R_2(t)$ contains bath operators via H_{SB}, Eq. (4.2.13) cannot be written in the simple form

$$\dot{\rho}^{\mathrm{I}}_{\mathrm{S}}(t) = f(t, \rho^{\mathrm{I}}_{\mathrm{S}}(t)) \tag{4.2.15}$$

by performing a trace over the bath DOF. Hence, the reduced density matrix can only be calculated after completion of the final step $\bar{l}$. Up to that point, the bath operators remain and yield more and more complex entanglement of the bath modes with each iteration step. Even though it can be shown analytically (see App. C) that only bath correlations up to quadratic order appear in expression (4.2.14), still all bath indices are coupled indirectly rendering even the evaluation of $\rho^{\mathrm{I}}_{[2]}(t)$ practically impossible. Any further thoughts regarding the decoupling of certain bath modes, e.g. in the fashion of the NRG formalism, shall not be subject of this thesis. The first order term, $\rho^{\mathrm{I}}_{[1]}(t)$, which can be interpreted as a second order perturbation in H_{SB}, however, can be calculated analytically and can thus serve as a benchmark for very short-time considerations of various QIMs (see Eq. (4.6.1.70)). To reliably reach more relevant timescales and, in addition, simulate correct thermalization a different route needs to be taken. Equation (4.2.15) can be realized by defining a factorization of the density matrix in the spirit of Eq. (4.2.9) for all times $t \geq 0$. This allows one to trace out the bath DOF and thus to set up an integro-differential equation in local system parameters only. In fact, different approximations are necessary to solve this equation, which we will elaborate on in Sec. 4.3.

4.3. Born-Markov Approximation

The first approximation we need in order to locally treat OQSs is the one which has the most impact at the same time, the so called Born approximation (BA) [39, 103]. Recall, that we defined the interaction term to be turned on at $t = 0$, so correlations between the system and the bath will still occur for positive times. We consider the density matrix to have a product form

$$\rho^{\mathrm{I}}(t) = \rho_{\mathrm{S}}^{\mathrm{I}}(t)\rho_{\mathrm{B}}. \tag{4.3.16}$$

for all times $t > 0$. This is defined as a BA. It is motivated by the assumption that the coupling term H_{SB} is weak relative to H_{S} and H_{B} and that there are no feedback processes onto the bath, so ρ_{B} is left unaltered. To understand the origin of this approximation consider the full density matrix $\rho(t) = \frac{1}{Z}e^{-\beta(H_{\mathrm{S}}+H_{\mathrm{B}}+H_{\mathrm{SB}})}$ as an expansion in the interaction Hamiltonian H_{SB}. Since terms of the order of $\mathcal{O}\left((\beta H_{\mathrm{SB}})^n\right)$ lead to $\mathcal{O}\left((\beta H_{\mathrm{SB}})^{n+2}\right)$ in Eq. (4.2.6), we consider terms with $n \geq 1$ to be negligible, if the coupling strength is small compared to the temperature. The factorization of the density matrix in Eq. (4.2.6) is crucial to trace out the bath DOF and thus to handle OQSs within our approach. Nevertheless, by neglecting correlations between system and bath modes, fundamental effects which rely on feedback processes, like the formation of the Kondo-singlet, cannot be explained. The recovery of those correlations is discussed in Chap. 5.

Let us briefly investigate the influence of the temperature on the approximation. In the limit $\beta \to 0$ the approximation becomes exact. In the case of finite temperature the effect is more pronounced. If the coupling is of the order of the local energies and the bath dispersion, a huge error can be expected in the limit of low temperatures.

To proceed with the evaluation of Eq. (4.2.6), we rewrite it as

$$\dot{\rho}_{\mathrm{S}}^{\mathrm{I}}(t) = -\int_0^t ds \mathrm{Tr}_{\mathrm{B}}\Big\{\left[\left[\rho_{\mathrm{S}}^{\mathrm{I}}(t-s)\rho_{\mathrm{B}}, H_{\mathrm{SB}}^{\mathrm{I}}(t-s)\right], H_{\mathrm{SB}}^{\mathrm{I}}(t)\right]\Big\}, \tag{4.3.17}$$

where we have substituted $t' = t - s$ for the sake of convenience.

As a first step (before applying any further approximations) the master equation (4.3.17) is written in the eigenbasis of the finite system Hamiltonian H_{S}, yielding

$$\dot{\rho}_{ab}(t) = -\sum_{mn}\int_0^t ds R_{ab,mn}(t,s)\rho_{mn}(t-s), \tag{4.3.18}$$

where the indices a, b, m, n denote the eigenstates of H_{S}. We have introduced the two-times-dependent BRT

$$R_{ab,mn}(t,s) = \delta_{bn}\sum_l \Gamma^{+}_{al,lm}(t,s) + \delta_{am}\sum_l \Gamma^{-}_{nl,lb}(t,s) - \Gamma^{+}_{nb,am}(t,s) - \Gamma^{-}_{nb,am}(t,s), \tag{4.3.19}$$

comprising the damping tensors

$$\begin{aligned}\Gamma^{+}_{ab,mn}(t,s) &= \mathrm{Tr_B}\Big\{\rho_\mathrm{B} H_{ab}(t) H_{mn}(t-s)\Big\}\\ \Gamma^{-}_{ab,mn}(t,s) &= \mathrm{Tr_B}\Big\{\rho_\mathrm{B} H_{ab}(t-s) H_{mn}(t)\Big\},\end{aligned} \tag{4.3.20}$$

where $\rho_{ab}(t) = \langle a|\, \rho^\mathrm{I}_\mathrm{S}(t)\, |b\rangle$ and $H_{ab}(t) = \langle a|\, H^\mathrm{I}_\mathrm{SB}(t)\, |b\rangle$ are the operators in the local eigenbasis. To proceed, let us introduce an explicit form of H_SB in analogy to Eq. (1.0.2). We assume a bilinear single-particle coupling between the local and the bath DOF that reads

$$H^\mathrm{I}_\mathrm{SB}(t) = \sum_k V_k \left(f^\dagger(t) c_k(t) + f(t) c^\dagger_k(t)\right). \tag{4.3.21}$$

Here f accounts for the annihilator of a local state in the Hilbert space of S and c_k annihilates a bath state. The momentum index k sums over the bath DOF and V_k is the corresponding hybridization. The appearing operators can easily be augmented by further indices (e.g. a spin or channel index), yielding more specific hybridization Hamiltonians. For the purpose of presenting the principal calculations, these DOF will be neglected for now.

Inserting Eq. (4.3.21) into the equations (4.3.20) of the damping tensors, bath correlation functions emerge. Considering the case of a bath $H_\mathrm{B} = \sum_k \epsilon_k c^\dagger_k c_k$ of non-interacting fermions in thermal equilibrium (cf. Eq. (1.0.1)), the time evolution of the bath annihilators simplifies to $c_k(t) = c_k(0) e^{-i\epsilon_k t}$, yielding the correlation functions

$$\begin{aligned}C_\mathrm{p}(s) &= \sum_{kk'} V_k V_{k'} \mathrm{Tr_B}\Big\{\rho_\mathrm{B} c_k(t) c^\dagger_{k'}(t-s)\Big\} = \sum_k V_k^2 f_\beta(-\epsilon_k) e^{-i\epsilon_k s}\\ C_\mathrm{h}(s) &= \sum_{kk'} V_k V_{k'} \mathrm{Tr_B}\Big\{\rho_\mathrm{B} c^\dagger_k(t) c_{k'}(t-s)\Big\} = \sum_k V_k^2 f_\beta(\epsilon_k) e^{i\epsilon_k s}\end{aligned} \tag{4.3.22}$$

for a particle and a hole respectively. The Fermi function $f_\beta(\epsilon_k) = \langle c^\dagger_k(0) c_k(0)\rangle_\mathrm{B}$ has been introduced with β being the inverse temperature of the environment. To deal with the infinite bath continuum, the sum over the bath excitations k is turned into an integral by introducing the DOS $\rho(\epsilon)$, such that $\rho(\epsilon)d\epsilon$ gives the number of excitations within the interval ϵ to $\epsilon + d\epsilon$. The spectral coupling function (see Eq. (1.0.3)) is then defined as

$$\Gamma(\epsilon) = \pi V^2(\epsilon)\rho(\epsilon) = \pi \sum_k V_k^2 \delta(\epsilon - \epsilon_k) , \tag{4.3.23}$$

turning the bath correlation functions of Eq. (4.3.22) into

$$C_{\mathrm{p/h}}(s) = \frac{1}{\pi} \int_{-\infty}^{\infty} d\epsilon \Gamma(\epsilon) f_\beta(\mp\epsilon) e^{\mp i\epsilon s} . \tag{4.3.24}$$

For a symmetric spectral coupling function the bath is particle-hole symmetric, yielding $C_{\mathrm{p}}(s) = C_{\mathrm{h}}(s) \equiv C(s)$. Using the definition $f_{ab}(t) = \langle a| e^{iH_{\mathrm{S}}t} f e^{-iH_{\mathrm{S}}t} |b\rangle = f_{ab} e^{i\omega_{ab}t}$ for the system operator in the local eigenbasis with $\omega_{ab} = E_a - E_b$ being the difference of local eigenenergies, the damping tensors (4.3.20) become

$$\begin{aligned} \Gamma^+_{ab,mn}(t,s) &= e^{i(\omega_{ab}+\omega_{mn})t} \left[f^\dagger_{ab} f_{mn} C_p(s) + f_{ab} f^\dagger_{mn} C_h(s) \right] e^{-i\omega_{mn}s} \\ \Gamma^-_{ab,mn}(t,s) &= e^{i(\omega_{ab}+\omega_{mn})t} \left[f^\dagger_{ab} f_{mn} C^*_p(s) + f_{ab} f^\dagger_{mn} C^*_h(s) \right] e^{-i\omega_{ab}s}. \end{aligned} \tag{4.3.25}$$

The second canonical approximation at this point is the Markov approximation (MA). The master equation (4.3.18) is non-Markovian, since the dynamics of $\rho^{\mathrm{I}}_{\mathrm{S}}(t)$ depends on its entire history $0 \leq s \leq t$, meaning that feedback processes between S and B are possible. This renders a complicated integro-differential equation. By assuming Markovian behavior those rebound processes are neglected which considerably simplifies the equation by lifting the convolution integral. The question arises under which circumstances this assumption is justified. The reader shall be reminded, that even though the BA neglects correlations between S and B, correlations between the single bath modes still occur. These correlations are expressed by the bath correlation functions $C_{\mathrm{p/h}}(t)$ of Eq. (4.3.24). For large times $t \to \infty$, these functions decay entirely, since the exponential terms $e^{\mp i\epsilon t}$ oscillate rapidly in this case and thereby cancel the kernel under the integral to zero. We define the time scale of the decay of $C_{\mathrm{p/h}}(t)$ as the bath correlation time t_{B}. If t_{B} is considered to be small in comparison to the local time scale t_{S} on which the density matrix varies, then local information decays rapidly in the bath, rendering B a constant background for S. This inhibits feedback loops of information going from S into B and then back to S and thus provides a Markovian system. It is left to show that $t_{\mathrm{B}} \ll t_{\mathrm{S}}$.

By the above made assumption that the coupling term H_{SB} is weak, the changing rate of the density matrix is small. Consequently, the density matrix can be seen as a slowly varying operator compared to the bath correlation time t_{B}. Let us consider a constant spectral coupling function

$$\Gamma(\epsilon) = \Gamma\Theta(D - |\epsilon|) \tag{4.3.26}$$

to exemplarily calculate the correlation function $C(t)$. The bandwidth D serves as an upper limit for the bath energies and the normalized bath DOS becomes

$$\rho(\epsilon) = \sum_k \delta(\epsilon - \epsilon_k) = \frac{1}{2D}\Theta(D - |\epsilon|). \tag{4.3.27}$$

For a hybridization V that is independent in k, we can derive

$$V = \sqrt{\frac{2D\Gamma}{\pi}}. \tag{4.3.28}$$

with Eq. (4.3.23). From Eq. (4.3.24) we obtain

$$\mathfrak{Re}C(t) = \frac{V^2}{2}\frac{\sin(t/t_{\mathrm{B}})}{t/t_{\mathrm{B}}} \tag{4.3.29}$$

for the real-part with the correlation time $t_{\mathrm{B}} = 1/D$. The imaginary-part vanishes for high temperatures and is

$$\mathfrak{Im}C(t) = \frac{V^2}{2}\frac{\cos(t/t_{\mathrm{B}}) - 1}{t/t_{\mathrm{B}}} \tag{4.3.30}$$

for $T = 0$.

In Fig. 4.1 the correlation functions are displayed on scaled axes. In the wideband limit $D \gg \Gamma$ the correlation function $C(t)$ converges to $\Gamma\delta(t)$, which is the desired behavior for the MA. Further discussion can be found in Sec. 4.6 and 5.3.3.

When t_{B} is considered to be small, the master equation (4.3.18) can be simplified twofold. The first approximation step is to replace $\rho_{mn}(t - s)$ by $\rho_{mn}(t)$ under the integral. Since correlations are practically vanished for $t \gg t_{\mathrm{B}}$, the upper limit of the integral can be set to ∞, which is the second approximation step. We end up with

$$\dot{\rho}_{ab}(t) = -\sum_{mn} R_{ab,mn}(t)\rho_{mn}(t), \tag{4.3.31}$$

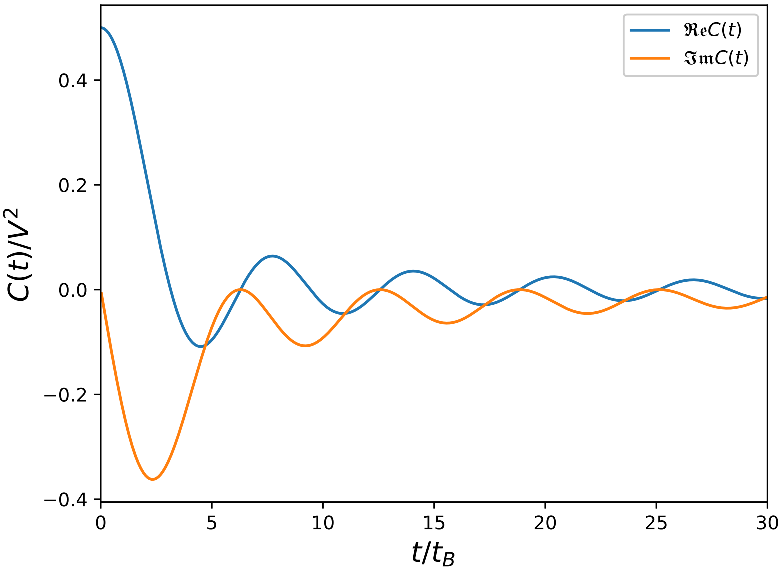

Figure 4.1.: The dimensionless correlation function $C(t)/V^2$ versus dimensionless times t/t_B for a constant spectral coupling function. For $\mathfrak{Im}C(t)$ we chose $T = 0$.

where $R_{ab,mn}(t) = \int_0^\infty ds R_{ab,mn}(t,s)$. Thus we obtain a Markovian equation, where the dynamics of the density matrix at time t only depends on its current state.

It shall be mentioned here, that the second approximation step is clearly problematic for short times $t < t_\mathrm{B}$. Here, a major part of the correlation function is falsely included in the integration and thereby in the relaxation rate of $\rho_\mathrm{S}^\mathrm{I}(t)$.

Let us investigate the master equation for short times, to obtain a non-Markovian estimation in the regime, where the MA is most problematic. In Eq. (4.3.25) we set $t = s = 0$ to obtain the damping matrices. The initial value of the correlation functions is $C(0) = \frac{\Gamma D}{\pi} = \frac{V^2}{2}$. The damping matrices are now given by

$$\Gamma^{\pm}_{ab,mn}(0,0) = \frac{V^2}{2}\left[f^\dagger_{ab} f_{mn} + f_{ab} f^\dagger_{mn}\right]. \tag{4.3.32}$$

The master equation (4.3.18) becomes

$$\dot{\rho}_{ab}(t) = -\sum_{mn} R_{ab,mn}(0,0)\int_0^t ds \rho_{mn}(t-s) \approx -\sum_{mn} R_{ab,mn}(0,0) t \rho_{mn}(t). \tag{4.3.33}$$

On the r.h.s. of the equation the first MA has been executed. The convolution integral yields a cosine-type short time evolution of the density matrix, while the first MA yields a Gaussian-type density matrix. In any case, the first non-vanishing contribution of t is quadratic. This is in accordance with $\dot{\rho}(t=0)=0$, which can easily be deduced from Eq. (4.3.18).

We proceed to the Markovian time scale of $t \gg t_\mathrm{B}$, where the damping matrices are transformed into

$$\begin{aligned}
\Gamma^+_{ab,mn}(t) &= e^{i(\omega_{ab}+\omega_{mn})t}\left[f^\dagger_{ab}f_{mn}C_\mathrm{p}(\omega_{mn}) + f_{ab}f^\dagger_{mn}C_\mathrm{h}(\omega_{mn})\right] \\
\Gamma^-_{ab,mn}(t) &= e^{i(\omega_{ab}+\omega_{mn})t}\left[f^\dagger_{ab}f_{mn}C^*_\mathrm{p}(\omega_{ba}) + f_{ab}f^\dagger_{mn}C^*_\mathrm{h}(\omega_{ba})\right]. \qquad (4.3.34)
\end{aligned}$$

Here we have defined the greater/lesser reservoir Green's functions (RGFs)

$$\begin{aligned}
C_{\mathrm{p/h}}(\omega) &= \int_0^\infty ds C_{\mathrm{p/h}}(s)e^{-i\omega s-0^+s} \\
&= \Gamma(\mp\omega)f_\beta(\omega) + \frac{i}{\pi}\mathrm{PV}\int_{-\infty}^{\infty} d\omega' \frac{\Gamma(\mp\omega')f_\beta(\omega')}{\omega'-\omega} \qquad (4.3.35)
\end{aligned}$$

as the half-sided Fourier transform of the correlation functions. PV denotes the Cauchy principal value. Naturally, the imaginary part of the RGFs is connected to the real part via a Kramers-Kronig relation.

The stage is set for the third and last approximation, the so-called secular approximation. It is based upon the secular effect which, in general, denotes a separation of the time scales of a system. In our case, we consider the local dynamics of $\rho^\mathrm{I}_\mathrm{S}(t)$ to happen on a much larger time scale than the fast oscillating terms $e^{i(\omega_{ab}+\omega_{mn})t}$ in Eq. (4.3.34). This assumption is again based on a weak coupling H_SB and thus a slowly varying density matrix. In this approximation, the master equation is secularized, i.e. averaged over the rapidly varying terms. As a result, those terms average to zero and any modulations over these short times are washed out. The only surviving terms are those that fulfill $\omega_{ab}+\omega_{mn}=0$. Hence, the exponential functions are turned into Kronecker-deltas and the damping matrices reach their final form

$$\begin{aligned}
\Gamma^+_{ab,mn} &= \delta_{\omega_{ab}+\omega_{mn},0}\left[f^\dagger_{ab}f_{mn}C_\mathrm{p}(\omega_{mn}) + f_{ab}f^\dagger_{mn}C_\mathrm{h}(\omega_{mn})\right] \\
\Gamma^-_{ab,mn} &= \left(\Gamma^+_{ab,mn}\right)^*. \qquad (4.3.36)
\end{aligned}$$

In Sec. 4.6 and 5.3.3 the occurring local energies are compared to the time scale of the local dynamics to discuss the accuracy of the approximation. To this end, the BRT is time-independent rendering the master equation (4.3.18) to become

$$\dot{\rho}_{ab}(t) = -\sum_{mn} R_{ab,mn}\rho_{mn}(t), \tag{4.3.37}$$

with the final time-independent BRT

$$R_{ab,mn} = \delta_{bn}\sum_{l}\Gamma^{+}_{al,lm} + \delta_{am}\sum_{l}\Gamma^{-}_{nl,lb} - \Gamma^{+}_{nb,am} - \Gamma^{-}_{nb,am}. \tag{4.3.38}$$

The first two terms of the BRT maintain particle number, and will thus be referred to as the unitary part, while the latter (dissipative) part connects two different particle subspaces. Equation (4.3.37) is a Lindblad-type master equation, where in canonical Lindblad theory, the entire BRT is denoted as the dissipator.

The BRT can be seen as a Lindblad super-operator or as a matrix R, if the density matrix is expanded as a super-vector. In the latter case, the master equation has the simple solution

$$|\rho(t)\rangle\rangle = e^{-Rt}\,|\rho(0)\rangle\rangle = \sum_{l} c_l e^{-\lambda_l t}\,|v_l\rangle\,, \tag{4.3.39}$$

with $c_l = \langle w_l|\rho(0)\rangle$. Here a bi-orthonormal eigenbasis of the BRT has been defined with left and right eigenvectors $\langle w_l|$ and $|v_l\rangle$, respectively, fulfilling $\langle w_l|v_m\rangle = \delta_{lm}$. This establishes the requirement for diagonalizing the BRT. Equation (4.3.39) is a sum of exponential decays supplemented by oscillations induced by the imaginary part of λ_l, which is often referred to as the Lamb-shift. As mentioned above, Eq. (4.3.39) resembles the dynamics well for large times. The correct equilibrium value for $t = 0$ is included as $|\rho(0)\rangle\rangle = \sum_l c_l\,|v_l\rangle$, which can be used to check numerical calculations. The correct gradient $|\dot{\rho}(t=0)\rangle\rangle = 0$, however, is not given. This can easily be seen by setting $t = 0$ in the master equation (4.3.37). The gradient can only be zero if $R\,|\rho(0)\rangle\rangle = 0$, which implies that the expression (4.3.39) is constant in time.

With Eq. (4.3.39) and (4.2.8) at hand, physical properties can be calculated in the system Hilbert space. The non-equilibrium expectation value of any local operator O_{S}

is given by

$$\begin{aligned}\langle O_{\mathrm{S}}(t)\rangle &= \mathrm{Tr}\Big\{e^{iH_{\mathrm{S}}t}O_{\mathrm{S}}e^{-iH_{\mathrm{S}}t}\rho^{\mathrm{I}}_{\mathrm{S}}(t)\Big\}\\ &= \sum_{ab}\sum_{l}(O_{\mathrm{S}})_{ab}\, c_l\,(|v_l\rangle)_{ba}\, e^{i\omega_{ab}t-\lambda_l t}\\ &= \sum_{f,l} X_{f,l}\, e^{i\omega_{l,f}t-\mathfrak{Re}\lambda_l t},\end{aligned} \tag{4.3.40}$$

where in

$$X_{l,f} = \sum_{ab}^{\omega_{ab}=\omega_f} (O_{\mathrm{S}})_{ab}\, c_l\,(|v_l\rangle)_{ba} \tag{4.3.41}$$

all identical energy differences $\omega_{ab} = \omega_f$ are aggregated and $\omega_{l,f} = \omega_f - \mathfrak{Im}\lambda_l$. Here the real part $\mathfrak{Re}\lambda_l$ allows for true relaxation of the system into the steady state, while the Lamb-shift $\mathfrak{Im}\lambda_l$ induces small supplemental oscillations. The closed system solution is recovered by setting the relaxation rates $\lambda_l \to 0$. Equation (4.3.40) then becomes

$$\begin{aligned}\langle O_{\mathrm{S}}(t)\rangle_{\mathrm{CC}} &= \sum_{ab}(O_{\mathrm{S}})_{ab}\sum_{l} c_l\,(|v_l\rangle)_{ba}\, e^{i\omega_{ab}t}\\ &= \mathrm{Tr}\Big\{e^{iH_{\mathrm{S}}t}O_{\mathrm{S}}e^{-iH_{\mathrm{S}}t}\rho^{\mathrm{I}}_{\mathrm{S}}(0)\Big\}.\end{aligned} \tag{4.3.42}$$

4.4. Adaptation of the Bloch-Redfield Equation to the χ-Operator

The time-dependent retarded equilibrium Green's function (TD-EGF) is defined as

$$G_{A,B}(t) = -i\Theta(t)\mathrm{Tr}\{\rho[A(t),B]_\varsigma\}, \tag{4.4.43}$$

with $[A(t),B]_\varsigma = AB - \varsigma BA$ and $\varsigma = 1$ for bosonic operators A, B and $\varsigma = -1$ for fermionic operators (cf. Eq. (3.8.39)). The time dependency is included in the operator $A(t) = e^{iHt}Ae^{-iHt}$. By exploiting the cyclicality of the trace, we can define $\chi(t) = e^{-iHt}[B,\rho]_\varsigma e^{iHt}$. Replacing $A \to d$ and $B \to d^\dagger$, with $d^{(\dagger)}$ being the local fermionic annihilation (creation) operator[1], we obtain the local GF

$$G_{\mathrm{d}}(t) \equiv G_{d,d^\dagger}(t) = -i\Theta(t)\mathrm{Tr}\{\chi(t)d\}, \tag{4.4.44}$$

with $\chi(t) = e^{-iHt}\left(\rho d^\dagger + d^\dagger\rho\right)e^{iHt}$ being a fermionic operator as well. In the spirit of Eq. (4.2.8) the trace is split into a system part S and a bath part B. This way Eq. (4.4.44) can be expressed in terms of local quantities only leading to

$$G_{\mathrm{d}}(t) = -i\Theta(t)\mathrm{Tr}_{\mathrm{S}}\{e^{-iH_{\mathrm{S}}t}\chi_{\mathrm{S}}^{\mathrm{I}}(t)e^{iH_{\mathrm{S}}t}d\}, \tag{4.4.45}$$

where $\chi_{\mathrm{S}}^{\mathrm{I}}(t) = \mathrm{Tr}_{\mathrm{B}}\left\{e^{iH_0 t}\chi(t)e^{-iH_0 t}\right\}$ is the reduced operator in the interaction picture. To calculate $\chi_{\mathrm{S}}^{\mathrm{I}}(t)$, the BRF discussed above needs to be adapted to this new fermionic operator. Since $\chi(t) = e^{-iHt}\chi e^{iHt}$, this operator evolves in time like the density matrix and thus the von-Neumann equation (4.2.2) can, analogly to $\rho(t)$, be used as the entry point of the BRF. The BA

$$\chi^{\mathrm{I}}(t) \approx \chi_{\mathrm{S}}^{\mathrm{I}}(t)\rho_{\mathrm{B}} \tag{4.4.46}$$

(cf. Eq. (4.3.16)) can be performed since $d^\dagger$ is a local operator and χ is linear in its constituents ρ and $d^\dagger$. The bath equilibrium density matrix ρ_{B} is then used to construct the correlation functions. The formalism deviates by a sign from the BRF for the density matrix, since χ has fermionic properties. By commuting $\chi_{\mathrm{S}}^{\mathrm{I}}(t)$ with a bath operator $c_k^{(\dagger)}$, which is necessary to build the correlation functions $C_{\mathrm{p/h}}(s)$ of Eq. (4.3.22), the sign of the dissipative part of the BRT is changed. This sign change, however, does not impact the following Markov and secular approximation (MSA) and thus we end up with the master equation

$$\dot{\chi}_{ab}(t) = -\sum_{mn} R_{ab,mn}\chi_{mn}(t), \tag{4.4.47}$$

where

$$R_{ab,mn} = \delta_{bn}\sum_{l}\Gamma^{+}_{al,lm} + \delta_{am}\sum_{l}\Gamma^{-}_{nl,lb} + \Gamma^{+}_{nb,am} + \Gamma^{-}_{nb,am} \tag{4.4.48}$$

---

[1] Note, that we choose d, instead of f for the local operator here. f shall denote a general operator of the system Hamiltonian H_{S}, while d is restricted to a specific impurity operator.

is the new modified BRT. The only difference to Eq. (4.3.38) lies in the sign of the last two terms.

It should be mentioned here, that the sign of the dissipative part does not have a significant effect on the overall dynamics of $\chi^{\mathrm{I}}_{\mathrm{S}}(t)$, if the system is particle-hole symmetric, since the dissipative terms always come in pairs of positive and negative sign, mediated by the local operators $f^{(\dagger)}$. The major difference between the master equations for ρ and χ lies in the fact that different particle number subspaces $\mathfrak{S}_n$ are coupled. The unitary terms of the BRT maintain the particle number of the operator, that shall be evolved in time, while the dissipative terms change it by one. The density matrix ρ is a block-diagonal operator in $\mathfrak{S}_n$, i.e. the unitary part couples $\mathfrak{S}_n$ to $\mathfrak{S}_n$ while the dissipative part couples it to $\mathfrak{S}_{n-1}$ and $\mathfrak{S}_{n+1}$, respectively. On the other hand, χ is a fermionic operator in the sense that it couples $\mathfrak{S}_n$ to $\mathfrak{S}_{n+1}$. The unitary part of the BRT maintains this scheme, while the dissipative part couples $(\mathfrak{S}_{n+1}, \mathfrak{S}_n)$ to $(\mathfrak{S}_n, \mathfrak{S}_{n-1})$ and $(\mathfrak{S}_{n+2}, \mathfrak{S}_{n+1})$, respectively. This fact has a major impact on the numerical implementation of the BRF in the context of the NRG, which operates in sub-blocks defined by quantum numbers.

With the formal solution

$$|\chi(t)\rangle = e^{-Rt}\,|\chi(0)\rangle = \sum_l c_l e^{-\lambda_l t}\,|v_l\rangle \tag{4.4.49}$$

one can write the TD-EGF in the eigenbasis of the local Hamiltonian H_{S} to obtain

$$G_{\mathrm{d}}(t) = -i\Theta(t)\sum_{ab}\sum_l d_{ab}c_l(|v_l\rangle)_{ba}e^{i\omega_{ab}t-\lambda_l t} \tag{4.4.50}$$

with the local annihilator d. A half-sided Fourier transform yields

$$\begin{aligned} G_{\mathrm{d}}(\omega) &= \sum_{ab}\sum_l \frac{d_{ab}c_l(|v_l\rangle)_{ba}}{\omega+\omega_{ab}-\mathfrak{Im}\lambda_l + i\mathfrak{Re}\lambda_l} \\ &= \sum_{f,l}\frac{Y_{l,f}}{\omega+\omega_{l,f}+i\mathfrak{Re}\lambda_l} \end{aligned} \tag{4.4.51}$$

where

$$Y_{l,f} = \sum_{ab}^{\omega_{ab}=\omega_f} d_{ab}\,c_l\,(|v_l\rangle)_{ba} \tag{4.4.52}$$

takes the role of a spectral density, in which all identical energy differences $\omega_{ab} = \omega_f$

are contained. From here, the spectral function

$$A_\mathrm{d}(\omega) = -\frac{1}{\pi}\mathfrak{Im}G_\mathrm{d}(\omega) = \frac{1}{\pi}\sum_{f,l}\frac{\mathfrak{Re}\lambda_l\,\mathfrak{Re}Y_{l,f} - (\omega+\omega_{l,f})\,\mathfrak{Im}Y_{l,f}}{(\omega+\omega_{l,f})^2 + (\mathfrak{Re}\lambda_l)^2} \tag{4.4.53}$$

can be derived. Clearly, $\mathfrak{Re}\lambda_l$ serves as a natural broadening for the lifetime of local excitations, while $\mathfrak{Im}\lambda_l$ produces an energy shift. Equation (4.4.53) resembles Lorentzians with weight $\mathfrak{Re}Y_{l,f}$ supplemented by a further term. It is easy to prove that our representation of the spectral function does not violate the sum rule. The Lorentzians are each normalized by nature, independent of their energy shift. The second term can be shifted to reveal its anti-symmetric nature and thus it vanishes when integrated over the entire real axis. It is left to show that $\sum_{f,l}\mathfrak{Re}Y_{l,f} = 1$. We obtain

$$\begin{aligned}\sum_{f,l} Y_{l,f} &= \sum_{ab} d_{ab}\sum_l c_l\left(|v_l\rangle\right)_{ba} = \sum_{ab} d_{ab}\,\chi_{ba}(0)\\ &= \sum_a \langle a|\, d\left(d^\dagger\rho_\mathrm{S} + \rho_\mathrm{S}d^\dagger\right)|a\rangle = \mathrm{Tr}_\mathrm{S}\Big\{\rho_\mathrm{S}\{d,d^\dagger\}\Big\} = 1,\end{aligned} \tag{4.4.54}$$

which is the required proof. The closed system solution is contained in Eq. (4.4.53) by setting $\lambda_l \to 0$, like in the non-equilibrium case above. We obtain

$$\begin{aligned}A_\mathrm{d}(\omega) &= \frac{1}{\pi}\sum_{f,l}\delta(\omega+\omega_f)\,\mathfrak{Re}Y_{l,f} - \mathfrak{Im}Y_{l,f}/(\omega+\omega_f)\\ &= \frac{1}{\pi}\sum_{ab} d_{ab}\chi_{ba}(0)\delta(\omega+\omega_{ab})\end{aligned} \tag{4.4.55}$$

since $\sum_l \mathfrak{Im}Y_{l,f} = 0$.

If the short time approximation (4.3.33) is applied to the Green's function (4.4.50), a time-dependence $\propto e^{-\lambda t^2}$ arises, leading in turn to a Gaussian broadening in the spectral function.

4.5. Features of the Bloch-Redfield Equation

Let us investigate some features of the above derived equation (4.3.37). Especially, we want to ensure that the applied approximations do not corrupt the fundamental properties of the time-dependent density matrix, i.e. positive semi-definiteness, hermiticity and the conservation of the trace for all times.

Firstly, the secular approximation adds an interesting feature to the BRT. The

Kronecker-deltas can be extracted from the damping matrices in Eq. (4.3.19), leading to

$$R_{ab,mn} \propto \delta_{\omega_{ab},\omega_{mn}}. \tag{4.5.56}$$

The unitary part of the BRT is now proportional to $\delta_{\omega_{am}}$ and $\delta_{\omega_{bn}}$, respectively. Note that the local operators $f^{(\dagger)}$ demand, that a, m (b, n) originate from the same particle number subspace of the Hilbert space. If there are no degeneracies within a subspace, we can replace $\delta_{\omega_{am}} \to \delta_{am}$. This is the case for all models investigated in this thesis, i.e. the RLM, the IRLM and the SIAM.

The BRT reads in its simple form

$$R_{ab,mn} = \delta_{am}\delta_{bn}\sum_{l}\left(\Gamma_{al,la} + \Gamma^{*}_{bl,lb}\right) - 2\mathfrak{Re}\Gamma_{nb,am}. \tag{4.5.57}$$

The unitary part can be incorporated into the density matrix by defining

$$\overline{\rho}_{ab}(t) \equiv e^{\sum_l \Gamma_{al,la}t}\rho_{ab}(t)e^{\sum_l (\Gamma_{bl,lb})^{*}t} \tag{4.5.58}$$

and then rewriting the master equation (4.3.37) for $\overline{\rho}_{ab}(t)$. However, this is no simplification to solving the master equation and is only intended to justify the term "unitary" in this context.

It is easy to conclude $R_{aa,mn} = R_{aa,mm}\delta_{mn}$, which means that the evolution of the diagonal part of the density matrix (DDM) is independent of the ODDM. For the DDM we can explicitly write

$$R_{aa,mm} = 2\mathfrak{Re}\Big[\delta_{am}\sum_{l}\Gamma_{al,la} - \Gamma_{ma,am}\Big]. \tag{4.5.59}$$

Obviously, the diagonal elements $R_{mm,mm} = 2\mathfrak{Re}\sum_l \Gamma_{ml,lm}$ of the BRT are given as a linear combination of the off-diagonal elements $R_{aa,mm} = -2\mathfrak{Re}\Gamma_{ma,am}, a \neq m$ (note, that $\Gamma_{aa,aa} = 0$). For that reason, the rank of the matrix is one below its dimension. Consequently, the matrix is singular and automatically contains one eigenvalue that is equal to zero.

Secondly, we investigate the conservation of the trace of the density matrix. By switching summation indices in $\sum_{am} R_{aamm}\rho_{mm}(t)$, one can show that the two parts of the BRT cancel each other out leading to $\sum_a \dot{\rho}_{aa}(t) = 0$, which is equivalent to the fact that the trace of the density matrix is conserved.

The positive definiteness of the density matrix, i.e. $\rho_{aa}(t) \geq 0 \forall a$, can be shown for all times $t \geq 0$. Since a master equation does not change the sign of any component of its function, we can guarantee that $\mathrm{sgn}(\rho_{aa}(t)) = const$ for all indices a and times t. Thus, the positive definiteness of the density matrix is always given if the initial value $\rho(t=0)$, which is an extrinsic quantity to the formalism, is positive definite.

The hermiticity of the density matrix is conserved as well. Note that the definition of the RGFs (4.3.35) implies that $G(\omega) = G^*(-\omega)$. From the symmetry $\left[\Gamma^{\pm}_{ab,mn}\right]^* = \Gamma^{\mp}_{nm,ba}$ it follows that

$$R^*_{ab,mn} = R_{ba,nm}, \tag{4.5.60}$$

which means that the master equation (4.3.37) yields identical dynamics for ρ and $\rho^\dagger$, respectively.

We show that the density matrix reaches the correct Boltzmann form $\rho_{\text{final}} \propto e^{-\beta H_{\text{S}}}$ in the steady-state. This is equivalent to prove that ρ_{final} is a stationary solution of the master equation. Plugging ρ_{final} into Eq. (4.3.37) leaves us to show that $\sum_m R_{aa,mm} e^{-\beta E_m} = 0$. This is easy to see by considering that $f_\beta(\omega) e^{\beta\omega} = f_\beta(-\omega)$.

In order for a master equation of the form $\dot{\rho} = -R\rho$ to reach a finite steady state, at least one eigenvalue needs to be zero, while the other eigenvalues are positive. This is guaranteed for any finite Liouvillian (i.e. the BRT) by Evans' theorem [104, 105] and the existence of the zero-eigenvalue is shown above. The normalized eigenstate of the zero eigenvalue (called Gibbs state or Kubo-Martin-Schwinger state) is equal to the final equilibrium density matrix. The existence of only one zero eigenvalue determines that the number of possible steady states is also one.

Above we have mentioned that $R_{ab,mn}$ is proportional to $\delta_{\omega_{ab},\omega_{mn}}$. That means that the master equation (4.3.37) couples $\dot{\rho}_{ab}(t)$ and $\rho_{mn}(t)$, iff $\omega_{ab} = \omega_{mn}$. The BRT is thus diagonal in the energy differences ω_{ab} and can be written as an array $R(\omega_{ab})$ of quadratic block-matrices. Each of those blocks is considerably smaller in dimension than the whole BRT, making an exact diagonalization of the BRT possible. The by far largest block is the part of the DDM for the subspace $\omega_{ab} = 0$. This block has dimension $n \times n$, where n is the system Hilbert space dimension, and provides n real eigenvalues, although it is an asymmetrical matrix. The complex conjugate eigenvalue pairs $\lambda = x \pm iy$ are connected to the energy differences $\pm\omega_{ab} \neq 0$. This immediately follows from the above derived identity Eq. (4.5.60). For details on the eigenspectrum of the BRT the reader is referred to Ref. [106, 107]. One has to bear in mind that information on the particular indices is lost by reducing the BRT to $R(\omega_{ab})$. This reduction is only expedient if the desired expression relies on the energy differences $\omega_{ab} = E_a - E_b$ alone, instead of the single local energies E_a. This is given for TD-NEVs (4.3.40), as well as the ESFs (4.4.51).

In general, the BRT is asymmetric, i.e. $R_{ab,mn} \neq R_{mn,ab}$, which holds for each block-matrix. However, its eigenvalues are not automatically complex. As an example consider the $\omega_{ab} = 0$ sub-block, which is asymmetric, but has real eigenvalues. The other sub-blocks have complex eigenvalues, whose imaginary parts are entirely defined by the imaginary part of the BRT. Thus the imaginary part of the BRT defines the Lamb-shift and artificially neglecting it deletes the Lamb-shift.

4.6. Discussion of the BMA

In the following section we discuss the approximations of the BRF, i.e. the Born, the Markov and the secular approximation. We investigate their impact on local non-equilibrium real-time dynamics in Sec. 4.6.1 and on local equilibrium spectral functions in Sec. 4.6.2. For this purpose, we choose the most simple case of a spinless local two-level model, which resembles the RLM in the limit of an exact coupling. Here analytical solutions are available (see App. A.2), which make this model a perfect benchmark. A non-trivial extension of the RLM can be obtained by include a spin DOF for all fermionic particles as well as a local Coulomb-repulsion. This local Hubbard-like model resembles the SIAM in the exact limit. Although no analytical solution exists, this model has been extensively studied for over 60 years and is well understood (see Sec. 2.4). The spectral coupling function $\Gamma(\omega)$ for the BRF is in all cases considered to be constant on the interval $[-D, D]$ (see Eq. (4.3.26)). The application of a more general power-law spectral coupling function to the BRF is discussed in App. B.

4.6.1. Non-Equilibrium Real-Time Dynamics

Non-Interacting Model

We start with a simple two-level system

$$H_{\mathrm{S}} = \epsilon_{\mathrm{d}} d^\dagger d \tag{4.6.1.61}$$

as the local Hamiltonian with energy ϵ_d and $d^{(\dagger)}$ being an annihilator (creator) of a local mode. The state $|0\rangle$ shall be the empty state, while $|1\rangle$ denotes the excited case. Let us briefly discuss the energy scales of this model. The local energy of S is ϵ_{d}, while the maximum scale of B is given by the bandwidth D and the hybridization strength between both systems is Γ. If the local energy level exceeds the bandwidth, transitions between S and B are prohibited. In the context of the BMA we expect good results, if Γ is small in comparison to the other energies. Large temperatures should even out the difference between the energy scale and by that improve the BA even if Γ is large. The bandwidth D influences the correlation time t_{B} and a large D is expected to yield good results in the context of the MA even for short times.

We will investigate local non-equilibrium occupation $n_{\mathrm{d}}(t) = \langle d^\dagger d\rangle(t)$ for the discontinuous parameter quench $\epsilon_{\mathrm{d}}(t) = \epsilon^{\mathrm{i}}_{\mathrm{d}}\Theta(-t) + \epsilon^{\mathrm{f}}_{\mathrm{d}}\Theta(t)$. If unambiguous, we will omit the superscript "f" for the final system parameters for the sake of clarity.

We obtain

$$n_{\mathrm{d}}(t) = \mathrm{Tr}\Big\{e^{-iH_{\mathrm{S}}t}\rho^{\mathrm{I}}_{\mathrm{S}}(t)e^{iH_{\mathrm{S}}t}n_{\mathrm{d}}\Big\} = \rho_{11}(t)\,, \tag{4.6.1.62}$$

with $\rho_{11}(t) = \langle 1|\,\rho^{\mathrm{I}}_{\mathrm{S}}(t)\,|1\rangle$. The system is considered to be in thermal equilibrium for $t = 0$, which implies that the initial density matrix $\rho_{11}(0) = f_\beta(\epsilon^{\mathrm{i}}_{\mathrm{d}})$ is given by the Fermi function. To calculate the occupied state component $\rho_{11}(t)$ of the time-dependent density matrix, Eq. (4.3.18) is used, i.e. no Markov or secular approximation has been applied so far. The non-vanishing components of the damping matrices are given by

$$\begin{aligned} \Gamma^{+}_{01,10}(t,s) &= C(s)e^{-i\epsilon_{\mathrm{d}}s}, & \Gamma^{+}_{10,01}(t,s) &= C(s)e^{i\epsilon_{\mathrm{d}}s}, \\ \Gamma^{-}_{01,10}(t,s) &= C^*(s)e^{i\epsilon_{\mathrm{d}}s}, & \Gamma^{-}_{10,01}(t,s) &= C^*(s)e^{-i\epsilon_{\mathrm{d}}s}\,. \end{aligned} \tag{4.6.1.63}$$

At this point it is obvious that the oscillating terms $e^{i(\omega_{ab}+\omega_{mn})t}$ vanish and thus no secular approximation is required or even possible. By exploiting the conservation of the trace, $\rho_{00}(t) + \rho_{11}(t) = 1\,\forall\, t \geq 0$, we end up with the equation

$$\dot\rho_{11}(t) = -\int_0^t ds f(s)\rho_{11}(t-s) + g(t) \tag{4.6.1.64}$$

with

$$
\begin{aligned}
f(s) &= \frac{2}{\pi}\int_{-\infty}^{+\infty} d\epsilon \Gamma(\epsilon)\cos((\epsilon+\epsilon_{\mathrm{d}})s) \\
&= \frac{2}{\pi}\Gamma\frac{\sin\left((D+\epsilon_{\mathrm{d}})s\right)+\sin\left((D-\epsilon_{\mathrm{d}})s\right)}{s}, \\
g(t) &= \frac{1}{\pi}\int_{0}^{t} ds \int_{-\infty}^{+\infty} d\epsilon \Gamma(\epsilon) f_{\beta}(\epsilon)\cos((\epsilon-\epsilon_{\mathrm{d}})s) \\
&= \frac{2}{\pi}\Gamma\int_{-D}^{D} d\epsilon \frac{\sin((\epsilon-\epsilon_d)t)}{\epsilon-\epsilon_d} f_{\beta}(\epsilon),
\end{aligned}
\tag{4.6.1.65}
$$

for the non-equilibrium density matrix in the BA. Here we have inserted Eq. (4.3.26).

Let us first calculate the equilibrium values of this equation. $\rho_{11}(0)$ is chosen extrinsically and is thus exact within the limitations of the BA. The time-derivative $\dot{\rho}_{11}(t)$ vanishes at $t=0$, which yields the correct short-time behavior. To calculate the limit $t\to\infty$, we have to consider several things. Firstly, the function $f(s)$ decays on a time scale $1/D$, meaning that the system becomes Markovian and a full MA can be performed. The sinc-function under the integral of $g(t)$ converges to a delta function for large times, so that $g(t\to\infty) = 2\Gamma f_{\beta}(\epsilon_{\mathrm{d}})\Theta(D-|\epsilon_{\mathrm{d}}|)$. Equation (4.6.1.64) thus turns into

$$
\dot{\rho}_{11}(t) = -2\Gamma(\epsilon_{\mathrm{d}})\left(\rho_{11}(t) - f_{\beta}(\epsilon_{\mathrm{d}})\right), \tag{4.6.1.66}
$$

which has the simple solution

$$
n_{\mathrm{d}}(t) = \left(f_{\beta}(\epsilon_{\mathrm{d}}^{\mathrm{i}}) - f_{\beta}(\epsilon_{\mathrm{d}})\right) e^{-2\Gamma(\epsilon_{\mathrm{d}})t} + f_{\beta}(\epsilon_{\mathrm{d}}) \tag{4.6.1.67}
$$

for the local occupation. The steady-state in the limit $t\to\infty$ is hence given by $f_{\beta}(\epsilon_{\mathrm{d}})$ which is, once again, exact within the BA.

Note, that in Eq. (4.6.1.67) the full BMA has been performed, leading to a simple exponential decay on the time scale 2Γ. Since the equilibrium values of $n_{\mathrm{d}}(t)$ are independently of the MA given by a Fermi distribution, one can assess the error of the BA by calculating the relative difference Δn_{d} between the Fermi value and the exact impurity occupation. For our simple problem the impurity spectral function $A_{\mathrm{d}}(\omega)$ is a Lorentzian of width Γ with an energy shift that vanishes in the wideband limit (see

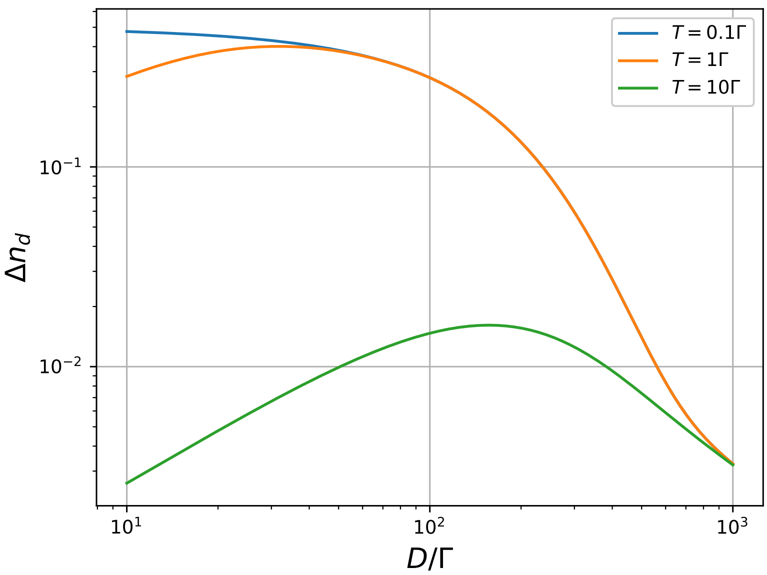

Figure 4.2.: The relative difference Δn_{d} of the exact impurity occupation n_{d} and the Fermi function $f(\epsilon_{\mathrm{d}})$ for different bandwidth D and temperature T. The local energy has been chosen as $\epsilon_{\mathrm{d}} = -0.1D$.

App. A). The equilibrium occupation can thus be calculated via

$$n_{\mathrm{d}} = \int_{-\infty}^{+\infty} d\omega f_{\beta}(\omega) A_{\mathrm{d}}(\omega). \tag{4.6.1.68}$$

In Fig. 4.2 the relative difference $\Delta n_{\mathrm{d}} = (f_{\beta}(\epsilon_{\mathrm{d}}) - n_{\mathrm{d}})/f_{\beta}(\epsilon_{\mathrm{d}})$ is plotted for a variation of D and different temperatures. The local energy ϵ_{d} is chosen to be $-0.1D$, to allow for transitions between S and B. For large values of ϵ_{d} and D the hybridization Γ can be seen as small and thus the systems S and B are approximately decoupled, which is the favored regime for the BA and consequently Δn_{d} is low. A large temperature T evens out the effect of a relatively larger Γ and by that improves the approximation.

To assess the MA, Eq. (4.6.1.64) needs to be solved numerically. Alternatively, the convolution integral can be factorized by using the first MA, which simplifies Eq. (4.6.1.64) to

$$\dot{\rho}_{11}(t) = -F(t)\rho_{11}(t) + g(t), \tag{4.6.1.69}$$

where $F(t)$ is the antiderivative of $f(s)$. However, by using the full MA one ends up with Eq. (4.6.1.66).

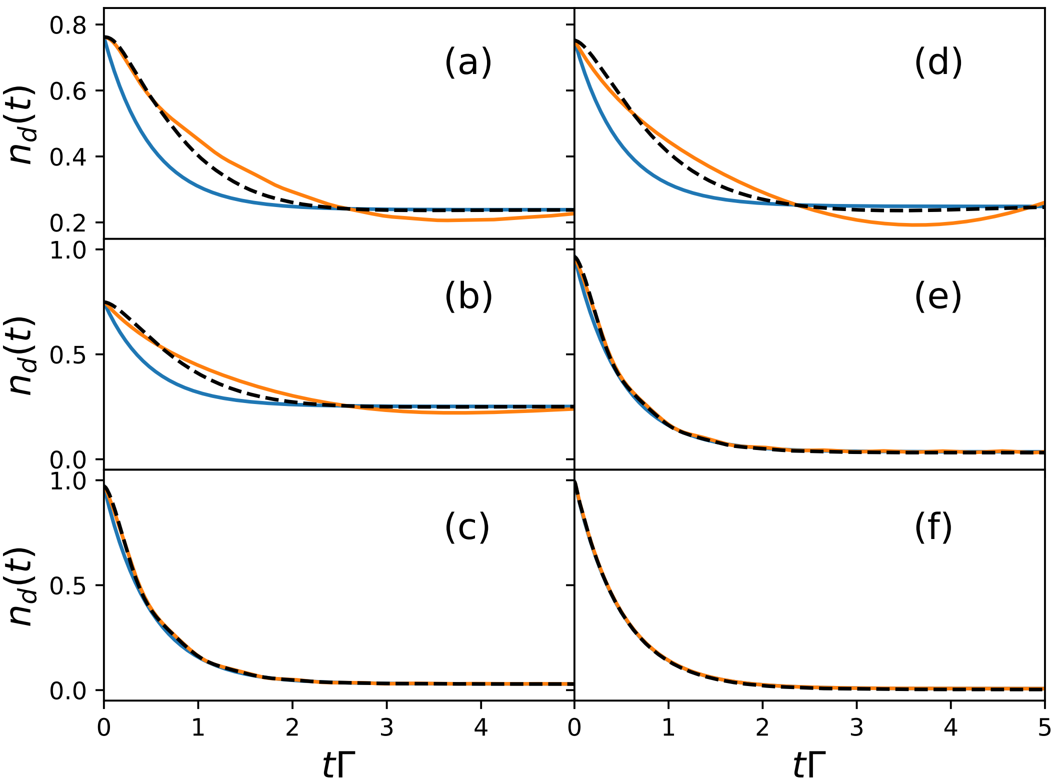

Figure 4.3.: Plot of the impurity occupation $n_{\mathrm{d}}(t)$ vs. dimensionless time $t\Gamma$ for $T = 0.1\Gamma$. The bandwidth D and the local energy ϵ_{d} have been varied in the following way: (a) $\epsilon_{\mathrm{d}} = 1, D = 10$, (b) $\epsilon_{\mathrm{d}} = 1, D = 100$, (c) $\epsilon_{\mathrm{d}}^{\mathrm{f}} = 10, D = 100$, (d) $\epsilon_{\mathrm{d}} = 1, D = 1000$, (e) $\epsilon_{\mathrm{d}} = 10, D = 1000$, (f) $\epsilon_{\mathrm{d}} = 100, D = 1000$. All values are given in units of Γ and $\epsilon_{\mathrm{d}}^{\mathrm{i}} = -\epsilon_{\mathrm{d}}$. The blue lines are the canonical BMA (4.6.1.67) and the orange lines are the BA plus the first MA (4.6.1.69). The analytical solution (A.2.22) is added as a black dashed line for comparison.

As a benchmark for the above discussed approximations, an exact solution of the two-level model in the wideband limit can be calculated with the Keldysh formalism (see App. A.2).

In Fig. 4.3 the local dynamics is investigated to assess the Born and the first MA. The curves are artificially scaled to the exact equilibrium values to allow for a better comparison of the qualitative shape of the curves. We have chosen the temperature $T = 0.1\Gamma$, where the low temperature limit is practically reached. As argued above, the effect of the approximations is most pronounced for low temperatures. The BMA is plotted as a blue curve, while the first MA is given as an orange curve and the exact solution is added as a black dashed line.

An interesting point is revealed in this plot, i.e. the effect of the MA goes beyond the correlation time $t_\mathrm{B} = 1/D$. For $t = 0$ the approximation is worst, since here the function falls off exponentially instead of being constant. The effect of the MA is carried on until the steady-state is reached at around $t = 2\Gamma$. In turn, the relative value of the local energy $\epsilon_\mathrm{d}/\Gamma$ has a strong effect on the short time behavior of the curve, improving the MA for large values. Mathematically, this can be seen in Eq. (4.6.1.64) by varying D and ϵ_d. Both generate oscillations in $f(t)$ and $g(t)$. Since we choose $\epsilon_\mathrm{d} < D$, the local energy is responsible for the slowly oscillating terms and thus defines the relevant time scale for the MA. In the general damping matrices $\Gamma^{\pm}_{ab,mn}(t,s)$ of Eq. (4.3.25) this effect is mediated by the complex exponential terms $e^{i\omega s}$, which oscillate in a frequency given by the eigenenergies of the system Hamiltonian H_S and thereby define the dominant time scale on which the BRT $R_{ab,mn}(t,s)$ converges to its steady-state predicted within the MSA (see Eq. (4.3.18) versus (4.3.37)). For small $\epsilon_\mathrm{d} \approx \Gamma$ the global rate of the master equation dampens the density matrix before the BRT is converged to its steady-state. In this case, the MA is off until the steady-state has been reached, as can be seen for the blue curves in Fig. 4.3. The bandwidth D, as the largest energy of the "unperturbed Hamiltonian" $H_0 = H_\mathrm{S} + H_\mathrm{B}$, controls the very short time behavior where the density matrix is approximately constant. Note that the exact solution always fulfills $\dot{n}_\mathrm{d}(t = 0) = 0$ (even for panel (f)), but that the time scale until the exponential decay steps in is short due to the large D.

Two things shall be mentioned here. Firstly, the exact solution is, as discussed above, only defined for the wideband limit. We artificially supplemented the equations by the real-part of the impurity self-energy (see App. A.2) to correct the equilibrium values, but still the qualitative shape of the black dashed curves in the panels (a) to (c) cannot be trusted, since we are not in the wideband limit here. Secondly, in Fig. 4.3 the first MA has been used for the orange curves. The effect of this approximation in comparison to the pure BA is still unclear.

To illustrate the two points above, the impurity occupation $n_\mathrm{d}(t)$ is plotted in Fig. 4.4. Several approximations (solid lines) are compared to the exact curve in the limit $t \to 0$ (red dashed line), which is obtained by calculating the density matrix $\rho^{\mathrm{I}}_{[1]}(t)$ via Eq. (4.2.14). This yields

$$\begin{aligned}\rho^{\mathrm{I}}_{[1]}(t) =& \rho_{11}(0) - 2\frac{\Gamma}{\pi}\left[g(D-\epsilon_d;t) + g(D+\epsilon_d;t)\right]\rho_{11}(0) \\ &+ 2\frac{\Gamma}{\pi}\left[g(D+\epsilon_d;t) - g(\epsilon_d;t)\right] \qquad (4.6.1.70)\end{aligned}$$

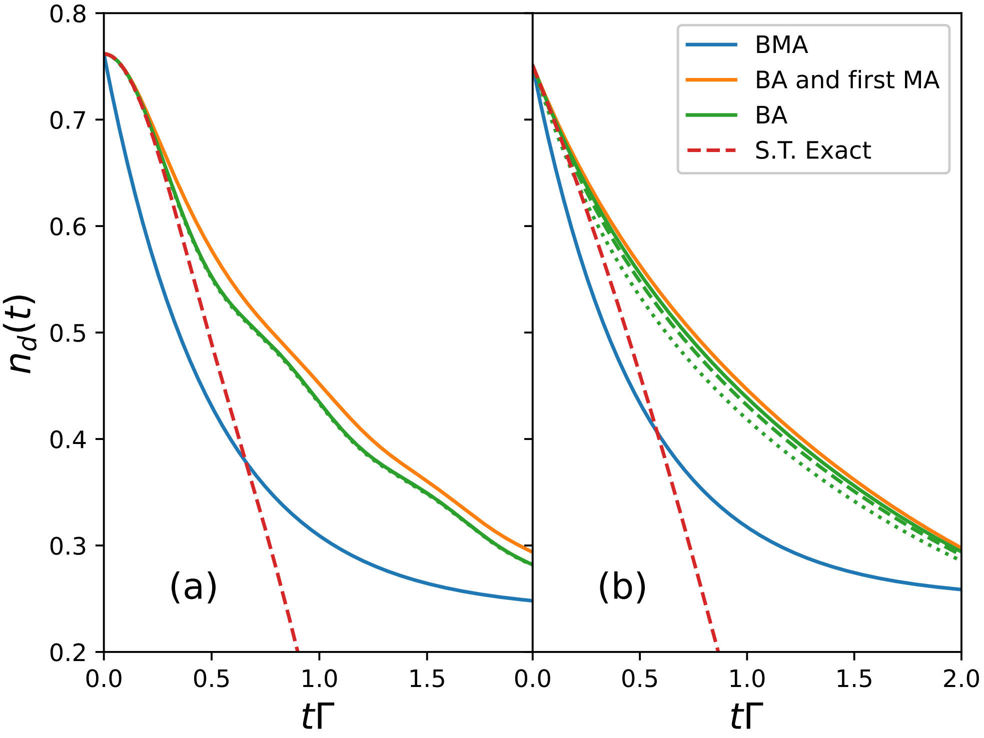

Figure 4.4.: The impurity occupation $n_\mathrm{d}(t)$ vs. short dimensionless times $t\Gamma$. The parameters have been chosen as $T = 0.1$, $\epsilon_\mathrm{d} = 1$ and $D = 10$ and $D = 1000$ for (a) and (b) respectively in units of Γ. The blue line is the canonical BMA (4.6.1.66), the orange line is the BA plus the first MA (4.6.1.69) and the green line only includes the BA (4.6.1.64). Here three different value for the number N_time of mesh-points are given (dotted line: $N_\mathrm{time} = 1000$, dashed line: $N_\mathrm{time} = 5000$, solid line: $N_\mathrm{time} = 10000$). The exact short time dynamics (4.6.1.70) are added as a red dashed line for comparison.

with $g(\epsilon; t) = t\mathrm{Si}(\epsilon t) + \frac{\cos(\epsilon t)-1}{\epsilon}$ and $\mathrm{Si}(x)$ being the sine integral function.

The blue curve is the full BMA, the orange one is the first MA and the green lines depict the pure BA. Here three different value for the number N_time of mesh-points are plotted to rule out the effects of numerical inaccuracy. The influence of the second MA turns out to be weak, since the green curves are almost identical to the orange ones. A large bandwidth D shortens the correlation time and thereby the time scale on which the convolution integral is relevant. In the wideband limit the first MA becomes exact in the limitations of the BA. By comparing to the red dashed curve, one can deduce from the figure that even the first MA is exact for short times and that the second MA is responsible for significant deviation from the exact solution for short times.

Apart from the above discussed approximations, the strength of the BRF in the BMA definitely lies in the thermalization process itself. By including a full environment continuum in the OQS, a true thermalization is guaranteed. Also, the relaxation rate of 2Γ resembles the exact rate of the analytical solution well.

Interacting Model

To investigate a more complex model, we can add the spin as a DOF for each particle of the fermionic system. A Coulomb repulsion U and an external magnetic field B can be added as well to obtain

$$H_\mathrm{S} = \sum_\sigma \left(\epsilon_\mathrm{d} - \frac{\sigma}{2}B\right) n_\sigma + U n_\uparrow n_\downarrow \,. \tag{4.6.1.71}$$

The Hamiltonian resembles the impurity part of the SIAM, i.e. an atomic Hubbard model. We have to consider the four states $|0\rangle, |{\uparrow}\rangle, |{\downarrow}\rangle$ and $|2\rangle$ of the occupation on the local site. We define

$$\begin{aligned} \rho_{\uparrow\downarrow} &= \langle\uparrow|\, \rho_\mathrm{S}^\mathrm{I} \,|\uparrow\rangle - \langle\downarrow|\, \rho_\mathrm{S}^\mathrm{I} \,|\downarrow\rangle \\ \rho_{02} &= \langle 0|\, \rho_\mathrm{S}^\mathrm{I} \,|0\rangle - \langle 2|\, \rho_\mathrm{S}^\mathrm{I} \,|2\rangle \end{aligned} \tag{4.6.1.72}$$

and exploit the conservation of the trace of the density matrix to obtain

$$\begin{aligned} n_\mathrm{d} &= 1 - \rho_{02} \\ S_\mathrm{z} &= \frac{1}{2}\rho_{\uparrow\downarrow} \end{aligned} \tag{4.6.1.73}$$

for the impurity occupation and magnetization, respectively. If we restrict ourselves to the SAM for the final parameter set, i.e. $\epsilon_\mathrm{d}^\mathrm{f} = -U^\mathrm{f}/2$ and $B^\mathrm{f} = 0$, the symmetries in the BRT yield

$$\begin{aligned} \dot{\rho}_{02}(t) &= -\frac{4}{\pi}\int_0^t ds \int_{-\infty}^{+\infty} d\epsilon \Gamma(\epsilon) f_\beta(\epsilon) \cos((\epsilon + U^\mathrm{f}/2)s)\rho_{02}(t-s) \\ \dot{\rho}_{\uparrow\downarrow}(t) &= -\frac{4}{\pi}\int_0^t ds \int_{-\infty}^{+\infty} d\epsilon \Gamma(\epsilon) f_\beta(\epsilon) \cos((\epsilon - U^\mathrm{f}/2)s)\rho_{\uparrow\downarrow}(t-s). \end{aligned} \tag{4.6.1.74}$$

Again, the secular approximation has not been used. With the first MA, the equations can be solved leading to

$$\begin{aligned} n_{\mathrm{d}}(t) &= 1 - \rho_{02}(0) e^{-F(+U;t)} \\ S_{\mathrm{z}}(t) &= \frac{1}{2} \rho_{\uparrow\downarrow}(0) e^{-F(-U;t)} \end{aligned} \tag{4.6.1.75}$$

with

$$F(U;t) = \frac{4}{\pi} \int_{-\infty}^{\infty} d\epsilon \Gamma(\epsilon) f_\beta(\epsilon) \frac{1-\cos((\epsilon+U/2)t)}{(\epsilon+U/2)^2}. \tag{4.6.1.76}$$

In the limit of a large bandwidth D and large times, we obtain $F(U; t \to \infty) = 4\Gamma(-U/2) f_\beta(-U/2) t$ and end up with

$$\begin{aligned} n_{\mathrm{d}}(t) &= 1 - \rho_{02}(0) e^{-4\Gamma(-U/2) f_\beta(-U/2) t} \\ S_{\mathrm{z}}(t) &= \frac{1}{2} \rho_{\uparrow\downarrow}(0) e^{-4\Gamma(+U/2) f_\beta(+U/2) t}. \end{aligned} \tag{4.6.1.77}$$

Note, that for $2D < |U|$ the BRT vanishes and so the density matrix is constant over time. For the initial parameters $B^{\mathrm{i}}/2 = \epsilon_{\mathrm{d}}^{\mathrm{i}} = \Gamma, U^{\mathrm{i}} = 0$ we obtain

$$\begin{aligned} \rho_{\uparrow\downarrow}(0) &= \frac{1}{2} - f_\beta(\Gamma) \\ \rho_{02}(0) &= \rho_{\uparrow\downarrow}(0)\,. \end{aligned} \tag{4.6.1.78}$$

The SIAM is a non-trivial model, meaning that no exact solution for the problem exists to estimate the quality of the BMA. However, the results of the TD-NRG (see Sec. 3.9 or Ref. [29]) can be used as a guideline. The first MA (4.6.1.75) is expected to be a good approximation, if the local energy U is large compared to the hybridization Γ. Low temperatures T might enhance the effect of the BA. The full BMA (4.6.1.77) is a good estimate if additionally the wideband limit $D \gg \Gamma$ is assumed.

In Fig. 4.5 the first MA (dashed lines) is compared to the BMA (blue solid line). A temperature of $T = \Gamma$ and $U \in \{\Gamma, 5\Gamma, 10\Gamma\}$ have been chosen for the sake of presentation. If the temperature is significantly higher, the U-dependence of the curves gets evened out, while a lower temperature enlarges them and by that significantly slows down the relaxation of $S_{\mathrm{z}}(t)$. The effect happens analogly for smaller and larger U, respectively. The time-axis has been chosen logarithmically, which amplifies differences in the short time behavior. If U is small, we basically obtain the two-level model

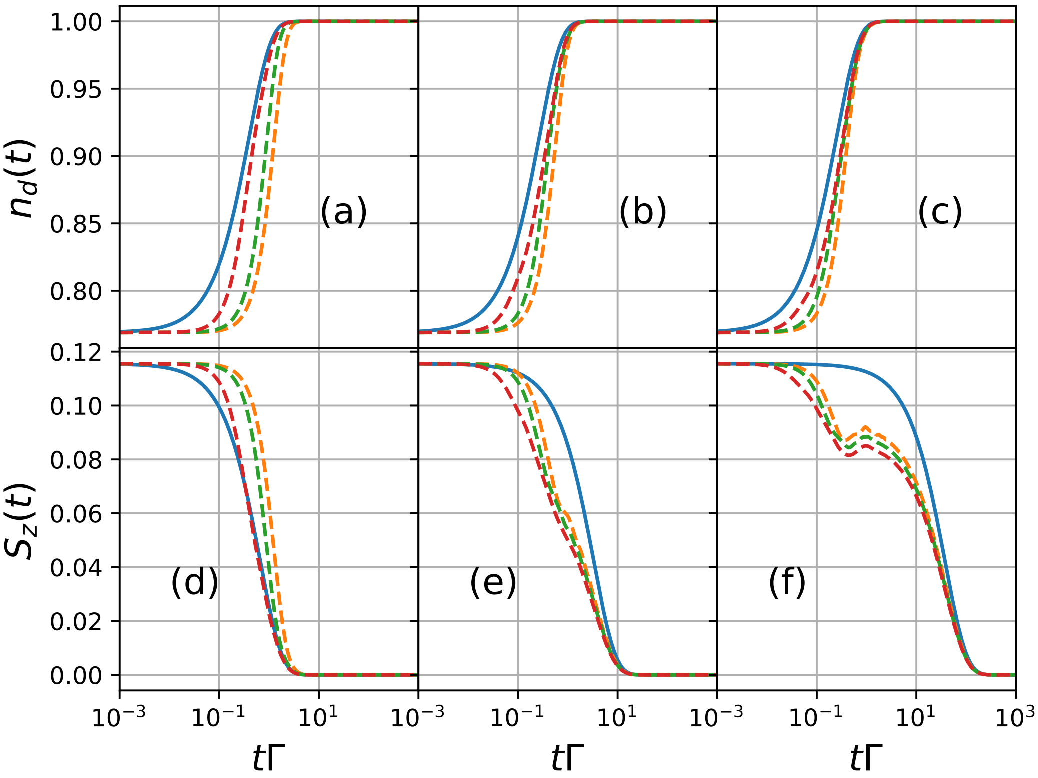

Figure 4.5.: Semi-logarithmic plot of the impurity occupation $n_\mathrm{d}(t)$ and the magnetization $S_z(t)$ vs. the dimensionless time $t\Gamma$ for temperature $T = \Gamma$. We display a quench from $B^\mathrm{i}/2 = \epsilon_\mathrm{d}^\mathrm{i} = \Gamma$ and $U^\mathrm{i} = 0$ to $B^\mathrm{f} = 0$ and $\epsilon_\mathrm{d}^\mathrm{f} = -U^\mathrm{f}/2$. The Coulomb repulsion is $U^\mathrm{f} = \Gamma$ for (a),(d), $U^\mathrm{f} = 5\Gamma$ for (b),(e) and $U^\mathrm{f} = 10\Gamma$ for (c),(f). The orange, green and red dashed curves are the first MA (4.6.1.75) for bandwidth $D = U, 2U$ and $10U$, respectively. The blue curves are calculated via Eq. (4.6.1.77).

discussed above with $\epsilon_\mathrm{d}^\mathrm{f} = 0$ and a different initial value. Thus, the first MA approaches the BMA solution in the wideband limit. The red dashed curves are basically converged for large D but still differ from the BMA. Analogly to the two-level system it shows, that controlling the bandwidth D, and thereby the correlation time of the bath, is not enough to justify the MA. Instead, increasing the local energies is required as well. Apart from that, the system shows a transition between the equilibrium values given by the Fermi distribution, which is exact in the BA. The gradient of the curves at $t = 0$ is almost zero for the magnetization and slightly larger for the occupancy. The first MA is able to guarantee a gradient of zero for $t = 0$.

The relaxation rate of the functions in the BMA scales with $4\Gamma f_\beta(\pm U/2)$ (see Eq.

(4.6.1.77)). The TD-NRG solution suggests a scaling with the Kondo temperature T_{K} [29]. In the SAM, T_{K} can be approximated for weak coupling as

$$T_{\mathrm{K}} = De^{-\frac{\pi U}{8\Gamma}} \tag{4.6.1.79}$$

(see Eq. (2.3.4) and (2.4.10)). Let us quickly compare this to the time scale of the magnetization in the BMA (4.6.1.77). We want to explicitly show that $f_\beta(U/2) \propto T_{\mathrm{K}}$. For $\beta U \gg 1$ we approximate the Fermi function as $f_\beta(U/2) \approx e^{-\beta U/2}$. The time scales are proportional, if $T = \frac{4}{\pi}\Gamma \approx \Gamma$, which is similar to the temperature of Fig. 4.5. In this approximation, U has to be chosen well above Γ, which is fulfilled in panel (f). This is another example for the quality of the BMA.

Let us conclude this section by investigating TD-NEVs in the interacting case for large local parameters, i.e. $U > 2D$. We restrict to $T = 0$, which simplifies Eq. (4.6.1.74) to

$$\begin{aligned}\dot{\rho}_{02}(t) &= -\frac{4\Gamma}{\pi}\int_0^t ds \frac{\sin((D-U/2)s) + \sin(U/2s)}{s}\rho_{02}(t-s)\\ \dot{\rho}_{\uparrow\downarrow}(t) &= -\frac{4\Gamma}{\pi}\int_0^t ds \frac{\sin((D+U/2)s) - \sin(U/2s)}{s}\rho_{\uparrow\downarrow}(t-s).\end{aligned} \tag{4.6.1.80}$$

Those equations can be solved numerically to obtain the local non-equilibrium occupation and magnetization in the BA. By applying the first MA, we can solve the equations analytically to obtain Eq. (4.6.1.75) with

$$F(U;t) = \frac{4\Gamma}{\pi}\left(g(U/2;t) + g(D-U/2;t)\right), \tag{4.6.1.81}$$

where the function $g(\epsilon;t)$ is defined in Eq. (4.6.1.70).

In Fig. 4.6 we display the above discussed approximations for $T \to 0$ and large U/D. For $U \leq 2D$ the occupation number in the BA converges to the correct steady-state of 1 (green curves in Fig. 4.6 (a) and (b)). However, in the case $U > 2D$ (green curves in Fig. 4.6 (c)), $n_{\mathrm{d}}(t)$ oscillates around $1 - 0.5\exp\Big(-\frac{16\Gamma D}{\pi U(U-2D)}\Big)$ for large times and converges to 0.5 for $U \to \infty$. The magnetization $S_z(t)$ oscillates for arbitrary U and large times around $0.25\exp\Big(-\frac{16\Gamma D}{\pi U(U+2D)}\Big)$ (green curves in Fig. 4.6 (d), (e) and (f)). The correct steady-state of 0 is reached only for $U \to 0$. This suggests a large error of the BA for large U/D. The first MA has no relevant impact on the steady-states (orange curves in Fig. 4.6). However, the second MA (blue curves in Fig. 4.6) completely prohibits transitions between S and B for $U > 2D$ and thus has an even

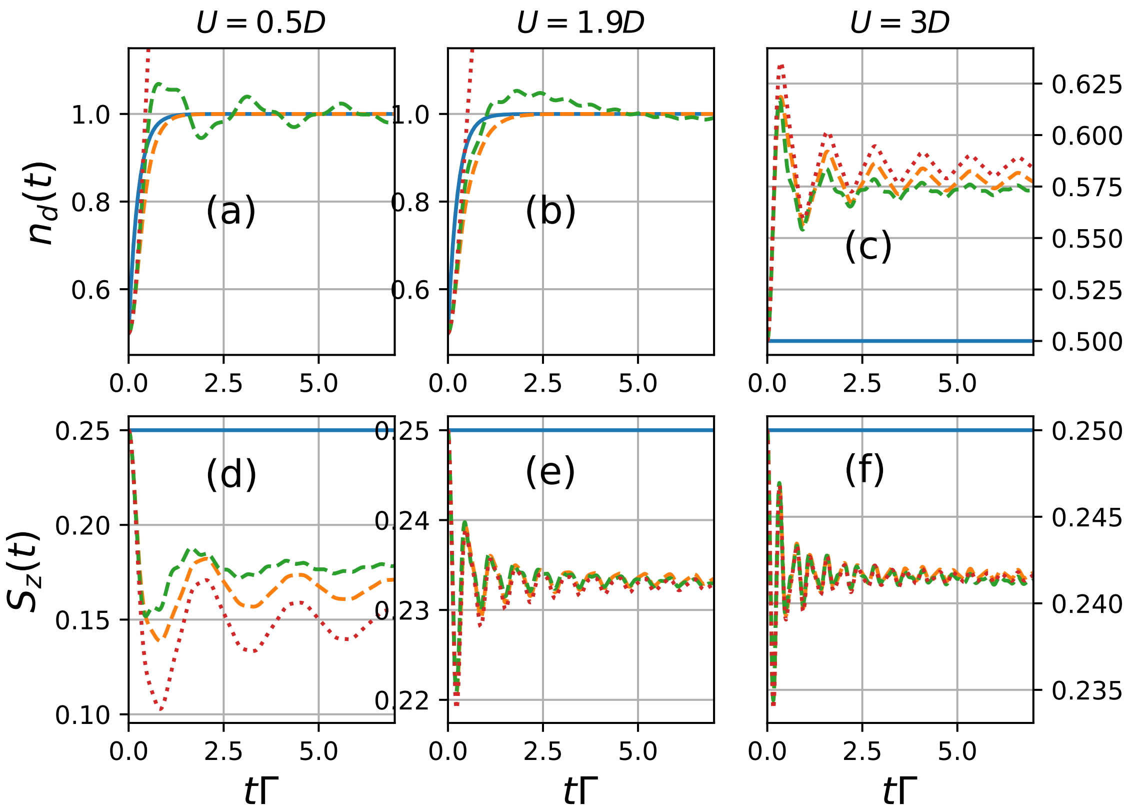

Figure 4.6.: Impurity occupation $n_\mathrm{d}(t)$ and the magnetization $S_z(t)$ vs. the dimensionless time $t\Gamma$ for temperature $T = 0$. We display a quench from $B^\mathrm{i}/2 = \epsilon_\mathrm{d}^\mathrm{i} = \Gamma$ and $U^\mathrm{i} = 0$ to $B^\mathrm{f} = 0$ and $\epsilon_\mathrm{d}^\mathrm{f} = -U^\mathrm{f}/2$. The Coulomb repulsion is $U^\mathrm{f} = 0.5D$ for (a),(d), $U^\mathrm{f} = 1.9D$ for (b),(e) and $U^\mathrm{f} = 3D$ for (c),(f). We have chosen a bandwidth of $D = 10\Gamma$. The orange dashed curves are the BA and the first MA (Eq. (4.6.1.75) with Eq. (4.6.1.81)). The green dashed curves represent the pure BA of Eq. (4.6.1.80). The blue solid curves are the full BMA calculated via Eq. (4.6.1.77) and the red dotted curves are the exact short-time solutions via Eq. (4.6.1.82).

stronger impact on the steady-states than the BA. Additionally, for $S_z(t)$ the Fermi-function erases all dynamics for finite U and $T \to 0$ due to the second MA (see Eq. (4.6.1.77)).

The effect of the first MA is to damp short-time oscillations (compare orange and green curves in Fig. 4.6 (a), (b) and (d)). For large U/D, the differences between the two curves vanish, suggesting that the first MA does not have a significant effect in this case.

For short times, the second MA turns the actual t^2 dependency of the TD-NEV into a linear dependency in t (see Fig. 4.6 (a) and (b)), which is identical to the non-interacting case (see Fig. 4.4 (a)).

To estimate the effect of the BA on short-time dynamics consider Eq. (4.2.14). We obtain

$$\begin{aligned} n_{\mathrm{d}}(t) &= 1-\rho_{02}(0)(1-F(+U;t)) = 1-\rho_{02}(0)(1-V^2t^2+\frac{3}{288}V^2U^2t^4+\mathfrak{O}(t^6)) \\ S_{\mathrm{z}}(t) &= \frac{1}{2}\rho_{\uparrow\downarrow}(0)(1-F(-U;t)) = \frac{1}{2}\rho_{\uparrow\downarrow}(0)(1-V^2t^2+\frac{3}{288}V^2U^2t^4+\mathfrak{O}(t^6)), \end{aligned} \tag{4.6.1.82}$$

which resembles Eq. (4.6.1.75) for short times. The curves of Eq. (4.6.1.82) are plotted in Fig. 4.6 as red dotted lines. It is depicted, that the dashed lines reproduce the correct short-time dynamics well, while the green lines are a slight improvement to the orange ones. Equation (4.6.1.82) shows the typical short-time behavior of Eq. (4.3.32), which scales by the squared hybridization $V^2 = 2D\Gamma/\pi$ in quadratic order in t. The Coulomb repulsion U first appears in fourth order in t. For increasing U the curves become flatter (not explicitly shown), suggesting a decreasing relaxation rate. Interestingly, the red dotted curves converge to the green dashed ones for large U/D. This suggests, that the validity of short-time approximations is extended to later times, if U is increased.

From Fig. 4.6 we can conclude, that for large U/D short-time dynamics are most impaired by the second MA, as is the case for the non-interacting QIM as well (see above). The first MA damps some oscillations on intermediate time scales, but does not relevantly influence dynamics. Also, its influence vanishes for $U \to \infty$. On the other hand, the BA has a significant impact on large time scales, as it corrupts the steady-state. Its influence on intermediate time scales, i.e. on the relevant relaxation rates of the TD-NEV, cannot be estimated at this point, since no exact solutions for the SIAM are available. More details on the case of large local energies can be found in Sec. 4.7.2.

4.6.2. Equilibrium Spectral Functions

Non-Interacting Model

The spectral function $A_{\mathrm{d}}(\omega)$ (see Eq. (4.4.53)) of the impurity can be calculated for the two-level system described above in a similar manner as the non-equilibrium occupation number. As a first step, the time-dependent reduced operator $\chi(t)$ is calculated in the interaction picture with the master equation (4.4.47) before the MA is applied. For the TD-EGF, only the component $\chi_{10}(t)$ is relevant. We obtain

$$\dot{\chi}_{10}(t) = -\int_0^t ds f(s) \chi_{10}(t-s) \tag{4.6.2.83}$$

with

$$\begin{aligned} f(s) &= \frac{1}{\pi} e^{i\epsilon_{\mathrm{d}} s} \int_{-\infty}^{+\infty} d\epsilon \Gamma(\epsilon) \cos(\epsilon s) \\ &= \frac{2}{\pi} \Gamma e^{i\epsilon_{\mathrm{d}} s} \frac{\sin(Ds)}{s}. \end{aligned} \tag{4.6.2.84}$$

Note that Eq. (4.6.2.83) is independent of the temperature. For large s the oscillating terms in $f(s)$ cancel each other out, letting the expression vanish in the limit $s \to \infty$. To evaluate the steady-state of the function we can thus use the MA which gives

$$\dot{\chi}_{10}(t) = -(\Gamma(\epsilon_{\mathrm{d}}) + i\gamma(\epsilon_{\mathrm{d}}))\chi_{10}(t) \tag{4.6.2.85}$$

with

$$\gamma(\epsilon) = \mathfrak{Im} C(\epsilon) - \mathfrak{Im} C(-\epsilon) = \frac{\Gamma}{\pi} \ln\left(\frac{D-\epsilon}{D+\epsilon}\right), \tag{4.6.2.86}$$

where $C(\epsilon) = C_{\mathrm{p/h}}(\epsilon)$ is the correlation function according to Eq. (4.3.35) for a symmetric spectral coupling function. Obviously, the function $\chi_{10}(t)$ vanishes for $t \to \infty$. The $t = 0$ value is given by $\chi_{10}(0) = \langle 1| d^\dagger \rho_{\mathrm{S}} + \rho_{\mathrm{S}} d^\dagger |0\rangle = 1$. According to Eq. (4.4.45) we obtain the TD-EGF

$$G_{\mathrm{d}}(t) = -i\Theta(t) e^{i\gamma(\epsilon_{\mathrm{d}}))t - i\epsilon_{\mathrm{d}} t - \Gamma(\epsilon_{\mathrm{d}})t}. \tag{4.6.2.87}$$

From here we obtain the spectral function

$$A_{\mathrm{d}}(\omega) = \frac{1}{\pi} \frac{\Gamma(\epsilon_{\mathrm{d}})}{(\omega - \epsilon_{\mathrm{d}} + \gamma(\epsilon_{\mathrm{d}}))^2 + (\Gamma(\epsilon_{\mathrm{d}}))^2}, \tag{4.6.2.88}$$

which resembles the exact spectral function of the RLM (see Eq. (A.1.10) in the appendix).

In Fig. 4.7 the functions $B(t) = -\mathfrak{Im} G_{\mathrm{d}}(t)$ and $A(\omega)$ are plotted in the BMA (black dashed line), in the BA plus first MA (blue line) and in the BA only (orange line), respectively. Note, that the BMA renders the exact solution. This implicates that the

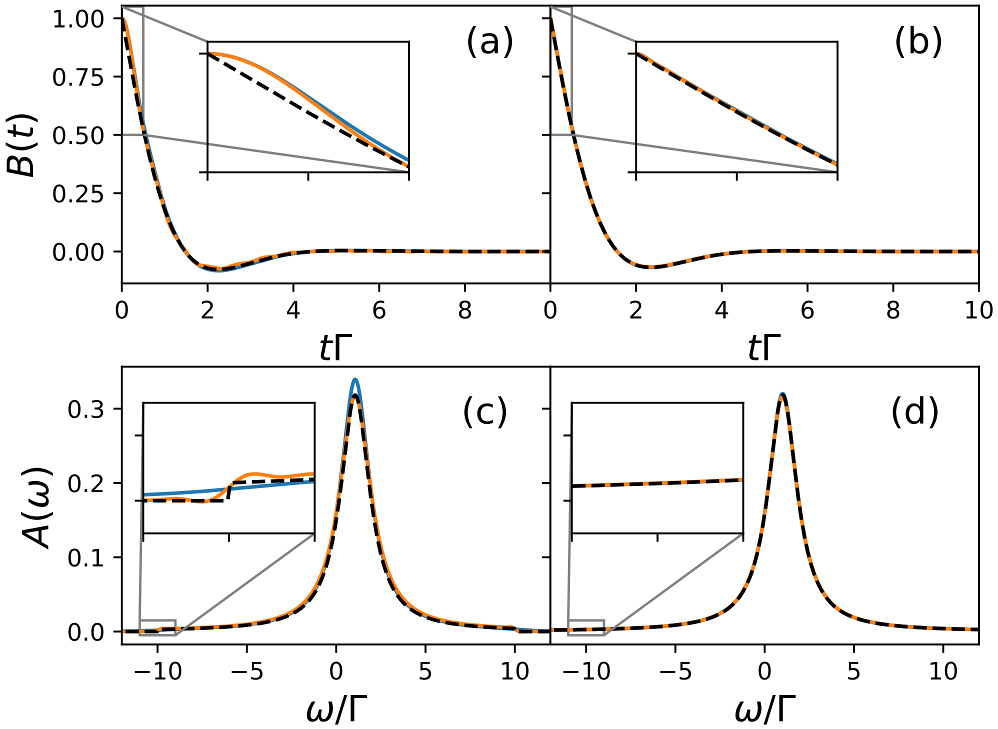

Figure 4.7.: Plot of $B(t) = -\mathfrak{Im} G_\mathrm{d}(t)$ and $A(\omega) = -\mathfrak{Im} G_\mathrm{d}(\omega)/\pi$ of the two-level model vs. dimensionless time $t\Gamma$ and energy ω/Γ respectively. The bandwidth has been chosen as $D = 10\Gamma$ ((a),(c)) and $D = 100\Gamma$ ((b),(d)), respectively. Different approximations according to the BRF are displayed. The blue lines are the BA plus the first MA and the orange lines only include the BA (4.6.2.83). The BMA according to Eq. (4.6.2.85) is added as a black dashed line. The parameter $\epsilon_\mathrm{d} = \Gamma$ has been chosen.

MA compensates the error done by the BA. However, both effects are minor. When the Green's functions are transformed into spectral functions, one can see that there is no sharp cut-off for $\omega = \pm D$ in the blue and orange curves. The convolution integral is able to compensate that with a smooth transition (panel (c)). The first MA lacks a cut-off and makes the spectral function too narrow. This effect is not due to numerical inaccuracy but a flaw of the approximation. The deviation from the exact solution is decreased by increasing the bandwidth D (panel (d)). A larger local energy ϵ_d simply adds oscillations in $\chi_{10}(t)$, which translate to an energy shift in $A_\mathrm{d}(\omega)$.

Interacting Model

Let us conclude this section by applying the BRF to the atomic Hubbard model (4.6.1.71). Since the local operator $d^{(\dagger)}$ gains a spin DOF σ, we obtain one TD-EGF for the spin up and one for the spin down case. Since we again restrict ourselves to the absence of an external magnetic field, those two GFs become identical. We define $\chi_\sigma(t) = d^\dagger_\sigma \rho + \rho d^\dagger_\sigma$ which has only two non-zero components $\chi_{\sigma 0}(t)$ and $\chi_{2\overline{\sigma}}(t)$ with $\overline{\sigma} \equiv -\sigma$. Note that χ is expressed here in the interaction picture representation. The equation of motion reads

$$\dot{\chi}(t) = -\frac{2}{\pi}\Gamma \int_0^t ds \frac{\sin(Ds)}{s} e^{-iUs/2} \Big[2\chi(t-s) - e^{-iU(t-s)}\chi^*(t-s) \Big] \tag{4.6.2.89}$$

with $\chi(t) \equiv \chi_{\sigma 0}(t) = \chi^*_{2\overline{\sigma}}(t)$. For the first time, oscillating terms enter where the secular approximation can be applied by replacing $e^{-iUt} \to \delta_{U,0}$. Note, that the $U = 0$ case recovers the non-interacting model (4.6.1.61), which we have calculated above. If U is large compared to Γ, the secular approximation can be applied and is expected to yield good results, since in this case the oscillating terms average themselves to zero. For $U = 0$ the secular approximation does not have to be applied and is thus exact. For small finite U, however, it will deviate significantly from the exact solution. To be precise, the secular approximation artificially sets $e^{-iUt} \to 0$ for $U > 0$. For $U \to 0$ those terms are not recovered leading to a discontinuous jump of the function $\chi(t)$.

To investigate this jump we first calculate the BMA of Eq. (4.6.2.89). We obtain

$$\dot{\chi}(t) = -2\left(\Gamma(U/2) + i\gamma(U/2)\right)\chi(t) + \Gamma(U/2)\delta_{U,0}\chi^*(t). \tag{4.6.2.90}$$

For $U > 0$ the Kronecker-deltas vanish and the spectral function resembles two Lorentzians of width 2Γ at positions $\omega = \pm(U/2 - \gamma(U/2))$, which is in accordance with analytical predictions [108]. They can be interpreted as so-called Hubbard peaks. In the wideband limit the Lamb-shift $\gamma(U/2)$ vanishes. In the non-interacting case we end up with the analytical solution of the RLM (4.6.2.88) for $\epsilon_\mathrm{d} = 0$.

The case $U \gg D$ can be investigated by applying the secular approximation $e^{-iUt} \to 0$ on the r.h.s. of Eq. (4.6.2.89) and replacing $\frac{\sin(Ds)}{s} \to D$. The equation can now be solved by a Laplace transform and yields $\chi(t) = \chi(0)$ for $U \gg D$. The spectral function is thus represented by two delta-peaks at $\omega = \pm U/2$. If the local energies exceed the bandwidth, transitions into the bath are suppressed and thus the lifetime of local excitations goes to infinity if the bandwidth vanishes.

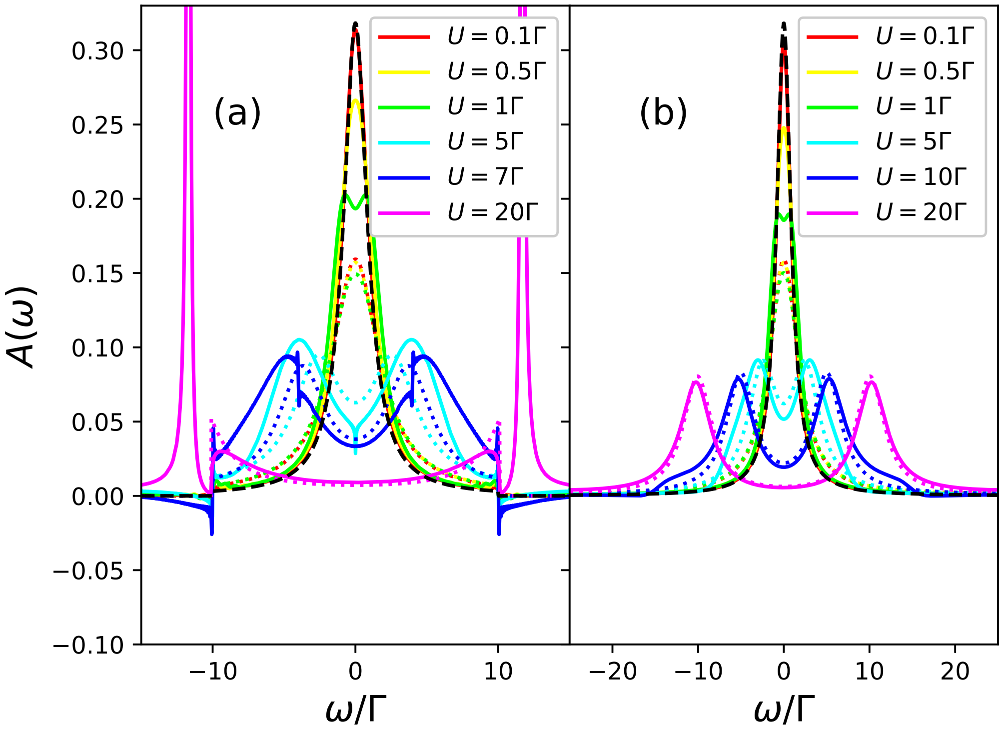

Figure 4.8.: The spectral function $A_\mathrm{d}(\omega) = -\mathfrak{Im} G_\mathrm{d}(\omega)/\pi$ of the symmetrical atomic Hubbard model $\epsilon_\mathrm{d} = -U/2$ for (a) $D = 10\Gamma$ and (b) $D = 100\Gamma$, respectively. The Coulomb repulsion U has been varied. In the case $U = 2D$ we have shifted the bandwidth by $+0.1$. The solid lines are the solution in the BA, the additional Markov plus secular approximation is added as a dotted line of the same color. The exact non-interacting solution $U = 0$ is added for comparison as a black dashed line.

In Fig. 4.8 we have plotted the spectral function in the above discussed approximations. It is shown, that by lowering U, Eq. (4.6.2.89) (solid lines) allows for a smooth transition to the $U = 0$ case (black dashed line). In contrast, the secular approximation (dotted lines) applied in Eq. (4.6.2.90) deviates from the exact curves for small U.

For large D (i.e. panel (b)) the MA becomes reliable and so the solid and dotted curves for $U = 20\Gamma$ match nicely. If, on the other hand, $U \geq 2D$, the MA cuts out the excitations at $\omega = \pm U/2$ (magenta dotted curve in panel (a)). In a non-Markovian environment, these excitations persist, even for large $U \gg D$ (magenta solid curve in panel (a)). Numerical calculations for $U \gg D$ show, that those peaks are basically Lorentzians with a width $\propto D$. They are located at $\omega = \pm(U/2 + \delta_\mathrm{shift})$ with a shift

$\delta_{\text{shift}} \propto \frac{D\Gamma}{U}$. Consequently, we obtain delta-peaks at $\omega = \pm U/2$, if $D \to 0$, which is in accordance with the estimates made above.

Raas *et al* [109] have examined the Hubbard peaks of the SAM for $U > 2D$ with DMRG calculations and backed their results by Fermi's golden rule considerations. They found $\delta_{\text{shift}} \propto V^2/U$ for a semi-elliptic DOS of the bath, which is in qualitative accordance to our findings, considering that we have chosen a constant DOS. The width of the Hubbard peaks has been found to be $\propto V^4/U^2$. This qualitatively contradicts our findings, which suggest that the width is independent of U. The deviation can only be attributed to the BA in second order.

Aside from the approximation effects, the BRF, even in the rough BMA, reveals the correct physical behavior with regard to the Hubbard peaks located at $\omega \approx \pm U/2$ (see Fig. 3.2). A small shift is included as well, that slightly shifts the peaks away from the center, depending on the bandwidth D. The Kondo resonance, however, is not included in such a crude approximation since all occurring energies are nowhere near the scale of the Kondo temperature T_{K}. Here the BRF faces the standard problem of the widely stretched energy scale required to explain the Kondo effect. The extension of the local system by the wide energy range of the NRG seems to be a promising approach to accomplish this task and will be further investigated in Chap. 5. Applying the BA in higher order is another possibility to resolve smaller energies. This will be addressed in the following section.

4.7. Improvements of the BMA

We have investigated the effect of the single approximations of the BRF in Sec. 4.6. Several aspects have turned out to be problematic in this context.

The second MA impairs short-time dynamics by restricting to exponential decay terms in the time-domain, which translates to Lorentzians in ESF. This is only correct in the limit, where the bandwidth D significantly exceeds the hybridization Γ. In Sec. 4.7.1 we briefly discuss an analytic solution for a general OQS in second order in Γ, that yields the exact short-time dynamics, but diverges for larger times.

The secular approximation relies on large system energies and becomes problematic for $U \sim \Gamma$ in the interacting case. However, this problem only appears in ESFs. The BA has a lesser impact on TD-EGFs, but significantly impairs the steady-states in TD-NEVs, since they are only calculated locally for the finite system in the BMA.

The fundamental part of this thesis is to improve the above mentioned points by enlarging the system Hamiltonian by certain bath excitations. If the system part resembles the equilibrium values more precisely, the BA is improved. Also, the coupling to the remaining bath is decreased, which generally improves the BMA. The sharp cut-off of the bath spectral coupling function is smoothed out, allowing for excitations, which exceed the bandwidth, to transition into the bath, which improves the second MA. Also, by enlarging the system Hamiltonian, small local energies are compensated for, which aids the secular approximation.

A simple way to enlarge the system Hamiltonian would be to successively decouple modes from the bath and couple them in the form of a tight-binding chain to the impurity. However, in this approach exponentially small energies, which are essential to the Kondo effect, cannot be reached. For that reason, we choose a Wilson chain with logarithmically decreasing coupling parameters, as is explained in detail in Chap. 5. The chain constructed in this way is called OWC. The Wilson chain allows for a truncation of the Fockspace of the system Hamiltonian, which is the foundation of the NRG. This way, the system Hamiltonian can be enlarged significantly, which is expected to improve the BMA even further. The implementation of the NRG to the OWC is covered in Chap. 6.

However, there is one case, in which the BMA is not expected to significantly improve by implementing the OWC, i.e. for large local energies, which exceed the bandwidth. The reason for that is a systematic shortcoming of the BA in second order, as will be explained in Sec. 4.7.2. This can be compensated for by either extending the BA to fourth order (see Sec. 4.7.1) or transitioning the interaction Hamiltonian H_{SB} (see Sec. 4.7.2). Both cases will be discussed briefly in the following sections, but will not be covered quantitatively in this thesis.

4.7.1. Higher-Order Formalism

Since the conventional BRF is calculated up to second order only, we suffer several errors due to the dependence on weak coupling to the bath. In principle, the integration and substitution of the density matrix in the von-Neumann equation could be iterated more often, to acquire the integro-differential equation (4.2.6) in higher order. Let us exemplarily investigate the fourth-order equation:

$$\begin{aligned}\dot{\rho}^{\mathrm{I}}(t) = &-\int_0^t dt_1 \left[\,\left[\rho^{\mathrm{I}}(0), H^{\mathrm{I}}_{\mathrm{SB}}(t_1)\right], H^{\mathrm{I}}_{\mathrm{SB}}(t)\right] \\ &+ \int_0^t dt_1 \int_0^{t_1} dt_2 \int_0^{t_2} dt_3 \left[\left[\left[[\rho^{\mathrm{I}}(t_3), H^{\mathrm{I}}_{\mathrm{SB}}(t_3)], H^{\mathrm{I}}_{\mathrm{SB}}(t_2)\right], H^{\mathrm{I}}_{\mathrm{SB}}(t_1)\right], H^{\mathrm{I}}_{\mathrm{SB}}(t)\right].\end{aligned} \tag{4.7.1.91}$$

At this point, the trace over all bath DOF is performed on both sides of the equation. First and third order terms cancel out due to particle conservation of the bath, which is why we have already omitted them in Eq. (4.7.1.91). We are able to solve the second order part of the equation analytically, so the MSA only need to be applied to the fourth-order part. By expressing the equation in the eigenbasis of the system Hamiltonian H_{S} and substituting the integration variables $t_3 = t_1 - s$ and $t_2 = t - s'$, respectively, we obtain

$$\dot{\rho}_{ab}(t) = R^2_{ab}(t) + \sum_{mn} \int_0^t dt_1 \int_{t-t_1}^{t} ds' \int_{t_1-t+s'}^{t_1} ds R^4_{ab,mn}(t, t_1, s, s')\rho_{mn}(t_1 - s), \tag{4.7.1.92}$$

which is analog to Eq. (4.3.18). Here we have condensed the first term on the r.h.s. of (4.7.1.91) in the expression $R^2_{ab}(t)$. The BRT $R^4_{ab,mn}(t, t_1, s, s')$ is still a fourth-order tensor with respect to the local DOF. However, it includes four nested commutators, which yields a total number of 16 terms. If we assume

$$H^{\mathrm{I}}_{\mathrm{SB}}(t) = \sum_{k,\nu} V_{k,\nu} \left(f^\dagger_\nu(t) c_{k,\nu}(t) + f_\nu(t) c^\dagger_{k,\nu}(t)\right) \tag{4.7.1.93}$$

for the interaction Hamiltonian $H^{\mathrm{I}}_{\mathrm{SB}}(t)$ with a general bath DOF ν and perform the trace over the bath DOF, we end up with 12 non-vanishing combinations of operators and indices for each of those 16 terms. Here we consider the fact, that all operators are fermionic, which excludes most combinations. Each non-vanishing term includes the two sums $\sum_{k,\nu}\sum_{k',\nu'}$. Let us exemplarily calculate one of the 12 possible terms of the type $\rho^{\mathrm{I}}(t_1-s)H^{\mathrm{I}}_{\mathrm{SB}}(t_1-s)H^{\mathrm{I}}_{\mathrm{SB}}(t-s')H^{\mathrm{I}}_{\mathrm{SB}}(t_1)H^{\mathrm{I}}_{\mathrm{SB}}(t)$. We start with

$$\begin{aligned}\sum_{\nu,\nu'}\int_0^t dt_1\int_{t-t_1}^t ds'\int_{t_1-t+s'}^{t_1} ds\rho^{\mathrm{I}}_{\mathrm{S}}(t_1-s)f_{\nu'}(t_1-s)f_\nu(t-s')f^\dagger_{\nu'}(t_1)f^\dagger_\nu(t)\times\\ \times\sum_{k,k'}V_k^2V_{k'}^2\mathrm{Tr}_{\mathrm{B}}\Big\{\rho_{\mathrm{B}}c^\dagger_{k'\nu'}(t_1-s)c^\dagger_{k\nu}(t-s')c_{k'\nu'}(t_1)c_{k\nu}(t)\Big\},\end{aligned}\tag{4.7.1.94}$$

where we have already used the BA of Eq. (4.3.16). Since $k\neq k'$, the second line can be transformed into

$$-\sum_{k,k'}V_k^2V_{k'}^2\mathrm{Tr}\Big\{\rho_{\mathrm{B}}c^\dagger_{k'\nu'}c^\dagger_{k\nu}c_{k'\nu'}c_{k\nu}\Big\}e^{-i\epsilon_k s'}e^{-i\epsilon_{k'}s}=C_{\mathrm{h},\nu}(-s')C_{\mathrm{h},\nu'}(-s)\tag{4.7.1.95}$$

with the definitions of Sec. 4.3. The correlation functions demand that $s,s'\leq t_{\mathrm{B}}$ and consequently $t-t_1\leq t_{\mathrm{B}}$. In the spirit of the MA, we assume the bath correlations to decay fast in comparison to the local dynamics, i.e. $t_{\mathrm{B}}\Gamma\ll 1$. With this argument we can substitute $\rho^{\mathrm{I}}_{\mathrm{S}}(t_1-s)\to\rho^{\mathrm{I}}_{\mathrm{S}}(t_1)$ and substitute all $t_1\to t$ in the time evolutions of the local operators. This is the first MA. Now we express Eq. (4.7.1.94) in the local eigenbasis (as has been done in Eq. (4.7.1.92)) to obtain

$$\begin{aligned}&\sum_{\nu,\nu'}\sum_{mncd}\delta_{am}\rho_{mn}(t)\left\langle n\right|f_{\nu'}\left|c\right\rangle\left\langle c\right|f_\nu\left|d\right\rangle\left\langle d\right|f^\dagger_{\nu'}f^\dagger_\nu\left|b\right\rangle e^{i(E_n-E_b)t}X(t,E_n-E_c,E_c-E_d),\\ &X(t,\omega,\omega')=\int_0^t d\tau\int_\tau^t ds'\int_{s'-\tau}^{t-\tau}dsC_{\mathrm{h},\nu}(-s')C_{\mathrm{h},\nu'}(-s)e^{-i\omega s}e^{-i\omega's'},\end{aligned}\tag{4.7.1.96}$$

where we have substituted $t_1=t-\tau$. According to the secular approximation, we can set $e^{i(E_n-E_b)t}\to\delta_{E_b,E_n}$, which reduces the number of summation terms. The only time-dependency of the new BRT lies in $X(t,\omega,\omega')$. It can be shown numerically, that this function decays on a similar time scale as the correlation functions, implying that we can set $X(t,\omega,\omega')\to X(t\to\infty,\omega,\omega')\equiv X(\omega,\omega')$, which is the second MA. Now $X(\omega,\omega')$ can be calculated analytically, leaving two integrals over ϵ and ϵ', respectively (see Eq. (4.3.24)), which need to be treated numerically.

We have seen, that the fourth-order BRT can, in principle, be calculated analogly to the second order BRT by applying the BMA. We obtain a similar tensor with four independent local indices, which can be diagonalized and then yields exponential decay terms for the time evolution of the density matrix. A huge advantage of this approach lies in the fact, that in order to solve the differential equation (4.7.1.92), we can integrate $R^2_{ab}(t)$ analytically, since it solely comprises exponential functions. This means, as argued above, that we not only improved the BA to fourth-order, but that we improved the MSA as well. A MA in second order provides a significant error in the dynamics for short times. In contrast, we have shown in Fig. 4.4, that a density matrix, which is exact in second order, yields the correct short-time dynamics up to a certain time, before the error of the MA in fourth-order starts. By reducing the impurity-bath coupling strength, we can shift this time to the right. At a certain time, the density matrix is thermalized and the contributions that are affected by the MA are entirely damped. In this context, we expect the fourth-order BRF to significantly improve the short-time dynamics, which is a major shortcoming of this formalism.

Since the numerical effort of the construction of the fourth-order BRT is tremendous compared to the second order, one might suggest a hybrid approach. For the long-time dynamics, the canonical BRF in second order is applied. To obtain reliable short-time dynamics, the second order contribution $R^2_{ab}(t)$ is calculated exactly. By decreasing the coupling strength, both approaches are expected to continuously transition into each other at a certain time with only small deviations.

4.7.2. Adaptation to Large Local Interactions

In Sec. 4.6 the BMA proved to be problematic in the case, where the local energies exceed the bandwidth. Especially the BA turned out to yield the wrong dependency of U in both TD-NEVs and ESFs. In Sec. 4.3 we have performed the BA, which effectively resembles a perturbative coupling of the impurity to the bath in second order in the hybridization Γ. In a simple view, this approximation is always applicable, if Γ is sufficiently small. However, let us discuss a case, where the BA is insufficient.

Consider the SAM with a Coulomb repulsion U that is large in comparison to the bandwidth D. Here the local one-particle state is favored and transitions between the impurity and the bath are restricted to spin-flip processes. However, the BA in second order, as performed in Sec. 4.3, only accounts for hopping processes of particles with the same spin. Consequently, the BA can be applied in higher order, as discussed in Sec. 4.7.1, to include higher-order coupling terms. However, the resulting BRT is very complicated and a practical implementation is hardly possible, unless new symmetries are found or further approximations are performed. An alternative approach would be to transition to a model, that only includes spin-flip processes, i.e. the Kondo model. For a small hybridization V_k we can transform the SIAM via a Schrieffer-Wolff transformation [16] (see Sec. 2.4). In the context of the BRF, the system parameters are renormalized and the interaction Hamiltonian H_{SB}, which is linear in the local operators, is turned into an expression, which is bilinear in the local operators. This is the Heisenberg spin-interaction of the Kondo model (see Eq. (2.2.1)). The operator H_{SB} is proportional to the spin-coupling J, which in turn is proportional to $\frac{V^2}{U}$ (see Eq. (2.4.10)). Consequently, the coupling parameter is small if U/D is large, suggesting it is an adequate choice for the BMA. Now, even in second order in J the required spin-flip processes are included. The BRT is here proportional to J^2, and consequently the eigenvalues are as well. This, in turn, leads to a scaling of the relaxation rates and broadening parameters with U^{-2}.

In this approach, the interaction Hamiltonian (4.7.1.93) is replaced by

$$H_{\mathrm{SB}} = \sum_{kk'} J_{kk'} \left(S^+ c^\dagger_{k\downarrow} c_{k'\uparrow} + S^- c^\dagger_{k\uparrow} c_{k'\downarrow} + S^z (c^\dagger_{k\uparrow} c_{k'\uparrow} - c^\dagger_{k\downarrow} c_{k'\downarrow}) \right) \tag{4.7.2.97}$$

with the coupling

$$J_{kk'} = V_k V_{k'} \left((\epsilon_k - \epsilon_+)^{-1} - (\epsilon_k - \epsilon_-)^{-1} + (\epsilon_{k'} - \epsilon_+)^{-1} - (\epsilon_{k'} - \epsilon_-)^{-1} \right) \tag{4.7.2.98}$$

and $\epsilon_+ = \epsilon_{\mathrm{d}} + U$, $\epsilon_- = \epsilon_{\mathrm{d}}$. According to Schrieffer and Wolff [16], the Coulomb interaction is in the symmetrical case $\epsilon_{\mathrm{d}} = -U/2$ renormalized to $U \to \tilde{U} = U + 8V^2/U$. With Eq. (4.7.2.97) inserted into Eq. (4.3.20), we obtain the time-dependent damping matrices as

$$\begin{aligned} \Gamma^+_{ab,mn}(t,s) &= e^{i(\omega_{ab}+\omega_{mn})t} \left(S^+_{ab} S^-_{mn} + S^-_{ab} S^+_{mn} + S^z_{ab} S^z_{mn} \right) e^{-i\omega_{mn}s} C(s) \\ \Gamma^-_{ab,mn}(t,s) &= e^{i(\omega_{ab}+\omega_{mn})t} \left(S^+_{ab} S^-_{mn} + S^-_{ab} S^+_{mn} + S^z_{ab} S^z_{mn} \right) e^{-i\omega_{ab}s} C(-s), \end{aligned} \tag{4.7.2.99}$$

with the time-dependent correlation function

$$\begin{aligned} C(s) =& \frac{1}{\pi^2} \int_{-\infty}^{+\infty} d\epsilon \int_{-\infty}^{+\infty} d\epsilon' \Gamma(\epsilon)\Gamma(\epsilon') f_\beta(\epsilon) f_\beta(-\epsilon') e^{i(\epsilon-\epsilon')s} \times \\ & \times \left((\epsilon - \epsilon_+)^{-1} - (\epsilon - \epsilon_-)^{-1} + (\epsilon' - \epsilon_+)^{-1} - (\epsilon' - \epsilon_-)^{-1} \right)^2 . \end{aligned} \tag{4.7.2.100}$$

Here we exploit the fact, that the bath modes are degenerate with respect to the spin DOF. In the symmetrical case and for $U \gg D$, only terms with $\epsilon, \epsilon' \ll U$ contribute. Here we can approximate

$$(\epsilon - \epsilon_+)^{-1} - (\epsilon - \epsilon_-)^{-1} + (\epsilon' - \epsilon_+)^{-1} - (\epsilon' - \epsilon_-)^{-1} \approx -8/U, \tag{4.7.2.101}$$

and consequently $C(s) \propto U^{-2}$. In the MSA we obtain

$$\begin{aligned}\Gamma^{+}_{ab,mn} &= \delta_{\omega_{ab}+\omega_{mn},0}\left(S^{+}_{ab}S^{-}_{mn} + S^{-}_{ab}S^{+}_{mn} + S^{z}_{ab}S^{z}_{mn}\right)C(\omega_{mn}) \\ \Gamma^{-}_{ab,mn} &= \left(\Gamma^{+}_{ab,mn}\right)^{*},\end{aligned} \tag{4.7.2.102}$$

with the RGFs

$$C(\omega) = \int_0^\infty dsC(s)e^{-i\omega s-0^+s} \tag{4.7.2.103}$$

given as the half-sided Fourier transform of Eq. (4.7.2.100).

We were able to show here, that the BMA reproduces the U^{-2}-dependence of its eigenvalues, as is predicted by analytical considerations, if the SIAM is transformed into the Kondo model.

4.8. Summary

We have investigated the BRF as a perturbative approach to OQSs. This approach yields true thermalization in non-equilibrium dynamics as well as a finite lifetime of local exciations. It is applicable to any QIM, arbitrary bath DOS and can even be adapted to treat transport phenomena. The BRF relies on the BMA which is exact in the limit of a small hybridization Γ between the local system and the environment. We have discussed the BRF in great detail in the case of an impurity coupled directly to a bath with a constant DOS. Especially, we have investigated the influence of the single approximations. The hybridization strength between the system and the bath is here the central quantity. The BMA can only be justified, if the hybridization is well below the system energies, the temperature and the bandwidth.

In non-equilibrium real-time dynamics the BMA allows for a true thermalization on the correct time scale, as has been shown for the RLM and the SIAM. The BA mainly influences equilibrium values and reduces them to the local values of a closed system. This approximation can be improved by increasing the temperature. The MA can be separated into two parts. The first approximation is the most essential one, that allows one to split the convolution integral and thus to solve the time-evolution of the density matrix analytically. This approximation relies on a short bath correlation time, i.e. a large bandwidth, and only has a minor effect. The second MA in combination with the secular approximation makes the BRT time-independent and thus yields a simple master equation for the density matrix, that can be solved by matrix diagonalization. These approximations are essential to treat large local systems, however, their impact on short-time dynamics can be significant, since the time-evolution of the density matrix is now restricted to exponential decay terms, which do not necessarily reflect the correct physical behavior. In order to improve the MSA, the local parameters, as well as the bandwidth, need to be increased in comparison to the hybridization. Also the second MA demands that the bandwidth is the largest energy scale of the system, as otherwise transitions into the bath are prohibited and the dynamics are frozen out.

The ESFs for the constant bath DOS have been calculated as well. Here the OQS character of the BRF yields a natural broadening of local excitations. Interestingly, the BMA reproduces the exact solution of the RLM and deviations can only be found in more complex models such as the SIAM. To investigate ESFs, the TD-EGFs can be examined in a first step, since they exhibit a similar influence of the BMA with respect to the MSA as TD-NEVs. In contrast, the BA does not impact the steady states of TD-EGFs, but short-time dynamics. In ESFs it is shown that the second MA cuts off excitations that lie outside the band. The secular approximation has a significant impact for small local energies and generates a discontinuous transition of the interacting to the non-interacting case in the SAM. Here the BA predicts Hubbard peaks with a width of 2Γ, if U/D is small, and a width proportional to the bandwidth, but independent of U, if the interaction is large compared to the bandwidth. This finding contradicts Fermi's golden rule estimations, which predict a dependence of $(D/U)^2$.

In contrast, in TD-NEVs the relaxation rates decrease with increasing U, when the SAM is chosen. This behavior is understandable in the context, that a large U/D strongly confines the local single electron and inhibits transitions to the conduction band. In that case, the BA produces a wrong steady-state and its influence on the relaxation rates is unknown. A restriction to a perturbative coupling in second order in Γ is expected to be a systematic problem here. However, since the BA is the foundation of the BMA, it cannot be avoided in this context. Also, the implementation of a BA in fourth order is practically infeasible at this point. Hence, for large U/D one might suggest a Schrieffer-Wolff transformation to the Kondo model, where one obtains a small coupling of $J \propto U^{-1}$. If the BMA is carried out as a perturbation in J, relaxation rates $\propto J^2$ are expected, which resembles analytical predictions.

In the following chapter we present the OCF that redefines certain excitations of the bath into the system Hamiltonian. Thus, the BRF is applied to several separate reservoirs, that are coupled by an increasingly small hybridization to the system. In that way, the BMA can successively be improved and the results are expected to converge to the real physical solutions.

5. Open Wilson Chain

The Wilson chain of a fixed length derived in Sec. 3.1 is a closed system, i.e. it does not include dissipative processes. Thus, parameters like energy and particle number are conserved within the system. In the case of real-time dynamics, so-called Pointcaré recurrences are unavoidable in conservative systems. They have been referred to as "revival effects" in Chap. 3. To allow for dissipation, a bath with an infinite amount of DOF is required. The objective of this chapter is now twofold. Firstly, we recover the $p \neq 0$ modes as so-called high-energy reservoirs and the oddment of the truncated Wilson chain as a low energy reservoir (for details see Sec. 3.1). This is achieved by successively decoupling the discrete Wilson chain modes from the infinite bath under the restriction that the bath spectral coupling function to the impurity is not altered by that process. The remainders of the bath are then carefully collected to form the reservoirs. Up to this point, the formalism is exact and recovers the full continuum that has been discarded by the closed Wilson chain (CWC) for arbitrary $\Lambda \geq 1$. Our second objective is to then couple the reservoirs to the chain and thus to turn the latter into an OQS. Here, the BRF from Chap. 4 comes into play to calculate the time-evolution of the density matrix. In this context the CWC constitutes the system S. The main purpose of the BRF is to extend the CWC by a natural intrinsic relaxation rate to introduce dissipation and thermalization. This is a way to reduce the discretization artifacts discussed in Sec. 3.10. Since the BRF is a second-order Markovian coupling mechanism, it brings back approximations to the OWC. To improve these approximations, the system Hamiltonian H_{S} needs to be enlarged so that it resembles the equilibrium density matrix more adequately. Here the equilibrium values are reached with increasing precision by increasing the chain length N_{C}.

Chapter 5 is organized as follows. In Sec. 5.1 we explain the process of constructing the above described reservoirs. In Sec. 5.2 the construction of the BRT for the OWC is illustrated. By diagonalizing this tensor, the time-dependent density matrix of the OQS can then be calculated. The quality of the BMA for different parameter regimes is discussed in Sec. 5.3. Here we restrict to a pure theoretical level by estimating the validity of the approximations based on the OWC parameters calculated in Sec. 5.1. In Sec. 5.4 we cover the numerical implementation of the OWC. In the sections 5.4.1 and 5.4.2 the OWC is realized to calculate TD-NEVs and ESFs, respectively. Here the reservoirs are coupled to a Wilson chain, which is treated exactly by restricting to a short chain length. The sections thus serve as a benchmark to test the BRF for the OWC without including relevant numerical errors. The adaptation of the OCF to the NRG, i.e. a truncated system eigenbasis, includes further challenges and will be covered in Chap. 6. Finally, in Sec. 5.5 we summarize the findings of the chapter.

The formalism for iteratively calculating the reservoirs comes in the form of a so-called CFE. It should be mentioned here that the CFE of the GF is a well-established tool to map QIMs to a chain [110, 111, 112]. Bruognolo et al. [113] constructed an OWC similar to the formalism described below. They used the reservoirs to calculate corrections to the on-site energies ϵ_n to ensure a correct energy shift $\mathfrak{Re}\Sigma(0)$ of the entire system. This effect is only relevant for a non-symmetric bath spectrum $\Gamma(\omega)$ as it occurs in bosonic systems. In our approach, however, all reservoir information is perturbatively included. Thus, the OWC in combination with the BRF turns out to be a powerful tool for incorporating dissipation and thermalization effects, as well as a finite lifetime, to the CWC.

5.1. Continued Fraction Expansion

The calculations of this section follow Ref. [113, 114], where the CFE for OWCs was first introduced. We present the formalism for a spinless OQS, which resembles the RLM. The extension to the spinful case (i.e. the SIAM) is straightforward.

For the simple RLM (cf. Sec. 2.5) the Hamiltonian can be written as

$$H = \epsilon_{\mathrm{d}} d^\dagger d + \sum_k V_k (d^\dagger c_k + c_k^\dagger d) + \sum_k \epsilon_k c_k^\dagger c_k, \tag{5.1.1}$$

comprising a local level with energy ϵ_d and an infinite fermionic bath with excitation energies ϵ_k. The hybridization strength between the impurity level and the bath excitation with momentum k is V_k. The normalization factor of $1/\sqrt{N}$ is absorbed in the V_k's, where N is the number of bath particles. The GF of the impurity level, governing its dynamical properties, can be calculated in a simple manner by using the equation of motion (see App. A.1) leading to

$$G_{d,d^\dagger}(\omega) = (\omega - \epsilon_\mathrm{d} - \Sigma(\omega))^{-1}. \tag{5.1.2}$$

Here

$$\Sigma(\omega) = \sum_k |V_k|^2 G_{c_k,c_k^\dagger}(\omega) \tag{5.1.3}$$

is the self-energy with $G_{c_k,c_k^\dagger}(\omega) = (\omega - \epsilon_k + i0^+)^{-1}$ being the GF of the non-interacting bath. From Eq. (4.3.23) we recognize $\Gamma(\omega) = \mathfrak{Im}\Sigma(\omega) = \pi \sum_k V_k^2 \delta(\omega - \epsilon_k)$ as the spectral coupling function[1]. This function contains all information on the bath spectrum and its influence on the impurity [113]. Now by coupling off certain modes of the bath and in this way creating new baths and a new local system, the local GF (5.1.2) needs to be conserved in order for this process not to influence the impurity dynamics.

In a zeroth step we start by decoupling the whole bath from the impurity and couple it to a single bath mode. This mode is then coupled to the impurity constructing a two-orbital system, analogly to Eq. (1.0.4). We define this system as the foundation of the chain with length $N_\mathrm{C} = 1$, while the index of the chain sites here starts at zero. Note that this definition deviates from the one introduced in Chap. 3, where we would have defined $N_\mathrm{C} = 0$ in this case. However, from now on we will stick to the new definition.

The Hamiltonian now reads

$$H = \epsilon_\mathrm{d} d^\dagger d + V(d^\dagger f_0 + f_0^\dagger d) + \epsilon_0 f_0^\dagger f_0 + \sum_k V_{0,k}(f_0^\dagger c_{0,k} + c_{0,k}^\dagger f_0) + \sum_k \epsilon_{0,k} c_{0,k}^\dagger c_{0,k}. \tag{5.1.4}$$

Here the impurity solely couples to the newly defined zeroth mode $f_0^{(\dagger)}$ via the hybridization V (see Eq. (4.3.28)), while the zeroth mode couples to the entire zeroth bath modes $c_{0,k}^{(\dagger)}$. The GF of the impurity thus becomes

$$G_{d,d^\dagger}(\omega) = (\omega - \epsilon_\mathrm{d} - V^2 G_{f_0,f_0^\dagger}(\omega))^{-1}. \tag{5.1.5}$$

with $G_{f_0,f_0^\dagger}(\omega)$ being the GF of the zeroth site that has just been constructed. The level coupled to the bath has simply been shifted from the impurity to the zeroth chain

---

[1] $\Gamma(\omega)$ is called hybridization function in the context of the NRG [25]

site meaning that its GF becomes

$$G_{f_0,f_0^\dagger}(\omega) = (\omega - \epsilon_0 - \Sigma_0(\omega))^{-1}. \tag{5.1.6}$$

The function $\Sigma_0(\omega)$ again serves as a self-energy that contains all information of the remaining bath. To conserve impurity dynamics, i.e. to retain the self-energy in Eq. (5.1.5), we require

$$\Sigma(\omega) = V^2 G_{f_0,f_0^\dagger}(\omega). \tag{5.1.7}$$

Together with Eq. (5.1.6) we obtain the simple equation

$$\Sigma_0(\omega) = \omega - \epsilon_0 - V^2\Sigma^{-1}(\omega) \tag{5.1.8}$$

for the new self-energy. The on-site energy is given by

$$\epsilon_0 = \frac{1}{\pi V^2}\int d\omega\omega\Gamma(\omega), \tag{5.1.9}$$

where the prefactor acts as a normalization. The on-site energy can thus be seen as the first momentum of the spectral coupling function. If we consider the fact that the spectral function is normalized by definition, Eq. (5.1.7) leads to

$$V^2 = \frac{1}{\pi}\int d\omega\Gamma(\omega), \tag{5.1.10}$$

which defines the hybridization strength V by the bath.

The system now describes a "super-impurity" of two sites connected via V, with one site being coupled to a bath with a spectrum of $\Gamma_0(\omega)$.

5.1.1. Construction of an Open Chain

To construct an open chain we proceed by repeating the above described procedure of extracting one mode from the bath and coupling it between the last chain site and the new bath. By retaining the self-energy $\Sigma_0(\omega)$ in Eq. (5.1.6) we arrive at the new self-energy

$$\Sigma_1(\omega) = \omega - \epsilon_1 - V_0^2\Sigma_0^{-1}(\omega). \tag{5.1.1.11}$$

Here V_0 enters as the coupling strength between the zeroth and the first chain site. It can be calculated similarly to Eq. (5.1.10) as $V_0^2 = \frac{1}{\pi}\int d\omega \Gamma_0(\omega)$.

Iterating the above given steps leads to the CFE

$$\Sigma_{n+1}(\omega) = \omega - \epsilon_{n+1} - V_n^2 \Sigma_n^{-1}(\omega). \tag{5.1.1.12}$$

with

$$\epsilon_{n+1} = \frac{1}{\pi V_n^2} \int d\omega \omega \Gamma_n(\omega) \tag{5.1.1.13}$$

for a chain of length N_{C} with a reservoir $\Gamma_{N_{\mathrm{C}}-1}(\omega)$ coupled to the last chain site. The coupling constants are defined by

$$V_n^2 = \frac{1}{\pi} \int d\omega \Gamma_n(\omega). \tag{5.1.1.14}$$

For a constant DOS the coupling constants are given by [115]

$$V_n = D \frac{n+1}{\sqrt{4n^2 + 8n + 3}}. \tag{5.1.1.15}$$

This equation can easily be derived[2] by evaluating

$$t_n = S \frac{1 - \Lambda^{-n-1}}{\sqrt{1 - \Lambda^{-2n-1}}\sqrt{1 - \Lambda^{-2n-3}}} \Lambda^{-n/2} \tag{5.1.1.16}$$

with

$$S = \frac{D}{2}(1 + \Lambda^{-1}) \tag{5.1.1.17}$$

(see Eq. (3.1.12)) for $\Lambda \to 1^+$. In Fig. 5.1 the numerically calculated coupling constants V_n are compared to the analytical values of Eq. (5.1.1.15). The excellent consistency of the results guarantees sufficient numerical accuracy.

For $n \to \infty$ the coupling constants converge to $V_n \to D/2$, which partially resembles a tight-binding chain with hopping parameters $t = D/2$. Considering a symmetrical DOS, the orbital energies ϵ_n vanish. The recursion relation of Eq. (5.1.1.12) can now

---

[2] To be precise, Λ is replaced by $1 + \epsilon$ and for each occurring power of Λ a Taylor expansion around $\epsilon = 0$ is used in first order. Then ϵ is set to zero to obtain the solution.

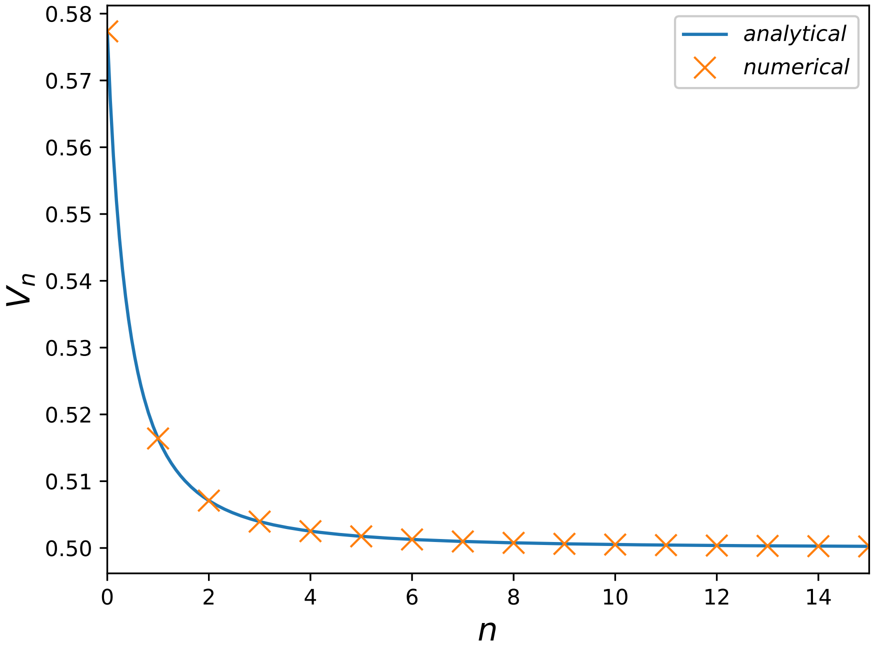

Figure 5.1.: The coupling constants V_n calculated numerically via Eq. (5.1.1.14) for iteration n in comparison to the analytical solution of (5.1.1.15).

easily be solved for its steady state by evaluating

$$\tilde{\Sigma}(\omega) = \omega - \frac{(D/2)^2}{\tilde{\Sigma}(\omega)}. \tag{5.1.1.18}$$

For the self-energies we obtain

$$\tilde{\Sigma}(\omega) = \frac{\omega \pm \sqrt{\omega^2 - D^2}\Theta(|\omega| - D)}{2} + i\frac{\pm\sqrt{D^2 - \omega^2}\Theta(D - |\omega|)}{2}. \tag{5.1.1.19}$$

The solution is ambiguous since Eq. (5.1.1.18) is a quadratic equation in $\tilde{\Sigma}(\omega)$. The real part either goes to zero, which is the physical solution, or diverges for large absolute values of ω. In our case, the imaginary part $\tilde{\Gamma}(\omega)$ is always positive for energies within the bandwidth D.

In Fig. 5.2 the reservoirs are displayed for the first 20 iterations of the recursion relation. Since the axes are scaled by the bandwidth D, no system parameters enter the calculation. A fast convergence to the steady-state solution (5.1.1.19) within the interval $[-1, 1]$ is apparent.

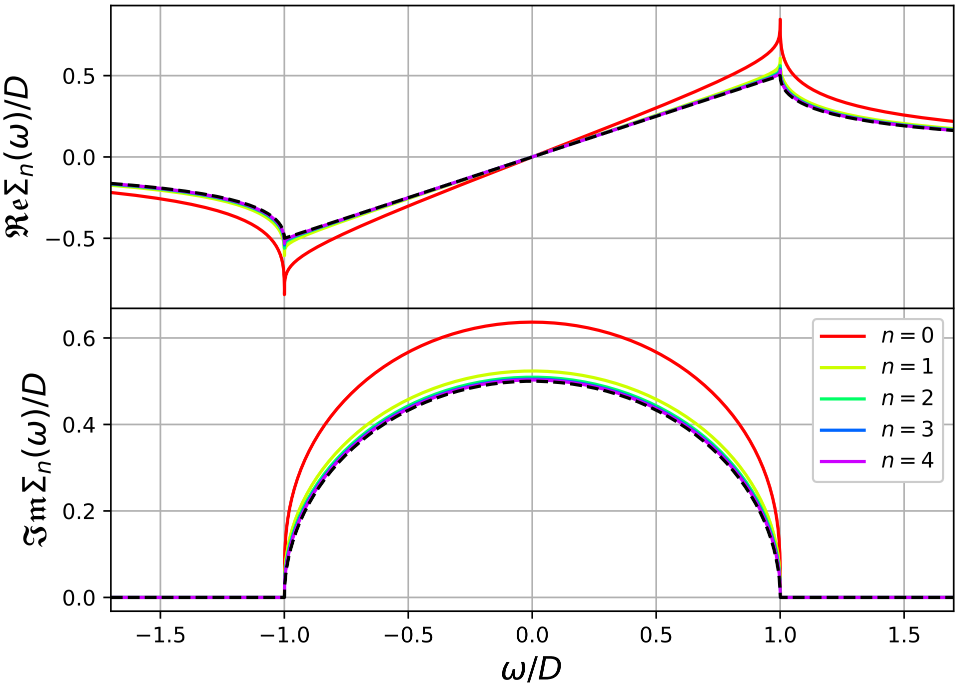

Figure 5.2.: Self-energies $\Sigma_n(\omega)$ calculated via Eq. (5.1.1.12), rescaled by the bandwidth D versus the rescaled energies ω/D. The steady state solution $\tilde{\Sigma}(\omega)$ of Eq. (5.1.1.19) is added as a black dashed line. The real part it connected to the imaginary part by a Hilbert transform.

5.1.2. Adaptation to the Wilson Chain

The coupling parameters V_n of Eq. (5.1.1.14) are the maximum values one can reach by using the entire remaining bath to construct the rest chain at each iteration. By splitting off a certain part, the remaining bath yields a smaller coupling parameter $t_n < V_n$. Since the coupling parameters t_n decrease along the chain, it is convenient to split the bath into a high- and a low-energy reservoir, i.e. $\Gamma_n(\omega) = \Gamma_n^{\mathrm{H}}(\omega) + \Gamma_n^{\mathrm{L}}(\omega)$. If the low-energy reservoir is then used to construct the remaining chain, the support of the reservoirs $\Gamma_n^{\mathrm{H/L}}(\omega)$ shrinks with each iteration analogly to the coupling parameters t_n. This fact is advantageous for a renormalization procedure (see Sec. 5.1.3). Note that the high-energy reservoirs cannot be neglected here. Instead, in order to retain the correct impurity self-energy they still remain coupled to their particular chain site. This way we construct a chain of coupling parameters t_n with a high-energy reservoir $\Gamma_n^{\mathrm{H}}(\omega)$ coupled to each chain site and a full reservoir $\Gamma_{N_{\mathrm{C}}}(\omega)$ coupled to the end of the chain (see Fig. 5.3).

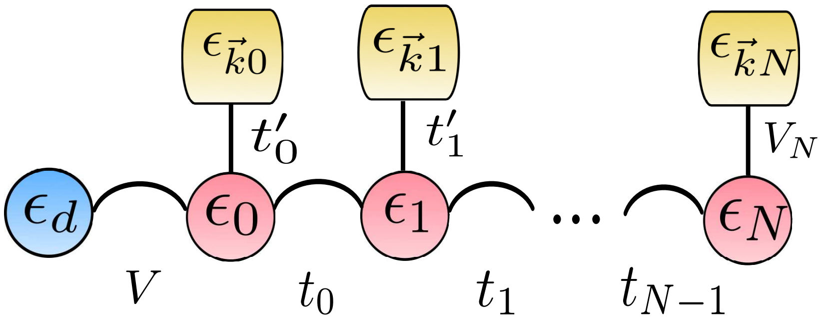

Figure 5.3.: Illustration of the OWC. The impurity level (blue) hybridizes via V to the Wilson chain. The chain sites (red) are coupled by t_n to each other, while the n-th high-energy reservoir (gold) is coupled by t'_n to the n-th chain site. To the last site $n = N$, a full reservoir is coupled by V_N. The modes of the n-th reservoir are denoted by $\epsilon_{\vec{k}n}$.

To split the reservoirs, a cut-off function $F(\omega, \omega_n^{\mathrm{C}})$ is defined with

$$\begin{aligned} \Gamma_n^{\mathrm{H}}(\omega) &= (1 - F(\omega, \omega_n^{\mathrm{C}}))\Gamma_n(\omega), \\ \Gamma_n^{\mathrm{L}}(\omega) &= F(\omega, \omega_n^{\mathrm{C}})\Gamma_n(\omega). \end{aligned} \tag{5.1.2.20}$$

For each iteration n it can be tuned by a particular cut-off-frequency ω_n^{C}. By definition of the high- and low-energy reservoirs it is required that $F(0, \omega_n^{\mathrm{C}}) = 1 \forall \omega_n^{\mathrm{C}} \in \mathbb{R}$ and that the function monotonously decreases for increasing $|\omega|$. The most simple choice would obviously be $F(\omega, \omega_n^{\mathrm{C}}) = \Theta(\omega_n^{\mathrm{C}} - |\omega|)$. However, since one needs to calculate $\mathfrak{Re}\Sigma_n^{\mathrm{H/L}}(\omega)$ from $\Gamma_n^{\mathrm{H/L}}(\omega)$ via a Kramers-Kronig relation, a smooth function is chosen. Kinks in the curve lead to logarithmic divergences and should be avoided from a numerical point. For that reason, we choose

$$F(\omega, \omega_n^{\mathrm{C}}) = e^{-(\omega/\omega_n^{\mathrm{C}})^4}. \tag{5.1.2.21}$$

The cut-off frequencies ω_n^{C} are defined by

$$t_n^2 = \frac{1}{\pi} \int d\omega F(\omega, \omega_n^{\mathrm{C}})\Gamma_n(\omega) \tag{5.1.2.22}$$

and need to be chosen in a way that recovers the Wilson chain parameters t_n. To numerically determine the value of ω_n^{C}, an approximation algorithm is required. We chose Newton's method (see App. D), where on average four steps are required to reach a relative convergence radius $|r| \leq 10^{-7}$.

The coupling t'_n to the high-energy reservoirs is determined by

$$(t'_n)^2 = \frac{1}{\pi} \int d\omega (1 - F(\omega, \omega_n^{\mathrm{C}})) \Gamma_n(\omega). \tag{5.1.2.23}$$

To proceed in the algorithm one has to keep in mind that Eq. (5.1.2.20) only determines $\Gamma_n^{\mathrm{H/L}}(\omega) = \mathfrak{Im}\Sigma_n^{\mathrm{H/L}}(\omega)$. To obtain the real part of the low energy reservoir, and thus to get $\Sigma_n^{\mathrm{L}}(\omega)$, a Hilbert transform of the imaginary part is required.

The recursion relation now becomes

$$\Sigma_{n+1}(\omega) = \omega - \epsilon_{n+1} - t_n^2 (\Sigma_n^L(\omega))^{-1}, \tag{5.1.2.24}$$

since the new reservoir of iteration $n+1$ is constructed from the low energy part of the previous reservoir n only. Since only the imaginary part of $\Sigma_{n+1}(\omega)$ is relevant for the algorithm, it is sufficient to calculate

$$\Gamma_{n+1}(\omega) = t_n^2 \frac{\Gamma_n^L(\omega)}{(\mathfrak{Re}\Sigma_n^L(\omega))^2 + (\Gamma_n^L(\omega))^2}, \tag{5.1.2.25}$$

instead of Eq. (5.1.2.24). In any case, the orbital energies

$$\epsilon_{n+1} = \frac{1}{\pi t_n^2} \int d\omega \omega \Gamma_n^{\mathrm{L}}(\omega) \tag{5.1.2.26}$$

vanish for a symmetric spectral coupling function $\Gamma(\omega)$ of the bath. Note that the parameters defined by

$$(V'_n)^2 = \frac{1}{\pi} \int d\omega \Gamma_n(\omega). \tag{5.1.2.27}$$

are for $\Lambda > 1$ no longer identical to the V_n defined in Eq. (5.1.1.14). In fact, we obtain $V'_n < V_n$ for all $n \geq 1$, since the subsequent reservoirs are constructed from the remaining low-energy ones. The coupling t'_n to the high-energy reservoirs (cf. Eq. (5.1.2.23)) can thus be calculated via

$$(t'_n)^2 = (V'_n)^2 - t_n^2. \tag{5.1.2.28}$$

The hopping parameters t_n, defined in Eq. (5.1.2.22), can now be chosen extrinsically. The hopping parameters for an OWC with a constant DOS are given by Eq. (5.1.1.16).

The OWC reservoirs obtained in that manner are plotted in Fig. 5.4. Here the

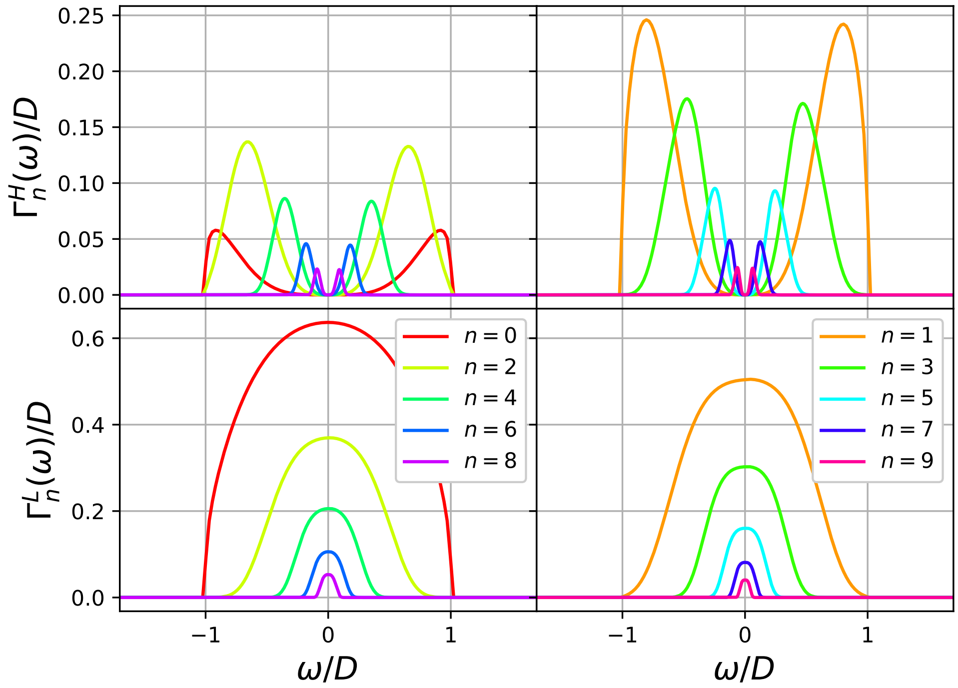

Figure 5.4.: The high-energy reservoirs $\Gamma^{\mathrm{H}}(\omega)$ (top) and the low-energy reservoirs $\Gamma^{\mathrm{L}}(\omega)$ (bottom), rescaled by the bandwidth D. The even iterations are plotted on the left and the odd iterations on the right. $\Lambda = 2$ has been chosen.

discretization parameter Λ enters, which defines the coupling parameters t_n of the chain. With each iteration n the reservoirs shrink roughly by a factor of $\sqrt{\Lambda}$ on both axes, analogly to the NRG energy scheme, letting the reservoirs vanish as $n \to \infty$.

The question arises whether the Wilson chain hopping parameters t_n are below V'_n for all iterations n. That determines whether an OWC of an arbitrary discretization parameter $\Lambda > 1$ can be realized. To answer that question, we recall that the hopping parameters t_n for $\Lambda \to 1^+$ converge to V_n of Eq. (5.1.1.15), meaning that the OCF without bath splitting produces a Wilson chain in the limit of $\Lambda \to 1^+$ with an additional reservoir at the end of the chain. Here we obtain $t_n \to V'_n \to V_n$ and $t'_n = 0$. Now, by increasing Λ the coupling to the high-energy reservoirs appears and increases. The Wilson chain parameters t_n, in turn, decrease below V_n. Thus, it can be expected that $V_n > V'_n > t_n$ for all $n \geq 1$. For the starting point of the recursion, namely $n = 0$, the condition $V_0 = V'_0 \geq t_0$ is always fulfilled, which can be seen by comparing Eq. (5.1.1.15) to Eq. (5.1.1.16). The analytical solution $V_0 = D/\sqrt{3}$ can furthermore be used as a measure for the accuracy of the numerical calculations.

To find a more intuitive explanation to the question, whether the OWC is con-

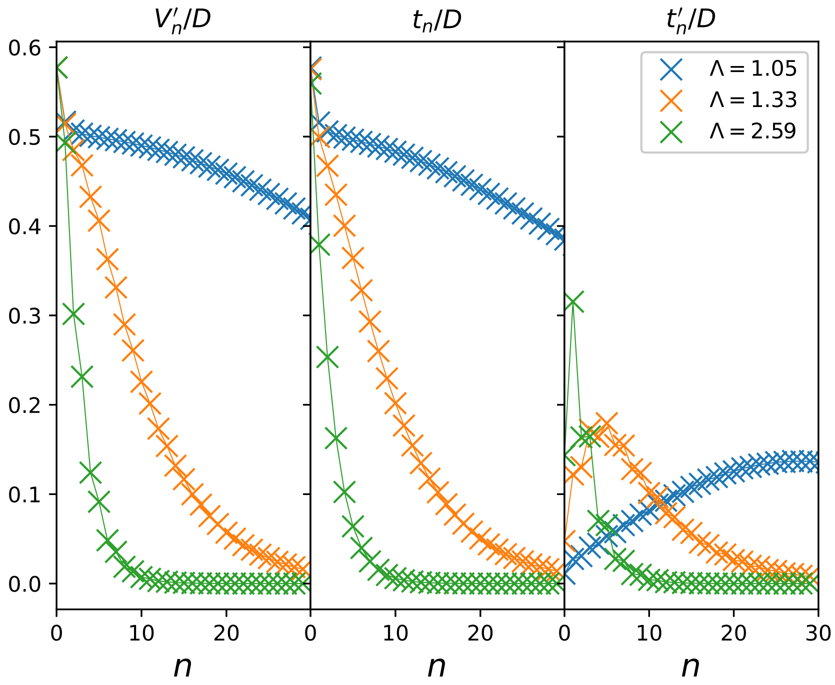

Figure 5.5.: The OWC parameters V'_n, t_n and t'_n scaled by the bandwidth D and plotted for the first 30 iterations. The discretization parameter has been chosen as $\Lambda = 1.05$ (blue), $\Lambda = 1.33$ (orange) and $\Lambda = 2.59$ (green). The discrete values are connected by a line for the sake of clarity.

structable for all $\Lambda > 1$, we point out the similarities of the CWC and the CFE. In both cases the construction of the chain is based upon the fact that the self-energy $\Sigma(\omega)$ of the impurity level is not altered (see Sec. 3.1). In contrast to the CWC, the OWC is an exact formalism which conserves the full continuum[3]. The OWC can thus be seen as an extension of the CWC or the CWC as a sub-part of the OWC. The parameter Λ here decides where to divide the system (i.e. the CWC) from the bath.

Aside from the DOS, which enters by the spectral coupling function of the bath and the cut-off function $F(\overline{\omega}, \overline{\omega}_n^{\mathrm{C}})$ that influences the smoothness on the edges of the reservoirs, the only parameter that specifies the recursion relations is Λ. For a constant DOS it is thus sufficient to only investigate a variation of the discretization parameter. Since all Λ-dependence of the algorithm is encoded in the reservoir parameters V'_n, t_n and t'_n, we stick to them to investigate a variation of the discretization parameter.

---

[3] To be precise: when applied to calculate a time-dependent density matrix, the OCF is not exact either, since here the approximations lie in the BRF, which couples the reservoirs to the chain, see Sec. 5.2

In Fig. 5.5 the coupling parameters V_n', t_n and t_n' (see Eq. (5.1.2.23)) are plotted for different values of Λ. For $\Lambda = 1.05$ (blue curves) the parameters V_n' and t_n change slowly with n and no particular even-odd behavior can be detected. For $\Lambda = 1.33$ (orange curves) and $\Lambda = 2.59$ (green curves) the parameters decay more rapidly and slight oscillations between even and odd iterations are depicted for V_n' and t_n'. A detailed discussion of these findings follows in Sec. 5.1.3.

In the limit of $\Lambda \to 1^+$ the high-energy reservoirs slowly vanish and consequently the t_n''s do so as well. In this way, the latter serve as a measure for the size of the additional reservoirs on chain site n while the t_n determine the Wilson chain. When Λ is increased from $\Lambda = 1$, the coupling parameters t_n' are increased as well. As Fig. 5.5 illustrates, the t_n''s first increase with iteration n to a maximum value and then slowly decrease to zero. The iteration n_{max} of the maximum value decreases with increasing Λ and goes to infinity if $\Lambda \to 1^+$. For the first iterations the t_n''s of small Λ (blue curve) lie below the coupling parameters for the larger Λ's (orange and green curves). Then, however, the higher Λ curves rapidly drop beneath the blue ones and go to zero much faster. The maximum iteration n_{max} roughly corresponds to a temperature $T_{n_{\mathrm{max}}} = D/2$. Here, T_n is the effective temperature of a Wilson chain of length n defined by

$$T_n = \frac{D}{2}(1 + \Lambda^{-1})\Lambda^{-(n-1)/2} \tag{5.1.2.29}$$

(see Eq. (3.5.28)).

5.1.3. Rescaled Reservoirs

The Wilson chain parameters t_n are proportional to $\Lambda^{-n/2}$. Consequently, the relevant energy scale of the Wilson chain is downscaled by a factor of $\sqrt{\Lambda}$ for each iteration. As mentioned above, the reservoirs exhibit a similar scaling behavior. As a result of the constantly shrinking scale, the numerical evaluation of large iterations n becomes increasingly problematic. That suggests a renormalization of the reservoirs in the manner of the NRG, which leads to similar even-odd steady-states of the reservoirs. In addition, a logarithmic mesh for the ω-axis is chosen, ensuring an adequate resolution even for the smallest energies of the system.

In principle, the starting point of the recursion can be scaled arbitrarily, as long as both axes are dilated by a factor of $\sqrt{\Lambda}$ on each iteration to ensure convergence. However, to obtain reservoirs that match the Wilson chain parameters, the dimensionless hopping parameters need to be scaled as $\bar{t}_n = t_n/\omega_{n+1}$ with the "NRG-scale"

$$\omega_n = \frac{D}{2}(1+\Lambda^{-1})\Lambda^{-(n-1)/2} \tag{5.1.3.30}$$

(see Eq. (3.2.19)). Consequently, the starting point of the recursion is the spectral coupling function

$$\overline{\Gamma}^{\mathrm{L}}_{-1}(\varpi) = \Gamma(\omega)/\omega_0, \tag{5.1.3.31}$$

rescaled on both axes by ω_0. The subscript "-1" and the superscript "L" are pure definition to match the notation of the algorithm. In that way, $V_{-1} = t_{-1} = V$ shall hold as well. The following steps are defined for an iteration n, starting with $n = -1$.

For a given rescaled low-energy spectral coupling function $\overline{\Gamma}^{\mathrm{L}}_n(\varpi)$, which is the imaginary part of the rescaled low-energy self-energy $\overline{\Sigma}^{\mathrm{L}}_n(\varpi)$, the orbital energy

$$\bar{\epsilon}_{n+1} = \frac{1}{\pi \bar{t}_n^2} \int d\varpi\, \varpi \overline{\Gamma}^{\mathrm{L}}_n(\varpi) \tag{5.1.3.32}$$

can be calculated. The energies $\bar{\epsilon}_{n+1}$ play no role in the algorithm, but since for a symmetrical DOS they are always zero, they may serve as a measure for numerical accuracy. As a first relevant element, the real-part of the self-energy is given via a Kramers-Kronig relation

$$\mathfrak{Re}\overline{\Sigma}^{\mathrm{L}}_n(\varpi) = \frac{1}{\pi} \int d\varpi' \frac{\overline{\Gamma}^{\mathrm{L}}_n(\varpi')}{\varpi - \varpi'}\,. \tag{5.1.3.33}$$

The spectral coupling function of the subsequent iteration is given by the recursion relation

$$\overline{\Gamma}_{n+1}(\varpi) = \bar{t}_n^2 \frac{\overline{\Gamma}^{\mathrm{L}}_n(\varpi)}{\left(\mathfrak{Re}\overline{\Sigma}^{\mathrm{L}}_n(\varpi)\right)^2 + \left(\overline{\Gamma}^{\mathrm{L}}_n(\varpi)\right)^2}\,. \tag{5.1.3.34}$$

The three latter equations are scaled by a factor of ω_{n+1} on both axes. However, to proceed in the algorithm, $\Gamma_{n+1}(\omega)$ needs to be scaled by $\omega_{n+2} = \omega_{n+1}/\sqrt{\Lambda}$, so we make the substitution

$$\overline{\Gamma}_{n+1}(\varpi) \to \overline{\Gamma}_{n+1}(\varpi\sqrt{\Lambda})/\sqrt{\Lambda}\,. \tag{5.1.3.35}$$

The hybridization

$$(\overline{V}'_{n+1})^2 = \frac{1}{\pi}\int d\overline{\omega}\,\overline{\Gamma}_{n+1}(\overline{\omega}) \qquad (5.1.3.36)$$

can be calculated as a measure for the size of the full reservoirs, but again has no relevance for the algorithm. Now the extrinsic Wilson chain parameter $\overline{t}_{n+1}$ is calculated according to Eq. (5.1.1.16) and is used to determine the cut-off frequency $\overline{\omega}^{\mathrm{C}}_{n+1}$ via

$$\overline{t}^2_{n+1} = \frac{1}{\pi}\int d\overline{\omega} F(\overline{\omega},\overline{\omega}^{\mathrm{C}}_n)\overline{\Gamma}_{n+1}(\overline{\omega}). \qquad (5.1.3.37)$$

The low-energy spectral coupling function $\overline{\Gamma}^{\mathrm{L}}_{n+1}(\overline{\omega}) = F(\overline{\omega},\overline{\omega}^{\mathrm{C}}_n)\overline{\Gamma}_{n+1}(\overline{\omega})$ and its high-energy counterpart $\overline{\Gamma}^{\mathrm{H}}_{n+1}(\overline{\omega}) = \overline{\Gamma}_{n+1}(\overline{\omega}) - \overline{\Gamma}^{\mathrm{L}}_{n+1}(\overline{\omega})$ are then stored for later usage.

Let us wrap up the algorithm. An arbitrary spectral coupling function $\Gamma(\omega)$ is chosen as defined in Eq. (5.1.3.31). Then the three steps Eq. (5.1.3.33), (5.1.3.34) and (5.1.3.37) are performed iteratively for each site of the chain to obtain the high- and low-energy reservoirs.

In Fig. 5.6 the reservoirs $\overline{\Gamma}^{\mathrm{H/L}}_n$ have been determined by the rescaled algorithm described above. In comparison to Fig. 5.4, both axes are scaled by the NRG scale ω_n (see Eq. (5.1.3.30)), meaning that $\overline{\Gamma}_n(\overline{\omega}) = \Gamma_n(\omega)/\omega_{n+1}$ and $\overline{\omega} = \omega/\omega_{n+1}$. A clear even-odd behavior of the reservoirs can be observed. Even though the Wilson chain coupling parameters t_n do not explicitly show this behavior, the resulting eigenspectrum does. Details on this can be found in Sec. 3.6. The alternating scheme of the energies of even and odd chains is also reflected in the reservoirs, which can be seen as a complement to the chain.

Let us discuss the scaling of the reservoirs. To start with the vertical axis, we derive

$$\overline{\Gamma}_n(0) = \sqrt{\Lambda}\frac{\overline{t}^2_{n-1}}{\overline{\Gamma}_{n-1}(0)} = \frac{\overline{t}^2_{n-1}}{\overline{t}^2_{n-2}}\overline{\Gamma}_{n-2}(0) \qquad (5.1.3.38)$$

from Eq. (5.1.3.34), since $\mathfrak{Re}\overline{\Sigma}^{\mathrm{L}}_n(0) = 0$. The rescaled hopping parameters $\overline{t}_n$ go to 1 for large n. Hence, on the vertical axis the rescaled reservoirs experience a distinct steady-state for even and odd iterations.

To investigate the scaling of the horizontal axis, we recall that the cut-off frequency ω^{C}_n is a measure for the width of the n-th reservoir and, in this way, for the scaling of the horizontal axis. It is left to calculate the scaling of ω^{C}_n. The integral of Eq.

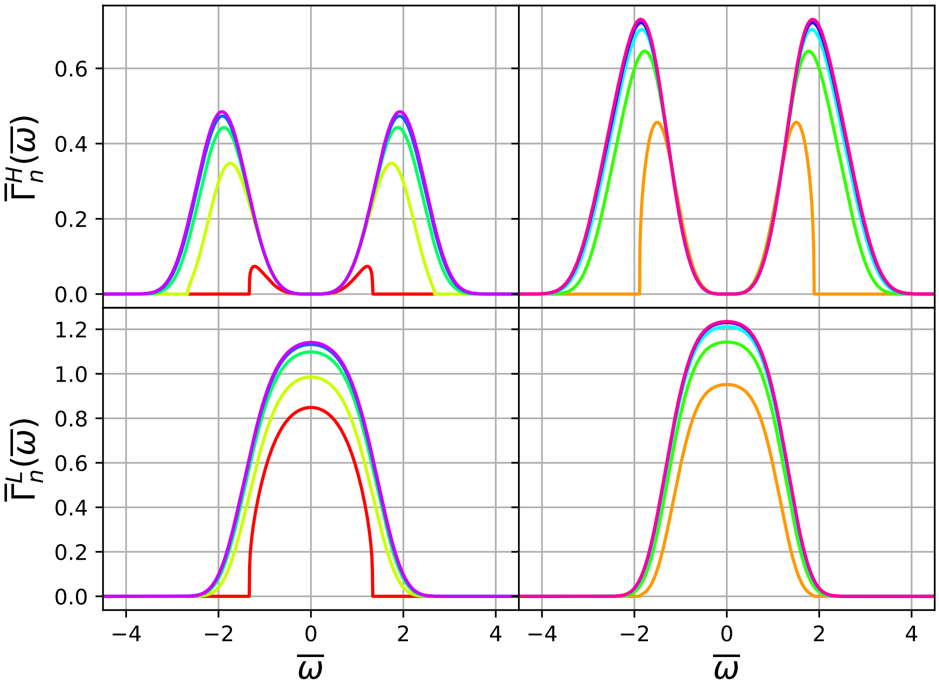

Figure 5.6.: The high-energy reservoirs $\overline{\Gamma}_n^{\mathrm{H}}(\overline{\omega})$ (top) and the low-energy reservoirs $\overline{\Gamma}_n^{\mathrm{L}}(\overline{\omega})$ (bottom), rescaled by the NRG scale ω_n. $\Lambda = 2$ has been chosen. Legend as in Fig. 5.4.

(5.1.2.22) can be approximated by

$$t_n^2 \approx \frac{1}{\pi}\Gamma_n(0) \int d\omega F(\omega, \omega_n^{\mathrm{C}}) \approx 0.577\, \Gamma_n(0)\, \omega_n^{\mathrm{C}}, \tag{5.1.3.39}$$

since the cut-off function $F(\omega, \omega_n^{\mathrm{C}})$ defines the shape of the curve. From here we can conclude

$$\omega_n^{\mathrm{C}} \propto \frac{t_n^2}{\Gamma_n(0)} = \Gamma_{n+1}(0), \tag{5.1.3.40}$$

meaning that the cutoff frequencies ω_n^{C} experience the same scaling as the height $\Gamma_{n+1}(0)$ of the reservoirs. This statement analogly counts for the rescaled parameters $\overline{\omega}_n^{\mathrm{C}}$ and $\overline{\Gamma}_{n+1}(0)$, respectively.

The validity of this finding is shown in Fig. 5.7 for rescaled parameters $\overline{\Gamma}_{n+1}(0)$ (see Eq. (5.1.3.38)) and $\overline{\omega}_n^{\mathrm{C}}$ (Eq. (5.1.3.37)). As suggested in Eq. (5.1.3.38) and (5.1.3.40), both parameters scale by $\sqrt{\Lambda}$ for higher iterations n, as can be seen by the steady-state of the rescaled parameters. The difference of the steady-states for even and odd

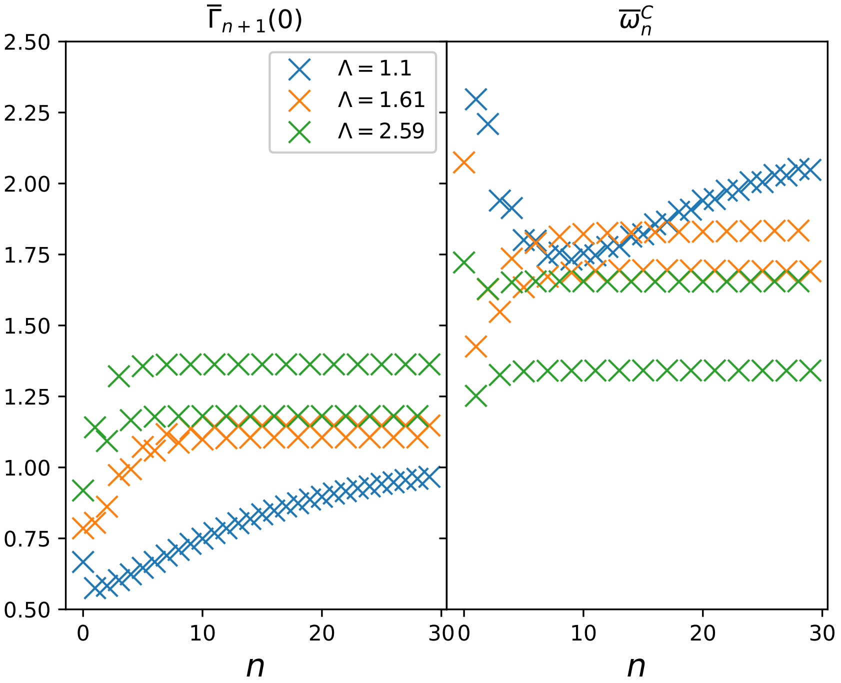

Figure 5.7.: The rescaled quantities $\overline{\Gamma}_{n+1}(0)$ and $\overline{\omega}_n^{\mathrm{C}}$, plotted for different iterations n and discretization parameters Λ.

iterations is increased with Λ and scales roughly by $\sqrt{\Lambda}$. The rescaled reservoir width $\overline{\omega}_n^{\mathrm{C}}$ shows a dip at $n \approx n_{\max}$, comparable to t'_n (see Fig. 5.5).

In Fig. 5.8 the reservoir parameters are plotted for the first 30 iterations. As done above, they are each scaled by a factor of ω_{n+1} to reveal their converging behavior. In contrast, the absolute parameters in Fig. 5.5 fall off to zero. Let us elaborate on the effect of Λ on the single OWC parameters. First of all, the steady-state value for all parameters is reached within the first 10 iterations for $\Lambda \geq 1.5$. For a smaller $\Lambda \to 1^+$ the convergence is significantly delayed. As discussed above, the maximum value of the absolute parameters is reached at $T_{n_{\max}} \approx D/2$. The steady-state can reliably be assumed at the iteration n_{SS} that translates to an effective temperature of $T_{n_{\mathrm{SS}}} = 0.1D$. Secondly, the oscillations between even and odd iterations are most pronounced for higher Λ. Both characteristics coincide with the Wilson chain eigenspectrum. Lastly, Λ influences the rescaled steady-state value of the reservoir parameters $\overline{V}'_n$ and $\overline{t}'_n$, and thus the coupling strength to the full and high-energy reservoirs respectively. This behavior also coincides with the Wilson chain spectrum.

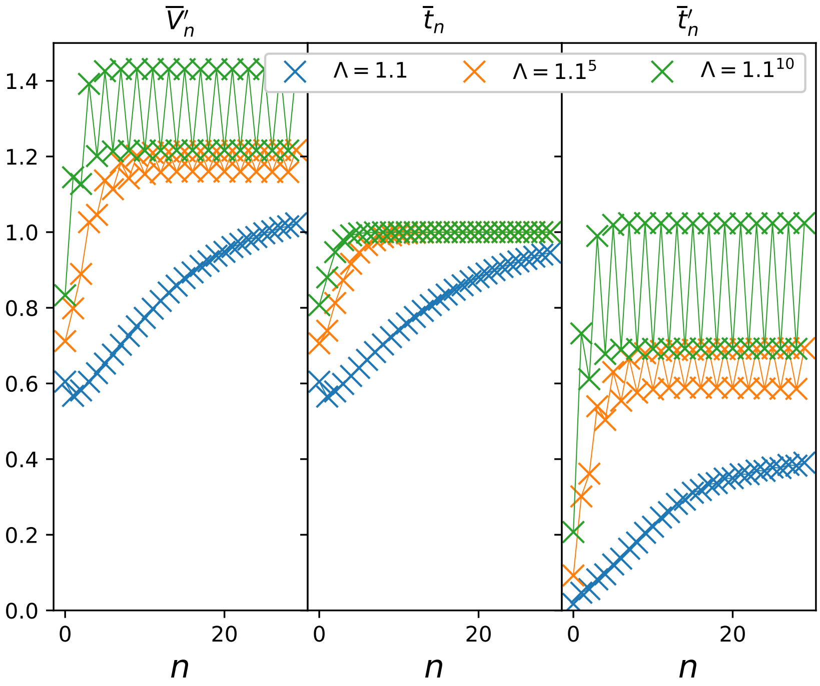

Figure 5.8.: The rescaled reservoir parameters $\overline{V}'_n, \bar{t}_n$ and $\bar{t}'_n$, plotted for the first 30 iterations. The discretization parameter has been chosen as $\Lambda = 1.1$ (blue), $\Lambda = 1.1^5$ (orange) and $\Lambda = 1.1^{10}$ (green). The discrete values are connected by a line for the sake of clarity.

5.2. Calculation of the Bloch-Redfield Tensor

To explicitly calculate the time-dependent density matrix $\rho_\mathrm{S}^\mathrm{I}(t)$ of the OWC, we need to combine all elements we have deduced so far. First of all, the CWC of length N_C is constructed according to Sec. 3.1 and is part of the new local Hamiltonian H_S. Here, all impurity parameters, as well as the bandwidth D and the discretization parameter Λ are defined. An adapted version of the reservoirs is then built to turn the CWC into an exact OQS. The total system Hamiltonian is extended by a bath part

$$H_\mathrm{B} = \sum_{n=0}^{N_\mathrm{C}-1} H_{\mathrm{R},n}, \tag{5.2.41}$$

comprising all reservoirs, and an interaction part

$$H_\mathrm{SB} = \sum_{n=0}^{N_\mathrm{C}-1} H_{\mathrm{SR},n} \tag{5.2.42}$$

with the bilinear Hamiltonian

$$H_{\mathrm{SR},n} = \sum_k t'_k \left(f_n^\dagger c_{n,k} + f_n c_{n,k}^\dagger \right) . \tag{5.2.43}$$

The operator $f_n^{(\dagger)}$ is the Wilson chain operator of the n-th chain site, while $c_{n,k}^{(\dagger)}$ stands for an excitation in the n-th reservoir. The BRF is performed with the interaction Hamiltonian (5.2.42) and consequently the BRT is given as a sum over the index n. To be precise, we need to calculate an independent BRT for each chain site n with a given global inverse temperature β of the system. The chain operator $f_n^{(\dagger)}$, as well as the reservoir $\Gamma_n(\omega)$, is different for each chain site n, while the local eigen-states and -energies are defined by the Hamiltonian H_S of the Wilson chain of length N_C.

Let us discuss the precise way to optimally construct the single BRTs for each Wilson chain site m. Here we assume the iterative construction of the CWC in the spirit of the NRG, while still treating the Wilson chain exactly and not truncating any eigenstates of the Hamiltonian. First of all, on each iteration n of the CWC construction we build the RGF of site $m = n$. Since we assume symmetric bath spectra, there is particle-hole symmetry for the correlation functions, i.e. $C_\mathrm{p}(\omega) = C_\mathrm{h}(\omega) = C(\omega)$. This way, only one RGF needs to be calculated for each iteration. After completion of the CWC, we parallely construct a BRT for each chain site m and then merge all parts at the end. We choose a logarithmic ω-mesh, to allow for a sufficient resolution of exponentially small energies. The RGF at energy ω is then calculated by interpolation, which is a limiting factor concerning runtime. For that reason, we construct a matrix from the RGF with indices (a, b) and components $C(\omega_{ab})$, i.e. for each difference $\omega_{ab} = E_a - E_b$ of local eigenenergies. This way, each relevant energy ω_{ab} only needs to be evaluated once.

For the construction of the BRT of site m we take Eq. (4.5.57) as a basis. The unitary part and the dissipative part are then handled independently. We define a vector $\vec{r}$ with $(\vec{r})_a = \sum_l \Gamma_{al,la}$ and the unitary part is calculated from $(\vec{r})_a + (\vec{r})_b^*$. The dissipative part, on the other hand, has a contribution, iff the Kronecker delta $\delta_{\omega_{ab}+\omega_{mn},0}$ is unequal to zero, which is fulfilled only for specific combinations of indices. Furthermore, since the dissipative part is proportional to the Fermi-function, one half of the non-zero components is effectively cut out for $T \to 0$.

The most effective and, at the same time, most complicated aspect of optimizing the construction of the BRT is the exploitation of quantum number symmetry. The CWC algorithm naturally divides the Fockspace into independent sub-matrices defined by quantum numbers, such as particle number and spin. In all non-zero components ρ_{ab} of the density matrix, both indices a and b originate from the same subspace. According to Eq. (4.3.37), the indices (a, b) need to form a pair of identical quantum numbers and (m, n) need to be such a pair as well. This significantly reduces the size of the BRT. For the unitary part we have $(m, n) = (a, b)$. For the dissipative part we need to construct

$$\Gamma_{nb,am} \propto \sum_{\nu} \left(f_\nu\right)_{am} \left(f_\nu\right)_{bn} + \left(f_\nu\right)_{ma} \left(f_\nu\right)_{nb} . \tag{5.2.44}$$

Here the index pairs differ by one particle of spin ν. This way, we only need to construct certain combinations of indices, which further reduces the building time of the BRT. In the dissipative part another symmetry, i.e. Eq. (4.5.60), can be exploited. Thus it is sufficient to explicitly calculate the cases $a \geq b, m \geq n$.

The case of the operator $\chi_\sigma = \rho d_\sigma^\dagger + d_\sigma^\dagger \rho$ is more complicated, since it connects two subspaces, which differ by a particle of spin σ. According to Eq. (4.4.47), this also counts for the index pairs (a, b) and (m, n), respectively. For that reason, a separate BRT for each value of σ needs to be calculated and stored. Combined with the index ν, the BRT connects a maximum of three adjacent subspaces.

Note that even with the application of the symmetries mentioned above and with proper parallelization, the construction of the BRTs still poses the bottleneck of the OCF with respect to runtime and memory demands.

5.3. Assessment of the BMA in the OCF

The purpose of the construction of the OWC is to improve the BMA. The Wilson chain corresponds to the local system S, while the reservoirs constitute the bath B. In Chap. 4 it has been argued that in order for the BMA to be applicable in the $N_\mathrm{C} = 0$ case, the hybridization strength $\Gamma = \frac{\pi V^2}{2D}$ has to be way below the impurity energies and the bandwidth D of the bath. Our approach is to increase the system and bath parameters in relation to the hybridization by transitioning to the $N_\mathrm{C} > 0$ case. This is expected to improve the BMA, which relies on the hybridization to be the smallest parameter of the total OQS. The OCF is then, to some extend, applicable for arbitrary impurity parameters and bandwidth. To evaluate the relation of the S and B parameters to the hybridization, we require a way to quantify the specific S and B energy scales depending on the length of the OWC.

In the first step of the OCF, the system energy scales are defined by the impurity parameters only, which depend on the specific QIM. Then Wilson chain sites are added to the impurity, influencing the system eigenspectrum by the introduction of the hopping parameters t_n. These parameters can thus be used to define the system energy scale for an OWC. For the first chain sites, the t_n's are on the order of the bandwidth, then they decay rapidly, depending on the choice of Λ. It is thus left to estimate, in what way the exponentially small local energies of a sufficiently long Wilson chain impact the quality of the BMA. Here we expect an influence especially in the second MA and the secular approximation. The former relies on a fast decay of the damping matrices (see Eq. (4.3.25)) with respect to the time s to safely extend the integral over s up to infinity. However, the damping matrices do not only comprise the correlation functions $C(s)$, but also oscillating terms $e^{i\omega s}$, which oscillate with frequencies ω, defined by the system Hamiltonian eigenenergies. Besides a small bath correlation time t_{B}, the second MA requires large system energies, to guarantee a fast decay of the damping matrices. The secular approximation, on the other hand, is the neglect of t-dependent rapid oscillations in the master equation. It also relies on large system energies and is discussed in detail in Sec. 5.3.4.

In the following section we will firstly discuss the system, the bath and the hybridization parameters of the OWC in Sec. 5.3.1 to lie the foundation of our argumentation. Secondly, the contribution, and thus the relevance, of the single reservoirs depending on the chain site number m is estimated in Sec. 5.3.2. Finally, the MA and the secular approximation are discussed in detail in the sections 5.3.3 and 5.3.4, respectively. With the insights of Sec. 5.3 we will then have a perspective to understand and assess the OWC results in the sections 5.4.1 and 5.4.2 with respect to the BMA.

5.3.1. OWC Parameters

In the case of $N_{\mathrm{C}} = 0$ (see Chap. 4), the bath energy scale has been defined by the bandwidth D. The equivalent in the OWC would be the width of the reservoirs $\Gamma_n(\omega)$. Here we recognize that the shape of $\Gamma_n^{\mathrm{L}}(\omega)$ is mainly determined by the cut-off function $F(\omega, \omega_n^{\mathrm{C}})$. By setting $F(\omega_{0.5}, \omega_n^{\mathrm{C}}) = 0.5$ one can see that the half mean width $\omega_{0.5} \approx \omega_n^{\mathrm{C}}$. That means that the cut-off frequency ω_n^{C} is a measure for the width of the n-th reservoir, high- and low-energy reservoir alike.

The hybridization strength between the chain site n and the corresponding reservoir

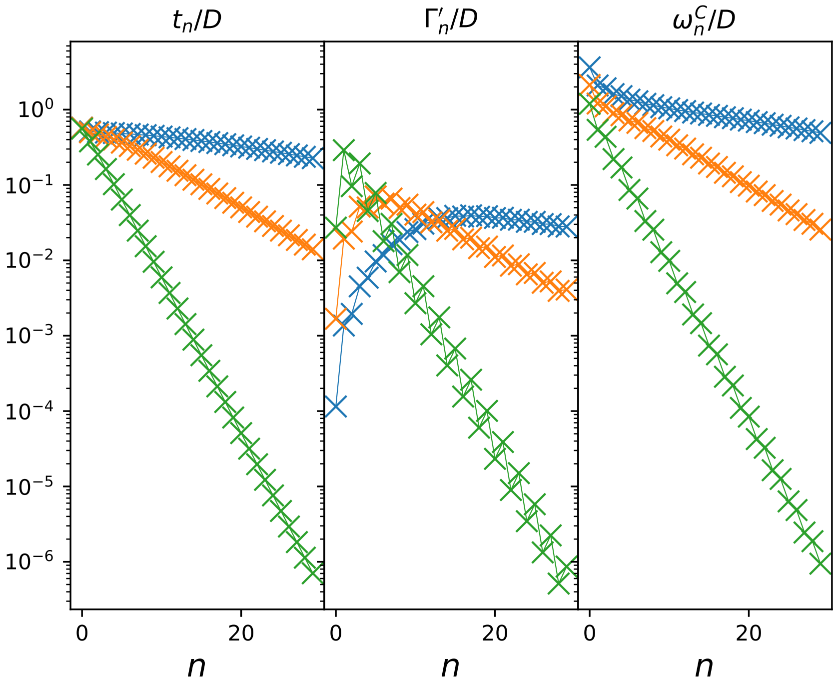

Figure 5.9.: The OWC parameters t_n, Γ'_n and ω_n^{C} scaled by the bandwidth D and plotted semi-logarithmically for the first 30 iterations. The discretization parameter has been chosen as $\Lambda = 1.05$ (blue), $\Lambda = 1.33$ (orange) and $\Lambda = 2.59$ (green). The discrete values are connected by a line for the sake of clarity.

can then be defined as

$$\Gamma'_n = \frac{\pi (t'_n)^2}{2\omega_n^{\mathrm{C}}}. \qquad (5.3.1.45)$$

This quantity plays the role of the hybridization Γ between the impurity and the bath and the question, whether it is small in comparison to the other energy scales is the key point of the BMA.

In Fig. 5.9 the parameters t_n, Γ'_n and ω_n^{C} are plotted for the first 30 iterations. The energy axis has been chosen logarithmically to compare the various energy scales of the parameters. It can be seen that the hybridization Γ'_n lies well below the other parameters for all iterations n. By increasing Λ, the difference between Γ'_n and the other parameters shrinks, which indicates that the BMA is impaired.

Obviously, the discretization parameter has a significant impact on the OWC. However, the role of the bandwidth with respect to the quality of the BMA has changed. In

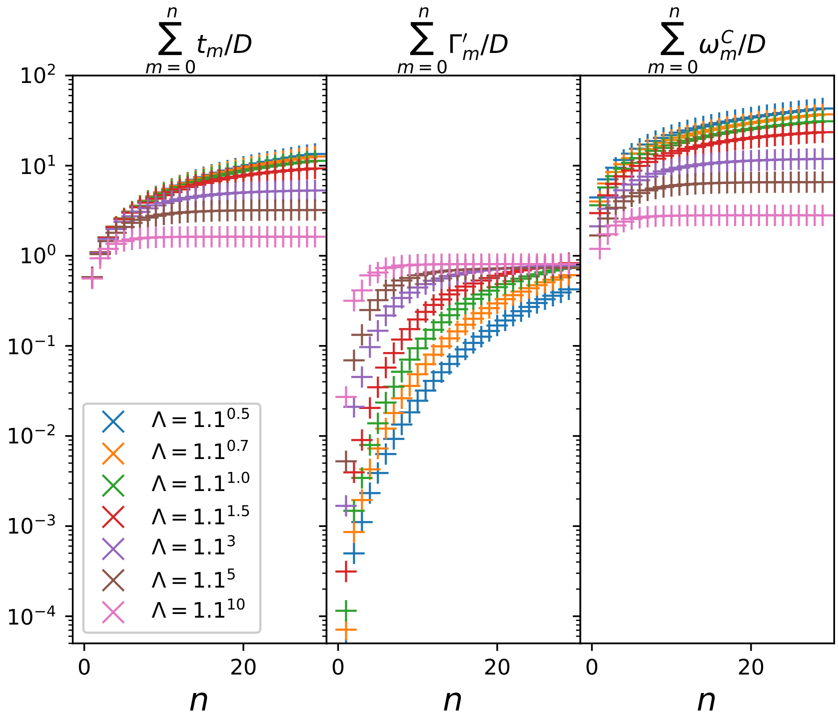

Figure 5.10.: The sum of the OWC parameters t_m, Γ'_m and ω^{C}_m up to iteration n scaled by the bandwidth D and plotted semi-logarithmically for the first 30 iterations. The discretization parameter Λ has been varied. The discrete values are connected by a line for the sake of clarity.

Chap. 4 the impurity was directly coupled to the bath, hence the bandwidth directly influenced the hybridization between the system and the bath and thus the BMA. Now, the impurity is coupled to the OWC, which comprises the CWC and the reservoirs. The BMA only influences the coupling of the reservoirs to the single chain sites within the OWC. All parameters of the OWC are scaled by the bandwidth, i.e. in the OWC alone, the bandwidth has no relevance at all, especially not with respect to the BMA. The bandwidth now only defines the size of the OWC in comparison to the impurity and the coupling Γ between the impurity and the OWC. From this standpoint, a small bandwidth is preferable, since here the impurity parameters are relatively large, which improves the MSA. However, the overall quality of the BMA is expected to be independent of the bandwidth.

The representation in Fig. 5.9 is suitable for investigating single chain sites. To evaluate the global effect of the OWC onto the BMA we plot the sum of the parameters upto iteration n in Fig. 5.10. Crosses have been chosen instead of stars to better depict the steady-states. For increasing chain length the difference between the hybridization

Γ'_n and the other two energy scales is increased. This effect is largest for small Λ. Here the coupling to the reservoirs is weak, while with each iteration a relatively high energy excitation is extracted from the bath and added to the chain, translating to a large t_n. If the coupling t_n to the rest-chain is large, the width of the subsequent reservoir is large as well. We can thus conclude that the BMA is best for a small Λ, while it can always be improved by increasing the chain length. For large Λ, however, this improvement is small.

One point is left to mention here. If the system Hamiltonian contains exponentially small energies, i.e. in the impurity or as hopping parameters for large n, these energies are reflected in the local eigenspectrum. Consequently, the second MA, as well as the secular approximation, are affected for $n \approx n_{\max}$, since here the hybridization Γ'_n is relatively large. This is expected to impair short-time dynamics of the time-dependent density matrix. However, the influence of the first reservoirs of long Wilson chains on the BRT is small, as will be discussed in Sec. 5.3.2.

It is relatively simple to assess the applicability of the BA in the OWC, as it is a perturbative coupling of the reservoirs in second order in the hybridization between the reservoir and the system. Thus, if the hybridization is relatively small in comparison to the other OWC parameters (which is proven in Fig. 5.9 and 5.10), the BA can be expected to yield good results. With increasing chain length, more and more excitations are extracted from the bath into the system. Thus the coupling from the system to the remaining bath (comprising the reservoirs) is decreased and the BA is improved. The main impact of the BA on the time-dependent density matrix lies in its equilibrium values, since in the dynamics of the master equation the hybridization is still included. The equilibrium values, however are defined by the CWC, which is known from NRG calculations to well reproduce physical values, if N_C is chosen large enough.

An assessment of the MSA is more complicated and consequently we devoted Sec. 5.3.3 and 5.3.4 to that topic.

5.3.2. Contribution of the Single Reservoirs

The OCF is based on a separate reservoir coupled to each single chain site n via distinct hybridization strengths. The BMA is effectively applied to each chain site, so it is advisable, to (a) assess the quality of the BMA depending on n and (b) estimate the contribution of the n-th reservoir to the total BRT.

The behavior of the eigenspectrum of a Wilson chain is well-known. Here lower and lower energy modes are added to the chain with each iteration, while for a given effective temperature T_{N_C} the high-energy modes are suppressed by the density matrix. The chain operators are expected to give the largest contribution for $n = N_\mathrm{C}$, while shrinking by a factor of $\sqrt{\Lambda}$ for each step backwards along the chain, since the overlap of CWC eigenstates is $\langle r, e; n | r', e'; n' \rangle \propto \Lambda^{-|n-n'|/2}$ (see Sec. 6.1.4). Since the operators appear in quadratic order in the BRT, the scaling effect is quadratic as well. The reservoirs, in turn, are largest for $n = 0$ and shrink on both axis by a factor of around $\sqrt{\Lambda}$. Note that the scaling arguments only count for $n > n_\mathrm{max}$ with n_max being defined by the effective temperature $T_{n_\mathrm{max}} = D/2$. Since the RGFs are proportional to the reservoir spectral functions, they damp the BRTs of higher n by a factor of $\sqrt{\Lambda}$ with each site along the chain. This effect, however, is not expected to fully compensate the quadratic scaling of the chain operators, making the later sites $n \approx N_\mathrm{C}$ dominant in comparison to the first sites $n \ll N_\mathrm{C}$. Another factor that enhances the contribution of later sites to the BRT is the shape of the reservoirs in relation to the distribution of the eigenspectrum.

To illustrate this effect, the RGF $G_n(\omega)$ (see Eq.(4.3.35)) are plotted for the first 30 iterations for two different values of Λ in Fig. 5.11. The real-part of the functions comprises a product of the reservoir spectral functions $\Gamma_n(\omega)$ and the Fermi-function, while the imaginary-part is obtained from a Hilbert transform of the real-part.

We know from the considerations above that the reservoirs are not converged yet after 30 iterations for $\Lambda = 1.05$, while for $\Lambda = 2$ the steady-state has been reached after around 10 iterations. In this context, it may seem confusing at first that the RGFs need around 20 iterations to reach a steady-state for $\Lambda = 2$. This is, however, due to the Fermi-function. At a fixed temperature T the Fermi-function practically appears to relatively broad functions as a Heaviside-function $\Theta(-\omega)$, while it is effectively constant at $\frac{1}{2}$ for functions that are very narrow in relation to the temperature T. Since for a larger Λ lower energy scales are reached, the two peaks of $\mathfrak{Re} G_n(\omega)$ (Fig. 5.11 (e) and (f)) become more and more symmetric, until $\mathfrak{Re} G_n(\omega) \to 0.5 \Gamma_n(\omega)$ in the limit of large n. Here the Fermi-function is effectively constant on the support of the reservoir.

To estimate the contribution of the RGFs to the BRT with respect to the chain site number n, we have to consider the distribution of the eigenspectrum of the Wilson chain. At a given iteration n, we know that the eigenspectrum of the Wilson chain spans from energies of the order of the bandwidth D down to the exponentially small "NRG-scale" ω_{N_C}. From Fig. 5.11 we can see that each $G_n(\omega)$ has its major contributions for energies $\omega \approx \omega_n$. Additionally, $\mathfrak{Im} G_n(\omega)$ has a significant contribution for small energies as well on the first Wilson chain sites, i.e. if n is small. The imaginary-part

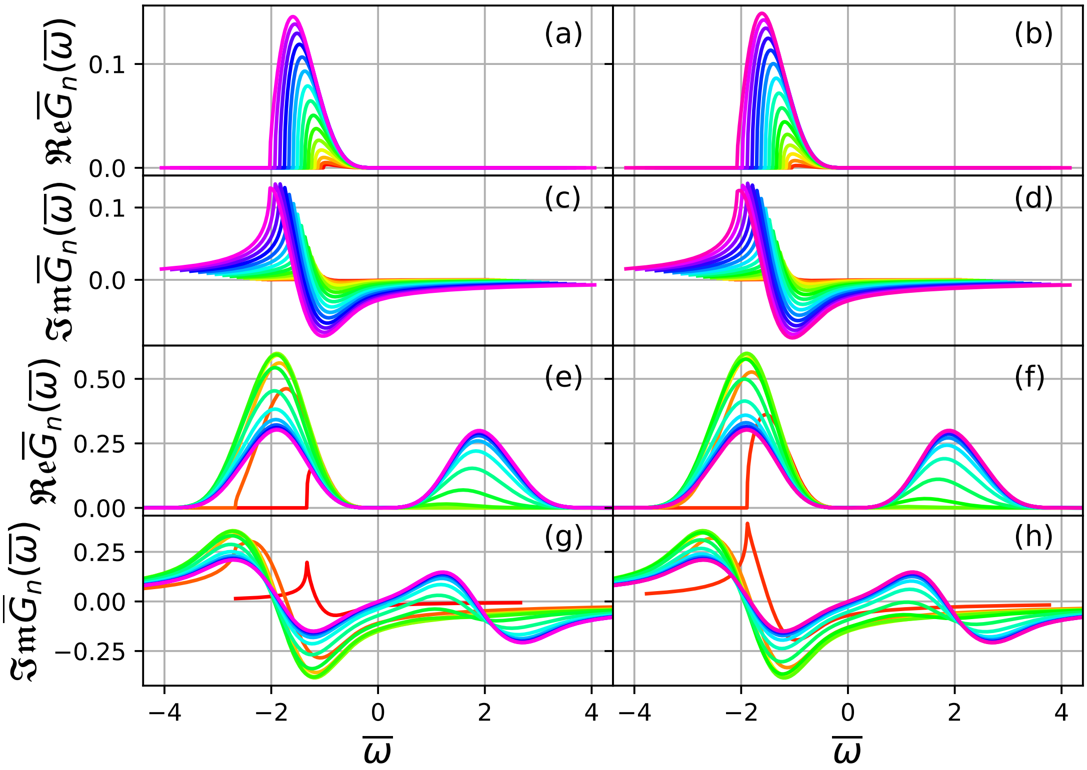

Figure 5.11.: The rescaled RGFs $\overline{G}_n(\overline{\omega})$ versus the rescaled energies $\overline{\omega}$. We start with iteration $n = 0$ (red) and proceed through the physical color spectrum to $n = 30$ (violett). The real-part is plotted in panels (a), (b), (e), (f) and the imaginary part in panels (c), (d), (g), (h), respectively. For the upper four panels a discretization parameter $\Lambda = 1.05$ has been chosen, while we have $\Lambda = 2$ in the lower four panels. The curves are constructed for $T = 1\Gamma$.

of the RGFs, in turn, defines the Lamb-shift generated by the imaginary part of the BRF. Considering the fact that in the logarithmically discretized bath the low-energies of the eigenspectrum are most relevant (see Sec. 3.3), the real-part of the BRT that defines the relaxation rates and the natural broadening, is mostly dominated by the last sites of the OWC.

To sum up, the contribution of the chain operators grows by a factor of Λ for each iteration, while the reservoirs shrink by $\sqrt{\Lambda}$, leading to a dominant contribution for $n \approx N_\mathrm{C}$. The shape of the RGFs suggests that $\mathfrak{Re}G_n(\omega)$ and $\mathfrak{Im}G_n(\omega)$ have a similar contribution for $n \approx N_\mathrm{C}$, while the $\mathfrak{Re}G_n(\omega)$ are damped more strongly for $n \ll N_\mathrm{C}$.

What can we assume regarding iterations $n > N_\mathrm{C}$? The chain operators will damp the BRT components by $\Lambda^{N_\mathrm{C}-n}$, while the reservoirs are further damped by $\sqrt{\Lambda}$ with each iteration, leading to a damping factor of $\sqrt{\Lambda}^3$ with each iteration. Since the RGFs shrink on the ω-axis as well, the eigenspectrum of the Wilson chain is relatively enlarged which further decreases the contribution of iterations $n > N_\mathrm{C}$, making them negligible. This fact will be relevant later on in Sec. 6.1.3.

5.3.3. Impact of the Markov Approximation

Before we proceed to calculate physical properties with the OCF, let us estimate the effect of the MSA. More precisely, we want to assess how the Wilson chain influences the applicability of those approximations. In the simple $N_\mathrm{C} = 0$ model of Sec. 4.6 we required to be in the wideband limit in order to ensure short correlation times. Furthermore, large local energies $\epsilon_\mathrm{d} \gg \Gamma$ were required to let the BRT from Eq. (4.3.19) decay fast with s compared to the local time scale defined by Γ. Since the BRT is a linear combination of the damping tensors, it is them we need to investigate. For particle-hole symmetric reservoirs the damping tensors are basically given by

$$(\Gamma_n)_{ab,cd}(t,s) = e^{i(\omega_{ab}+\omega_{cd})t}\left[(f_n)^\dagger_{ab}(f_n)_{cd} + (f_n)_{ab}(f_n)^\dagger_{cd}\right] C_n(s) e^{-i\omega_{cd}s} \tag{5.3.3.46}$$

for the n-th chain site. If the correlation time of $C_n(s)$ is short, the MA can be applied without restriction. Thus, the correlation functions $C_n(t)$ make an important contribution to the behavior of the density matrix in the master equation (4.3.18), since they contain the entire information on the n-th reservoir. The reservoirs are responsible for any true dissipative processes. The time-dependent correlation functions are defined by the reservoir coupling function $\Gamma_n(\epsilon)$ as

$$C_n(t) = \frac{1}{\pi}\int_{-\infty}^{+\infty} d\epsilon \Gamma_n(\epsilon) f_\beta(\epsilon) e^{i\epsilon t} \tag{5.3.3.47}$$

(see Eq. (4.3.24)). Since the reservoir functions $\Gamma_n(\epsilon)$ are symmetrical, the Fermi-function $f_\beta(\epsilon)$ vanishes in $\mathfrak{Re} C_n(t)$ and thus the real-part is independent of temperature. The imaginary part vanishes in the limit of high temperatures, where the Fermi-function is constant, and is maximal for $T = 0$.

The correlation functions $C_n(t)$ are plotted in Fig. 5.12 for $\Lambda = 1.1$. For such a small discretization parameter the even-odd behavior is small and the decay rate of the amplitude low. This provides a smooth transition between the iterations which is preferable for plotting even and odd curves for high iterations n within one single

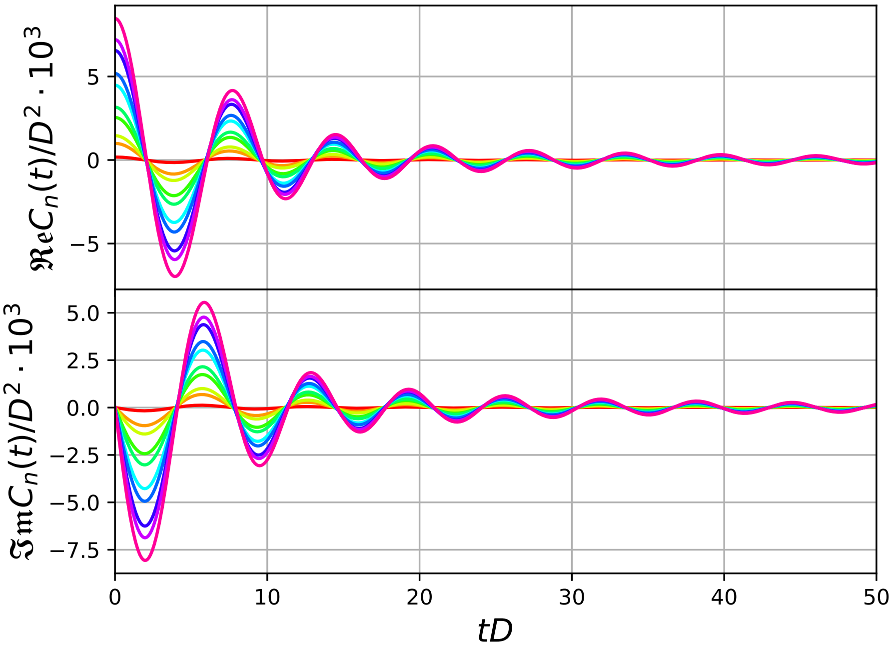

Figure 5.12.: The time-dependent correlation functions $C_n(t)/D^2$ versus the dimensionless time tD. We start with iteration $n = 0$ (red) and proceed to $n = 10$ (violett). The real-part is plotted on the top while the imaginary part is plotted on the bottom. A discretization parameter $\Lambda = 1.1$ and a temperature $T = 1\Gamma$ have been chosen.

figure. The correlation time is defined as the time $t = t_{\text{corr}}$ when the envelope function of $\mathfrak{Re}C(t)$ has sufficiently decayed. According to the figure that time can be estimated as $t_{\text{corr}} \approx 20/D$ for chain site number $n = 10$.

The question remains, how the correlation time scales with Λ and with the iteration n. For higher Λ there is a larger energy separation between the iterations, leading to a faster change in the correlation functions. For that reason, the scaling of the correlation functions needs to be investigated.

The maximum value at $t = 0$ is given by

$$C_n(0) = \frac{1}{\pi}\int_{-\infty}^{+\infty} d\epsilon \Gamma_n(\epsilon) f_\beta(\epsilon) = \frac{1}{2\pi}\int_{-\infty}^{+\infty} d\epsilon \Gamma_n(\epsilon) = \frac{(t'_n)^2}{2}. \tag{5.3.3.48}$$

The correlation functions are expected to decay quadratically with the reservoir coupling parameters t'_n, when the iteration number n is increased above $n_{\max}$. Let us develop an approach to determine the correlation times. We approximate the spectral functions by a box function

$$\Gamma_n(\omega) = \Gamma_n(0)\Theta(\omega_n^{\mathrm{C}} - |\omega|), \tag{5.3.3.49}$$

whose dimensions are determined by the findings made above. The real-part of the correlation function is then given as

$$\mathfrak{Re}C_n(t) = \frac{\Gamma_n(0)}{\pi} \int_{-\omega_n^{\mathrm{C}}}^{+\omega_n^{\mathrm{C}}} d\epsilon f_\beta(\epsilon)\cos(\epsilon t) = \frac{\Gamma_n(0)}{\pi}\frac{\sin(\omega_n^{\mathrm{C}} t)}{t}. \tag{5.3.3.50}$$

The envelope function can be obtained by setting the sine-function to 1, which removes the oscillations. For the initial value $t = 0$ it follows $\mathfrak{Re}C_n(0) = \frac{\Gamma_n(0)\omega_n^{\mathrm{C}}}{\pi}$. The time when the envelope function is decayed to 10% of the initial value is then given by

$$t_{n,0.1} = \frac{10}{\omega_n^{\mathrm{C}}}. \tag{5.3.3.51}$$

The cut-off frequencies ω_n^{C} can hence be used as an estimate for the inverse correlation times. This suggests that $t_{\mathrm{corr},n} \propto \Lambda^{n/2}$, meaning that the correlation times grow significantly for large Λ. Note that $t_{\mathrm{corr},n} \approx 1/\omega_n^{\mathrm{C}}$ is consistent with the finding of Sec. 5.1.3 that the cut-off frequencies are a measure of the width of the corresponding reservoirs.

As a possible absolute measure for the MA, the correlation times can be determined graphically. The axes need to be rescaled by ω_n to depict larger values of Λ. To find the correct scaling we investigate the convergence of the correlation functions $C_n(t)$. For this purpose, we exploit the convergence of the reservoirs $\Gamma_n(\omega)$ and define

$$\begin{aligned} C_n(t) &= \frac{1}{\pi}\int_{-\infty}^{\infty} d\epsilon \Gamma_n(\epsilon) f_\beta(\epsilon) e^{i\epsilon t} \\ &= \frac{\omega_{n+1}^2}{\pi}\int_{-\infty}^{\infty} d\overline{\epsilon}\,\overline{\Gamma}_n(\overline{\epsilon}) f_{\overline{\beta}}(\overline{\epsilon}) e^{i\overline{\epsilon}\overline{t}} \\ &= \omega_{n+1}^2 \overline{C}_n(\overline{t}) \end{aligned} \tag{5.3.3.52}$$

with the dimensionless time $\overline{t} = t\omega_{n+1}$ and the dimensionless inverse temperature $\overline{\beta} = \beta\omega_{n+1}$. From here it is obvious that the correlation times scale with $\Lambda^{n/2}$, while the amplitude of the correlation functions scales with Λ^{-n}. For a fixed temperature T the dimensionless inverse temperature $\overline{\beta}$ decreases along the chain, meaning that $\mathfrak{Im}\overline{C}_n(\overline{t})$ is maximal for small n.

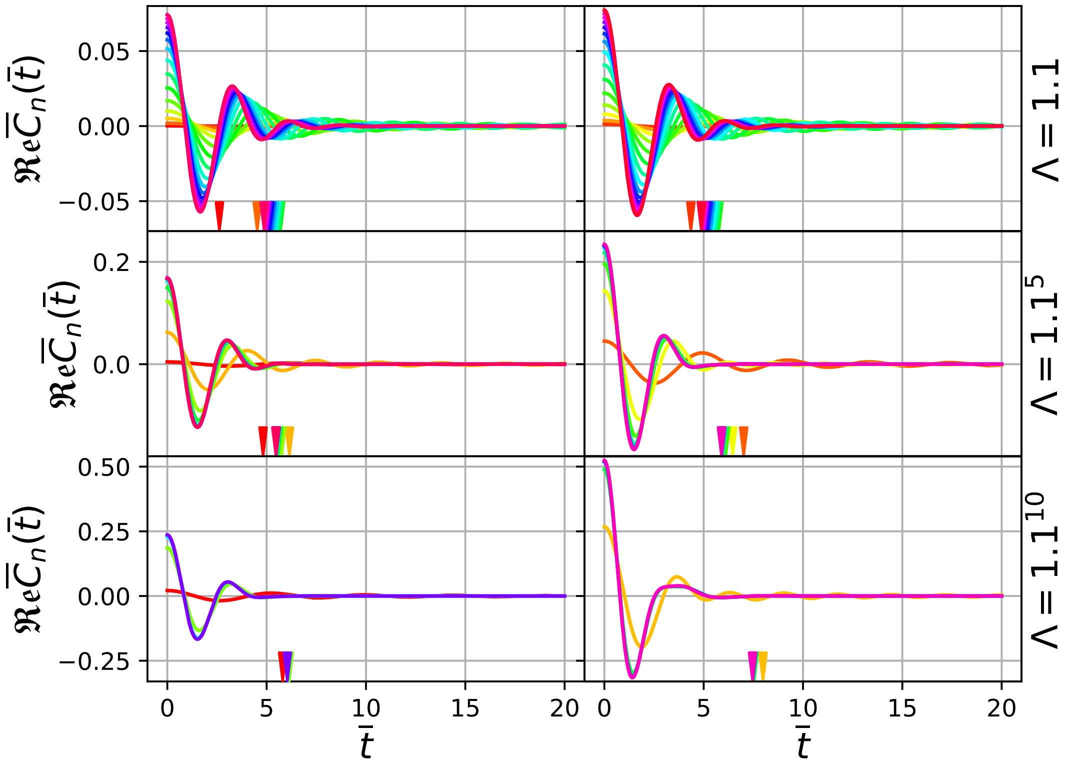

Figure 5.13.: The real-part of the rescaled time-dependent correlation functions $\mathfrak{Re}\overline{C}_n(\bar{t})$ versus the dimensionless time $\bar{t}$. We start with iteration $n = 0$ (red) and proceed to $n = 17$ (violett). As arrows with the same color scheme, $t_{n,0.1}$ is added to the horizontal axis. The discretization parameter Λ has been varied according to the notation on the right. The panels on l.h.s. depict the even and on the r.h.s. the odd chain sites.

In Fig. 5.13 the real-part of the rescaled time-dependent correlation functions $\overline{C}_n(\bar{t})$ is plotted for different iterations n and different discretization parameters Λ. The behavior is similar to the reservoir functions with respect to the even-odd convergence. The number of iterations n has been chosen in such a way that a sufficient convergence is reached. For a Wilson chain of length N_C, the effective temperature can be defined as $T_{N_C} = \omega_{N_C}$ (see Eq. (3.5.28)). Convergence is thus reached when the effective temperature drops below a convergence temperature T_{n_SS}. As discussed above with respect to Fig. 5.9, a temperature of $T_{n_\mathrm{SS}} = 0.1D$ is sufficient for appropriate convergence.

We have already pointed out that the time $t_{n,0.1}$, when the envelope of the correlation function has dropped below around 10% of its initial value, appears to be a promising candidate to estimate the correlation times. For that reason, those times are added in a rescaled version as arrows on the horizontal axis. The figure suggests that in our chosen parameter interval of Λ the correlation times can reliably be estimated as $\bar{t}_{\mathrm{corr},n} \approx 5$. For an exemplary effective temperature of $T = 0.1\Gamma$ this relates to the absolute times $\Gamma t_{\mathrm{corr},n} = 50$, which is way above typical time scales of the local density matrix. Any local system would be thermalized for a long time before the reservoir correlations have decayed. In this context, the MA appears outright unsuited. However, as discussed above, the correlation times of the reservoirs, which are mediated by their particular widths, are not the only relevant time scale for the convergence of the BRT to its steady-state. From Eq. (5.3.3.46) it follows that the damping tensors are proportional to $C(s)e^{i\omega s}$, meaning that the decay rate with respect to s is not only defined by the oscillation frequency of the correlation function $C(s)$ but of the sum with the system energies as well. Further assessment of the quality of the BMA approximation is given in the subsequent section. Here, local non-equilibrium dynamics as well as local spectral functions are investigated for small chain lengths. The OWC results are compared to the closed chain and the influence of the parameters onto the bath discretization and the BMA is discussed. In Chap. 6 the truncation scheme of the NRG is implemented into the BRF to construct chains of higher length N_{C} and thus to access parameter regimes more favorable to the above mentioned approximations.

5.3.4. Accuracy of the Secular Approximation

The block-diagonalization of the BRT is based on the secular approximation, i.e. $R_{ab,cd} \propto \delta_{\omega_{ab}+\omega_{cd},0}$ (see Eq. (4.5.56)). Within this approximation we consider rapidly oscillating terms in the master equation for the density matrix to average out. However, a Kronecker-delta here implies that only those frequencies with $\omega_{ab} + \omega_{cd} = 0$ can contribute to the dynamics of the density matrix. A more realistic definition would be to define a small Δ that determines the window of relevant energies. The Kronecker-delta is in this way replaced by the Heaviside function $\Theta(\Delta - |\omega_{ab} + \omega_{cd}|)$, where in the case $\Delta \to 0$ the Kronecker-delta is recovered.

The specific choice for Δ now needs to be discussed. Let us therefore consider the most simple case of a one-dimensional master equation without secular approximation

$$\dot{\rho}(t) = -\gamma e^{i\omega t}\rho(t), \tag{5.3.4.53}$$

which represents a differential equation with an oscillation frequency[4] ω and a re-

---

[4] Note that in the secular approximation we would choose $\omega = 0$ here.

spective relaxation rate γ. The purpose of Eq. (5.3.4.53) is to resemble the master equation (4.3.37) before the secular approximation has been applied. The relaxation rate γ is then defined by the damping matrix elements of the BRT and ω is a difference of eigenenergies of the system Hamiltonian. Equation (5.3.4.53) can be expanded to a sum over j of different parameters γ_j and ω_j, however, this would not impact the following argumentation.

To assess the quality of the secular approximation depending on the parameters γ and ω, we solve the master equation (5.3.4.53) to obtain

$$\rho(t) = \rho(0) f(\omega/\gamma; t\gamma) \tag{5.3.4.54}$$

with

$$f(\omega; t) = \exp\left(i(e^{i\omega t} - 1)/\omega\right). \tag{5.3.4.55}$$

If Eq. (5.3.4.53) comprises a sum of different frequencies ω_j and rates γ_j, then the solution represents a product function of the type of Eq. (5.3.4.55).

In what cases is the secular approximation $e^{i\omega t} \to \delta_{\omega,0}$ appropriate in Eq. (5.3.4.53)? Obviously, for $\omega \to 0$ we can substitute $e^{i\omega t} \to 1$. No secular approximation is necessary here. A slight increase of ω will not significantly change the resulting $\rho(t)$, which justifies the introduction of a small interval $[-\Delta, \Delta]$, in which all frequencies are accepted as effectively zero. On the other hand, by increasing the absolute value of ω beyond Δ, a regime is entered, in which the secular approximation is no longer applicable. The other extreme of the spectrum is $\omega/\gamma \to \infty$. Here $f(\omega/\gamma; t\gamma) \approx 1 \,\forall\, t$, i.e. $\rho(t) = const$ and we can safely replace $e^{i\omega t} \to 0$ in Eq. (5.3.4.53), which means that the secular approximation is perfectly justified. Consequently, our objective is to estimate the interval, in which the secular approximation is expected to yield a significant error.

In Fig. 5.14 the function $f(\omega/\gamma; t\gamma)$ of Eq. (5.3.4.55) has been plotted for different values of ω/γ. Curves with $\omega \sim \gamma$ already significantly deviate from the $\omega = 0$ curve. This suggests to choose $\Delta < 10^{-2}\gamma$. On the other hand, the secular approximation requires all frequencies $\omega > \Delta$ to be at least around $10^3\gamma$ to justify neglecting them.

The purpose of the investigation of Eq. (5.3.4.53) is to estimate the error of the secular approximation in the OWC. The energy scale γ is here given by the single reservoirs, which span from the order of the bandwidth D down to exponentially small energies of the scale of the effective Wilson chain temperature. The frequency ω represents the system energies, i.e. the eigenenergies of the Wilson chain Hamiltonian.

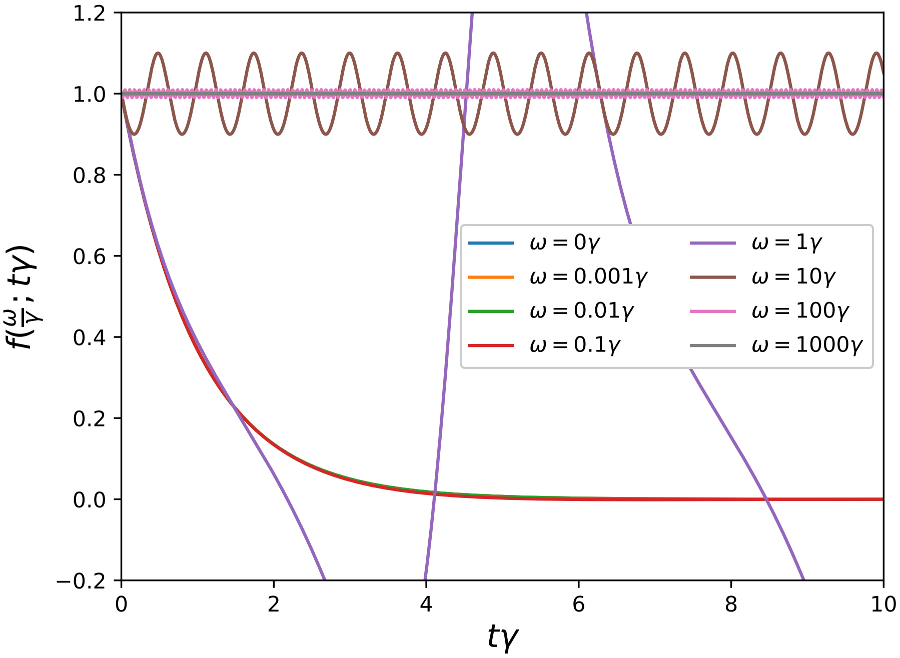

Figure 5.14.: $f(\omega/\gamma; t\gamma)$ plotted versus dimensionless time $t\gamma$ to estimate the cut-off frequency Δ for the secular approximation. The real-part of the function is depicted as a solid line, while the imaginary part is not plotted, but exhibits a comparable convergence behavior.

These energies are of a comparable order as the reservoir coupling functions $\Gamma_n^{\mathrm{H/L}}(\omega)$. Consequently, the case $\omega/\gamma < 10^{-2}$ can only be fulfilled for small system energies and for reservoirs of the first chain sites. However, these sites are least relevant for the dynamics of the time-dependent density matrix, as has been discussed in Sec. 5.3.2. In most relevant cases $\omega/\gamma < 10^{-2}$ can only be fulfilled, if the indices of $\omega_{ab} + \omega_{cd}$ combine in such a way that the net result is zero. Thus, Δ can effectively be chosen as zero, in the limit of the numerical accuracy of the eigenenergies.

At this point, it cannot simply be estimated, to what extend the other case, $\omega/\gamma > 10^3$, is fulfilled for all $\omega > 0$. The most relevant chain sites at the end of the chain are attributed with the smallest reservoirs, however, for exponentially small system energies, the secular approximation might not be applicable. Note that Γ defines the actual relevant time scale for the dynamics of the density matrix. Thus all oscillations with $\omega \ll \Gamma$ will be damped before they have any relevant contribution to the dynamics. If n is large, then ω_n is small and the critical frequencies are small as well.

To quantitatively support the arguments made above, we plot $\frac{\omega}{\Gamma_n^{\mathrm{H/L}}(\omega)}$ in Fig. 5.15.

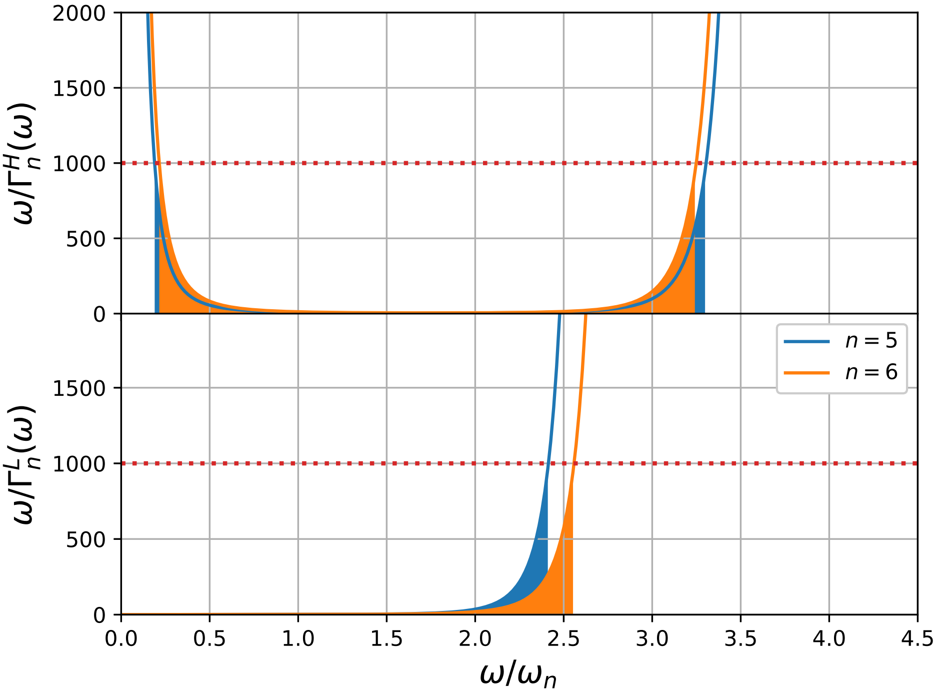

Figure 5.15.: $\omega/\Gamma_n(\omega)$ plotted versus the positive dimensionless energies ω/ω_n for $\Lambda = 2$. We consider high- and low-energy reservoirs for chain sites $n = 5, 6$. The filled area under the curves represents the critical frequency interval in which $\omega/\Gamma_n(\omega) < 10^3$.

Since the reservoirs are symmetrical, we restrict to $\omega \geq 0$. We can deduce the frequency, below which the secular approximation is no longer applicable, as around $3.5\omega_n$ for high-energy and $2.5\omega_n$ for the low-energy reservoirs. For any frequency below that, the secular approximation is considered to produce a significant error. In the case of the high-energy reservoirs, $\omega < 0.2\omega_n$ is accepted as well.

If n is large enough that $\omega_n \ll \Gamma$, the oscillations induced by the problematic frequencies have no impact on the total dynamics generated by the master equation. If n is small, and consequently ω_n is relatively large, a large amount of problematic oscillations can occur that possibly impact the dynamics on time scales $\sim 1/\Gamma$. However, as argued above, these chain sites do not significantly contribute to the overall dynamics and thus one is advised to choose N_C as high as possible with a preferably low effective temperature to maximally reduce the impact of the secular approximation.

We conclude that ω/γ is always large in the relevant cases, except for the case $\omega_{ab} = E_a - E_b = 0$, where the energies are identical. The application of a Kronecker-delta for the secular approximation is thus justified within the limit of the expected machine precision of the system eigenenergies. As a criterion for the maximum value of Δ we can use the above mentioned block-diagonal structure of the BRT. The largest subblock of this matrix connects the DDM and has the associated energy $\omega_{ab} = 0$. The eigenvalues of this submatrix are entirely real and semi-positive (for details on that see Sec. 4.5). If, by choosing Δ too large, too many components are assigned to this subspace, complex eigenvalues emerge. In other cases, eigenvalues with negative real-part may occur. Thus, Δ will be chosen sufficiently small to avoid these unphysical cases.

5.4. Numerical Implementation of the OCF

In this section we present results for local impurity quantities of the OWC in the RLM. We choose a chain length $N_\mathrm{C} \leq 10$ to be able to treat the spectrum of the Wilson chain exactly and calculate TD-NEVs and ESFs. Truncation of high-energy states is covered in Chap. 6.

The TD-NEVs are investigated by calculating the impurity occupation number $\langle n_\mathrm{d}(t)\rangle$ according to Eq. (4.3.40). Firstly, two separate CWCs are constructed parallely. The first chain is constructed for the initial parameter $\epsilon_\mathrm{d} = \epsilon_\mathrm{d}^\mathrm{i}$ to generate the initial density matrix. For the second one we choose the parameter $\epsilon_\mathrm{d} = \epsilon_\mathrm{d}^\mathrm{f}$ to obtain the eigenbasis of the final Hamiltonian. With these elements we are able to simulate a sudden quench at $t = 0$. In all cases, we choose $\epsilon_\mathrm{d}^\mathrm{f} = -\epsilon_\mathrm{d}^\mathrm{i} > 0$, to obtain a symmetrical relaxation process from the impurity site into the bath in the sense that $\langle n_\mathrm{d}(0)\rangle - 0.5 = 0.5 - \langle n_\mathrm{d}(t \to \infty)\rangle > 0$.

The ESF $A_\mathrm{d}(\omega)$ is calculated via Eq. (4.4.53) and only one CWC is necessary. Here $\epsilon_\mathrm{d} = 0$ is chosen, since this value corresponds to a symmetrical spectrum around $\omega = 0$.

The CWCs are constructed iteratively in the spirit of the NRG, even though no truncation of eigenstates is applied. At each iteration n we calculate the respective reservoirs $\Gamma_n^{\mathrm{H/L}}(\omega)$ and from here on the correlation functions $C_n(\omega)$ according to Eq. (4.3.35). After completion of all iterations $n < N_\mathrm{C}$, the BRT is constructed for all sites of the Wilson chain and then diagonalized exactly by exploiting its block-diagonality with respect to the system energy differences (see Eq. (4.5.56)). The construction of the BRT can be parallelized for each chain site and the diagonalization is parallelized for each block. This way the program is almost entirely parallelized, and we have used a maximum of 12 threads.

We have chosen a logarithmic frequency mesh in accordance with the logarithmic discretization procedure of the CWC formalism. This ensures an adequate resolution of the different energy scales of the Wilson chain. We choose a symmetric energy mesh with

$$\omega_i = 2D \left(\omega_{N_\mathrm{C}-1}\delta/(2D)\right)^{2i/N_\mathrm{m}}, i \in [0, N_\mathrm{m}/2] \tag{5.4.56}$$

for the positive half of the spectrum. Here D is the bandwidth, $\omega_{N_\mathrm{C}-1}$ is the NRG-scale at the last chain iteration and δ is the relative maximum resolution of the mesh. We have chosen $\delta = 5 \cdot 10^{-4}$.

To construct the BRT of the m-th chain site, the particular correlation function needs to be evaluated at specific system energy differences ω_{ab}. Since the energy mesh of $C_m(\omega)$ is fixed, the values $C_m(\omega_{ab})$ are evaluated via a linear interpolation between the mesh points. This approximative step does not impair the results in any significant way, however, it takes up most of the runtime. The number of mesh points N_m is thus not only a marker for the numerical accuracy of the BRT, but also for the runtime of the program. We have chosen $N_\mathrm{m} = 10^3$ in all cases to obtain a sufficient resolution of the correlation functions for all iterations n. To justify our choice of the mesh for the correlation functions, let us briefly discuss the drawbacks of alternative construction schemes.

One option is to collect all eigenenergy differences ω_{ab} of the complete CWC Hamiltonian, before calculating the reservoirs. These energy differences are ordered and used to construct the mesh for the reservoirs. This way we do not evaluate the reservoirs for continuous energies ω, but for discrete indices a, b. Hence no interpolation is necessary and the construction time of the BRT would be decreased significantly. Here the number N_m of mesh points is not necessarily equal to the quadratic number N_S^2 of CWC eigenenergies, since several energies ω_{ab} can be degenerate. In fact, N_m is here equal to the number of blocks of the BRT. However, if the chain length is large, the number of necessary mesh points by far exceeds $N_\mathrm{m} = 10^3$ and this likely also counts in the case of a truncated eigenbasis of the Wilson chain. Even though the construction time of the BRT is now decreased, the construction time of the reservoirs and their respective RGFs is significantly increased. Since the CFE algorithm is iterative (see Sec. 5.1), no parallelization with respect to the iteration n is possible here. Furthermore, the numerical stability of integrating over these specific meshes is uncertain and needed a more careful investigation.

A second option is to exploit the steady-state of the correlation functions $C_n(\omega)$ (see

Sec. 5.2). At a certain effective temperature $T_{n_{\mathrm{SS}}} \approx 0.1D$, which depends on the chain length N_{C} and the discretization parameter Λ, an even-odd steady-state of $C_n(\omega)$ is reached (see Sec. 5.3.3). From here on, the correlation functions are simply scaled by a factor of Λ on both axes for each increment of 2 of the iteration number n, meaning that

$$C_{n+2}(\omega) = C_n(\omega\Lambda)/\Lambda \tag{5.4.57}$$

for $n \geq n_{\mathrm{SS}}$. Thus, by rescaling the BRT of chain site n and the respective eigenenergies ω_{ab} by a factor of $\sqrt{\Lambda}^{n-n_{\mathrm{SS}}}$, the correlation functions $C_{n_{\mathrm{SS}}}(\omega)$ and $C_{n_{\mathrm{SS}}+1}(\omega)$ could be reused for all consecutive chain sites and N_{m} could be kept relatively low. However, in order to use this scheme, we require effective temperatures of the Wilson chain well below $0.1D$. Also, the logarithmic discretization of Eq. (5.4.56) is so well-adapted to the energy spectrum of a Wilson chain, that the number of required mesh points is almost independent of the effective temperature. For that reason, we discarded the two alternative mesh schemes and accept the linear interpolation.

Besides the construction of the BRT, the second bottleneck of the program is the diagonalization of the BRT and the construction of physical quantities. The block-diagonality of the BRT with respect to the system eigenenergy differences ω_{ab} allows for a second parallelization. The diagonalization within these "energy-subspaces" is exact. Since we choose $N_{\mathrm{m}} = 10^3$, the diagonalization of the BRT takes up a similar amount of time as its construction. Thus, a reduction of N_{m} could in the best case reduce the total program runtime by around 50%. The energy-subspaces of the BRT are highly inhomogeneous in dimension, with the subspaces for $\omega_{ab} \approx 0$ being the by far largest ones. The question, when to interpret two energy differences ω_{ab} and ω_{cd} as degenerate and thus, when to assign them to the same subspace, influences the size of the blocks of the BRT. However, if energies are interpreted as degenerate for $\Delta \leq \omega_n \cdot 10^{-5}$, the results are practically converged to the $\Delta = 0$ version[5]. The largest blocks of the BRT could be diagonalized numerically to accelerate the program. A Lanczos method would be appropriate here, since it significantly reduces the number of eigenstates to the low-energy ones, which are most relevant for the long-time behavior of the time-dependent density matrix and thus for the relaxation. A concrete implementation of the Lanczos method for the diagonalization of sub-blocks of the BRT is described in Sec. 6.1.8. For the construction of the χ-operator, which is required for ESFs, the $\omega_{ab} = 0$ subspace

---

[5] For details on Δ and the closely linked secular approximation see Sec. 5.3.4

is not included in the BRT, since $\chi_{aa} = 0$. This decreases the CPU time required for the diagonalization.

For the following results of the OCF we have chosen $N_\mathrm{m} = 10^3$, $\epsilon_\mathrm{d}^\mathrm{f} \equiv \epsilon_\mathrm{d} = -\Gamma$, $D = 100\Gamma$, $N_\mathrm{C} = 10$ and $\Lambda = 2$, if not stated otherwise. The dimensionless inverse temperature $\overline{\beta}$ is adapted to always guarantee $T = \Gamma$. A black dashed line, added to the figure, in any case represents the analytical exact solution for the RLM (see App. A), both for TD-NEVs and ESFs.

As mentioned above, we restrict to the two-level problem with an impurity Hamiltonian

$$H_\mathrm{imp} = \epsilon_\mathrm{d} d^\dagger d \tag{5.4.58}$$

coupled to a closed and open Wilson chain, respectively. In the thermodynamic limit this resembles the RLM. Since its exact solution is known analytically, it serves as the perfect toy model to benchmark the OWC results.

5.4.1. Non-Equilibrium Real-Time Dynamics

We investigate the impurity occupation number

$$\begin{aligned} n_\mathrm{d}(t) &= \mathrm{Tr}\Big\{ e^{iH_\mathrm{S}t} n_\mathrm{d} e^{-iH_\mathrm{S}t} \rho_\mathrm{S}^\mathrm{I}(t) \Big\} \\ &= \sum_{ab} \sum_{l} (n_\mathrm{d})_{ab}\, c_l\, (|v_l\rangle)_{ba}\, e^{i\omega_{ab}t - \lambda_l t} \\ &= \sum_{f,l} X_{f,l}\, e^{i\omega_{l,f}t - \mathfrak{Re}\lambda_l t}. \end{aligned} \tag{5.4.1.59}$$

with $X_{l,f} = \sum_{ab}^{\omega_{ab}=\omega_f} (n_\mathrm{d})_{ab} c_l (|v_l\rangle)_{ba}$ and $\omega_{l,f} = \omega_f - \mathfrak{Im}\lambda_l$ (see Eq. (4.3.40)). The CWC solution is obtained by setting the eigenvalues λ_l of the BRT to zero. The CWC solution accounts for a correct short-time behavior by the oscillation frequencies ω_f, while those oscillations stay coherent on longer timescales and thus yield charge reflections back to the impurity site. The real-part of λ_l generates a relaxation of these oscillations, while $\lambda_0 = 0$ of the $\omega_f = 0$ subspace accounts for the long-time steady-state. For that reason, we refer to $\mathfrak{Re}\lambda_l$ as the relaxation rates. The Lamb-shift $\mathfrak{Im}\lambda_l$, on the other hand, adds slow oscillations to the ODDM.

In Fig. 5.16 the impurity occupation is displayed for chain length $N_\mathrm{C} \in [0, 10]$. Here $N_\mathrm{C} = 0$ accounts for the system being reduced to the bare impurity, while $N_\mathrm{C} = 1$ adds the zeroth Wilson chain site to the system Hamiltonian. With increasing chain length

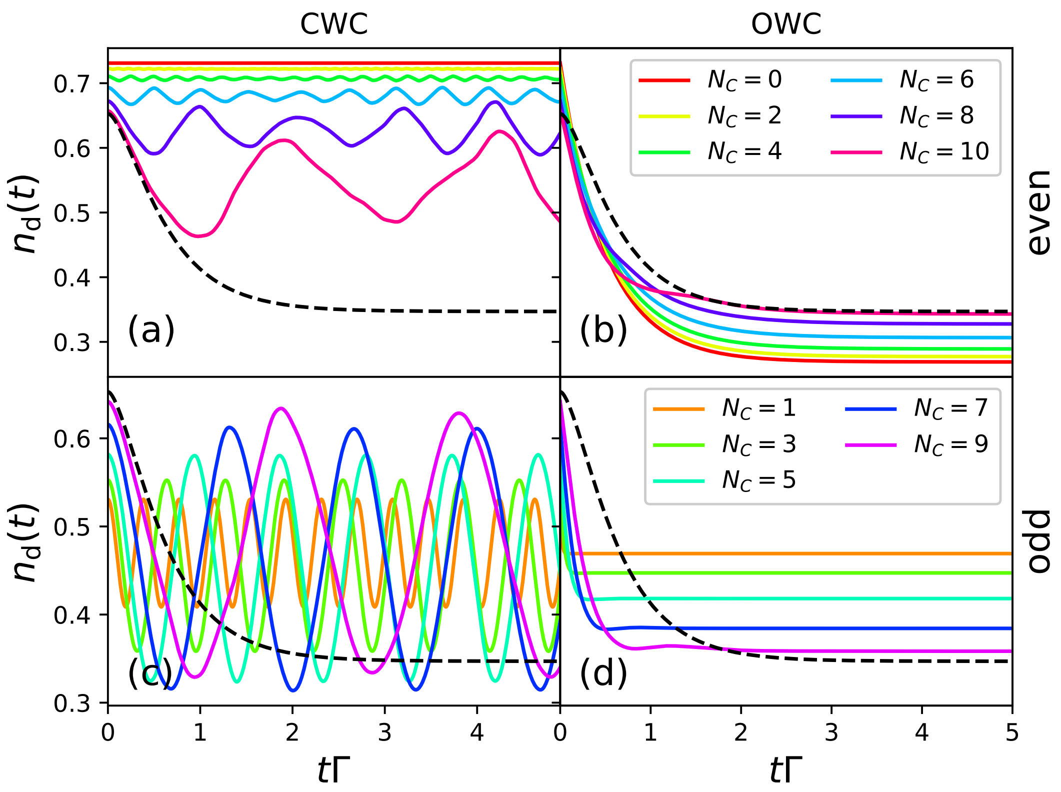

Figure 5.16.: Impurity occupation $n_\mathrm{d}(t)$ for various chain lengths N_C. Even chain lengths are depicted in the upper panels (a) and (b) while odd chain-lengths appear in the lower panels (c) and (d). On the r.h.s. in panels (b) and (d) we present the OWC solutions, on the l.h.s. in (a) and (c) only the CWC is displayed.

H_S grows, and thus the BA is improved. This translates to improved equilibrium values $n_\mathrm{d}(t = 0)$, both for the CWC (depicted on the left) and the OWC (on the right). The steady-state $n_\mathrm{d}(t \to \infty) = 1 - n_\mathrm{d}(t = 0)$ is reached with a deviation of 0.1%, which solely stems from numerical inaccuracy by choosing $N_\mathrm{m} = 10^3$. This shows that the OWC curves relaxate to the equilibrium value predicted by the CWC.

An interesting feature of Fig. 5.16 is the difference between even and odd chain lengths. The equilibrium values $n_\mathrm{d}(t = 0)$ approach the exact solution (black dashed line) from below (even N_C) and above (odd N_C), respectively. This suggests that the even-odd behavior is incorporated in the energy spectrum of the Wilson chain and that it converges for long chains. Indeed, it is a well-known fact, that the spectrum of the Wilson chain exhibits an even-odd behavior. Since in the CWC the particle number is conserved, the one-particle subspace is sufficient to understand this effect.

The one-particle contribution to the equilibrium occupation number is

$$n_{\mathrm{d}}^{1} = (Z)^{-1} \langle 1,0,0,...| \, e^{-\beta H} \, |1,0,0,...\rangle \, . \tag{5.4.1.60}$$

In the Wilson chain the hopping parameters $t_0, t_1, ...$ are defined by the bandwidth D, while the local impurity energy shall be $|\epsilon_{\mathrm{d}}| \ll D$. For odd chain lengths the spectrum is almost symmetrical around the Fermi level, while for even chain lengths a small eigenvalue $E_0 \approx \epsilon_{\mathrm{d}}$ is always present. The corresponding eigenstate has a strong overlap with the one-particle impurity state and so E_0 always has the dominant contribution to the equilibrium value of the impurity occupation. Since for short chains E_0 is much smaller in absolute value than the smallest eigenenergies of odd chains, $n_{\mathrm{d}}(t=0)$ always deviates more from half-filling for even chains. With increasing chain length the logarithmically decreasing Wilson chain parameters t_n split up the eigenspectrum for small energies and thus decrease the even-odd effect.

The closed chain real-time dynamics

$$n_{\mathrm{d}}^{1}(t) = (Z^{\mathrm{i}})^{-1} \langle 1,0,0,...| \, e^{-iH^{\mathrm{f}}t} e^{-\beta H^{\mathrm{i}}} e^{iH^{\mathrm{f}}t} \, |1,0,0,...\rangle \tag{5.4.1.61}$$

for the one-particle subspace can be explained in a similar manner[6]. For $N_{\mathrm{C}} = 0$ the impurity is isolated and so no transitions are possible. For even chain lengths $N_{\mathrm{C}} > 0$ the eigenenergy E_0 still has the dominant contribution to the state where the impurity level is occupied. Here, the oscillation frequency is $\omega_f = E_0 - E_0 = 0$. Oscillating terms are added with a small amplitude and this effect increases with the chain length. The $N_{\mathrm{C}} = 1$ case describes a simple oscillation between the impurity and the zeroth Wilson chain site with a frequency $\Omega \approx 2V$. With increasing chain length the eigenenergies closest to the Fermi-level shrink, and thus the oscillation amplitude is decreased. In any case, the even and odd chains slowly converge to each other with increasing chain length. The convergence can be accelerated by choosing a higher Λ, which ensures that the small energies converge to each other faster.

To explain the behavior of $n_{\mathrm{d}}(t)$ in the OWC, a different argumentation is required. The initial equilibrium value is reached by definition for $t = 0$, while the final steady-state is always reached by construction (see Sec. 4.5). At temperatures $T = \Gamma$, the Lamb-shift is much smaller than the relaxation rates. Hence, the slow oscillations it generates are already damped by $\mathfrak{Re}\lambda_l$ before they can contribute to the dynamics. Thus, the difference between even and odd chains lies in the dominant relaxation

---

[6] Note, that we quench the Hamiltonian at $t = 0$ from the initial one H^{i} to the final one H^{f}.

rates. For each chain the eigenvalue $\lambda_l = 0$ of the energy subspace with $\omega_f = 0$ has an important contribution as it defines the steady-state. Even chains always have a real eigenvalue $\lambda_l \approx 2\Gamma$ with a large weight c_l. The eigenvalues with largest weight for odd chains are (besides $\lambda_l = 0$) a complex conjugate pair z, z^* with $\mathfrak{Re} z \gg \mathfrak{Im} z$ and $\mathfrak{Re} z \gg 2\Gamma$. With increasing chainlength, even and odd chains align.

Let us explicitly cover the relevant dynamics of the first OWC curves of Fig. 5.16 for $-\epsilon_{\mathrm{d}}^{\mathrm{f}} = \Gamma \ll D$. In the $N_{\mathrm{C}} = 0$ case we observe a simple exponential decay with a relaxation rate $\gamma = 2\Gamma_{-1}(\epsilon_{\mathrm{d}}^{\mathrm{f}}) = 2\Gamma$, i.e. the reservoir evaluated at the lowest local one-particle energy $\epsilon_{\mathrm{d}}^{\mathrm{f}}$. If we proceed to $N_{\mathrm{C}} = 1$ the dynamics is $\propto \cos(2Vt)e^{-\gamma t}$. Since $\gamma = \Gamma_0(V) \approx \frac{2}{\pi} D \gg 2V$, the oscillating term is almost immediately damped by the decay term and so no oscillations can be observed in the figure. Note, that the $\cos(2Vt)$ term resembles the oscillations that occur within the CWC one-particle subspace. The relaxation rate γ is, once again, given by the reservoir coupling function at the lowest one-particle energy. If the chain length is increased then the dominant relaxation rate γ is basically defined by the last reservoir $\Gamma_{N_{\mathrm{C}}-1}(\omega)$ of the chain at $\omega \approx 0$. Since the reservoirs shrink with the iteration n, the relaxation rate of odd chains decreases further. However, with increasing chain length an eigenvalue emerges in the $\omega_f = 0$ subspace that converges to 2Γ from above and thus becomes the dominant rate of the relaxation. Even chains possess this eigenvalue of 2Γ for all chain lengths and thus exhibit the correct relaxation rate even for short chains.

To illustrate these findings, we have plotted the single contributions to the occupation number $n_{\mathrm{d}}(t)$ in Eq. (5.4.1.59) in Fig. 5.17. We represent ω_f as blue points, $\mathfrak{Re}\lambda_l$ as orange crosses and $\mathfrak{Im}\lambda_l$ as green stars. The specific energy value of these components is plotted on the horizontal axis, while their respective weight $|X_{f,l}|$ in the expression for $n_{\mathrm{d}}(t)$ is plotted on the vertical axis. While the $\mathfrak{Re}\lambda_l$ are semi-positive, ω_f and $\mathfrak{Im}\lambda_l$ are located symmetrically around $\omega = 0$. To avoid redundancy, most negative energies are cut off on the horizontal axis. The value ω_f is associated with $\sum_l |X_{f,l}|$ and the values $\mathfrak{Re}\lambda_l$ and $\mathfrak{Im}\lambda_l$ with $\sum_f |X_{f,l}|$. This way, Fig. 5.17 gives an overview over the most important relaxation rates and oscillation frequencies of the RLM for short OWCs. In turn, these elements explain the resulting non-equilibrium curves of Fig. 5.16.

The symbols at the upper left of each panel represent the steady-state of the occupation number for $\lambda_l = 0$. The height of each symbol is proportional to its importance in the expression. Consequently, the second most important eigenvalue of the BRT has a large real-part for odd chains that constantly shrinks with increasing chain length

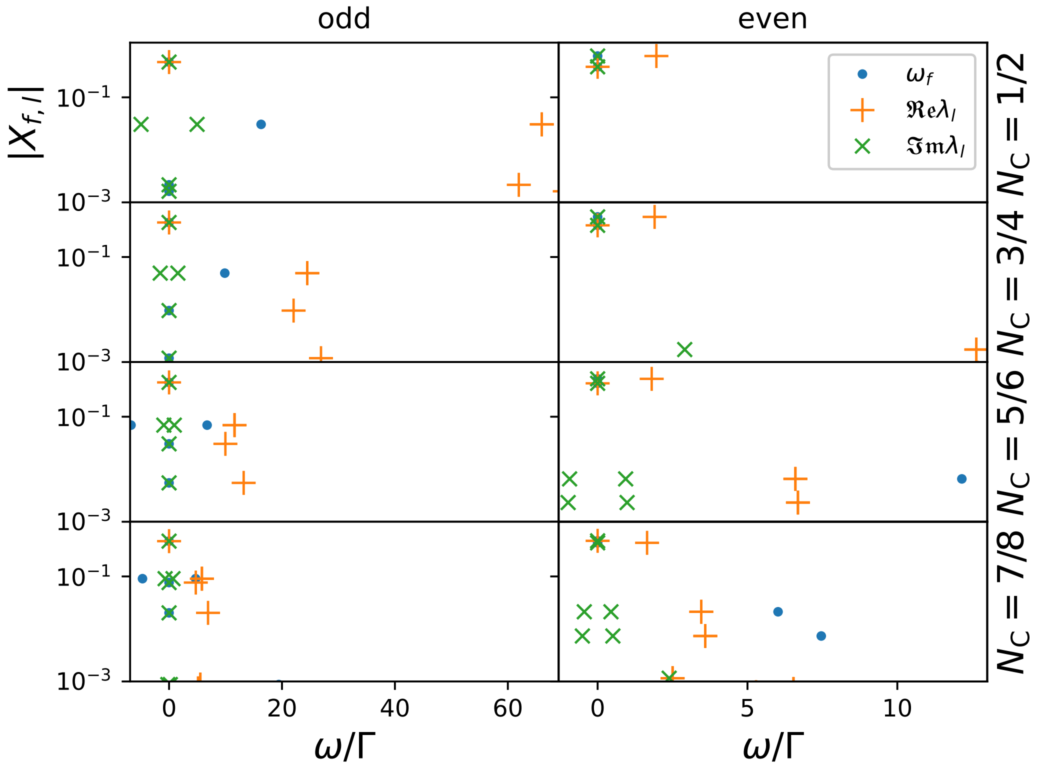

Figure 5.17.: A display of the single components of Eq. (5.4.1.59) for different chain lengths N_C. ω_f (blue points), $\mathfrak{Re}\lambda_l$ (orange crosses) and $\mathfrak{Im}\lambda_l$ (green stars) are plotted on the x-axis in units of Γ and their respective weight $|X_{f,l}|$ on the y-axis. Odd chains are plotted on the l.h.s., starting with $N_\mathrm{C} = 1$ at the top and even chains starting with $N_\mathrm{C} = 2$. Both axes are scaled by Γ.

(see the orange crosses in the l.h.s. panels). On the other hand, smaller eigenvalues gain importance with N_C and eventually converge to 2Γ. For even chains this eigenvalue is present for all chain lengths (single upper orange crosses in the r.h.s. panels). The imaginary-part of the eigenvalues (green stars) is always way below its respective real-part and thus the Lamb-shift induces slow oscillations, which are damped almost immediately. The blue points represent the influence of the CWC. As long as $\omega_f \ll \mathfrak{Re}\lambda_l$, the CWC oscillations are damped by the relaxation rates. For longer chains, however, the influence of those oscillations in the occupation number grows in their absolute values as well as their weight relative to the relaxation rates. For that reason, the damping of the CWC oscillations happens later in time for longer chains and the influence of the CWC on the short-time dynamics grows, which explains the

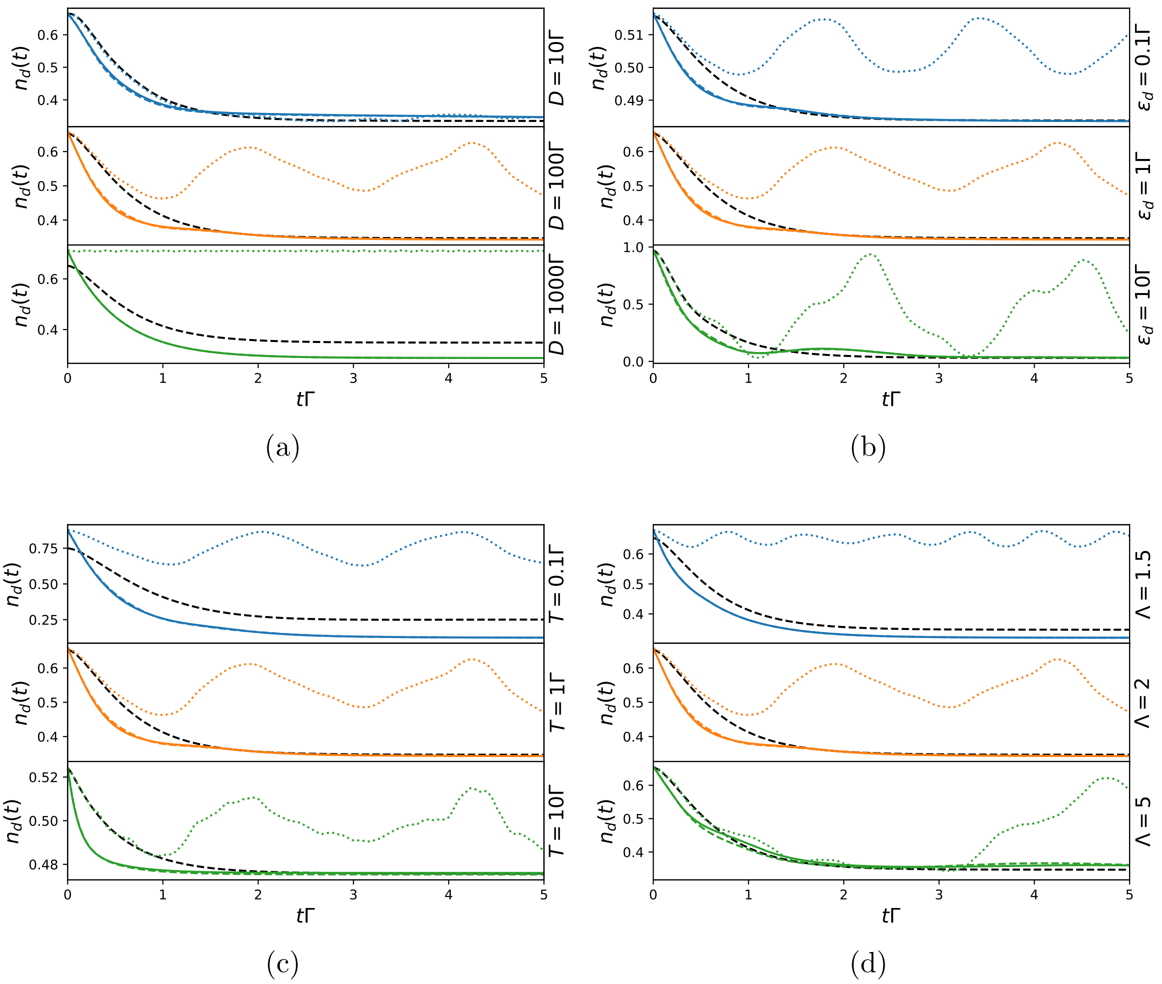

(a) (b)

(c) (d)

Figure 5.18.: Impurity occupation $n_\mathrm{d}(t)$ for chain length $N_\mathrm{C} = 10$. In each panel a different parameter is varied. We have varied (a) the bandwidth D, (b) the impurity level ϵ_d, (c) the temperature T and (d) the discretization parameter Λ. In all panels, except for (c), the temperature is chosen to be $T = \Gamma$. In all case, $\overline{\beta}$ has been adjusted to reach the desired temperature. The OWC is depicted as a solid line, the CWC as dotted. The OWC without the Lamb-shift is presented as a dashed line and the analytical solution according to App. A.2 is added as a black dashed line.

"bumps" in the r.h.s. panels of Fig. 5.16 for longer chains. Since the CWC is known to yield the exact short-time dynamics increasingly well with longer chains, those unphysical bumps are expected to converge to the exact dynamics with increasing N_C. This will be investigated in Chap. 6, since truncation of the high-energy states is required to calculate chains with $N_\mathrm{C} \gg 10$.

In Fig. 5.18 the OWC with (solid lines) and without (dashed lines) Lamb-shift is compared to the CWC (dotted lines) in different parameter regimes for a chain length of $N_\mathrm{C} = 10$. Obviously, the effect of the Lamb-shift is small. Only by increasing Λ a significant influence of the Lamb-shift can be observed. As predicted in Sec. 4.6, increasing the local parameter ϵ_d improves the MA, while increasing the temperature T improves the BA.

5.4.2. Equilibrium Spectral Functions

In analogy to Sec. 5.4.1, we start by defining the TD-EGF

$$\begin{aligned} G_\mathrm{d}(t) &= -i\Theta(t)\mathrm{Tr}\{\rho[d(t), d^\dagger]_s\} \\ &= \sum_{f,l} Y_{l,f} e^{i\omega_{l,f}t - \mathfrak{Re}\lambda_l t} \end{aligned} \tag{5.4.2.62}$$

of the impurity in the time domain (for details on the definitions see Sec. 4.4). The GF in the frequency domain is obtained via a half-sided Fourier transform

$$\begin{aligned} G_\mathrm{d}(\omega + i0^+) &= \int_0^\infty dt \sum_{f,l} Y_{l,f} e^{i(\omega+\omega_{l,f})t - \mathfrak{Re}\lambda_l t} \\ &= \sum_{f,l} \frac{Y_{l,f}}{\omega + \omega_{l,f} + i\mathfrak{Re}\lambda_l} \end{aligned} \tag{5.4.2.63}$$

slightly above the real axis in the complex plain. The ESF of the impurity follows as

$$\begin{aligned} A_\mathrm{d}(\omega) &= -\frac{1}{\pi}\mathfrak{Im}G_\mathrm{d}(\omega + i0^+) \\ &= \frac{1}{\pi}\sum_{f,l} \frac{\mathfrak{Re}\lambda_l\,\mathfrak{Re}Y_{l,f} - (\omega + \omega_{l,f})\,\mathfrak{Im}Y_{l,f}}{(\omega + \omega_{l,f})^2 + (\mathfrak{Re}\lambda_l)^2}. \end{aligned} \tag{5.4.2.64}$$

The CWC solution can be obtained by $\lambda_l \to 0$. Since the CWC spectrum naturally consists of delta-peaks, it is artificially broadened by a logarithmic Gaussian and, for small ω, by a Lorentzian. Details on this broadening scheme can be found in Sec. 3.8. A broadening of the ESF peaks relates to a damping in the time domain. Consequently, a small/large relaxation rate of the OWC translates to a narrow/wide broadening of the spectrum peaks.

An initial value $G_\mathrm{d}(t = 0) = 1$ corresponds to the sum-rule of the ESF and should always be fulfilled. In fact, this value is a simple way to assess the correctness and the

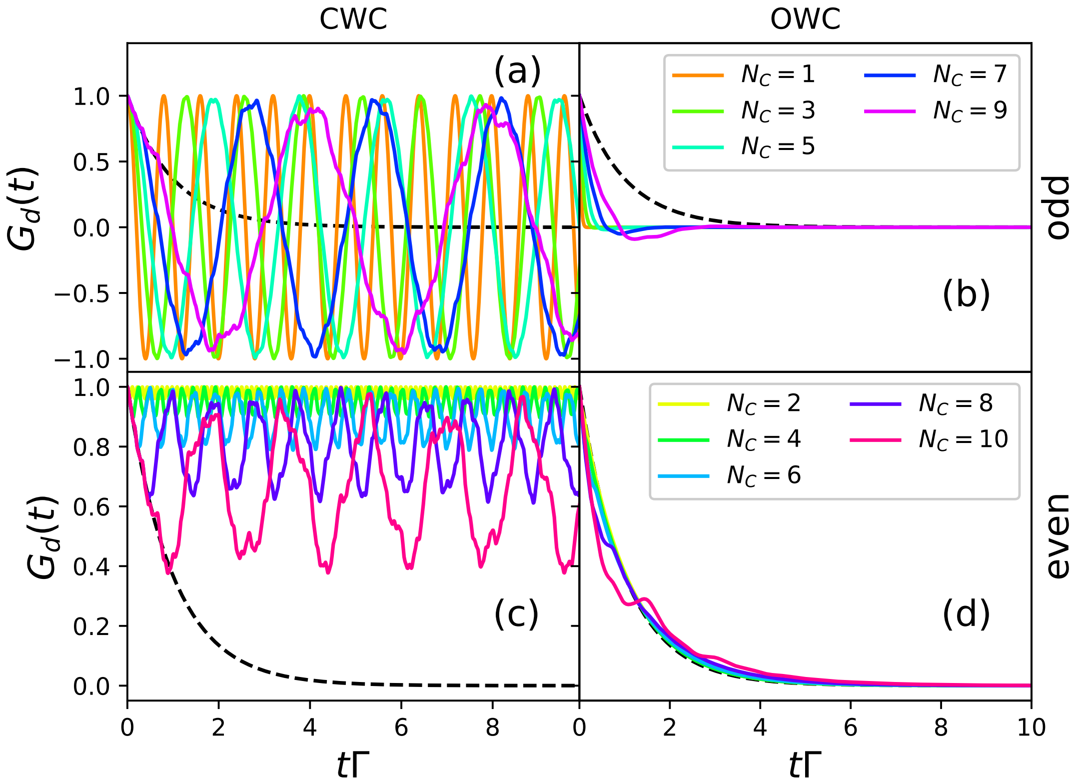

Figure 5.19.: The time-dependent retarded Green's function $G_\mathrm{d}(t)$, calculated via (5.4.2.62), versus dimensionless time $t\Gamma$ for the CWC (left panels (a) and (c)) and the OWC (right panels (b) and (d)). The analytical solution $e^{-\Gamma t}$ is added as black dashed lines for comparison.

numerical accuracy of the method.

In the case of the RLM and a constant DOS, $G_\mathrm{d}(t)$ resembles a simple exponential decay with rate Γ, while the corresponding ESF is a Lorentzian of width Γ (see App. A.1). This once again makes the RLM the perfect foundation to benchmark the OCF before proceeding to non-trivial models in Chap. 7.

We begin by choosing a discretization parameter of $\Lambda = 2$ and a bandwidth of $D = 100\Gamma$, as already done in the previous section. The chain length is varied and the temperature is in all cases adapted to be $T = \Gamma$. We choose an impurity energy at the Fermi-level to obtain a symmetrical spectral function around $\omega = 0$.

In Fig. 5.19 the TD-EGF $G_\mathrm{d}(t)$ is plotted to compare the CWC and the OWC. Firstly, $G_\mathrm{d}(t = 0) = 1$ is always fulfilled, which is clear in view of the fact, that it is solely defined by the closed chain and no numerical approximation has been performed here. Secondly, the CWC resembles the analytical solution for short times well, while it then exhibits periodic revival oscillations and does not approach a steady-state. The OWC solution, on the other hand, relaxates to its steady-state. Here the even-odd behavior resembles the non-equilibrium dynamics of Fig. 5.16 for similar reasons. The steady-state $G_{\mathrm{d}}(t \to \infty) = 0$ is guaranteed by the fact, that $\chi_{aa} = 0$, and so the corresponding BRT does not include the $\omega_f = 0$ sub-space. However, this subspace is the only one that includes the $\lambda_l = 0$ eigenvalue responsible for a finite steady-state of the system. Thus, all eigenvalues of the BRT occur in complex conjugate pairs with $\mathfrak{Re}\lambda_l > 0$ and lead to a complete dissipation of $\chi(t)$. The "bumps" around $t \approx \Gamma$ in the OWC solution stem from the influence of the CWC, which becomes dominant on short time scales if the chain length is increased. This effect has been well covered in Sec. 5.4.1. The corresponding spectral functions could be obtained by a numerical Fourier transformation. However, we analytically calculate them from the parameters $Y_{l,f}, \omega_f$ and λ_l as in Eq. (5.4.2.64).

In Fig. 5.20 the spectral functions are plotted in an analog manner to Fig. 5.19. The dominance of the one-particle energies $\approx \pm V$ in the even chains is depicted as the two peaks in the upper panels. Those peaks are expected to merge in the limit of long Wilson chains. The CWC shows a reverse behavior with increasing chain length. Here the dominant contribution to the ESF starts around the local energy level and then splits up into two peaks and thereby decreases the height of the resulting peak. However, in the limit of long Wilson chains the CWC is expected to yield good results for the spectral function. Similar to the non-equilibrium case in Sec. 5.4.1, the BRT contains the 2Γ-eigenvalue for all odd chain lengths, and thus the correct Lorentzian is obtained in each case. The "bumps" of Fig. 5.19 translate to small oscillations at the sides of the Lorentzian. However, with increasing chain length, the CWC solution of $G_{\mathrm{d}}(t)$ is valid for increasingly longer time scales, which is the same effect as seen in $n_{\mathrm{d}}(t)$. Under this aspect, the unphysical oscillations are expected to vanish for longer chains, and the OWC is expected to converge to the correct solution. This will be further investigated in Sec. 6.2.

At low temperatures, the OWC solution of $\chi(t)$ exhibits an interesting behavior, i.e. the contribution of the dissipative part of the BRT shrinks, making it effectively diagonal. Since the off-diagonal elements of the BRT, i.e. the dissipative part, are proportional to Fermi functions and the Fermi function vanishes for positive energies, the BRT becomes a triangular matrix, if T is sufficiently small. Consequently, the dissipative part has no influence on the eigenspectrum of the BRT. In fact, those elements have no impact on $\chi(t)$ at all. This can be understood by examining the

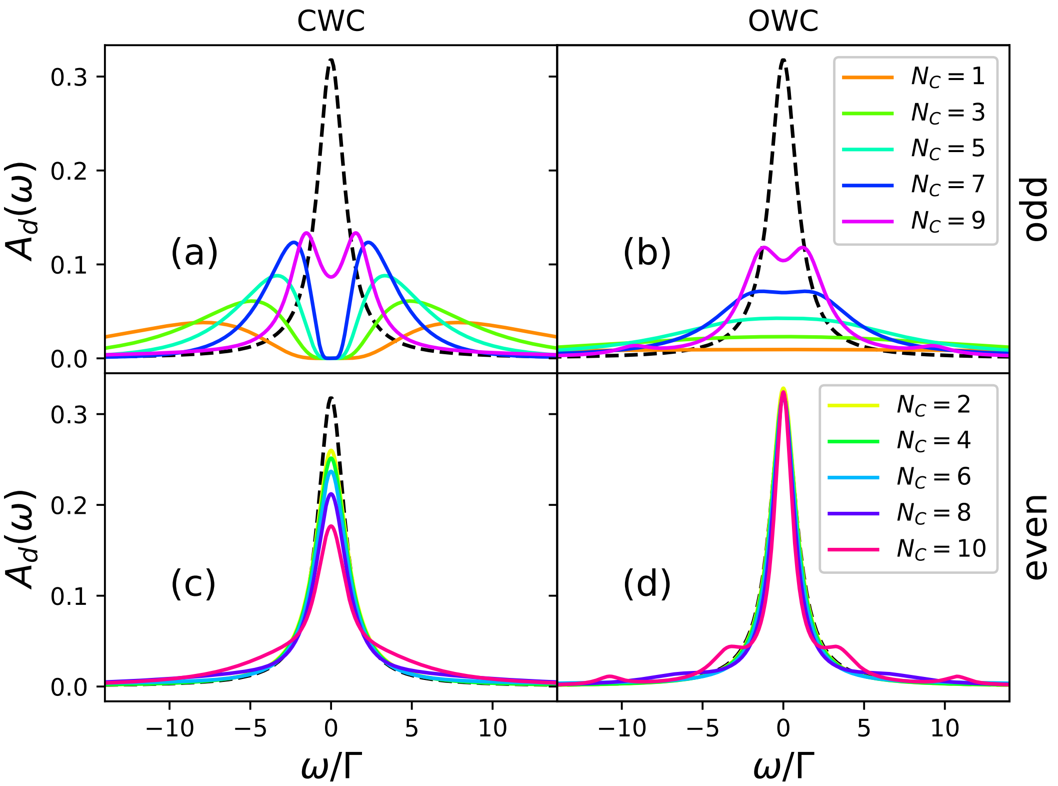

Figure 5.20.: The spectral functions $A_\mathrm{d}(\omega)$, calculated via (5.4.2.64), versus dimensionless energy ω/Γ for the CWC (left panels (a) and (c)) and the OWC (right panels (b) and (d)). The analytical solution is added as black dashed lines for comparison. The CWC curves are broadened with a logarithmic Gaussian factor of $b = 0.8$ and we choose a bandwidth of $D = 100\Gamma$.

operator $\chi(0)$. In the untruncated system eigenbasis we obtain

$$\chi_{mn}(0) = \langle m| \chi(0) |n\rangle = \frac{e^{-\beta E_m} + e^{-\beta E_n}}{Z} d^\dagger_{mn}. \tag{5.4.2.65}$$

If both eigenenergies $E_m, E_n > 0$, the expression vanishes for $T \to 0$. In general, $\chi_{mn}(0)$ is damped quickly, if the energies are relatively large. Let us define the equation

$$O_{ab} = \sum_{mn} R_{ab,mn} P_{mn} \tag{5.4.2.66}$$

in the system eigenbasis, with O and P being arbitrary local operators and R being the BRT. To examine the off-diagonal elements, consider $a \neq m$ and $b \neq n$, i.e. the BRT is equal to the dissipative part, which is $\propto \delta_{E_a - E_b, E_m - E_n} f_\beta(E_a - E_m)$ (see Eq.

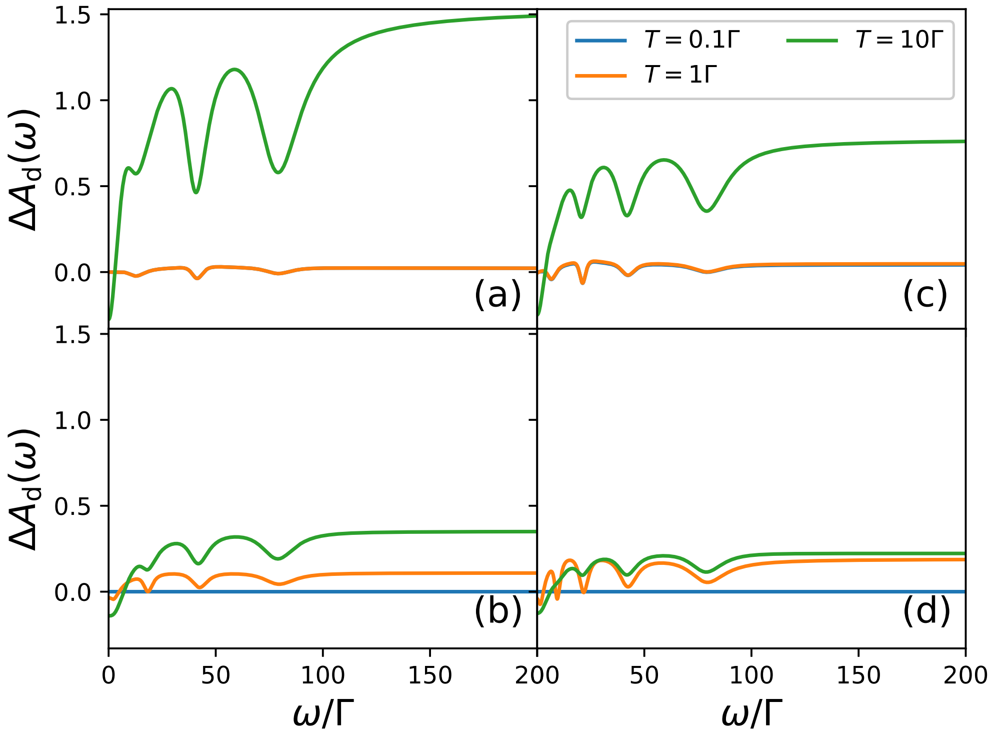

Figure 5.21.: Relative (and thus dimensionless) difference $\Delta A_{\rm d}(\omega)$ of the OWC ESF with and without the dissipative part for different temperatures T. The chain lengths are chosen as (a) $N_{\rm C} = 6$, (b) $N_{\rm C} = 7$, (c) $N_{\rm C} = 8$ and (d) $N_{\rm C} = 9$.

(4.5.57)). These elements are non-zero, iff $E_a - E_m = E_b - E_n \leq 0$, which means, that the indices m and n are associated with relatively large eigenenergies. If we choose $P \equiv \chi(0)$, then the elements P_{mn} of large eigenvalues E_m, E_n are zero and the operator O is independent of the dissipative elements. As a consequence, the expression

$$|\chi(t)\rangle = e^{-Rt} |\chi(0)\rangle \,. \tag{5.4.2.67}$$

has no contribution of the dissipative elements.

Up to this point, the discussion has been rather intuitive. To prove the statement, that the dissipative part of the BRT can effectively be neglected for $T \to 0$, we have plotted the relative difference of the OWC ESF $A_{\rm d}(\omega)$ with and without the dissipative part of the BRT in Fig. 5.21. The inverse temperature $\overline{\beta}$ has been varied to set different temperatures T. Since the spectra are symmetric, we have restricted ourselves to the positive part of the spectrum. The differences decrease with lower temperature, as has been suggested above. For even chain length the diagonal version of the BRT becomes exact at $T \leq 0.1\Gamma$. For odd chains a small difference between the spectral functions remains. With increasing chain length, we expect the even-odd behavior to reduce and the influence of the dissipative part to decrease further for small temperatures.

With a diagonal BRT, the computation simplifies significantly. We can express the unitary, i.e. the diagonal, part of the BRT as $R_{ab,ab} = r_a + r_b^*$ (cf. Sec. 5.2). It is thus sufficient to construct and store the first order tensor $r_a = \sum_l \Gamma_{al,la}$. The GF can then be expressed as

$$G_{\mathrm{d}}(\omega) = \sum_{ab} \frac{d_{ab}\chi_{ba}(0)}{\omega + \omega_{ab} + i(r_a + r_b^*)}, \tag{5.4.2.68}$$

which represents a simplification of Eq. (5.4.2.63) by neglecting the dissipative part of the BRT. The diagonal elements $r_a + r_b^*$ of the BRT serve as direct broadening parameters for the CWC spectrum. In contrast to Eq. (5.4.2.63), we have changed the indices here. The index l can be dropped, since no diagonalization of the BRT is necessary and the index f is split up into a and b according to $\omega_{ab} = \omega_f$. The reduction to the diagonal part of the BRT renders a diagonalization obsolete. Furthermore, there is no requirement to construct a fourth order BRT, but instead the first order tensor r is sufficient. Thus the program complexity of the OWC reaches the orders of magnitude of the CWC. In this regime, the alternatives to optimize the construction of the RGFs mentioned at the beginning of this section are relevant.

5.5. Summary

We defined a CFE, that restores the continuum for a logarithmically discretized bath by iteratively coupling reservoirs to the Wilson chain, and thus constructing an OWC. To adapt the formalism to arbitrary discretization parameters $\Lambda \geq 1$, the low-energy reservoir at the end of the chain is at each iteration n divided into a high- and a low-energy part by a cut-off function with a cut-off frequency ω_n^{C}. The remaining OWC is then constructed from the low-energy reservoir. Since there are strict criteria for the cut-off function, its precise form does not significantly influence the RGFs and is effectively no DOF of the OWC. The OCF is adaptable to arbitrary bath DOS, where symmetric spectra are preferable to simplify the algorithm. To numerically calculate the reservoir coupling functions, which shrink exponentially with n, a logarithmic mesh needs to be chosen. The finite number of mesh points represents a source of numerical inaccuracy, however, with our chosen number of 10^3 mesh points, this inaccuracy is negligible.

The purpose of the extension of the system part by the Wilson chain, and thus the construction of the OWC, is to improve the BMA. As pointed out in Chap. 4, the BMA is based upon the assumption that the hybridization between the system and the bath is small with respect to the other parameters of the OQS. This criterion is now shifted to the hybridization between the single chain sites and the respective reservoirs. We have shown, that the system energies of the OWC are defined by the local impurity parameters, as well as the Wilson chain coupling parameters t_n. The bandwidth D only influences the coupling between the impurity and the OWC and has no direct effect on the BMA. The width of the reservoir coupling functions can be estimated by ω_n^{C}, and we have shown, that all parameters mentioned above are larger than the respective hybridization t'_n to the single reservoirs. In the limit of $\Lambda \to 1^+$, the t'_n's vanish and the BMA becomes exact.

The most significant error of the BMA is expected to occur for the first chain sites $n \ll N_{\mathrm{C}}$, which is due to the fact that the t'_n increase with n, if n is small, and only start to decrease for an effective Wilson chain temperature below $0.5D$. If Λ is small, n is required to be relatively large for the reservoir hybridization to be small. Nevertheless, the contribution of the first chain sites to the total BRT is increasingly small with decreasing effective temperature.

The reservoir coupling functions exhibit an even-odd behavior and a scaling of Λ between each iteration n and $n+2$. This behavior is already known from the level spectrum of the Wilson chain, which exhibits two distinct fixed points. An increase of Λ enhances the difference between even and odd iterations. For an effective temperature of $0.1D$, the steady-state of the RGFs is reached and thus the even-odd effect has effectively vanished.

The even-odd effect is also depicted in TD-NEVs, TD-EGFs and ESFs, respectively, for CWC and OWC curves alike. With increasing n these differences even out, and the solutions converge to the exact solution, in the limit of the BMA. The RLM has been examined for chain lengths $N_{\mathrm{C}} \leq 10$ to allow for an exact treatment without truncation of high-energy system eigenstates. This way, we can assume the impact of numerical errors on the solutions to be minimal.

In TD-NEVs the steady-states are in the BMA completely defined by the system eigenenergies. For increasing chain length the Wilson chain is known to reproduce these equilibrium values well. Additionally, the BRT provides a thermalization on the correct time scale for the RLM. The MSA restricts the time-evolution of the density matrix to exponential decay terms and thus a physically correct short-time behavior cannot be simulated by the BMA. However, we were able to show, that the CWC solution begins to dominate for short times, if the chain length is increased, which improves the OWC curves. In that context, the OWC in the BMA in second order seems to be an adequate approach for TD-NEVs.

The TD-EGFs show a similar behavior as the TD-NEVs. Short-time dynamics is governed by the CWC, while the reservoirs allow for a complete relaxation within few units of $1/\Gamma$. In contrast to TD-NEVs, the steady-states of the TD-EGFs are not influenced by the BMA, and are thus exact up to numerical precision. With increasing chain length N_C and discretization parameter Λ, unphysical oscillations appear due to the discretization error. These oscillations translate to bumps in the outer regions of the respective ESF. We expect the CWC TD-EGF short-time dynamics to improve for smaller Λ and thus the bumps in the OWC ESF results to be reduced.

For low temperatures, the dissipative part of the BRT appears to be negligible when calculating ESFs. A reduction of the BRT to the unitary part has the potential to spare a significant amount of runtime, making the OWC program runtime comparable to that of the CWC. This will be especially relevant for large Wilson chains, since here the effective system temperature is naturally lower, if all other parameters are fixed.

6. Hybrid NRG-BRF Approach

Up to this point we have restricted our investigations of closed and open Wilson chains for purely practical reasons to chain lengths $N_\mathrm{C} \leq 10$. The Hilbertspace of a Wilson chain grows exponentially by a factor of d with each additional chainsite. The local Hilberspace dimension $d = 2$ of the simple RLM is increased, if DOF such as spin or additional channels are included. This sets a rather tight limit to the application of a Wilson chain. Furthermore, dynamical quantities require long chains in order to avoid major finite-size effects to occur up to a certain point in time of interest. Long chains also allow for reaching exponentially small energy scales, and even the Kondo scale, without choosing a large Λ and, thereby, suffering significant discretization errors (see Sec. 3.10). For Wilson chains of length $N_\mathrm{C} \gg 10$ the NRG introduces a truncation scheme that discards certain states at each iteration to keep the Hibertspace constant. Thus, the complexity grows linearly with N_C, instead of exponentially. Initially, the NRG has only been applied to the equilibrium case (see e.g. Ref. [22]). Though, within the last 20 years significant progress has been made in applying the NRG to the calculation of non-equilibrium dynamics and spectral functions [29, 23, 24, 88]. The suitability of a truncation scheme for all of these cases is based on a simple fact. Since the construction of a Wilson chain implies a logarithmic discretization of the band, a wide range of energies is included in the system, spanning from the bandwidth D down to the effective temperature T_{N_C} of the Wilson chain of length N_C (see Eq. (3.5.28)). By increasing N_C, while keeping Λ fixed, T_{N_C} can be decreased quickly by orders of magnitude. Low-energy states $\beta(E - E_\mathrm{g}) < 1$ are favored by the Boltzmann-distribution. At $T \approx T_{N_\mathrm{C}}$, high-energy states with $E - E_\mathrm{g} \gg T_{N_\mathrm{C}}$ can reliably be neglected since the density matrix damps their contributions (see Sec. 3.3). This truncation scheme has already successfully been applied to an NRG hybrid approach (see Sec. 3.11). Our objective is to apply the NRG to the OWC to construct a hybrid system, which combines the properties of a true OQS with the versatility of the NRG.

Note that flavor DOF, such as spin or band indices, of local operators is omitted since it does not impact the following argumentation. Where necessary, the incorporation of

DOF is explicitly addressed.

6.1. Master Equation for the Truncated Wilson Chain

We start with the time-evolution of an arbitrary local operator

$$O_{\mathrm{S}}(t) = \mathrm{Tr}\Big\{ e^{-iH_{\mathrm{S}}t} \rho^{\mathrm{I}}_{\mathrm{S}}(t) e^{iH_{\mathrm{S}}t} O_{\mathrm{S}} \Big\}. \tag{6.1.1}$$

By choosing $\rho^{\mathrm{I}}_{\mathrm{S}}(t)$ as the reduced density matrix obtained by the BRF the limitations of the BMA are included in the system. The quality of the approach is then determined by the system Hamiltonian H_{S}. In Chap. 4 we have reduced H_{S} to the bare impurity. In Chap. 5 the local system has been enlarged to a relatively short Wilson chain, which already significantly improved the BMA. Consequently, Eq. (6.1.1) has been expressed in the complete basis

$$\mathbf{1} = \sum_r |r; N_{\mathrm{C}}\rangle \langle r; N_{\mathrm{C}}| \tag{6.1.2}$$

of a Wilson chain of length N_{C}. Here $|r; N_{\mathrm{C}}\rangle$ denotes an eigenstate of the CWC Hamiltonian and the sum runs over all of those eigenstates. In the context of the NRG, at iteration $n = n_{\mathrm{min}}$ the truncation scheme starts, i.e. all eigenstates are divided into a discarded set of high-energy states $|l; n_{\mathrm{min}}\rangle$ and a kept set of low-energy states $|k; n_{\mathrm{min}}\rangle$. With increasing NRG iteration n the number of possible configurations of charge on the Wilson chain grows. To account for that fact, an index e is added to the system state, which aggregates all EDOF of the rest chain $N_{\mathrm{C}} - n$. The state $|r, e; n\rangle$ is thus degenerate by a factor of $d^{N_{\mathrm{C}}-n}$ to be compatible to the states of higher iterations $> n$. The basis

$$\mathbf{1}_{n_{\mathrm{min}}} = \sum_{r,e} |r, e; n_{\mathrm{min}}\rangle \langle r, e; n_{\mathrm{min}}| \tag{6.1.3}$$

is still complete, if r includes all kept and discarded states on iteration n_{min}. By dividing the kept states $|k, e; n_{\mathrm{min}}\rangle$ into kept and discarded states on iteration $n_{\mathrm{min}} + 1$, a different set of basis states is obtained. By defining all states of the last iteration $n = N_{\mathrm{C}}$ to be discarded, we can write a complete set of eigenenergies in the context of a truncated Wilson chain as

$$\mathbf{1}_m = \sum_{n=n_{\min}}^{m} \sum_{l,e} |l,e;n\rangle \langle l,e;n| + \sum_{k,e} |k,e;m\rangle \langle k,e;m| \tag{6.1.4}$$

with $n_{\min} \leq m \leq N_{\mathrm{C}}$. The exact case without truncation is recovered for $n_{\min} = N_{\mathrm{C}}$. The time-evolution of a local operator O_{S} in the basis of the truncated chain is given by (cf. Eq. (3.9.55))

$$O_{\mathrm{S}}(t) = \sum_{n=n_{\min}}^{N_{\mathrm{C}}} \sum_{r,s \notin \{k,k'\}} \rho_{sr}^{\mathrm{red}}(n;t) O_{rs}^{n} e^{i(E_r^n - E_s^n)t}, \tag{6.1.5}$$

where

$$\begin{aligned} \rho_{sr}^{\mathrm{red}}(n;t) &\equiv \sum_{e} \langle s,e;n| \rho_{\mathrm{S}}^{\mathrm{I}}(t) |r,e;n\rangle \\ &= \sum_{\alpha,e} e^{-\lambda_\alpha t} c_\alpha \langle s,e;n| \rho_\alpha^{\mathrm{r}} |r,e;n\rangle . \end{aligned} \tag{6.1.6}$$

is the time-dependent density matrix, which is reduced both with respect to the trace Tr_{B} over the bath DOF and the sum over the rest chain environment e. The quantities λ_α are the eigenvalues, $\rho_\alpha^{\mathrm{r/l}}$ the r.h.s./l.h.s. eigenoperators of the BRT and $c_\alpha \equiv \mathrm{Tr}\left[\rho_\alpha^{\mathrm{l}} \rho_{\mathrm{S}}(t=0)\right]$. To obtain $\langle s,e;n| \rho_\alpha^{\mathrm{r}} |r,e;n\rangle$, the BRT has to be diagonalized in the complete eigenbasis $\mathbf{1}_n$ of the truncated Wilson chain. For that reason, we rewrite the BRT of Eq. (4.5.57) in the form

$$R_{12,34} = \delta_{13}\delta_{24} \sum_{5} \left(\Gamma_{15,51} + \Gamma_{25,52}^{*}\right) - 2\delta_{\omega_{12},\omega_{34}} \mathfrak{Re}\Gamma_{42,13} \tag{6.1.7}$$

with the damping tensor

$$\Gamma_{12,34} = \sum_{m=0}^{N_{\mathrm{C}}} C_{\mathrm{m,p}}(\omega_{34}) f_{m,12}^{\dagger} f_{m,34} + C_{\mathrm{m,h}}(\omega_{34}) f_{m,12} f_{m,34}^{\dagger}. \tag{6.1.8}$$

The numbers in the subscript are defined by $i \equiv |r_i, e_i; n_i\rangle$ and thus account for a kept or discarded state at iteration n_i. The sum over 5 needs to comprise the complete basis set $\mathbf{1}_n$. The master equation is consequently given by

$$\dot{\rho}_{12}(t) = -\sum_{34} R_{12,34}\rho_{34}(t), \tag{6.1.9}$$

where $\sum_{34}$ needs to comprise complete basis sets as well. For each element n of the sum over all truncated NRG iterations in Eq. (6.1.5) a basis set $\mathbf{1}_n$ needs to be chosen, that includes the kept states of iteration n and the discarded states of iterations m with $n_{\mathrm{min}} \leq m \leq n$.

In its most general form, the BRT $R_{12,34}$ may couple states of four independent NRG iterations. For $n = n_{\mathrm{min}}$ the BRT is self-contained on its iteration, while for $n = N_{\mathrm{C}}$ all iterations $\geq n_{\mathrm{min}}$ are coupled. To assess the dimension of such a tensor, let us first estimate the number of states of the complete basis set. Independent of the iteration n the total number of states that comprise the complete basis set $\mathbf{1}_n$ is around $N_{\mathrm{S}} d^{N_{\mathrm{C}}-n_{\mathrm{min}}}$. The definition of the EDOF e keeps this number constant over all iterations. Obviously, this number is equal to the number of states of the untruncated Wilson chain and is thus exponentially large. The TD-NRG overcomes this problem by reducing the sum over two complete basis sets in Eq. (6.1.5) to a sum over n and r, s. The EDOF are condensed in the reduced density matrix (see Eq. (3.9.56)). A similar strategy can be used in the master equation (6.1.9) to reduce it to

$$\dot{\rho}_{12}(t) = -\sum_{5}\left(\Gamma_{15,51} + \Gamma^{*}_{25,52}\right)\rho_{12}(t) + 2\sum_{n_3,n_4=n_{\mathrm{min}}}^{N_{\mathrm{C}}} \delta_{n_3,n_4} \sum_{r_3,r_4\notin\{k,k'\}} \delta_{\omega_{12},\omega_{34}} \sum_{e_3,e_4} \mathfrak{Re}\Gamma_{42,13}\rho_{34}(t). \tag{6.1.10}$$

While the unitary part immediately follows from the Kronecker-deltas in Eq. (6.1.7), the origin of the summation in the dissipative part is not so obvious. Let us for that reason explicitly show that

$$\sum_{34} \delta_{\omega_{12},\omega_{34}}\Gamma_{42,13}\rho_{34}(t) = \sum_{n_3,n_4=n_{\mathrm{min}}}^{N_{\mathrm{C}}} \delta_{n_3,n_4} \sum_{r_3,r_4\notin\{k,k'\}} \delta_{\omega_{12},\omega_{34}} \sum_{e_3,e_4} \Gamma_{42,13}\rho_{34}(t). \tag{6.1.11}$$

Firstly, we reverse the second MA and the secular approximation to obtain

$$\begin{aligned}
&\sum_{34} \delta_{\omega_{12},\omega_{34}} \Gamma_{42,13} \rho_{34}(t) \\
&\to \sum_{34} \sum_{m=0}^{N_{\mathrm{C}}} \int_0^t ds \Big[C_{\mathrm{m,p}}(s) \left\langle 4 \right| f_m^\dagger(t) \left| 2 \right\rangle \left\langle 1 \right| f_m(t-s) \left| 3 \right\rangle \\
&+ C_{\mathrm{m,h}}(s) \left\langle 4 \right| f_m(t) \left| 2 \right\rangle \left\langle 1 \right| f_m^\dagger(t-s) \left| 3 \right\rangle \Big] \left\langle 3 \right| \rho_{\mathrm{S}}^{\mathrm{I}}(t) \left| 4 \right\rangle \\
&= \int_0^t ds \sum_{34} \left\langle 4 \right| X_{12}(t,s) + Y_{12}(t,s) \left| 3 \right\rangle \left\langle 3 \right| \rho_{\mathrm{S}}^{\mathrm{I}}(t) \left| 4 \right\rangle \qquad (6.1.12)
\end{aligned}$$

with

$$\begin{aligned}
X_{12}(t,s) &\equiv \sum_{m=0}^{N_{\mathrm{C}}} C_{\mathrm{m,p}}(s) f_m^\dagger(t) \left| 2 \right\rangle \left\langle 1 \right| f_m(t-s) \\
Y_{12}(t,s) &\equiv \sum_{m=0}^{N_{\mathrm{C}}} C_{\mathrm{m,h}}(s) f_m(t) \left| 2 \right\rangle \left\langle 1 \right| f_m^\dagger(t-s). \qquad (6.1.13)
\end{aligned}$$

The sum over 3 can be dropped while the sum over 4 corresponds to a trace. The last line of Eq. (6.1.12) is the trace of a product of two operators and thus it can be treated analogly to Eq. (6.1.5). By reapplying the two approximations, Eq. (6.1.11) is shown.

The EDOF are still coupled in the master equation (6.1.10), which makes it practically impossible to be calculated. By choosing $n_1 = n_2 \equiv n$, $e_1 = e_2 \equiv e$ and performing the sum over e, we construct the reduced density matrix of Eq. (6.1.5) on the l.h.s. of the master equation. To discuss the EDOF we investigate the unitary and the dissipative part separately in the subsequent sections.

6.1.1. Unitary Part of the Master Equation

The unitary part comprises two terms of the type

$$\begin{aligned}
&\sum_5 \sum_e \Gamma_{15,51}\rho_{12}(t)\\
=&\sum_5 \sum_e \sum_{m=0}^{N_\mathrm{C}} \Big(C_{\mathrm{m,p}}(\omega_{51}) f^\dagger_{m,15} f_{m,51} + C_{\mathrm{m,h}}(\omega_{51}) f_{m,15} f^\dagger_{m,51} \Big) \rho_{12}(t)\\
=&\sum_{n'=n_\mathrm{min}}^{N_\mathrm{C}} \sum_{l_5} \sum_{e_5,e} \sum_{m=0}^{N_\mathrm{C}} \Big[C_{\mathrm{m,p}}(E^{n'}_{l_5} - E^n_{r_1}) \langle r_1, e; n| f^\dagger_m |l_5, e_5; n'\rangle \langle l_5, e_5; n'| f_m |r_1, e; n\rangle +\\
&+ C_{\mathrm{m,h}}(E^{n'}_{l_5} - E^n_{r_1}) \langle r_1, e; n| f_m |l_5, e_5; n'\rangle \langle l_5, e_5; n'| f^\dagger_m |r_1, e; n\rangle \Big] \langle r_1, e; n| \rho^\mathrm{I}_\mathrm{S}(t) |r_2, e; n\rangle\\
=&\sum_{n'=n_\mathrm{min}}^{N_\mathrm{C}} \sum_{l_5} \sum_{m=0}^{N_\mathrm{C}} \Big[C_{\mathrm{m,p}}(E^{n'}_{l_5} - E^n_{r_1}) (F_m)^{r_1}_{l_5}(n,n') + C_{\mathrm{m,h}}(E^{n'}_{l_5} - E^n_{r_1}) (\overline{F}_m)^{r_1}_{l_5}(n,n') \Big] \rho^\mathrm{red}_{r_1 r_2}(n;t).
\end{aligned} \tag{6.1.1.14}$$

In the first step we simply inserted Eq. (6.1.8). In the second step we defined $\sum_5 |5\rangle\langle 5| = \mathbf{1}_{N_\mathrm{C}}$ with $n_5 = n'$ and expanded the short-form notations in their explicit form. In the last step we have used

$$\langle s, e; n| \rho^\mathrm{I}_\mathrm{S}(t) |r, e; n\rangle = \rho^\mathrm{red}_{sr}(n;t) d^{n-N_\mathrm{C}}, \tag{6.1.1.15}$$

which is in accordance with Eq. (6.1.6), and defined

$$\begin{aligned}
(F_m)^{r_1}_{r_2}(n_1,n_2) &= d^{n_1-N_\mathrm{C}} \sum_{e_1,e_2} \langle r_1, e_1; n_1| f^\dagger_m |r_2, e_2; n_2\rangle \langle r_2, e_2; n_2| f_m |r_1, e_1; n_1\rangle\\
(\overline{F}_m)^{r_1}_{r_2}(n_1,n_2) &= d^{n_1-N_\mathrm{C}} \sum_{e_1,e_2} \langle r_1, e_1; n_1| f_m |r_2, e_2; n_2\rangle \langle r_2, e_2; n_2| f^\dagger_m |r_1, e_1; n_1\rangle .
\end{aligned} \tag{6.1.1.16}$$

The explicit calculation of $(F_m)^{r_1}_{r_2}(n_1,n_2)$ and $(\overline{F}_m)^{r_1}_{r_2}(n_1,n_2)$ is described in Sec. 6.1.4.

The last line of Eq. (6.1.1.14) includes the discarded states of all iterations $n' > n$. However, these states can also be expressed by the kept states of iteration n and so we can substitute

$$\begin{aligned}&\sum_{n'=n}^{N_\mathrm{C}}\sum_{l_5}\sum_{m=0}^{N_\mathrm{C}}\Big[C_{\mathrm{m,p}}(E^{n'}_{l_5}-E^{n}_{r_1})(F_m)^{r_1}_{l_5}(n,n')+C_{\mathrm{m,h}}(E^{n'}_{l_5}-E^{n}_{r_1})(\overline{F}_m)^{r_1}_{l_5}(n,n')\Big]\rho^{\mathrm{red}}_{r_1r_2}(n;t)\\ \rightarrow&\sum_{r_5}\sum_{m=0}^{N_\mathrm{C}}\Big[C_{\mathrm{m,p}}(E^{n}_{r_5}-E^{n}_{r_1})(F_m)^{r_1}_{r_5}(n,n)+C_{\mathrm{m,h}}(E^{n}_{r_5}-E^{n}_{r_1})(\overline{F}_m)^{r_1}_{r_5}(n,n)\Big]\rho^{\mathrm{red}}_{r_1r_2}(n;t).\end{aligned} \tag{6.1.1.17}$$

The indices r_5 here include kept and discarded states of the iteration n.

6.1.2. Dissipative Part of the Master Equation

The off-diagonal elements of the BRT are defined by the dissipative term of Eq. (6.1.10), where we have

$$\begin{aligned}&\sum_{n_3,n_4=n_\mathrm{min}}^{N_\mathrm{C}}\delta_{n_3,n_4}\sum_{r_3,r_4\notin\{k,k'\}}\delta_{\omega_{12},\omega_{34}}\sum_{e,e_3,e_4}\mathfrak{Re}\Gamma_{42,13}\rho_{34}(t)\\ =&\sum_{n_3,n_4=n_\mathrm{min}}^{N_\mathrm{C}}\delta_{n_3,n_4}\sum_{r_3,r_4\notin\{k,k'\}}\delta_{\omega_{12},\omega_{34}}\sum_{e,e_3,e_4}\sum_{m=0}^{N_\mathrm{C}}f_\beta(\omega_{13})\Big[\Gamma_{\mathrm{m,p}}(\omega_{13})f^\dagger_{m,42}f_{m,13}+\\ &+\Gamma_{\mathrm{m,h}}(\omega_{13})f_{m,42}f^\dagger_{m,13}\Big]\rho_{34}(t)\\ =&\sum_{n'=n_\mathrm{min}}^{N_\mathrm{C}}\sum_{r_3,r_4\notin\{k,k'\}}\delta_{E^n_{r_1}-E^n_{r_2},E^{n'}_{r_3}-E^{n'}_{r_4}}\sum_{e,e_3,e_4}\sum_{m=0}^{N_\mathrm{C}}f_\beta(E^n_{r_1}-E^{n'}_{r_3})\times\\ &\times\Big[\Gamma_{\mathrm{m,p}}(E^n_{r_1}-E^{n'}_{r_3})\left\langle r_4,e_4;n'\right|f^\dagger_m\left|r_2,e;n\right\rangle\left\langle r_1,e;n\right|f_m\left|r_3,e_3;n'\right\rangle+\\ &+\Gamma_{\mathrm{m,h}}(E^n_{r_1}-E^{n'}_{r_3})\left\langle r_4,e_4;n'\right|f_m\left|r_2,e;n\right\rangle\left\langle r_1,e;n\right|f^\dagger_m\left|r_3,e_3;n'\right\rangle\Big]\rho_{34}(t)\\ \approx&\sum_{n'=n_\mathrm{min}}^{N_\mathrm{C}}\sum_{r_3,r_4\notin\{k,k'\}}\delta_{E^n_{r_1}-E^n_{r_2},E^{n'}_{r_3}-E^{n'}_{r_4}}f_\beta(E^n_{r_1}-E^{n'}_{r_3})\rho^{\mathrm{red}}_{r_3r_4}(n';t)\times\\ &\times\sum_{m=0}^{\min(n,n')}\Big[\Gamma_{\mathrm{m,p}}(E^n_{r_1}-E^{n'}_{r_3})(F_m)^{r_1r_2}_{r_3r_4}(n,n')+\Gamma_{\mathrm{m,h}}(E^n_{r_1}-E^{n'}_{r_3})(\overline{F}_m)^{r_1r_2}_{r_3r_4}(n,n')\Big].\end{aligned} \tag{6.1.2.18}$$

Here, similar steps have been performed as in Eq. (6.1.1.14) and the Kronecker-deltas

$\delta_{E^n_{r_1}-E^n_{r_2},E^{n'}_{r_3}-E^{n'}_{r_4}}$ add another restriction to the sums. We have defined

$$(F_m)^{r_1r_2}_{r_3r_4}(n,n') = d^{n'-N_\mathrm{C}} \sum_{e,e_3,e_4} \delta_{e_3,e_4} \langle r_4,e_4;n'| f^\dagger_m |r_2,e;n\rangle \langle r_1,e;n| f_m |r_3,e_3;n'\rangle$$
$$(\overline{F}_m)^{r_1r_2}_{r_3r_4}(n,n') = d^{n'-N_\mathrm{C}} \sum_{e,e_3,e_4} \delta_{e_3,e_4} \langle r_4,e_4;n'| f_m |r_2,e;n\rangle \langle r_1,e;n| f^\dagger_m |r_3,e_3;n'\rangle\,. \tag{6.1.2.19}$$

In the last step of Eq. (6.1.2.18) we have introduced our first approximation in the context of expressing the master equation for the truncated system. Here we assume that the index $m \leq n, n'$, which we denote by the local operator approximation (LOA) (see Sec. 6.1.3). This approximation allows us to interpret the chain operators $f^{(\dagger)}_m$ as local operators with respect to the EDOF e, e_3 and e_4, respectively[1].

Consequently, for $n' \geq n$ we obtain $e_3 = e_4$ in Eq. (6.1.2.19), which allows us to substitute $\langle r_3,e_3;n'| \rho^\mathrm{I}_\mathrm{S}(t) |r_4,e_4;n'\rangle = \rho^\mathrm{red}_{r_3r_4}(n';t)d^{n'-N_\mathrm{C}}$. Furthermore, the sum over e_3 cancels out the factor of $d^{n'-N_\mathrm{C}}$ and the sum over e yields another factor of $d^{n'-n}$. Since we assume $n' \geq n$, this factor enlarges the particular terms. However, if the temperature is sufficiently low, the Fermi-function $f_\beta(E^n_{r_1} - E^{n'}_{r_3})$ suppresses these terms, since $E^n_{r_1} - E^{n'}_{r_3} > 0$ in most cases. Additionally, the overlap $\langle r,e;n| f^{(\dagger)}_m |r',e';n'\rangle$ is expected to decrease if $|n - n'|$ is large. For that reason, the terms $n' \gg n$ can be see as negligibly small.

The case $n' < n$ needs to be treated with more caution. The indices e in Eq. (6.1.2.19) demand the last $N_\mathrm{C} - n$ elements of e_3 and e_4 to be identical and here the reduced density matrix can be constructed. However, the first $n - n'$ elements are not necessarily identical, since the operator $|r_2,e;n\rangle \langle r_1,e;n|$ is not diagonal in these EDOF. Here we require a further assumption of

$$\langle s,e;n| \rho^\mathrm{I}_\mathrm{S}(t) |r,e';n\rangle \approx \rho^\mathrm{red}_{sr}(n;t)d^{n-N_\mathrm{C}}\delta_{ee'}, \tag{6.1.2.20}$$

i.e. we assume that the density matrix is diagonal in the EDOF for all times t. This restriction demands $e_3 = e_4$ and so the sum over e_3 yields a factor of $d^{n-n'}$, while the sum over e yields $d^{N_\mathrm{C}-n}$. Together, both factors cancel out $d^{n'-N_\mathrm{C}}$ in Eq. (6.1.2.19). Opposed to the case $n' \geq n$, the Fermi-function has a relevant contribution for all temperatures, since in most cases $E^n_{r_1} - E^{n'}_{r_3} < 0$ if $n' < n$. Hence, these terms are

---

[1] It should be stressed, that in the original NRG context, only sites $\leq n_\mathrm{min}$ are defined as "local". Here we expand this term to all sites that are equal or below the respective indices n, n'.

neither damped by a pre-factor, nor by the Fermi-function and the assumption Eq. (6.1.2.20) needs to be evaluated.

Obviously, the density matrix is diagonal in the EDOF in the equilibrium case $t \to \infty$, since the density matrix relaxates into the Boltzmann distribution in the final NRG basis. For $t = 0$ this does not hold and the density matrix is not diagonal in the EDOF (see Sec. 3.9). To assume diagonality for all times thus generates an error of, up to this point, undefined quantity in the short-time behavior. However, one has to keep in mind, that the error grows with $n - n'$ and vanishes for $n' \to n$. As mentioned above, the overlap $\langle r, e; n| f_m^{(\dagger)} |r', e'; n'\rangle$ is expected to decrease, if $|n - n'|$ is large. From that perspective, the terms $n' \approx n$ have the most important contribution in the master equation and the approximation is well justified.

6.1.3. Local Operator Approximation

Let us discuss the impact of the approximation $m \leq n, n'$. In fact, our argument is that $C_{\mathrm{m,p/h}}(E_r^{n'} - E_s^n)$ is negligible, if at least one of the numbers n, n' is smaller than m. We have already mentioned this approximation in Sec. 5.3.2, however, here we want to give a more rigorous justification.

To assess the LOA, we present the NRG spectrum for the first $n = 20$ iterations in Fig. 6.1. For demonstration purposes we have chosen the small number of $N_{\mathrm{S}} = 30$ kept states (green lines) and thus the truncation of the high-energy states (red lines) starts at $n_{\min} = 3$. Since we restrict ourselves to the spinless RLM, $d = 2$ and thus 30 states are discarded at each iteration. Note that we have plotted the absolute energies and so no ground-state-shift has been applied (see Sec. 3.3). The black dashed lines represent the edge of the effective support of the correlation function $C_n(\omega)$ (called correlation width), which is roughly given by $\pm 5\,\omega_m$ with ω_m being the NRG-scale (see Fig. 5.11).

To assess the approximation, several different cases need to be addressed. In the first part of the last step in Eq. (6.1.1.14), $n' < n$ is always fulfilled and the energies $E_{l_5}^{n'}$ are all discarded. Let us first concentrate on the case $n' \ll n$. Here, the energy difference $E_{l_5}^{n'} - E_{r_1}^n \approx E_{l_5}^{n'} > 0$ is mainly defined by $E_{l_5}^{n'}$. In Fig. 6.1(a) we can see, that the discarded energies of iteration n are well outside of the correlation width of iterations $m > n$. Thus, $C_{\mathrm{m,p/h}}(E_{l_5}^{n'} - E_{r_1}^n) \to 0$ and the approximation $m \leq n, n'$ becomes exact for $n' \ll n$.

The other extreme case, $n' = n$, is more problematic in the context of the LOA. Figure 6.1(b) shows, that only some kept-discarded energy differences (blue lines) lie

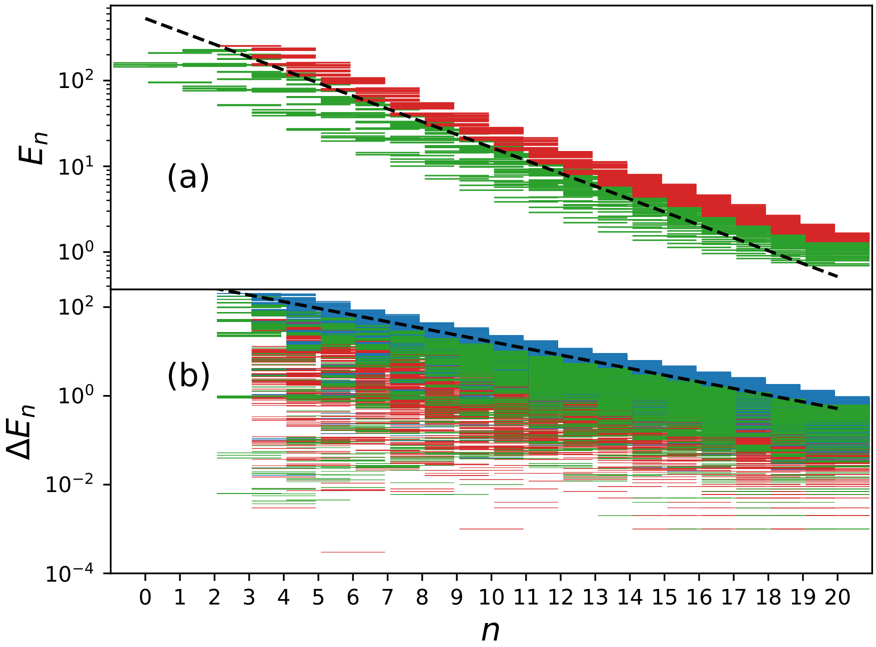

Figure 6.1.: Eigenenergies of the truncated Wilson chain for different NRG iterations n. The vertical axis is given in units of Γ and scaled logarithmically. We have chosen $D = 100\Gamma$ and $\Lambda = 2$. In panel (a) we present the bare energies E_r^n, divided into kept states (green) and discarded states (red). All values are shifted by an offset of $+152\Gamma$ to allow for a logarithmic presentation. In panel (b) we plot the energy differences $\Delta E_n = E_r^n - E_s^n$ within one iteration, where we distinguish discarded-discarded (red), discarded-kept (blue) and kept-kept differences (green), respectively. The plot is symmetrical on the vertical axis and thus the negative half is omitted. As a black dashed line $5\omega_n$ is added.

outside of the correlation width for $n < m$. All other energies can only be neglected if $n \ll m$ and if Λ is large. Precisely, we expect to neglect significant contributions of the correlation functions for relatively large n', n and $n', n \neq N_\mathrm{C}$. However, compared to the total number of all possible combinations of the indices n', n, m the effect of the approximation $m \leq n, n'$ is to decrease the relaxation rates of the density matrix by only a small amount. Since the master equation is significantly simplified by the LOA, we accept this small additional error. Furthermore, the contribution of the chain operators of site m is small in the basis of iteration n, if $n < m$, as discussed in Sec. 5.3.2.

6.1.4. Calculation of the Matrix Elements of the Chain Operators

We turn to the explicit calculation of the tensors $F_{r_1 r_2}(n_1, n_2)$ of Eq. (6.1.1.16). The case $n_1 = n_2 = n$ is trivial. Since the chain operators are assumed to be local, they are diagonal in the EDOF e_1, e_2. Thus we obtain

$$\begin{aligned}(F_m)^{r_1}_{r_2}(n,n) &= d^{n-N_\mathrm{C}} \sum_{e_1,e_2} \delta_{e_1,e_2} \langle r_1, e_1; n| f^\dagger_m |r_2, e_2; n\rangle \langle r_2, e_2; n| f_m |r_1, e_1; n\rangle \\ &= \langle r_1; n| f^\dagger_m |r_2; n\rangle \langle r_2; n| f_m |r_1; n\rangle \,. \end{aligned} \tag{6.1.4.21}$$

The prefactor is cancelled by the trace over e_1, and we have defined the chain operators in the basis of the NRG iteration n without the EDOF.

Let us proceed to the case $n_1 < n_2$. We insert two complete basis sets $\mathbf{1}_{n_1}$ into Eq. (6.1.1.16) to obtain

$$\begin{aligned}(F_m)^{r_1}_{r_2}(n_1,n_2) =& d^{n_1-N_\mathrm{C}} \sum_{e_1,e_2} \langle r_1, e_1; n_1| f^\dagger_m \mathbf{1}_{n_1} |r_2, e_2; n_2\rangle \langle r_2, e_2; n_2| \mathbf{1}_{n_1} f_m |r_1, e_1; n_1\rangle \\ =& d^{n_1-N_\mathrm{C}} \sum_{k,k'} \sum_{e_1,e_2} \langle r_1, e_1; n_1| f^\dagger_m |k, e_1; n_1\rangle \langle k, e_1; n_1 | r_2, e_2; n_2\rangle \times \\ & \times \langle r_2, e_2; n_2 | k', e_1; n_1\rangle \langle k', e_1; n_1| f_m |r_1, e_1; n_1\rangle \\ =& d^{n_1-n_2} \sum_{k,k'} S^{(n_1,n_2)}_{kk',r_2r_2} \langle r_1; n_1| f^\dagger_m |k; n_1\rangle \langle k'; n_1| f_m |r_1; n_1\rangle \,. \end{aligned} \tag{6.1.4.22}$$

As above, the chain operators are diagonal in the EDOF and thus demand that $e = e' = e_1$. Of the complete basis set $\mathbf{1}_{n_1}$ only the kept states of iteration n_1 have a contribution, since the discarded states of iterations n_1 are orthogonal to all states of iterations $n_2 > n_1$. In the last step we have summed over e_2, which yields a factor of $d^{N_\mathrm{C}-n_2}$. We are left with the calculation of the general overlap tensor

$$S^{(n_1,n_2)}_{kk',rr'} = \sum_{\bar{e}} \langle k, \bar{e}; n_1 | r; n_2\rangle \langle r'; n_2 | k', \bar{e}; n_1\rangle \,, \tag{6.1.4.23}$$

where the index $\bar{e}$ sums over all $d^{n_2-n_1}$ EDOF which occur on the iterations $n_1 + 1$ to n_2. Consequently, we need a way to successively transition the state $|r; n_2\rangle$ down to a state of iteration n_1. The first step can be performed as

$$|r; n_2\rangle = \mathbf{1}_{n_2-1} |r; n_2\rangle = \sum_{k,\alpha} P^{n_2-1}_{r,k}[\alpha] \, |k, \alpha; n_2 - 1\rangle \,. \tag{6.1.4.24}$$

From the complete basis set $\mathbf{1}_{n_2-1}$ only the kept states of iteration n_2-1 remain, since the discarded states of iterations $< n_2$ are diagonal to $|r;n_2\rangle$. The index α runs over all d EDOF of the n_2-th chainsite. The real matrix elements

$$P^{n_2-1}_{r,k}[\alpha] = \langle k,\alpha;n_2-1|r;n_2\rangle \tag{6.1.4.25}$$

are an integral part of the conventional NRG algorithm (see Sec. 3.4) and connect the tensor-product state $|k,\alpha;n_2-1\rangle$ to the eigenstates of the subsequent NRG iteration. If Eq. (6.1.4.24) is inserted into (6.1.4.23), we can define the overlap tensor recursively via

$$S^{(n_1,n_2)}_{kk',rr'} = \sum_{\overline{k},\overline{k}',\alpha} P^{n_2-1}_{r,\overline{k}}[\alpha] P^{n_2-1}_{r',\overline{k}'}[\alpha] S^{(n_1,n_2-1)}_{kk',\overline{k}\overline{k}'}. \tag{6.1.4.26}$$

Since $S^{(n_1,n_2)}_{kk',rr'}$ is not defined for $n_1 > n_2$, the recursion starts at

$$S^{(n_1,n_2=n_1)}_{kk',rr'} = \delta_{kr}\delta_{k'r'} \tag{6.1.4.27}$$

and then successively increases n_2. The overlap tensor is a tensor of fourth order in the state indices and of second order in the iteration indices. Thus its dimension is of the order $N_\mathrm{C}^2 N_\mathrm{S}^4$. If each NRG iteration is handled separately, the OWC requires around N_C BRTs of the order N_S. These tensors are highly sparse, but yet their construction constitutes a bottleneck to the total program. Consequently, the construction of all required overlap tensors is not feasible with typical modern workstations. A more efficient way of recursively calculating the tensors $F_{r_1r_2}(n_1,n_2)$ is to define

$$(F_m)^{r_1}_{r_2r_3}(n_1,n_2) = \sum_{k,k'} S^{(n_1,n_2)}_{kk',r_2r_3} \langle r_1;n_1|\, f^\dagger_m \,|k;n_1\rangle \langle k';n_1|\, f_m \,|r_1;n_1\rangle\,, \tag{6.1.4.28}$$

which is only of third order in N_S. Equation (6.1.4.26) can be inserted here to define the recursion relation

$$(F_m)^{r_1}_{r_2r_3}(n_1,n_2) = \sum_{k,k',\alpha} P^{n_2-1}_{r_2,k}[\alpha] P^{n_2-1}_{r_3,k'}[\alpha] F^{r_1}_{kk'}(n_1,n_2-1) \tag{6.1.4.29}$$

with

$$(F_m)^{r_1}_{r_2r_3}(n_1,n_2=n_1) = \langle r_1;n_1|\, f^\dagger_m \,|r_2;n_1\rangle \langle r_3;n_1|\, f_m \,|r_1;n_1\rangle \tag{6.1.4.30}$$

as the recursion start. The required tensor can be recovered by

$$(F_m)^{r_1}_{r_2}(n_1,n_2) = d^{n_1-n_2}(F_m)^{r_1}_{r_2r_2}(n_1,n_2). \tag{6.1.4.31}$$

The case $n_1 > n_2$ can simply be obtained via

$$(F_m)^{r_1}_{r_2}(n_1,n_2) = (\overline{F}_m)^{r_2}_{r_1r_1}(n_2,n_1). \tag{6.1.4.32}$$

Here, the horizontal line indicates that the chain operators f_m and $f_m^\dagger$ are switched.

Let us discuss a useful approximation to conclude this section. In Eq. (6.1.1.16) the operator $(F_m)^{r_1}_{r_2}(n_1,n_2)$ includes two different EDOF, e_1 and e_2 respectively. Since the sum over these EDOF is included, the terms of $f_m^\dagger$ and f_m cannot be treated independently. That is the reason why we need the third order tensors $(F_m)^{r_1}_{r_2r_3}(n_1,n_2)$. However, if we approximate the EDOF of the lower NRG iteration as independent, we can separate those terms. To illustrate that idea, we choose $n_1 > n_2$, without loss of generality, and obtain

$$\begin{aligned}(F_m)^{r_1}_{r_2}(n_1,n_2) &= d^{n_1-N_\mathrm{C}}\sum_{e_1,e_2}\langle r_1,e_1;n_1|\, f_m^\dagger \,|r_2,e_2;n_2\rangle\,\langle r_2,e_2;n_2|\, f_m \,|r_1,e_1;n_1\rangle \\ &= \sum_{\overline{e}_2}\Big[\langle r_2,\overline{e}_2;n_2|\, f_m \,|r_1;n_1\rangle\Big]^2 \\ &\approx \Big[\sum_{\overline{e}_2}\langle r_2,\overline{e}_2;n_2|\, f_m \,|r_1;n_1\rangle\Big]^2. \end{aligned} \tag{6.1.4.33}$$

The EDOF e_2 are redefined as

$$e_2 = \{\overline{e}_2, \overline{e}_1\}, \tag{6.1.4.34}$$

where $\overline{e}_2$ denotes the EDOF for the chainsites $n_2+1,...,n_1$. The LOA demands that $m \le n_1, n_2$ and thus the chain operators are diagonal in the EDOF. For that reason, we can set $\overline{e}_1 = e_1$. We sum over e_1, which yields a factor of $d^{N_\mathrm{C}-n_1}$ that cancels out the factor of $d^{n_1-N_\mathrm{C}}$. Consequently, we are left with the sum over $\overline{e}_2$, which means that all combinations of EDOF $\{\alpha_{n_2+1},...,\alpha_{n_1}\}$ contribute to the sum. In the last step, we interpret the sum over $\overline{e}_2$ as two independent sums and thus we are able to factorize $(F_m)^{r_1}_{r_2}(n_1,n_2)$. We denote this approximation by the name factorized local operator approximation (FLOA).

6.1.5. Single Shell Approximation

Let us discuss another approximation, the single shell approximation (SSA), that is equally useful as the LOA. The objective of this section is to reduce the master equation (6.1.9) to $N_\mathrm{C} - n_\mathrm{min}$ isolated equations, which each only include one single NRG iteration n. The term "shell" originates from the fact that in the context of the Wilson chain each chain site corresponds to an energy shell, which is arranged concentrically around the impurity.

As illustrated in Eq. (6.1.1.17), the unitary part of the master equation comprises a sum of kept and discarded states on the iteration $n' = n$, and discarded states for the iterations $n' < n$. The energy of these latter discarded states is typically larger than all energies on the iteration n (see Fig. 6.1). Consequently, $E^{n'}_{l_5} - E^{n}_{r_1} > 0$ in most cases. The real-part of the correlation functions is $\mathfrak{Re} C_\mathrm{m}(\omega) = \Gamma_\mathrm{m}(\omega) f_\beta(\omega)$ and the Fermi-function suppresses all positive energy contributions. Hence, the terms with $n' < n$ can be neglected in the last line of Eq. (6.1.1.14), if the temperature is sufficiently low (and this is typically the case in systems, where a truncation of high-energy states is justified).

However, the imaginary part of the correlation functions is not proportional to the Fermi-function and thus its is not suppressed for positive energies. Neglecting the terms $n' \neq n$ is expected to produce a relatively large error in the Lamb-shift. In Sec. 6.1.9 we discuss the effect of the truncation on the Lamb-shift and propose several approximations. Since the impact of the Lamb-shift on the final result is relatively small, we can set the imaginary part of the BRT to zero to obtain a valid approximation.

For the dissipative part a different argument holds to calculate the master equation within one single NRG iteration. As discussed in Sec. 6.1.2, terms in which the absolute difference of n and n' is large have an increasingly small contribution in the master equation. Furthermore, the Kronecker-delta $\delta_{E^n_{r_1} - E^n_{r_2}, E^{n'}_{r_3} - E^{n'}_{r_4}}$ in Eq. (6.1.2.18) adds another restriction that favors $n = n'$. Here all terms are prohibited, which do not fulfill $E^n_{r_1} - E^n_{r_2} = E^{n'}_{r_3} - E^{n'}_{r_4}$. Since this restriction originates from the secular approximation, a small energy window Δ might be chosen and all combinations of energies might be accepted which suffice $|E^n_{r_1} - E^n_{r_2} - E^{n'}_{r_3} + E^{n'}_{r_4}| < \Delta$ (see Sec. 5.3.4). In any case, it is unlikely to find identical energy differences $E^n_{r_1} - E^n_{r_2}$ for $r_1 \neq r_2$ on different NRG iterations n and n' (the case $r_1 = r_2$ and $r_3 = r_4$, which allows for $n \neq n'$ is discussed in Sec. 6.1.7). In this context, the approximation $n = n'$ appears valid for the dissipative part as well.

In the SSA the master equation (6.1.10) can be turned into

$$\begin{aligned}\dot{\rho}^{\text{red}}_{r_1r_2}(n;t) = &- \sum_{m=0}^{n}\sum_{r_5} f_\beta(\omega_{r_5r_1})\Gamma_m(\omega_{r_5r_1})F^{(m)}_{r_1r_5,r_5r_1}\rho^{\text{red}}_{r_1r_2}(n;t)\\ &- \sum_{m=0}^{n}\sum_{r_5} f_\beta(\omega_{r_5r_2})\Gamma_m(\omega_{r_5r_2})F^{(m)}_{r_2r_5,r_5r_2}\rho^{\text{red}}_{r_1r_2}(n;t)\\ &+ 2\sum_{m=0}^{n}\sum_{r_3r_4} \delta_{E^n_{r_1}-E^n_{r_2},E^n_{r_3}-E^n_{r_4}} f_\beta(\omega_{r_1r_3})\Gamma_m(\omega_{r_1r_3})F^{(m)}_{r_4r_2,r_1r_3}\rho^{\text{red}}_{r_3r_4}(n;t).\end{aligned} \tag{6.1.5.35}$$

The indices r_i denote kept and discarded states. We assume a particle-hole symmetric bath continuum and defined the general spectral coupling function $\Gamma_m(\omega)$ for the reservoirs, which stands for a high-energy reservoir if $m < N_\text{C}$ and a complete reservoir if $m = N_\text{C}$. Furthermore, the short-form notations

$$\begin{aligned}\rho^{\text{red}}_{r_1r_2}(n;t) &= \langle r_1;n|\,\rho^{\text{I}}_{\text{S}}(t)\,|r_2;n\rangle\\ F^{(m)}_{r_1r_2,r_3r_4} &= \langle r_1;n|\,f^\dagger_m\,|r_2;n\rangle\,\langle r_3;n|\,f_m\,|r_4;n\rangle + \langle r_1;n|\,f_m\,|r_2;n\rangle\,\langle r_3;n|\,f^\dagger_m\,|r_4;n\rangle\end{aligned} \tag{6.1.5.36}$$

have been used.

The master equation (6.1.5.35) constitutes the bare minimum for an OWC formulation in the context of a BMA. The fundamental physics of the correct relaxation time and steady-state value are already well included in this crudely simplified version of the complete master equation (6.1.9). With increasing chain length, the short-time behavior is also reproduced correctly, since here the CWC dominates (see Sec. 5.4.1). However, one major problem arises in the context of the SSA. Over time, the weight of the density matrix relaxates from the high-energy states into the low-energy states. Since all iterations are disconnected in our approximation, the weight flows from the discarded-discarded sector of iteration n into its respective kept-kept sector, where the latter is not included in the summation of Eq. (6.1.5) and so relevant information is lost. In a correct formulation, the high-energy states would serve as source terms for the low-energy states and thus transport information from the beginning of the Wilson chain up to its end. This source term effect will be discussed in more detail in the following section.

6.1.6. Source Term Effect

As already mentioned, the time-dependent density matrix performs a transition from a mixed state at $t = 0$ to a Boltzmann distribution for $t \to \infty$ in the context of the BMA. Consequently, information flows from the high-energy states to the low-energy states and so the complete master equation (6.1.9) can be interpreted as a differential equation that uses the high-energy states as source terms for the low-energy states. To explicitly prove this fact, we recall from Eq. (6.1.3) that $\mathbf{1}_{n_{\mathrm{min}}}$ yields a complete basis set including only the NRG iteration $n = n_{\mathrm{min}}$. If we choose this basis set for all indices $1, 2, 3, 4, 5$ that appear in the master equation[2], $\rho^{\mathrm{red}}(n_{\mathrm{min}}; t)$ can be calculated exactly within one single NRG iteration only, since it is an isolated quantity with respect to the lower energy states of the Wilson chain. The SSA or any other approximation besides the LOA is not required in this context. Starting from the initial time $t = 0$, all indices of the density matrix will relaxate into the kept-kept sector (i.e. the low-energy sector) to form the Boltzmann distribution for $t \to \infty$. However, this sector has no contribution in the final expression (6.1.5) and so the contribution of $\rho^{\mathrm{red}}(n_{\mathrm{min}}; t)$ will vanish entirely.

In fact, the information of the kept-kept sector is not lost over time. For iterations $n > n_{\mathrm{min}}$ we formulate the master equation with complete basis sets $\mathbf{1}_n$ and so $\rho^{\mathrm{red}}(n; t)$ is connected to all previous iterations, which serve as source terms for the lower energy states of iteration n. The information that would dissipate into the kept-kept sector of $\rho^{\mathrm{red}}(n_{\mathrm{min}}; t)$ now flows into $\rho^{\mathrm{red}}(n_{\mathrm{min}} + 1; t)$ and then, later on, dissipates into its respective kept-kept sector. In this way, information flows from the early high-energy iterations to the later low-energy iterations. Since for $n = N_{\mathrm{C}}$ all states are discarded by definition and thus included in Eq. (6.1.5), $\rho^{\mathrm{red}}(N_{\mathrm{C}}; t)$ aggregates all information for $t \to \infty$. If one applies the SSA, the iterations are not connected and so all information of the iterations $n < N_{\mathrm{C}}$ is lost for $t \to \infty$. The physically most relevant effect of this is a continuous loss of the trace

$$\mathrm{Tr}\rho_{\mathrm{S}}(t) = \sum_{n=n_{\mathrm{min}}}^{N_{\mathrm{C}}} \sum_{l} \rho_{ll}(n; t). \tag{6.1.6.37}$$

The total trace of the density matrix is supposed to be normalized to 1. Instead, if each NRG iteration is treated separately, the trace is conserved on each single iteration only (see Sec. 4.5). Since the discarded-discarded sector for iterations $n < N_{\mathrm{C}}$ is

---

[2] ... and apply the LOA, which we assume from here on

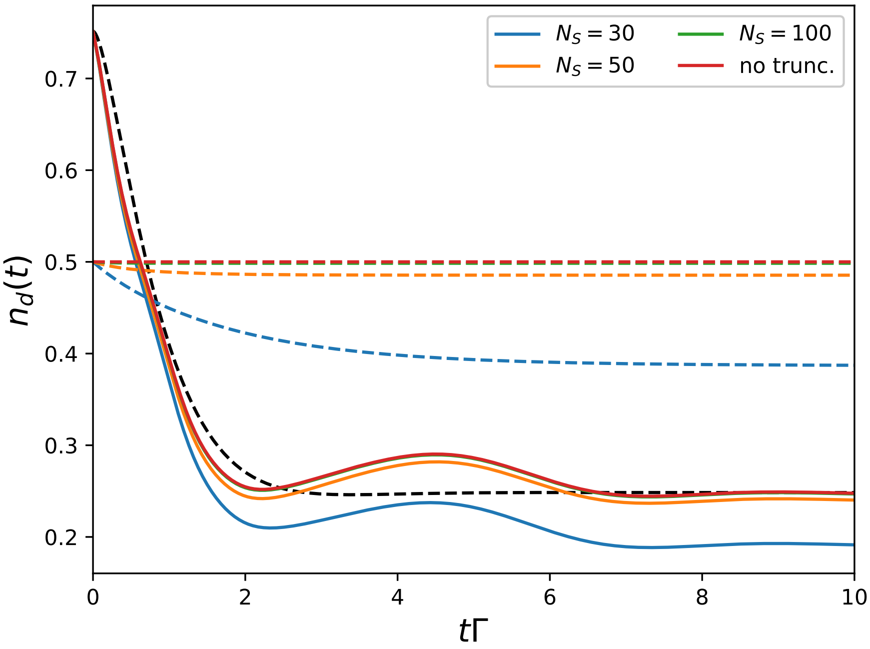

Figure 6.2.: $n_\mathrm{d}(t)$ versus $t\Gamma$ for $N_\mathrm{C} = 10, \Lambda = 10, D = 100\Gamma, T = 0.01\Gamma$. The number of kept states is chosen as $N_\mathrm{S} = 30$ (blue), $N_\mathrm{S} = 50$ (orange), $N_\mathrm{S} = 100$ (green) and N_S =max. (red). The corresponding half trace of the density matrix is added as dashed lines of the same color and the Lamb-shift is set to zero. The analytical solution is added as a black dashed line.

depopulated over time, only $\sum_l \rho_{ll}(N_\mathrm{C}; t)$ contributes to the trace for $t \to \infty$ and so the trace of the density matrix relaxates to a steady-state < 1. In Sec 4.5 it has been shown, that the density matrix thermalizes to the Boltzmann distribution in the context of the BMA. However, it is only guaranteed, that the single components of the DDM fulfill the Boltzmann distribution relative to each other, i.e.

$$\lim_{t\to\infty} \frac{\rho^{\mathrm{red}}_{aa}(n;t)}{\rho^{\mathrm{red}}_{bb}(n;t)} = e^{-\beta(E^n_a - E^n_b)}. \tag{6.1.6.38}$$

The absolute weight $Z_n(t \to \infty)$ is not automatically correct, i.e. equal to $\sum_l e^{-\beta E^n_l}$.

In Fig. 6.2 the impurity occupation number $n_\mathrm{d}(t)$ for the RLM is plotted against the dimensionless time $t\Gamma$. A chain length $N_\mathrm{C} = 10$ has been chosen to allow for a comparison with the non-truncated case. Furthermore, $\Lambda = 10$ is picked to be quite large in order to maximally enhance the effect of the loss of the trace of the density matrix. The functions are practically converged for $N_\mathrm{S} = 100$, while for a lower number of kept states the curves start to deviate significantly from the untruncated case. Since the CWC is still almost exact for $N_{\mathrm{S}} = 30$, the deviation is to be attributed mainly to the loss of the trace. In the trace of the density matrix (dashed lines) this behavior is clearly depicted.

In the following section we discuss several ways to recover the conservation of the trace for a truncated Wilson chain.

6.1.7. Conservation of the Trace of the Density Matrix

We presume the SSA for all truncated NRG iterations. Here all kept and discarded states are included within one iteration. As discussed above, the trace of the density matrix is not conserved in that case, leading to an unphysical drop of local operator expectation values $O_{\mathrm{S}}(t)$ over time. In the following we discuss four simple ways to compensate for that trace loss. Here each approach yields different results, which is why a comparison of the approaches is required to assess their validity.

Ad-Hoc Compensation of the Trace Loss

A simple way to compensate for the loss of the trace is to substitute the density matrix by a normalized version

$$\overline{\rho}(t) \equiv \frac{1}{\mathrm{Tr}\Big[\rho_{\mathrm{S}}(t)\Big]} \rho_{\mathrm{S}}(t). \tag{6.1.7.39}$$

An alternative approach would be to only normalize the DDM and to keep the ODDM unchanged.

Another simple possibility to keep the trace of the density matrix constant is to artificially include the kept-kept sector in Eq. (6.1.5). Normally, one would calculate $\rho^{\mathrm{red}}_{ab}(n;t)$ for each iteration n separately with the master equation, including all kept and discarded combination. As an initial value the entire equilibrium density matrix $\rho^{\mathrm{red}}_{ab}(n;t=0)$ is used. Then the kept-kept sector is cut out for all times to construct $O_{\mathrm{S}}(t)$. Alternatively, we only cut out the kept-kept sector in the initial value $\rho^{\mathrm{red}}_{ab}(n;t=0)$ and calculate the time-evolution from here on. By this "over-counting" of the kept states, a relaxation of the density matrix into the low-energy sector is included. The relaxation time of the high-energy states into the low-energy states is considered to be approximately correct within the SSA. In the case of iterations $n \approx n_{\mathrm{min}}$, the coupling to the lowest energies is missing. However, this coupling is considered to have a relatively weak influence. For iterations $n \approx N_\mathrm{C}$ the source term effect is missing, but since we include the kept-kept sector in Eq. (6.1.5), no information is lost. Per definition, the trace is conserved for all times. The steady-state value $n_\mathrm{d}(t \to \infty)$ is met correctly as well, since the density matrix converges to the correct Boltzmann-distribution, on the one hand, and, on the other hand, keeps the trace constant.

A third, fairly simple way to combat the loss of the trace would be to artificially rescale the density matrices $\rho^\mathrm{red}(n;t)$ to ensure the correct values of $\mathrm{Tr}\Big[\rho^\mathrm{red}(n;t)\Big]$ for all times. Let

$$Z_n^\mathrm{kept}(t) = \sum_k \rho_{kk}^\mathrm{red}(n;t), \qquad Z_n^\mathrm{disc}(t) = \sum_l \rho_{ll}^\mathrm{red}(n;t), \tag{6.1.7.40}$$

where k/l sums over all kept/discarded states of iteration n. In the SSA we obtain

$$\begin{aligned} Z_n^\mathrm{kept}(t) + Z_n^\mathrm{disc}(t) &= \mathit{const}, \\ Z_n^\mathrm{disc}(t \to \infty) &= 0, \text{ if } n < N_\mathrm{C} \text{ and} \\ Z_n^\mathrm{disc}(t) &= \mathit{const}, \text{ if } n = N_\mathrm{C}. \end{aligned} \tag{6.1.7.41}$$

Obviously, $\sum_{n=n_\mathrm{min}}^{N_\mathrm{C}} Z_n^\mathrm{disc}(t) = \mathit{const}$ is not fulfilled this way. Hence, one could define a time-dependent scheme to correct for the unphysical loss of $Z_n^\mathrm{disc}(t)$. Since the correct behavior of the trace is unknown with respect to the single iterations n, we propose a scheme, that uses the portion lost in the discarded-discarded sector as a source term for later iterations. Precisely, we successively substitute the single shell values

$$Z_n^\mathrm{disc}(t) \to Z_n^\mathrm{disc}(t) + \frac{Z_n^\mathrm{disc}(t)}{Z_n^\mathrm{disc}(0)} \sum_{n'=n_\mathrm{min}}^{n-1} \left[Z_{n'}^\mathrm{disc}(0) - Z_{n'}^\mathrm{disc}(t) \right] \tag{6.1.7.42}$$

with $Z_{n_\mathrm{min}}^\mathrm{disc}(t)$ being the start of the procedure, since we know that this iteration is given correctly in the SSA. The density matrices $\rho^\mathrm{red}(n;t)$ now need to be scaled to match the calculated $Z_n^\mathrm{disc}(t)$.

To conclude the list of simple approaches to conserve the trace let us mention the case, where we separate the time-evolution of the DDM from the one of the ODDM. The ODDM is calculated via the conventional SSA, while for the DDM we approximate the master equation (6.1.5.35) even further by neglecting the coupling of the discarded states and the kept states. In fact, we demand that $r_i = l_i$ for all indices. This decoupling keeps information from dissipating from the discarded into the kept sector. Thus, the trace of the discarded part of the density matrix is conserved on all iterations.

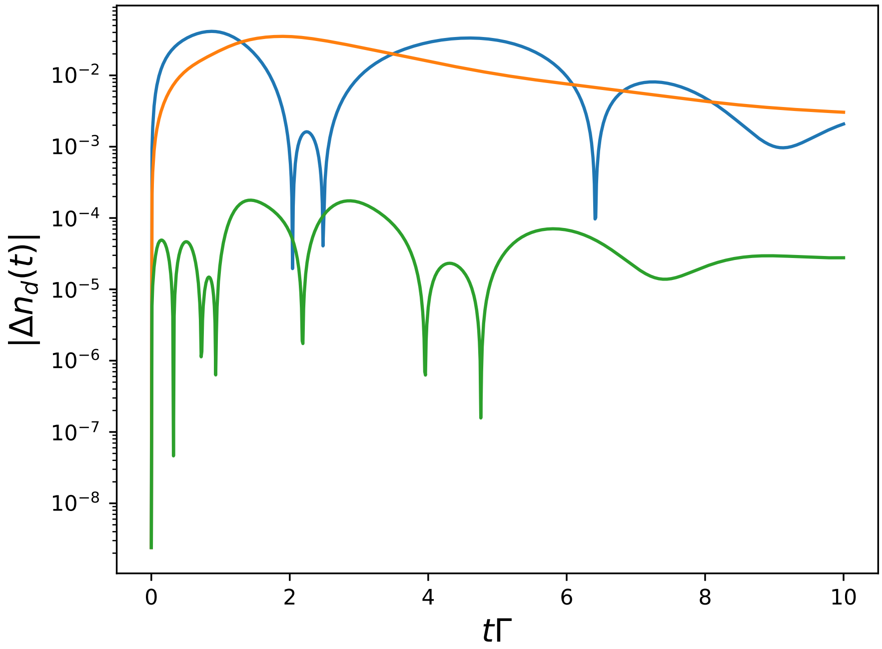

Figure 6.3.: Absolute value of the relative difference $\Delta n_{\mathrm{d}}(t)$ of the approximate and the exact results versus $t\Gamma$ for $N_{\mathrm{C}} = 10, \Lambda = 10, D = 100\Gamma, T = 0.01\Gamma$. The Lamb-shift is set to zero. The number of kept states is chosen as $N_{\mathrm{S}} = 30$ in the approximate cases. We include the cases in which the whole occupation number is weighted by the time-dependent trace (blue), only the DDM is weighted by the trace (orange) and the case where we include all kept states and simply cut out the kept-kept sector for $t = 0$ (green). The vertical axis has been chosen logarithmic.

In Fig. 6.3 we compare three different cases of approximately recovering the trace of the density matrix. We plot the relative difference $\Delta n_{\mathrm{d}}(t)$ of each approximation with the exact version, where no truncation of high-energy states has been included. The blue curve represents the impurity occupation $n_{\mathrm{d}}(t)$ in the SSA, divided by the time-dependent trace of the density matrix $\mathrm{Tr}\rho(t)$. This case is realized by calculating the density matrix coupling all states and cutting out the kept-kept sector in the equilibrium particle number operator n_{d}. The kept-kept sector is thus automatically cut out in Eq. (6.1.5). The orange curve is similar to the blue curve, only here we treat the DDM and the ODDM separately and solely divide the former by the trace of the density matrix. The green curve is constructed by cutting out the kept-kept sector in $\rho(t = 0)$ only, to correctly meet the equilibrium value $n_{\mathrm{d}}(t = 0)$, and then including all kept states from here on. By this "over-counting" of the kept states a relaxation of the density matrix into the low-energy sector is included, as argued above. Instead of relaxating into the last iteration $n = N_\mathrm{C}$, the density matrix relaxates into the kept-kept sectors of all iterations without down-scaling these iterations over time. This allows to recover the untruncated results almost exactly. For that reason, we favor this approach as the most simple way to calculate non-equilibrium dynamics for a truncated OWC.

Even though the previously discussed approaches produce results that match the analytical solution quite well, they lack a physical motivation and thus cannot be trusted to yield correct results in all cases. For that reason, we propose two alternative approaches which are significantly more tedious, but can be derived systematically. Here a correct coupling of all NRG iterations is included.

Iteration Coupling for the Diagonal Part of the Density Matrix

We rewrite the master equation for the DDM as

$$\dot{\rho}^\mathrm{red}_{r_1 r_1}(n_1;t) = -\sum_2 \Big[\Xi_{r_1 r_2}(n_1,n_2)\rho^\mathrm{red}_{r_1 r_1}(n_1;t) - \Xi_{r_2 r_1}(n_2,n_1)\rho^\mathrm{red}_{r_2 r_2}(n_2;t)\Big] \qquad (6.1.7.43)$$

with

$$\begin{aligned}\Xi_{r_1 r_2}(n_1,n_2) \equiv & 2 f_\beta(E^{n_2}_{r_2} - E^{n_1}_{r_1}) \sum_{m=0}^{\min\{n_1,n_2\}} \Big[\Gamma_\mathrm{m,p}(E^{n_2}_{r_2} - E^{n_1}_{r_1})(F_m)^{r_1}_{r_2}(n_1,n_2) + \\ & + \Gamma_\mathrm{m,h}(E^{n_2}_{r_2} - E^{n_1}_{r_1})(\overline{F}_m)^{r_1}_{r_2}(n_1,n_2)\Big]. \end{aligned} \qquad (6.1.7.44)$$

The set 2 in Eq. (6.1.7.43) can be chosen freely, as long as it comprises a complete basis set. For this approach we choose $\sum_2 |2\rangle\langle 2| = \mathbf{1}_{n_1}$ to exploit the source term effect. The r.h.s. of Eq. (6.1.7.43) can thus be divided into a part $\rho^\mathrm{red}_{rr}(n_1;t)$ which includes kept and discarded states and a part $\rho^\mathrm{red}_{ll}(n_2;t), n_2 < n_1$ which solely includes discarded states. This second part comprises the source terms which vanish in the limit $t \to \infty$. We thus define

$$\dot{\boldsymbol{\rho}}(n_1;t) = -X(n_1)\boldsymbol{\rho}(n_1;t) + \sum_{n_2=n_\mathrm{min}}^{n_1-1} Y(n_1,n_2)\boldsymbol{\rho}(n_2;t) \qquad (6.1.7.45)$$

with the vector

$$(\boldsymbol{\rho}(n;t))_r = \rho^\mathrm{red}_{rr}(n;t) \qquad (6.1.7.46)$$

and the matrices

$$\begin{aligned}(X(n_1))_{r_1r_2} &= \sum_3 \Xi_{r_1r_3}(n_1,n_3)\delta_{r_1,r_2} - \Xi_{r_2r_1}(n_1,n_1)\\ (Y(n_1,n_2))_{r_1r_2} &= \Xi_{r_2r_1}(n_2,n_1)\delta_{r_2,l_2}.\end{aligned} \tag{6.1.7.47}$$

The first matrix $X(n_1)$ is solely defined on iteration n_1 and can thus be diagonalized as $X(n_1)\boldsymbol{\rho}^{\mathrm{r}/1}_{\alpha} = \lambda^1_\alpha \boldsymbol{\rho}^{\mathrm{r}/1}_{\alpha}$. The source terms $\boldsymbol{\rho}(n_2;t)$ for $n_2 < n_1$ are already known. Equation (6.1.7.45) can be solved as

$$\begin{aligned}\boldsymbol{\rho}(n_1;t) =& e^{-X(n_1)t}\boldsymbol{\rho}(n_1;t=0) - e^{-X(n_1)t}\sum_{n_2=n_{\min}}^{n_1-1}\int_0^t dt' e^{X(n_1)t'}Y(n_1,n_2)\boldsymbol{\rho}(n_2;t)\\ =& \sum_\alpha e^{-\lambda^1_\alpha t}\boldsymbol{\rho}^{\mathrm{r},1}_\alpha\Big[c^1_\alpha - \boldsymbol{\rho}^{\mathrm{l},1}_\alpha \sum_{n_2=n_{\min}}^{n_1-1} Y(n_1,n_2)\int_0^t dt' e^{\lambda^1_\alpha t'}\boldsymbol{\rho}(n_2;t')\Big],\end{aligned} \tag{6.1.7.48}$$

where the time integral can be calculated recursively with $\boldsymbol{\rho}(n_{\min};t) = e^{-X(n_{\min})t}\boldsymbol{\rho}(n_{\min};t=0)$.

The realization of this approach in the TD-NRG program works as follows. First we need a complete TD-NRG run to construct the reduced density matrices $\boldsymbol{\rho}(n;t=0)$ for each iteration. Then we need a second TD-NRG run to construct the $X(n)$ and $Y(n,n')$ matrices. On each iteration, $X(n)$ is diagonalized and $\rho(n;t)$ is constructed via Eq. (6.1.7.48). The time integral can either be calculated analytically or numerically. The analytical expression is rather complicated, since it includes multiple nested integrals over exponential functions. In any case, it should be stressed that this approach is relatively fast, since the matrices $X(n)$ have the dimension $dN_{\mathrm{S}} \times dN_{\mathrm{S}}$, which is equal to the size of the NRG Hamiltonian, and can thus be diagonalized quite efficiently. Simultaneously, the BRTs for the ODDM are set up for each iteration and then stored on the hard drive together with the DDM $\boldsymbol{\rho}(n;t)$. Alternatively, if the analytical integration is chosen, it would be sufficient to save the matrices $X(n)$ and $Y(n,n'), n' < n$. Finally, on the backward TD-NRG run the DDM and the ODDM are combined to construct the time-dependent $O_{\mathrm{S}}(t)$ via Eq. (6.1.5).

A more simple, but at the same time more runtime consuming alternative would be to directly solve the master equation

$$\dot{\rho}^{\mathrm{red}}_{l_1l_1}(n_1;t) = -\sum_{n_2=n_{\min}}^{N_{\mathrm{C}}}\sum_{l_2} R_{l_1,l_2}(n_1,n_2)\rho^{\mathrm{red}}_{l_2l_2}(n_2;t) \tag{6.1.7.49}$$

by diagonalizing the BRT

$$R_{l_1,l_2}(n_1,n_2) = \sum_{n_3=n_{\min}}^{N_\mathrm{C}} \sum_{l_3} [\Xi_{l_1 l_3}(n_1,n_3)\delta_{n_1,n_2}\delta_{l_1,l_2}] - \Xi_{l_2 l_1}(n_2,n_1). \tag{6.1.7.50}$$

Here we choose $\mathbf{1}_{N_\mathrm{C}}$ as a complete basis set to obtain a master equation that only includes discarded states. The BRT (6.1.7.50) is a large matrix that couples all NRG iterations. Therefore, its dimension is $dN_\mathrm{S}(N_\mathrm{C} - n_{\min})$. The calculation of all tensors $(F_m)^{r_1}_{r_2}(n_1,n_2)$ that appear in the BRT (6.1.7.50) is theoretically possible via the procedure detailed in Sec. 6.1.4. However, since the weight of the components of the BRT shrinks exponentially with increasing $|n_1 - n_2|$, the tensor $\Xi_{l_1 l_2}(n_1,n_2)$ is calculated exactly only for $|n_1 - n_2| \leq 1$. A tridiagonal $\Xi_{l_1 l_2}(n_1,n_2)$ is already sufficient to guarantee the conservation of the trace. This can be seen by a summation over all discarded states in Eq. (6.1.7.43). Precisely, we obtain

$$\sum_{n_1=n_{\min}}^{N_\mathrm{C}} \sum_{l_1} \dot\rho^{\mathrm{red}}_{l_1 l_1}(n_1;t) = - \sum_{n_1=n_{\min}}^{N_\mathrm{C}} \sum_{n_2=n_1-1\geq n_{\min}}^{n_1+1\leq N_\mathrm{C}} \sum_{l_1,l_2} \Big[\Xi_{l_1 l_2}(n_1,n_2)\rho^{\mathrm{red}}_{l_1 l_1}(n_1;t) - \Xi_{l_2 l_1}(n_2,n_1)\rho^{\mathrm{red}}_{l_2 l_2}(n_2;t)\Big]. \tag{6.1.7.51}$$

The conservation of the trace is shown by switching $n_1 \leftrightarrow n_2$ and $l_1 \leftrightarrow l_2$ in one of the two terms on the r.h.s. of the equation which leads to $\mathrm{Tr}\dot\rho_\mathrm{S}(t) = 0$. At first, it might seem confusing, that the trace is already conserved in the tridiagonal case. In fact, even the diagonal case $\Xi_{l_1 l_2}(n_1,n_2) \propto \delta_{n_1,n_2}$ conserves the trace, as has been explained above. However, this SSA in combination with the decoupling of kept and discarded states is a very rough approximation that does not include any source term effect, since the iterations are not connected. In the tridiagonal case, all iterations are connected and information is allowed to flow from the high-energy states down to the low-energy ones. Since a direct coupling of distant iterations $|n_1 - n_2| \gg 1$ is not included, this information flow is expected to be rather slow though. For that reason, we propose an approximation for the tensors $\Xi_{l_1 l_2}(n_1,n_2)$ with $|n_1 - n_2| > 1$. In fact, the explicit form of $\Xi_{l_1 l_2}(n_1,n_2)$ is of less importance, since as long as

$$\Xi_{l_1 l_2}(n_1,n_2) \propto f_\beta(E^{n_2}_{l_2} - E^{n_1}_{l_1}) \tag{6.1.7.52}$$

is fulfilled, the correct steady-state of the density matrix (which is the Boltzmann-distribution) is always reached for $t \to \infty$. The other components of $\Xi_{l_1 l_2}(n_1,n_2)$ only influence the relaxation rate and the short-time dynamics. Furthermore, as explained above, the single components with $|n_1 - n_2| > 1$ are expected to be exponentially small, and so their exact value is of little importance. It is rather their sheer number and their role as mediators between distant iterations that makes them important for the correct relaxation time of the density matrix. To find an adequate approximation for particular components, we concentrate on approximating the most complicated part of $\Xi_{l_1 l_2}(n_1, n_2)$, which is the chain operators. In fact, we propose to choose

$$(F_m)^{r_1}_{r_2}(n_1, n_2) = \mu \delta_{Q_1, Q_2+1} d^{\min(n_1, n_2) - n_2} \tag{6.1.7.53}$$

which covers the degeneracy in the EDOF, the correct subspace combinations and, by that, it also reproduces the correct scaling of the exact equation. Here Q_i stands for the number of particles in the subspace of the state r_i. The chain operator $f_m^{(\dagger)}$ annihilates (creates) a particle, and thus the tensor only has contributions for specific indices r_1, r_2. If the chain operators have an additional flavor index, e.g. a spin or a channel DOF, these restrictions to the states have to be covered by additional Kronecker-deltas. The factor μ is of entirely artificial origin and allows for a scaling of these approximative components. Per default, $\mu = 1$.

We investigate the effect of coupling all NRG shells in the master equation for the density matrix and depict the results in Fig.6.4.

In the simple SSA (blue curve) the trace of the density matrix decreases, since information of the iterations $n < N_\mathrm{C}$ is lost over time, and so the curve drops to an unphysical steady-state, which lies significantly below the real steady-state of the Boltzmann-distribution. By including the kept-kept sector for $t > 0$ (orange curve) the trace is conserved and the NRG equilibrium value, i.e. the Boltzmann-distribution indicated by the black arrow, is met with machine precision. Since for all solid curves of Fig. 6.4 a z-averaging with $N_\mathrm{z} = 4$ has been used, the $N_\mathrm{z} = 1$ version of the curve is added as an orange dashed line. Here the effect of the z-averaging becomes apparent, since it damps the unphysical oscillations. For the green curve we have chosen the SSA and additionally decoupled the kept states from the discarded states in the master equation. In other words, we have solved the master equation (6.1.7.49) with the restriction of a diagonal tensor $\Xi_{l_1 l_2}(n_1, n_2) \propto \delta_{n_1, n_2}$. Here the trace of the density matrix is conserved for all times, since no information from the high-energy states is lost into the kept-kept sector. However, this also implies that the terms $Z_n^\mathrm{disc}(t)$ do not relaxate in a correct way. Hence, even though the density matrix comprises the Boltzmann-

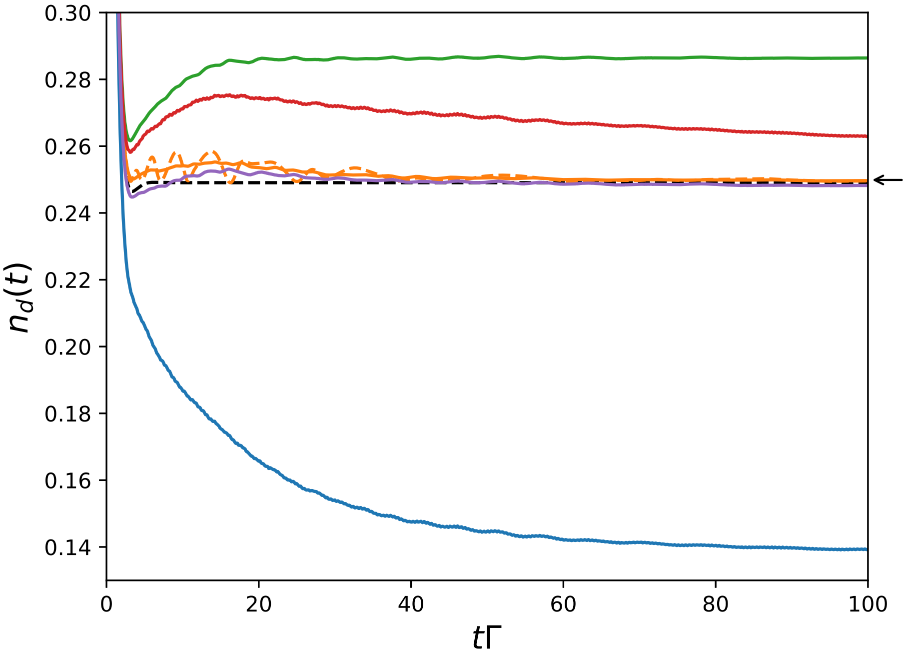

Figure 6.4.: Impurity occupation $n_\mathrm{d}(t)$ versus $t\Gamma$ in the RLM for $N_\mathrm{C} = 50, \Lambda = 1.59, D = 1000\Gamma, T = 0.01\Gamma$. The Lamb-shift is set to zero. We have performed a z-averaging with $N_\mathrm{z} = 4$. The number of kept states is chosen as $N_\mathrm{S} = 1000$. We compare the SSA (blue, orange, green) to a coupling of adjacent shells (red) and an approximate coupling of all shells (purple). The blue and orange curves include kept and discarded states, while the green curve only couples discarded states in the density matrix. In the orange curve, all kept states are included in the final expression, as for the green curve in Fig. 6.3. The black arrow on the right indicates the equilibrium NRG value. The analytical solution is added as a black dashed line. The $N_\mathrm{z} = 1$ counterpart to the orange curve is added as a dashed line.

distribution for $t \to \infty$, a wrong steady-state is reached. This fundamentally changes when adjacent shells $|n_1 - n_2| = 1$ are included in $\Xi_{l_1 l_2}(n_1, n_2)$ (red curve). Now the correct steady-state can be reached for $t \to \infty$, since all information will flow from the high-energy to the low-energy states, if t is chosen sufficiently high. However, the relaxation time clearly is significantly too low. The reason lies in the fact, that terms with $|n_1 - n_2| \approx N_\mathrm{C} - n_\mathrm{min}$ are missing in $\Xi_{l_1 l_2}(n_1, n_2)$, which means that the highest energy states do not couple directly to the lowest energy states, but instead have to take the "long route" via all iterations that lie between n_1 and n_2. For that reason, we have included a coupling of all shells with approximate values for the chain operators for $|n_1 - n_2| > 1$ (purple curve). Here the relaxation rate is met correctly, and the short time dynamics seems to be even more accurate than for the orange curve. However, one has to keep in mind, that though the approximation (6.1.7.53) is considered to have the correct magnitude on average, its concrete impact on the dynamics cannot be estimated. In this context, the short time behavior of the purple curve in Fig. 6.4 is to be taken with caution. Furthermore, the BRT (6.1.7.50) that couples all shells is relatively large, as discussed above. For that reason, an exact diagonalization is no longer possible. We use a Lanczos-method instead, to numerically calculate the relevant eigenvalues. This method is rather efficient here, since the BRT is a sparse matrix due to the Kronecker-delta in Eq. (6.1.7.53). The Lanczos-method induces an unevitable numerical error to the results. Its accuracy is defined by the "Lanczos-depth" m_{Lan} which we have chosen to be 1000 for the results shown in Fig. 6.4. On the one hand, this Lanczos-depth is a measure for the maximum time we can reliably resolve the calculated curve. In our case, this time is chosen to be large enough to guarantee that the density matrix is relaxated before significant errors occur. This way, the occupation number has a constant steady-state for all times. On the other hand, the Lanczos-depth controls the accuracy of the m_{Lan} calculated eigenvalues and -vectors of the BRT. This numerical inaccuracy is the cause for the minor oscillations of the red and purple curve, as well as the fact, that the steady-state is not met exactly for the purple curve. However, for $m_{\mathrm{Lan}} = 1000$ the diagonalization of the BRT for DDM is already the bottleneck of the program and thus could not have be chosen higher on our workstations. In the following section 6.1.8, the Lanczos-method, adapted to our case, is discussed in more detail.

6.1.8. Biorthogonal Lanczos Method

This section is intended to give a short introduction to the biorthogonal Lanczos method [116] for diagonalizing non-hermitian matrices $R \neq R^{\dagger}$. The main intention, however, is to adapt the Lanczos method to the particular case of diagonalizing the BRT of Eq. (6.1.7.50). The Lanczos method is a diagonalization scheme that calculates the m_{Lan} extreme eigenvalues of R. Their corresponding eigenvectors can be obtained as well which, in turn, requires more memory capacity. The bottleneck of the method regarding its complexity is a matrix-vector multiplication, which has to be performed $2m_{\mathrm{Lan}}$-fold in the course of the algorithm. If m_{Lan} is chosen to be much smaller than the dimension D of R, the method is efficient for diagonalizing R. Another factor for the efficiency is the sparseness of R, which can be exploited to accelerate multiplications. The BRT of (6.1.7.50) is sparse, since only specific combinations of states contribute to the BRT, as has been argued above. The BRT of the DDM is real, but the Fermi-functions cause it to be non-symmetric and thus the biorthogonal version of the Lanczos method is required.

The conventional Lanczos method starts by choosing a, to some degree, arbitrary normalized starting vector $\boldsymbol{\varphi}_0$ and than spanning the so-called Krylov-space

$$\mathfrak{K}^{m_{\mathrm{Lan}}} = \{\boldsymbol{\varphi}_0, R\boldsymbol{\varphi}_0, ..., R^{m_{\mathrm{Lan}}-1}\boldsymbol{\varphi}_0\}. \tag{6.1.8.54}$$

This Krylov-space is then orthonormalized by a Gram-Schmidt method to obtain the m_{Lan} Lanczos-vectors φ_i, where $i = 0$ serves as a point of reference for the orthonormalization procedure. The Lanczos-vectors can thus be written as a linear combination of the Krylov-space vectors. As a by-product of the Gram-Schmidt procedure, a tridiagonal matrix T of dimension $m_{\mathrm{Lan}} \times m_{\mathrm{Lan}}$ can be constructed, whose eigenvalues (called Ritz values) are the desired m_{Lan} extreme eigenvalues of R. To obtain the corresponding eigenvectors of R (Ritz vectors), the eigenvector-matrix of T needs to be multiplied by the matrix of the Lanczos-vectors. The specific m_{Lan} Ritz vectors of R are thus a linear combination of the Lanczos-vectors and of the Krylov-space vectors at the same time.

Since for non-symmetric matrices the left and right eigenvectors generally do not coincide, the biorthogonal version of the method requires an additional left starting vector $\boldsymbol{\phi}_0$, which spans the corresponding Krylov-space with the adjungated matrix $R^\dagger$ similar to Eq. (6.1.8.54). The orthogonalization then generates left and right Lanczos-vectors $\boldsymbol{\phi}_i$ and $\boldsymbol{\varphi}_i$, respectively, which fulfill the biorthonormality criterion $\boldsymbol{\phi}_i \cdot \boldsymbol{\varphi}_j = \delta_{i,j}$. All quantities involved are no longer real, but in general complex. The explicit algorithm we have used is described in App. F and is taken from netlib.org [117].

To ensure optimal compatibility of the Lanczos method to our BRT (6.1.7.50), we have to choose the normalized version of the vector $\boldsymbol{\rho}(t = 0)$ as the starting vector for both $\boldsymbol{\phi}_0$ and $\boldsymbol{\varphi}_0$. Here $\boldsymbol{\rho}(t = 0)$ is the diagonal part of the reduced equilibrium density matrix that includes all discarded states of all truncated iterations. To justify this choice, we define R as the BRT that connects all iterations according to Eq. (6.1.7.50) and write the time-dependent DDM as

$$\boldsymbol{\rho}(t) = e^{-Rt}\boldsymbol{\rho}(t=0) = \sum_{k=0}^{\infty} \frac{(-t)^k}{k!} R^k \boldsymbol{\rho}(t=0), \tag{6.1.8.55}$$

where we have expanded the exponential function as a simple Taylor series in the second step. Obviously, the first m_{Lan} elements of the series are proportional to the vectors of the right Krylov-space (6.1.8.54). Suppose we diagonalize R exactly and find all D eigenvalues λ_α and corresponding left and right eigenvectors $\boldsymbol{w}_\alpha, \boldsymbol{v}_\alpha$. Let us divide these eigenenergies into the first m_{Lan}, that are found by the Lanczos-method as the Ritz values, and the remaining ones. As discussed above, the corresponding m_{Lan} right eigenvectors of R are part of the right Krylov-space $\mathfrak{K}^{m_{\mathrm{Lan}}}$. Since all elements of $\mathfrak{K}^{m_{\mathrm{Lan}}}$ are linearly independent, each of them is biorthogonal to the $D - m_{\mathrm{Lan}}$ left eigenvectors of R. We can exploit that fact by inserting a complete basis set of D eigenvectors into Eq. (6.1.8.55). We then divide the sum over k into the three parts

$$\begin{aligned}\boldsymbol{\rho}(t) = &\sum_{k,\alpha=0}^{m_{\mathrm{Lan}}-1} \frac{(-t)^k}{k!} \boldsymbol{v}_\alpha \boldsymbol{w}_\alpha^{\mathrm{T}} R^k \boldsymbol{\rho}(t=0) + \\ &+ \sum_{k,\alpha=m_{\mathrm{Lan}}}^{D-1} \frac{(-t)^k}{k!} \boldsymbol{v}_\alpha \boldsymbol{w}_\alpha^{\mathrm{T}} R^k \boldsymbol{\rho}(t=0) + \mathcal{O}(t^D).\end{aligned} \tag{6.1.8.56}$$

The first part contains the lowest powers of t and is thus relevant for the short-time dynamics. As it contains the Krylov-space vectors, it is biorthogonal to the remaining $D - m_{\mathrm{Lan}}$ eigenvectors of R. In this context, the Lanczos-method is exact up to times defined by m_{Lan}. In the second part the contrary argument holds. If one performs a Lanczos-method with $m_{\mathrm{Lan}} = D$ steps, one would find, that the remaining $D - m_{\mathrm{Lan}}$ eigenvectors are part of the subspace spanned by the Krylov-space vectors $R^i\boldsymbol{\rho}(t = 0)$ with $i \in \{m_{\mathrm{Lan}}, ..., D-1\}$. For that reason, the first m_{Lan} eigenvectors have no contribution here. Since D is large in our case, the third part of Eq. (6.1.8.56) will only be relevant for times, where the density matrix has already thermalized and thus this part can be neglected in our argumentation.

We have seen, that the short-time dynamics is well covered by the Lanczos method, but what can we say about the long-time behavior and the steady-state in particular? As discussed in Sec. 4.5, all eigenvalues of the BRT are semi-positive, which includes exactly one zero-eigenvalue, which is part of the DDM and thus of R. Since the Lanczos method is intended to find the extreme eigenvalues of a matrix first, we can be sure to find the zero-eigenvalue in any case and in that way the steady-state will be reached. The objective is now to choose m_{Lan} large enough that the density matrix is practically thermalized before the error of the Lanczos method grows to be significant.

It should be mentioned, that the Ritz values and vectors found be the Lanczos method are not expected to be identical to the corresponding exact eigenvalues and -vectors. In fact, with increasing m_{Lan} the extreme Ritz values converge to the exact eigenvalues, while the Ritz values in the middle cannot be trusted at all. However, only the smallest eigenvalues of R are relevant for the time evolution on intermediate and large time scales, since the MA is expected to impair the behavior on very short times in any case. Also, the choice of the correct initial states has a huge impact on the quality of the results, as has been argued above.

6.1.9. Correction of the Lamb-Shift

We have already mentioned, that the SSA is expected to generate a relatively large error in the imaginary part of the BRT and thus in the Lamb-shift. The part of the BRT, which generates the time-evolution of the DDM, is entirely real and thus the steady-state of the density matrix is not impaired by this error.

In Fig. 6.5 we present approximative curves to recover the correct Lamb-shift for the truncated OWC in the SSA. If the Lamb-shift is artificially set to zero, the truncated and the untruncated curves align (as shown in Fig. 6.2). The blue dashed curve is the exact untruncated case, where in the orange case we restrict the number of kept states to $N_{\mathrm{S}} = 100$. This value guarantees an almost complete conservation of the trace (see Fig. 6.2), while it clearly reveals the error of the Lamb-shift at the same time. Here we observe wrong oscillations in the short-time dynamics, which are damped over time, since all complex components of the BRT, relevant for the ODDM, decay to zero. The remaining curves represent an extension to the SSA by including the coupling of different shells in the unitary part of the BRT. Precisely, the terms $n' < n$ of Eq. (6.1.1.14) are recovered for $r_1 \neq r_2$. The terms $n' > n$ are already included in the kept states of n. The components $r_1 = r_2$ are real and would only impact the trace. For $n' < n - 1$ we use the approximation from Eq. (6.1.7.53) with a factor of $\mu \neq 1$. The green curve only includes the adjacent shell coupling $n' = n - 1$. It is clearly a good interpolation between the orange curve (truncated OWC without Lamb-shift correction) and the blue dashed curve (untruncated OWC). The dotted line represents the solid green curve in the FLOA. Since we observe almost no deviation, the FLOA appears to be a valid approximation, at least if $|n_1 - n_2|$ is small.

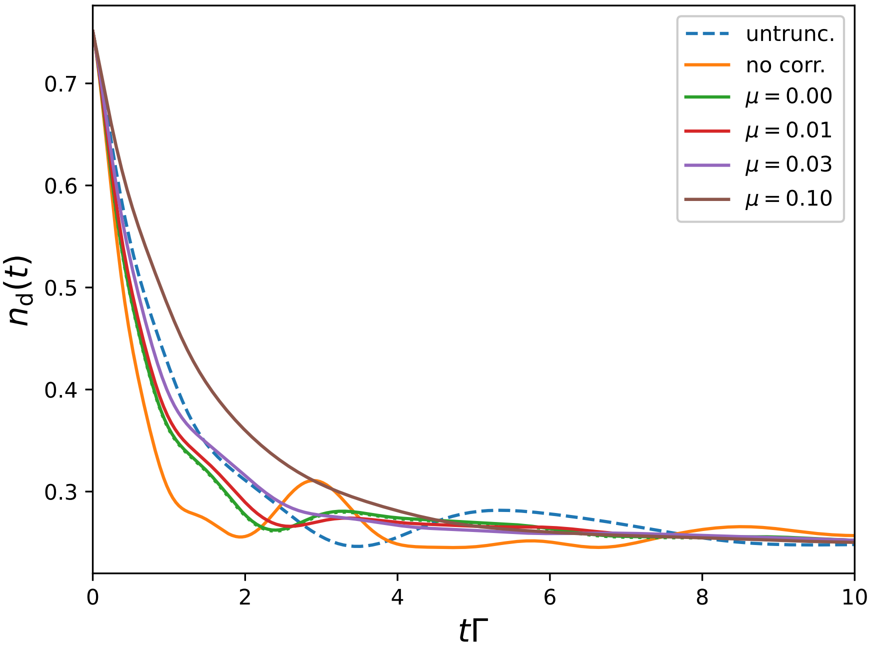

Figure 6.5.: $n_\mathrm{d}(t)$ versus $t\Gamma$ for $N_\mathrm{C} = 10, \Lambda = 10, D = 100\Gamma, T = 0.01\Gamma$. The blue dashed curve represents the untruncated case ("untrunc."), while the number of kept states is chosen as $N_\mathrm{S} = 100$ for the solid curves. Here the orange curve represents the case, where no correction to the Lamb-shift has been attempted ("no corr."). The remaining curves include the Lamb-shift correction for all iteration where the approximation (6.1.7.53) is used with the factor μ. The green curves ($\mu = 0$) consequently represent the $|n - n'| \leq 1$ case. Here the FLOA is added as a green dotted line.

When increasing μ the approximate operators are added to couple more distant iterations. When $\mu > 0.03$ the qualitative shape of the curve is significantly impaired by the approximation. For that reason we propose to choose μ fairly small. The approximation (6.1.7.53) is necessary in Fig. 6.4 to artificially obtain the correct relaxation times, but the qualitative behavior is captured fairly badly by it. A calculation of the exact operators for $n' = n - 2$ is possible in principle and would be our recommendation, if further improvement of the Lamb-shift is desired. However, we will not go this route in this thesis.

Apart from the truncation error, the influence of Λ needs to be discussed regarding the Lamb-shift. Precisely, we want to differentiate between the oscillations induced by a wrong Lamb-shift and those of the discretization error by choosing a large Λ. As in the previous cases, we have chosen a large discretization parameter $\Lambda = 10$ to illustrate

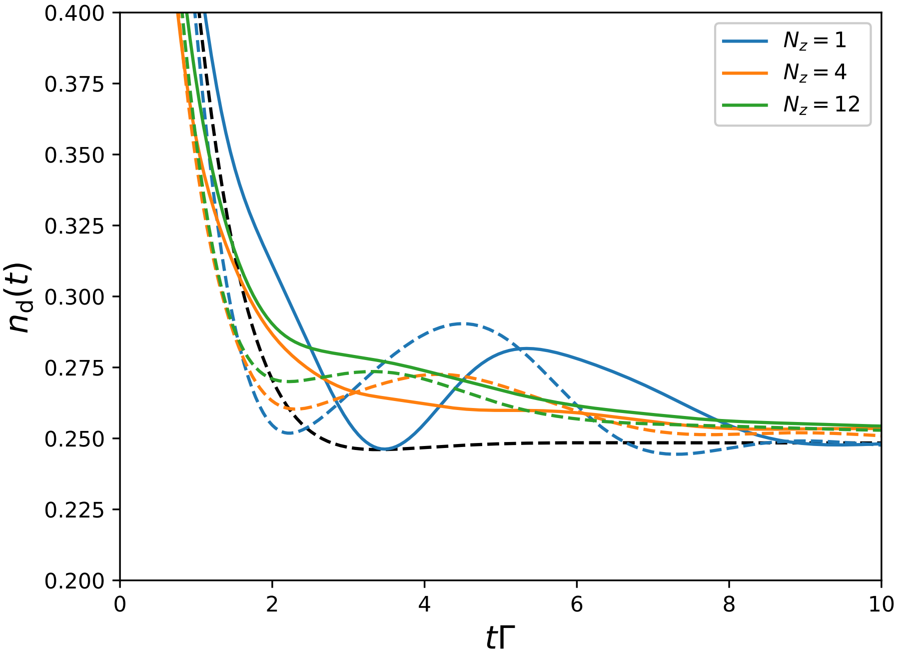

Figure 6.6.: $n_\mathrm{d}(t)$ versus $t\Gamma$ for $N_\mathrm{C} = 10, \Lambda = 10, D = 100\Gamma, T = 0.01\Gamma$. No states have been discarded. The dashed colored lines represent the curves without Lamb-shift. The z-averaging has been used with different values for N_z. The analytical solution is added as a black dashed line.

the truncation effect. For a smaller Λ the effects are significantly less pronounced for a chain of length $N_\mathrm{C} = 10$ and would only emerge if the chain is elongated and smaller energies are reached by the NRG. It is well understood (see Sec. 3.10) that a large Λ generates a large discretization error, which includes unphysical oscillations in non-equilibrium dynamics.

These oscillations are depicted in Fig. 6.6 (blue curves). Here the difference between the curves with (solid lines) and without Lamb-shift (dashed lines) is illustrated as well. The canonical way of compensating these oscillations is by implementing a z-averaging over N_z independent Wilson chains (see Sec. 3.10). As shown in the figure, this method significantly smooths the oscillations. The fact that the difference between the curves with and without Lamb-shift persists, even for $N_\mathrm{z} = 12$, shows that the oscillations induced by the Lamb-shift are not an artifact of the discretization.

6.2. Results for the Spectral Function

In the following section we discuss the adaptations, which are required to calculate OWC ESFs for a truncated system eigenbasis. The influence of the truncation of high-energy states, as well as the NRG parameters Λ and N_{C}, is investigated. We basically ourselves to methodological considerations in the RLM. The extension to interacting QIMs is covered in Chap. 7.

6.2.1. Calculation of the χ-Operator for a Truncated OWC

The calculation of the χ-operator implies different challenges compared to the density operator ρ, since it has a different subspace structure. In the master equation of the density matrix we have coupled different NRG iterations only for the DDM (see Sec. 6.1.7). In the χ-operator the diagonal elements equal zero, and so the elements $R_{aa,mm}$ of the BRT are irrelevant. From this perspective, the SSA should be sufficient, when truncating high-energy states in the master equation of χ. The imaginary part of the BRT possibly includes growing errors when the number of truncated states is increased, which is why the Lamb-shift correction (see Sec. 6.1.9) might be necessary here.

In order to validate our hypotheses, we plot the ESF of the RLM with different numbers N_{S} of kept states at each iteration in Fig. 6.7. Since the NRG is the foundation of our OCF, we take the artificially broadened CWC as a guideline for the effect of the truncation. In Fig. 6.7 (a) we can see, that the CWC ESF is basically converged for $N_{\mathrm{S}} = 100$. In contrast, the OWC curve in Fig. 6.7 (b) requires $N_{\mathrm{S}} = 500$ for convergence, suggesting that the SSA alone is not optimal in our case. To identify the source of the error, we compare the OWC (c) without Lamb-shift and (d) without dissipative part, respectively, with the complete OWC curves. We observe, that the Lamb-shift only has a minor influence on the curves and on the truncation as well. In contrast to the calculation of the density matrix, the dissipative part seems to be the relevant factor, which influences the truncation error, since the OWC curves match the convergence behavior of the CWC, when the dissipative part of the BRT is switched off. Due to the different subspace structure of the χ-operator, energy combinations $E^n_{r_1} - E^n_{r_2} = E^{n'}_{r_3} - E^{n'}_{r_4}$ with $n \neq n'$ are assumed to occur and to have a significant contribution in the master equation. However, implementing a master equation, which includes a coupling of $\chi(n;t)$ for different iterations n is not feasible at this point.

We have shown in Sec. 5.4.2, that the influence of the dissipative part of the BRT on the χ-operator becomes irrelevant if T is sufficiently small. When calculating OWC

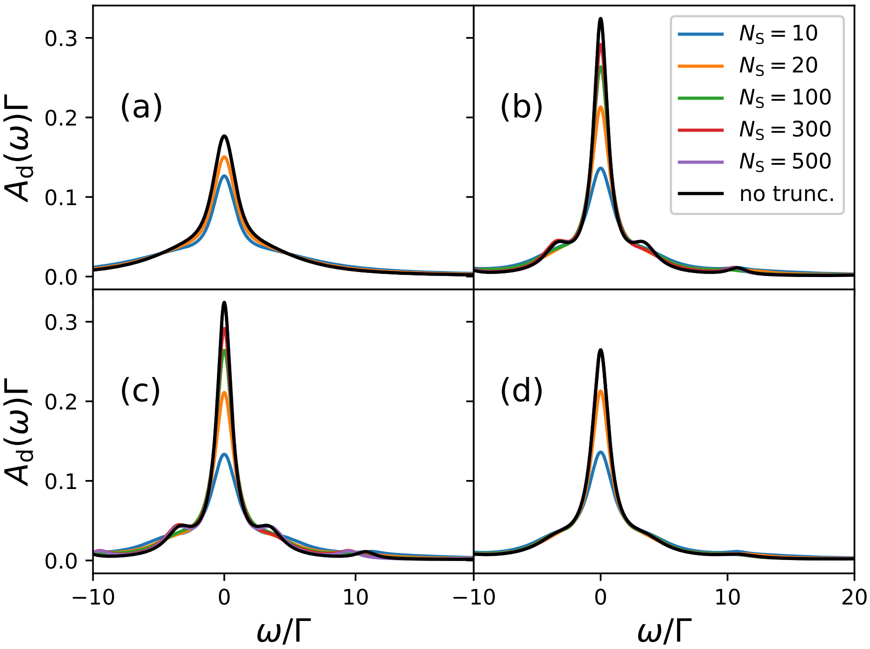

Figure 6.7.: Spectral function $A_\mathrm{d}(t)$ versus dimensionless energy ω/Γ for $N_\mathrm{C} = 10, \Lambda = 2, D = 100\Gamma, T = \Gamma$ in the RLM with $\epsilon_\mathrm{d} = 0$. The number of kept states N_S is varied and the untruncated curve is in each panel added as a black line. We plot the (a) CWC, (b) OWC, (c) OWC without Lamb-shift and (d) OWC solution without dissipative part, respectively.

ESFs with a truncated system eigenbasis we thus recommend to concentrate on the low temperature case. Here the BRT can be treated as diagonal and the coupling of different NRG iterations in the dissipative part is hence obsolete. This also significantly reduces program runtime. The imaginary part of the BRT can either be set to zero, or a Lamb-shift correction according to Sec. 6.1.9 can be implemented. In the following we choose $T \leq 0.1\Gamma$ and neglect the Lamb-shift.

6.2.2. Discretization Artifacts in OWC ESFs

Apart from the effect of truncating high-energy states, there is another source of error for the OWC ESFs. The curves in Fig. 5.20 exhibit increasing oscillations when the chain length is increased. This effect shows in TD-NEVs as well (see Fig. 5.16). By increasing the discretization parameter Λ, this effect is enhanced (see Fig. 6.6). Obviously, the unphysical oscillations are not generated by truncation of high-energy

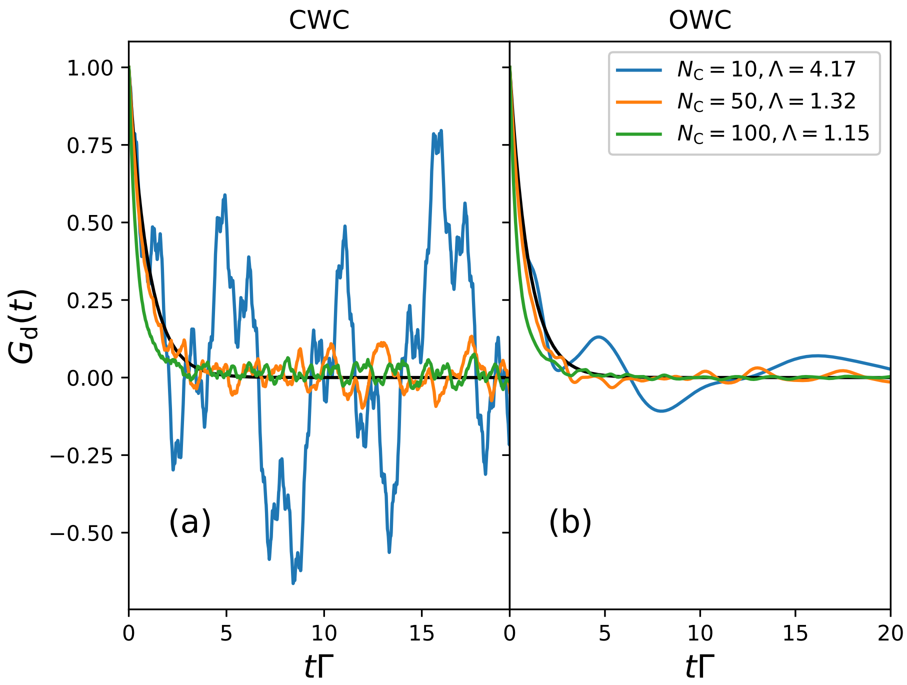

Figure 6.8.: Time-dependent equilibrium impurity Green's function $G_\mathrm{d}(t)$ with $\epsilon_\mathrm{d} = 0, D = 100\Gamma, N_\mathrm{S} = 1000$ for the RLM. The chain length N_C is varied and the discretization parameter Λ is adapted to guarantee $T = 0.1\Gamma$. On the l.h.s. we plot the CWC solution (panel (a)) and on the r.h.s. the OWC solution (panel (b)). The analytic solution is added as a black line.

states, but instead by the discretization of the NRG itself. We know from TD-NEVs (see Fig. 6.4), that the discretization error of a Wilson chain of an effective temperature T can be improved by decreasing Λ and simultaneously increasing N_C to maintain a fixed temperature.

In Fig. 6.8 we have applied this approach to the TD-EGF for the RLM at an effective temperature $T = 0.1\Gamma$, which approximately corresponds to the low-temperature limit. Since the function $G_\mathrm{d}(t)$ is time-dependent, it exhibits similar effects as non-equilibrium curves of local operators. Since the ESF is unambiguously connected to the TD-EGF via a Fourier transform, the latter is a perfect testing ground for the OCF.

The oscillations of $G_\mathrm{d}(t)$ are significantly reduced in the CWC solution in Fig. 6.8, if Λ is lowered, and the short-time dynamics approaches the exact solution. The OWC solution is identical to the CWC solution with additional natural damping of the oscillations. Thus the OWC exhibits the expected behavior, which is similar to OWC non-equilibrium dynamics, although some oscillations remain, that are damped only on very large time scales (not shown). This indicates, that some eigenvalues of the BRT that correspond to relevant excitations of the Wilson chain are too small to induce a significant damping. This behavior has already been observed for the ODDM in TD-NEVs and has been countered by z-averaging (see Fig. 6.4). Since the discretization error of $G_{\mathrm{d}}(t)$ translates to unphysical oscillations in the ESF, one is advised to incorporate z-averaging. We will leave this to future investigations and concentrate on the effect of lowering Λ on the discretization error in ESFs.

By lowering Λ, while still maintaining a constant effective temperature, the chain length needs to be increased. For long OWCs a truncation of the system eigenbasis is inevitable. However, if one truncates a significant number of high-energy states with a small $\Lambda \to 1^+$, a large truncation error can be expected. We accept this error in our investigations to illustrate the discretization effect on ESFs. However, we then require a way to distinguish the discretization error from the truncation error, i.e. we need benchmark curves, that include an analog truncation error, without suffering the discretization error. Obviously, the exact solution for the RLM is not suitable here. The CWC curves include the truncation error, however the Gaussian broadening of the curves is artificial and to a small degree arbitrary, even for small ω. For that reason we introduce a different, more natural broadening scheme for the CWC spectrum, that will serve as a benchmark to assess the discretization effect of the OWC curves for a truncated system eigenbasis.

6.2.3. Comparison of Different Broadening Schemes

In Fig. 6.9 we illustrate the discretization effect on ESFs. The OWC solution (Fig. 6.9 (c)) exhibits large oscillations, induced by finite-size effects, that are reduced when Λ is lowered, while simultaneously maintaining a fixed effective temperature by increasing the chain length N_{C}.

In Fig. 6.9 (a) the canonical Gaussian broadening scheme of the CWC ESF (see Eq. (3.8.49)) is displayed. Here for $|\omega| < 0.22\Gamma$ the Lorentzian broadening (see Eq. (3.8.50)) is used.

Friedel's sum rule demands $A_{\mathrm{d}}(\omega = 0)\Gamma\pi = 1$. The curves in Fig. 6.9 clearly violate this rule, especially for low Λ. This is partially due to the truncation error, which is generated by choosing a number of $N_{\mathrm{S}} = 1000$ kept states at each iteration. A small discretization parameter even enhances this effect. Nevertheless, in the OWC curves of Fig. 6.9 (c) we cannot trivially distinguish between the truncation effects and the errors induced by the discretization. As mentioned above, the CWC solution with

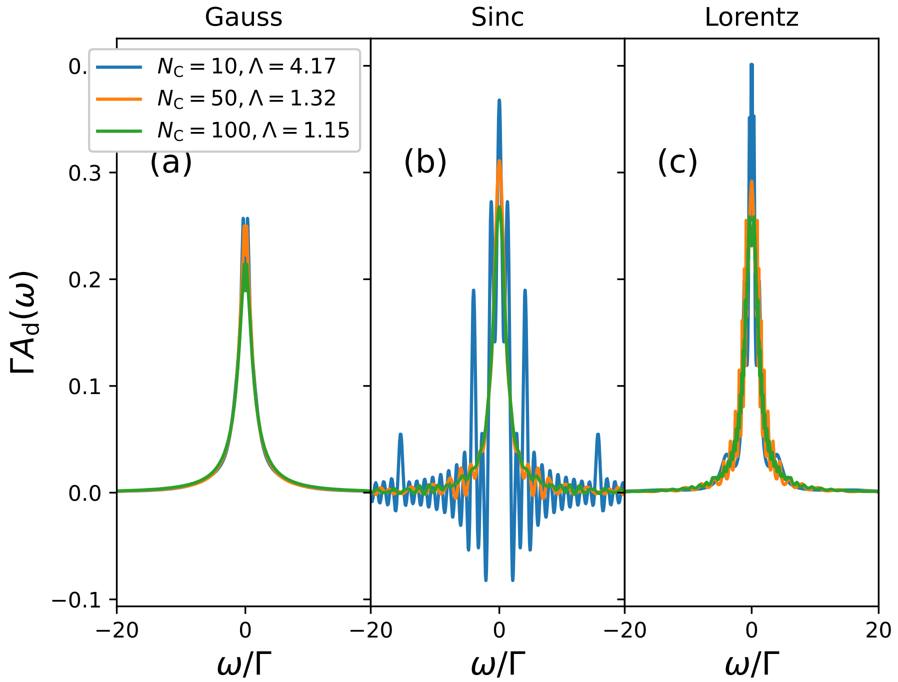

Figure 6.9.: Equilibrium impurity spectral function $A_\mathrm{d}(t)$ with $\epsilon_\mathrm{d} = 0, D = 100\Gamma, N_\mathrm{S} = 1000$ for the RLM. The chain length N_C is varied and the discretization parameter Λ is adapted to guarantee $T = 0.1\Gamma$. We compare the canonical Gaussian CWC broadening with $b = 0.8$ (panel (a)) to the sinc-broadening with $\gamma = 0.2\Gamma$ (panel (b)) and Lorentzian broadening by the BRF (panel (c)).

Gaussian broadening in panel (a) does not provide a reliable benchmark for the OWC solutions here, since the broadening is artificial.

In Fig. 6.9 (b) we depict $A_\mathrm{d}(\omega)$ obtained by a sinc-broadening. This broadening is based on the assumption, that the CWC TD-EGF

$$G_{\mathrm{d,CWC}}(t) = -i\Theta(t)\sum_{ab} d_{ab}\chi_{ba}(0)e^{i\omega_{ab}t} \tag{6.2.3.57}$$

approaches the exact physical solution for short-times $t \leq T$, if Λ is sufficiently small. The time T can be increased by increasing N_C. Since $G_\mathrm{d}(t)$ converges to zero for $t \to \infty$, we can always choose the parameters in such a way, that for $t = T$ the GF has sufficiently decayed. Thus we define the energy-dependent approximate GF as

$$G_{\mathrm{d,CWC}}(\omega) = \int_0^T dt G_{\mathrm{d,CWC}}(t) e^{i\omega t} = -\sum_{ab} d_{ab}\chi_{ba}(0)\frac{e^{i(\omega+\omega_{ab})T}-1}{\omega+\omega_{ab}} \tag{6.2.3.58}$$

and the spectral function is consequently given as

$$A_{\mathrm{d,CWC}}(\omega) = \frac{1}{\pi\gamma}\sum_{ab} d_{ab}\chi_{ba}(0)\mathrm{sinc}\left(\frac{\omega+\omega_{ab}}{\gamma}\right) \tag{6.2.3.59}$$

with the broadening $\gamma = 1/T$ and $\mathrm{sinc}(x) = \sin(x)/x$. According to Fig. 6.8 (b), $G_{\mathrm{d}}(t)$ has, for a sufficiently small Λ, effectively decayed to its theoretical steady-state at $T = 5/\Gamma$, i.e. $\gamma = 0.2\Gamma$. Given that it is chosen small enough, the precise choice of the broadening γ has only a numerical impact on the solution and not a physical one. Details on the sinc-broadening can be found in App. G. Here we illustrate, exemplarily for the RLM, that a superposition of different oscillations, as they occur in the CWC TD-EGF in Eq. (6.2.3.57), can reproduce decoherence up to a certain time T. This time T is finite, but arbitrary, if the numerical accuracy is adequately adapted by increasing the system size. One can thus choose T for the TD-EGF arbitrarily, as long as $G_{\mathrm{d}}(t)$ has sufficiently thermalized for $t \geq T$ and as long as N_{C} is chosen large enough to guarantee for a sufficient numerical accuracy. In turn, the arbitrariness of T and the broadening $\gamma = 1/T$, respectively, support the assumption, that the sinc-broadening is a natural broadening, which is effectively not impacted by the choice of T. We can thus assume, that the curves of Fig. 6.9 (b) are correct in the limit of the truncation and the discretization error, whereby the discretization error is reduced in the green curve. The latter shows a good agreement with the green OWC curve of Fig. 6.9 (c), suggesting, that the broadening induced by the BRT is of the correct order of magnitude.

6.3. Comparison to the Auxiliary Master Equation Approach

Dorda *et al* [45, 46] proposed an approach, which is in some way similar to the OCF. After we have revised our approach in detail, we now compare it to the AMEA for QISs. Here a number of N_{B} discrete modes are extracted from the bath to form an auxiliary system and are coupled to the impurity (central region). In contrast to the OCF, the AMEA is not restricted to Wilson chains, but allows for an arbitrary set of energy levels and hybridizations in the system. The auxiliary modes are then coupled to continuous reservoirs via a Lindblad approach [47, 48] to form a buffer zone [42, 43, 44] between the impurity and the bath. This approach implies Markovian reservoirs, however, the resulting local dynamics is non-Markovian, as in the case of the OWC. The precise Lindblad master equation to calculate the reduced time-dependent density matrix in the interaction picture is given by

$$\begin{aligned}\dot{\rho}_{\mathrm{S}}^{\mathrm{I}}(t) = &-\sum_{i,j}\Gamma_{ij}^{(1)}\left(\{\rho_{\mathrm{S}}^{\mathrm{I}}(t), f_i^\dagger f_j\} - 2f_j\rho_{\mathrm{S}}^{\mathrm{I}}(t)f_i^\dagger\right)\\ &-\sum_{i,j}\Gamma_{ij}^{(2)}\left(\{\rho_{\mathrm{S}}^{\mathrm{I}}(t), f_j f_i^\dagger\} - 2f_i^\dagger\rho_{\mathrm{S}}^{\mathrm{I}}(t)f_j\right). \qquad (6.3.60)\end{aligned}$$

To define the auxiliary system, as well as the Lindblad parameters $\mathbf{\Gamma}^{(1/2)}$, a fit is performed, which is intended to optimize the effective bath hybridization function of the system (cf. Sec. 5.1) with respect to the physical one for a given number N_{B}. Dorda *et al* restricted their calculations to a particle-hole symmetric SIAM, to reduce the number $C(N_{\mathrm{B}})$ of free fit parameters. Additionally, they compared different geometries of the auxiliary system, which significantly reduce $C(N_{\mathrm{B}})$ as well, and found that a double chain is significantly superior to a single chain or a star geometry to reproduce a flat DOS [46]. Since the OWC corresponds to a single chain with on-site reservoir coupling in this picture, the findings suggest, that the Wilson chain is an inadequate choice for a buffer zone.

However, one can not simply compare the Lindblad formalism to our BRF. To reproduce the chain geometry in the system, one has to set $i = j$ in Eq. (6.3.60), which then translates to the summation index n over the single chain sites in Eq. (5.2.42). To turn the Lindblad equation (6.3.60) into a Bloch-Refield equation (4.3.36), two steps are still missing that reveal the complexity of the latter. Firstly, the introduction of the secular approximation, i.e. the Kronecker-delta, allows one to exploit the block-diagonal structure of the BRT and thus to efficiently diagonalize it. In contrast, Dorda *et al* diagonalize the entire tensor using Lanczos exact diagonalization or matrix product states [46]. Secondly, and most importantly, the operator $\Gamma_n^{(1/2)} f_n$ needs to be turned into a different operator, that is a complex combination of the system operator f_n and the corresponding RGF $C_n(\omega)$ (see Eq. (4.3.36)), evaluated at an energy, which depends on the components of the system operator. Precisely, this means

$$\Gamma_n^{(1/2)} \langle a| f_n |b\rangle \to C_n(E_a - E_b) \langle a| f_n |b\rangle \,, \qquad (6.3.61)$$

with $|\alpha\rangle$ being a system eigenstate with the corresponding eigenenergy E_α. The r.h.s. of Eq. (6.3.61) is thus a complex operator, that is not linearly dependent on f_n, and thus the Bloch-Redfield master equation (4.3.37) cannot be reproduced by the l.h.s. of the equation, i.e. the Lindblad equation (6.3.60). To achieve this, in each term of the Lindblad equation one of the system operators would have to be replaced by an entirely new operator, whose components would need to be included in the fit process. This, in turn, would render the fitting of the auxiliary system effectively infeasible. In contrast, the Bloch-Redfield equation could be turned into a Lindblad equation by assuming $C_n(\omega) = const.$ This implies the high-temperature and wideband limits, respectively, as well as a constant reservoir coupling function $\Gamma_n(\omega)$ (see Eq. (4.3.35)).

Despite the incompatibility of both approaches, two key points might be transferred to the OCF. Firstly, the bath hybridization function is an excellent measure for the quality of the approximation. In the case of the OWC, we guarantee to maintain this function by the implementation of the CFE (see Sec. 5.1), but then distort it to a certain degree by the BMA. By calculating the bath hybridization function of the OWC from the GF of the zeroth Wilson chain site, while decoupling the impurity (i.e. setting $V = 0$), one would obtain a measure for the quality of the BMA, that only depends on the size and the shape of the OWC, i.e. on N_C and Λ, respectively. Secondly, the superiority of the double chain in relation to the single chain in the AMEA might inspire one to consider two OWCs, by splitting the bath into a high- and a low-energy part, before constructing the chains. This would render a high-energy chain with a gapped bath hybridization function and an additional low-energy chain with a renormalized bandwidth. In general, one could imagine to investigate numerous buffer zone geometries in the AMEA with respect to their bath hybridization function convergence per $C(N_\mathrm{B})$. The best choice is then reproduced rigorously as close as possible in the spirit of the OWC, which would give a physical justification to the approach, as well as render a possible opportunity to exploit a truncation scheme or system symmetries.

6.4. Summary

One of the key components of the NRG is the truncation of high-energy states, which allows for the CPU time to increase linearly with the Wilson chain length, instead of exponentially. To exploit this effect with the OCF, the ASB needs to be inserted in the master equation of the density matrix, leading to a coupling of all energy shells of the NRG. Since a full treatment of this master equation is infeasible on modern workstations, we discussed several approximations and their impact on the OWC solution in this chapter.

For TD-NEVs a time-dependent density matrix is calculated via the master equation. Here it turned out to be sufficient to couple different shells in the DDM only, to guarantee physical behavior such as the conservation of the trace and a correct thermalization. Additionally, more efficient alternatives have been discussed, that artificially conserve the trace of the density matrix.

For ESFs a compound operator of the density matrix and an impurity creator is evolved in time in the master equation. Due to its inner structure, this operator has a trace of zero, which renders a conservation of the trace obsolete. In contrast, the coupling of different iterations is relevant for the dissipative part of the BRT. However, for sufficiently low temperatures, this part has no influence on the compound operator and can safely be neglected.

The imaginary part of the BRT enters as a small Lamb-shift in all OWC results. When truncating high-energy states, this Lamb-shift has shown to induce a disproportionately large error. We outlined a procedure how to compensate this error, however, we chose to simply neglect the Lamb-shift for practical reasons.

The discretization scheme of the NRG is known to induce a finite-size error to the system. This error has an influence on OWC dynamics in both TD-NEVs and TD-EGFs, which is especially strong on intermediate time scales, where the relaxation terms have not yet damped the unphysical finite-size oscillations. In ESFs these oscillations occur analogly, effectively washing out low-energy information of the spectrum. Here the z-averaging is a simple scheme to compensate for this finite-size error, as has been shown for TD-NEVs. In ESFs we leave the investigation of the compensation of finite-size effects to future works.

7. Interacting Quantum Impurity Models

In Chap. 5 and 6 we have applied the OCF to the RLM to benchmark the approach with respect to the BMA and the truncation of high-energy eigenstates, respectively. In this chapter we test our formalism with relatively simple QIMs that include a local interaction term U, namely the IRLM (see Sec. 2.5) and the SIAM (see Sec. 2.4). Here no exact solutions are known, however, numerous analytical and numerical predictions to those models are available [36, 109, 13, 22, 29]. The purpose of this chapter, and of this thesis in general, is not to reveal new physics, but to establish our OCF and to assess its applicability in a variety of testing grounds.

7.1. Local Non-Equilibrium Real-Time Dynamics

In this section we investigate TD-NEVs for the IRLM and the SIAM, respectively. The results are obtained analogly to Sec. 5.4.1, but for the interacting case. When a truncation of high-energy states is applied, the trace of the density matrix is conserved by artificially normalizing $n_\mathrm{d}(t)$ with the numerically calculated $\mathrm{Tr}\rho(t)$, if not stated otherwise.

7.1.1. Interacting Resonant Level Model

We proceed to our first non-trivial QIM for the OWC by adding a Coulomb repulsion U between the impurity and the zeroth Wilson chain site. This is denoted by the IRLM. The impurity Hamiltonian becomes

$$H_\mathrm{imp} = \epsilon_\mathrm{d} d^\dagger d + V\left(d^\dagger f_0 + d f_0^\dagger\right) + U\left(d^\dagger d - \frac{1}{2}\right)\left(f_0^\dagger f_0 - \frac{1}{2}\right). \tag{7.1.1.1}$$

Here the zeroth site of the Wilson chain is included in H_imp and so the remaining OWC, as well as the zeroth reservoir, couple directly to this "super-impurity". For vanishing

U the system resembles the RLM. We will restrict the non-equilibrium dynamics to a quench with $\epsilon_{\mathrm{d}}^{\mathrm{f}} = -\epsilon_{\mathrm{d}}^{\mathrm{i}} = \Gamma$ at $t = 0$.

The impurity dynamics corresponds to an oscillation with frequency

$$\Omega = \sqrt{E_d^2 + 4V^2}, \tag{7.1.1.2}$$

which is identical to the CWC dynamics of the RLM for $N_{\mathrm{C}} = 1$, and an additional slow decay with a relaxation time τ. This motivates the analytical solution [30] for the occupation dynamics

$$\begin{aligned} n_{\mathrm{d}}(t) =& (n_{\mathrm{d}}^{\mathrm{i}} - n_{\mathrm{d}}^{\mathrm{f}})e^{-t/\tau} + n_{\mathrm{d}}^{\mathrm{f}} \\ &+ A\left(\cos(\Omega t)\sqrt{1-\cos^2(\theta)e^{-t/\tau}}e^{-t/(2\tau)} - \sin(\theta)e^{-t/\tau}\right) \end{aligned} \tag{7.1.1.3}$$

in the limit $U \gg D, T$ (see App. E). Here

$$\tau = \frac{\pi^4}{256}\frac{\Omega}{D\Gamma}\left(\frac{U}{D}\right)^2 \tag{7.1.1.4}$$

is the above mentioned relaxation time and A and θ are constants, which are to be defined by a fitting procedure. In the limit of $U/D \to \infty$ the relaxation time τ diverges, meaning that the "super-impurity" is practically decoupled from the OWC and the zeroth reservoir. For $U \to 0$ the relaxation time τ vanishes, instead of being of the order of Γ, proofing that the expression of Eq. (7.1.1.4) is not valid for small U.

Let us exemplarily compare τ of Eq. (7.1.1.4) with the relaxation rate of the shortest OWC possible in the IRLM, which has a length of $N_{\mathrm{C}} = 1$. The dominant relaxation rate in the BMA can be derived analytically as

$$\tau^{-1} = \mathfrak{Re}\Big\{C_0(U/2 - V) + C_0(U/2 + V)\Big\} \tag{7.1.1.5}$$

for $\epsilon_{\mathrm{d}} \ll D$, where $C_0(\omega)$ is the correlation function of the zeroth reservoir. Since the support of the reservoir spectral function is limited to the bandwidth, the relaxation rate is always zero for $U > 2D + 2V$, meaning that here the reservoir does not accept any charge from the system and so we basically obtain a closed system. This effect can already be seen for $U > 2V$ in the limit of $T \to 0$, since here the Fermi-functions in $C_0(\omega)$ produce a sharp cut-off.

In Fig. 7.1 the relaxation rates of Eq. (7.1.1.5) are compared to the analytical

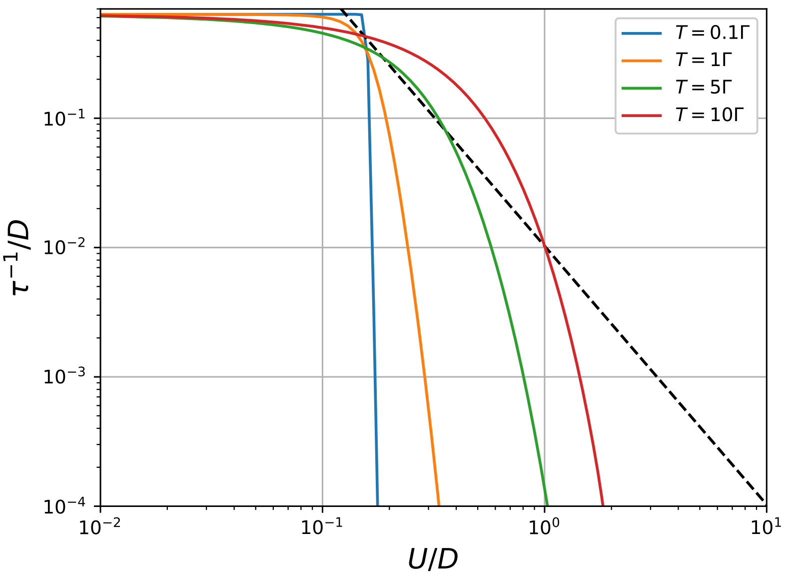

Figure 7.1.: The relaxation rates of the OWC of chain length $N_C = 1$ for different temperatures T, calculated via Eq. (7.1.1.5). As a comparison, the rate calculated according to Eq. (7.1.1.4) is added as a black dashed line. The axes are both scaled by the bandwidth D and plotted logarithmically.

prediction of Eq. (7.1.1.4) for different temperatures T. For small U both results deviate significantly from each other. In this case the OWC is superior to the analytical prediction, since the relaxation rate is finite. By increasing U, the intercept of the analytical prediction and the OWC solution is located at $U \approx 0.2D$. Here U is still considered to be small and Eq. (7.1.1.4) does not hold. For large U the OWC rates quickly drop below the analytic prediction. A behavior $\propto U^{-2}$ cannot be observed. The reason is that the relaxation rates of the OWC are always composed of the correlation functions evaluated at different Wilson chain energies. The parameter U only directly influences the eigenspectrum of the Wilson chain and not the values of the correlation functions, and so the relaxation rates cannot be a simple function of U. The inability of the OWC to reproduce $\tau \propto U^2$ clearly is a consequence of the BMA in second order, as discussed in Sec 4.7. In the following we concentrate on the effect of increasing the chain length N_C on the results, especially the relaxation times.

When comparing curves for different chain length N_C, the temperature needs to be adapted by $\overline{\beta}$, as has been done in Fig. 5.16, since a different temperature leads to different equilibrium values. A finite U has a similar effect on the curves. It has been shown (see Sec. 2.5 or Ref. [68]) that the fixed points of the IRLM are identical to those of the RLM, if Γ is replaced by an effective hybridization Γ_{eff}. This is identical to a rescaling of the energies, which allows for the equilibrium values of the IRLM to be identical to those of the RLM. The non-equilibrium dynamics, however, deviate strongly from the RLM for finite U, independent of the choice of Γ_{eff}. To be precise, a finite U effectively suppresses the coupling of the Wilson chain to the super-impurity and so charge is reflected back from the zeroth chain site to the impurity, leading to oscillations that relaxate on a time scale of τ into the chain. In the CWC of finite length we experience an unphysical revival effect at a certain time, when charge is reflected at each site of the chain back to the impurity [19]. With increasing U this effect occurs more early in time. In the limit of $U \to \infty$ dissipation is suppressed and any chain basically resembles the CWC with $N_{\text{C}} = 1$.

What is the precise influence of increasing U on short OWCs? In chains with an even number of sites the dynamics in the non-interacting case are almost entirely determined by the DDM, which yields the relaxation rate of 2Γ. When U is increased, the DDM quickly changes to be constant in time and thus it no longer has an impact on the relaxation of the system. This way, the oscillations induced by the CWC become dominant on short time scales. On longer time scales the real-part of the ODDM damps these oscillations with a lower relaxation rate and thus inhibits the revival effect. The Lamb-shift is weak and does not significantly impact the occupation dynamics.

Odd chains show a different behavior. Here the ODDM is prominent also in the non-interacting case. When increasing U the influence of the DDM again vanishes, but the relaxation rate of the ODDM is much lower than that of the even chains. In this way, the IRLM shifts the ratio of the effective relaxation rates of even and odd chains.

In Fig. 7.2 the impurity occupation $n_{\text{d}}(t)$ is displayed for two distinct sets of parameters. The CWC curves are plotted on the left and the OWC curves on the right, respectively. Obviously, the OWC has a higher relaxation rate for short times than the CWC. This is the case for all combinations of parameters and a considerable numerical inaccuracy can be excluded, since the only numerical parameter here is N_{m} (see Sec. 5.4), which is chosen high enough for sufficient convergence. One possible reason for the discrepancy between CWC and OWC relaxation rates are finite size effects in the CWC. Reflections of charge back onto the impurity can lead to a slower relaxation. These revival effects are expressed in oscillations of the envelope of the function (see the upper left panel). In the figure it is not possible to exactly estimate up to which time the CWC curves can be interpreted as approximately correct, as it is possible for the RLM . For that reason, the relaxation rate of the CWC cannot be used as a

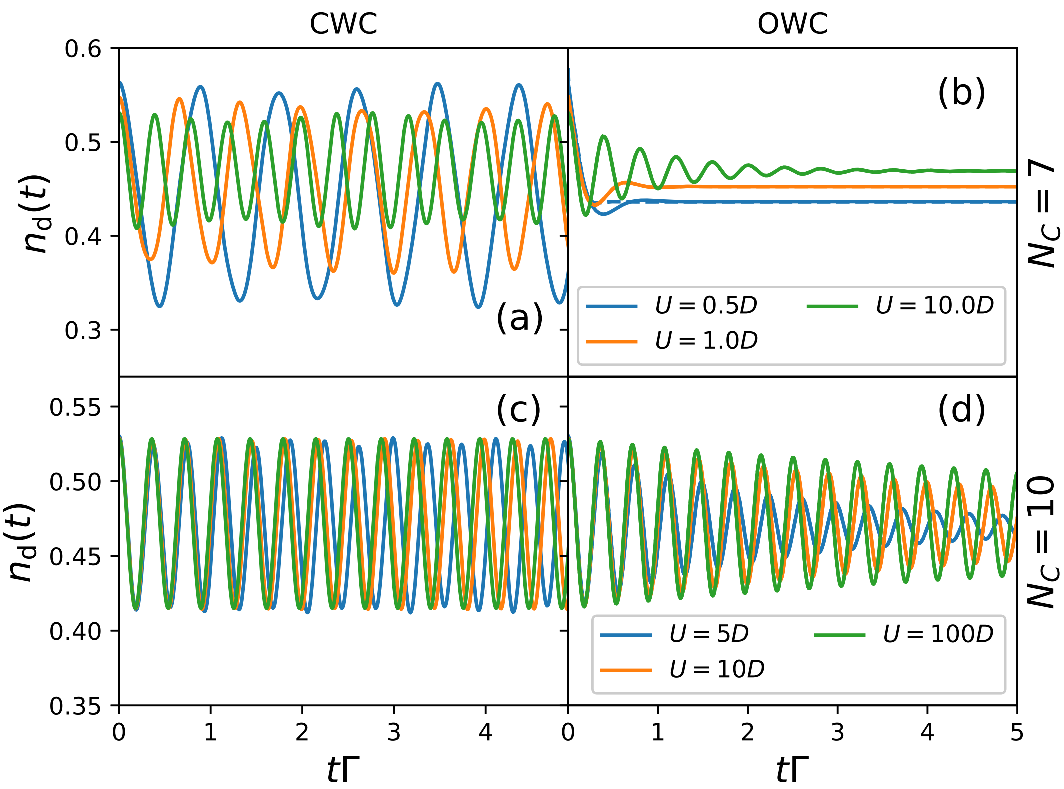

Figure 7.2.: Non-equilibrium occupation number for different parameter sets. The upper two panels (a) and (b) are created with $N_\mathrm{C} = 7, \Lambda = 2, T = \Gamma$ and the lower two panels (c) and (d) with $N_\mathrm{C} = 10, \Lambda = 5, T = 0.1\Gamma$. Different values for U are chosen, as depicted in the legends of the panel. On the l.h.s. in panels (a) and (c) the CWC results are presented, while on the r.h.s. in panels (b) and (d) the corresponding OWC version for identical parameters is shown. A fit with the function (7.1.1.3) is added as dashed lines in the same color for the OWC.

benchmark for the OWC solution.

As expected for an OQS, the OWC relaxates to the correct steady-state, while performing oscillations with a constant frequency. Increasing U increases the relaxation time τ, which is explained by the fact, that U holds back charge to the impurity and thus slows down relaxation. To estimate the quality of the OWC results we use the analytical prediction Eq. (7.1.1.3) for local non-equilibrium dynamics $n_\mathrm{d}(t)$. By choosing $\Omega = 0$, Eq. (7.1.1.3) yields the envelope function. By demanding that the first derivative of the envelope function with respect to time t is zero at $t = 0$, one obtains the restriction

$$\sin(\theta) = -\frac{A}{2(n_\mathrm{d}^\mathrm{i} - n_\mathrm{d}^\mathrm{f})}. \tag{7.1.1.6}$$

This restriction is equal to the fact that $\dot{\rho}(t) \overset{!}{=} 0$, which follows from the von-Neumann equation. However, if we apply the MA, this correct short-time behavior cannot be fulfilled by the BRF. Instead, the only possible choice is $\theta = \frac{\pi}{2}$, which reduces $n_\mathrm{d}(t)$ to a sum of exponential decay terms.

We have fitted Eq. (7.1.1.3) to the OWC data in Fig. 7.2 (dashed lines). The qualitative concordance for $U \geq D$ is significant and suggests, that Eq. (7.1.1.3) is applicable even when U is of the order of the bandwidth. For $U \geq 10D$ the fitted frequencies of the OWC comply with Eq. (7.1.1.2) within a variance of 5%. The relaxation times τ, however, are lower than predicted, and increasingly deviate from Eq. (7.1.1.4) for higher U.

To quantitatively investigate this behavior, we examine the OWC solutions for the effective hybridization Γ_eff. All parameters are now expressed in the new energy scale Γ_eff, while the ratio between the scales is $\frac{\Gamma}{\Gamma_\mathrm{eff}}$. The effective parameters are given by

$$\begin{aligned}
V &= \sqrt{\frac{2}{\pi} D\Gamma} = \sqrt{\frac{2}{\pi}\frac{D}{\Gamma_\mathrm{eff}}\frac{\Gamma}{\Gamma_\mathrm{eff}}}\Gamma_\mathrm{eff}, \\
\Omega &= \sqrt{\left(\frac{\epsilon_\mathrm{d}}{\Gamma_\mathrm{eff}}\right)^2 + \frac{8}{\pi}\frac{D}{\Gamma_\mathrm{eff}}\frac{\Gamma}{\Gamma_\mathrm{eff}}}\Gamma_\mathrm{eff}, \\
\tau\Gamma_\mathrm{eff} &= \frac{\pi^4}{256}\left(\frac{U}{D}\right)^2 \frac{\Omega}{D}\frac{\Gamma_\mathrm{eff}}{\Gamma}.
\end{aligned} \tag{7.1.1.7}$$

The ratio $\frac{\Gamma}{\Gamma_\mathrm{eff}}$ is predicted [36] as

$$\begin{aligned}
\frac{\Gamma}{\Gamma_\mathrm{eff}} &= \left(\frac{\Gamma_\mathrm{eff}}{D}\right)^\alpha \leq 1, \\
\alpha &= 2\delta - \delta^2, \\
\delta &= \frac{2}{\pi}\arctan\left(\frac{\pi}{4}\frac{U}{D}\right).
\end{aligned} \tag{7.1.1.8}$$

In the limit of $U/D \to \infty$ we obtain $\frac{\Gamma}{\Gamma_\mathrm{eff}} = \frac{\Gamma_\mathrm{eff}}{D}$. Hence, the bandwidth cancels out in all parameters and the relaxation rate is $\tau\Gamma_\mathrm{eff} \approx 0.717\left(\frac{U}{D}\right)^2$ for $\epsilon_\mathrm{d} = \Gamma_\mathrm{eff}$.

In Fig. 7.3 the rescaled curves for $N_\mathrm{C} = 7$ are plotted for the CWC (top) and the

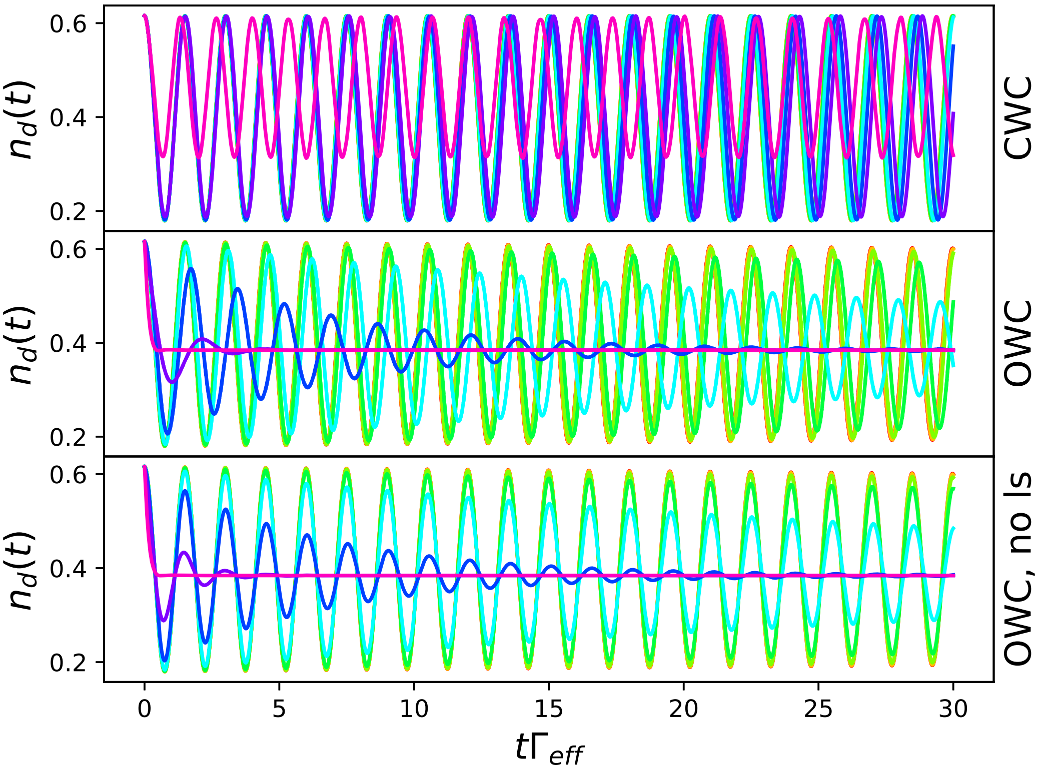

Figure 7.3.: Non-equilibrium occupation number for different U/D for $N_\mathrm{C} = 7, \Lambda = 2, D = 100\Gamma, T = \Gamma$. On the top we present the CWC, in the middle the corresponding OWC without and on the bottom the OWC with Lamb-shift. For the violet curve $U/D = 0$ has been chosen, while we have $U/D = 2^n, n \in \mathbb{N}_0$ up to the red curve. A fit with the function (7.1.1.3) is added as dashed lines in the same color for the curves with $U > D$ of the OWC with Lamb-shift.

OWC with Lamb-shift (middle) and without Lamb-shift (bottom). Γ has been rescaled to meet the equilibrium values defined by the NRG. Clearly, the CWC and the OWC (without Lamb-shift) solutions coincide in the oscillation frequency, which is given by Eq. (7.1.1.2). As already mentioned, the oscillating part of the OWC occupation number for $U \gg D$ is entirely defined by the CWC plus a small Lamb-shift, that vanishes for $U \gg D$, so this does not come as a surprise. The contribution of the DDM basically vanishes for large U and so the relaxation rate of the OWC is defined by the real-part of the ODDM.

To compare the OWC to the analytical predictions for $\Gamma/\Gamma_\mathrm{eff}, \Omega$ and τ, we have fitted the OWC curves of Fig. 7.3 with Eq. (7.1.1.3) and plotted the results in Fig. 7.4.

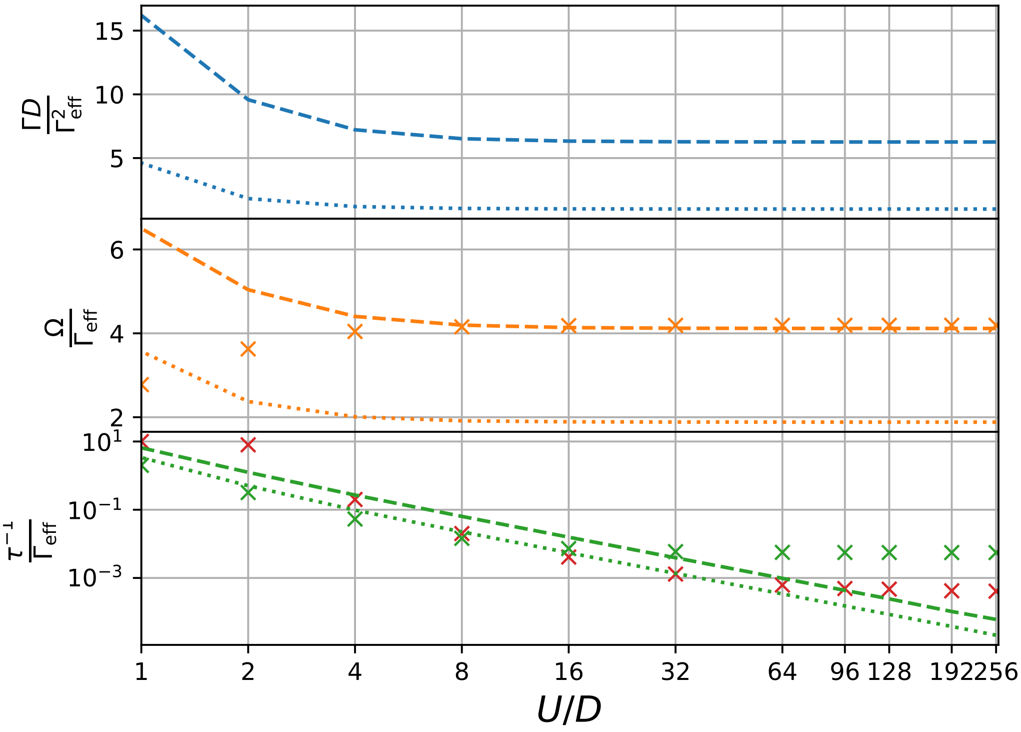

Figure 7.4.: Effective parameters $\Gamma/\Gamma_{\mathrm{eff}}$, $\Omega/\Gamma_{\mathrm{eff}}$ and $\tau^{-1}\Gamma_{\mathrm{eff}}$ for different U/D. The dotted lines are the pure theoretical predictions via Eq. (7.1.1.8) and (7.1.1.7). The dashed lines are the parameters calculated via (7.1.1.7) for a numerically determined $\Gamma/\Gamma_{\mathrm{eff}}$. The stars represent the fitted parameters of Fig. 7.3. We have chosen $N_{\mathrm{C}} = 7, \Lambda = 2, D = 100\Gamma, T = \Gamma$. The horizontal axis, as well as the vertical axis for the green curves, are chosen logarithmically. The red stars are calculated for $N_{\mathrm{C}} = 7, \Lambda = 1.2, D = 100\Gamma, T = \Gamma$, where $\overline{\beta}$ has been adapted accordingly. The red stars are additionally shifted upwards by a factor of 10^4 to facilitate their comparison with the green stars.

The parameters of Fig. 7.4 have been calculated as follows. The blue dotted curve is obtained via Eq. (7.1.1.8) with $D = 100\Gamma_{\mathrm{eff}}$, while the dashed line is obtained by comparing the equilibrium values for $U > 0$ with those of the non-interacting case and varying $\Gamma/\Gamma_{\mathrm{eff}}$ in the first case until those values align. The orange curves are calculated via Eq. (7.1.1.7). Again, we have chosen $\epsilon_{\mathrm{d}} = \Gamma_{\mathrm{eff}}$ and $D = 100\Gamma_{\mathrm{eff}}$. The dotted orange curve is calculated from the values $\Gamma/\Gamma_{\mathrm{eff}}$ from the dotted blue line and the dashed line vice versa. The orange stars are the fitted OWC parameters. The relaxation rates of the green lines are obtained via Eq. (7.1.1.7) by using the values $\Gamma/\Gamma_{\mathrm{eff}}$ and $\Omega/\Gamma_{\mathrm{eff}}$

from the dotted and dashed curves, respectively. The stars again represent the fitted parameters, while we have maintained Λ at 2 for the green stars and changed Λ to 1.2 for the red ones. For the fitting process we expanded the time-axis up to $t\Gamma = 10^6$, to reliably measure the large relaxation times that occur for larger U/D.

A systematic deviation of the fitted parameters (stars) from the analytical predictions (dotted lines) is apparent. However, if we correct the effective scale $\Gamma/\Gamma_{\text{eff}}$ for the numerically determined values (dashed lines), we obtain a much better agreement with the fitted parameters Ω. There seems to be a systematic deviation of the effective scale for the CWC equilibrium value, which seems logical in view of the fact that we have chosen a chain length of $N_{\mathrm{C}} = 7$. For longer chains we expect Eq. (7.1.1.8) to be met with more precision.

The fitted relaxation rates τ^{-1} (green stars) differ significantly from the analytical predictions (green dashed and dotted lines). Equation (7.1.1.3) only holds for large U/D, so we expect an error of the green dashed and dotted curves for small U/D. We have shown in Fig. 5.16 that the OWC relaxation rates are too large for $N_{\mathrm{C}} = 7$ in the non-interacting case, and consequently we expect the green stars to be slightly too high for small U/D in Fig. 7.4. Furthermore, the fitting process with Eq. (7.1.1.3) is not reliable here, since the fit-function is not suited for small U/D. For intermediate values of U, i.e. $U \approx 10D$, the green stars lie below the dashed line, which suggests that the relaxation rates generated by the BRT are too small, if we consider the analytical predictions to be correct in this regime. The BMA is performed in second order only, meaning that the coupling to the reservoirs, and consequently the relaxation, is too weak in this approximation. For $U > 50D$ the relaxation rates converge to a constant value, which is independent of U. This behavior is a strong contradiction to the expected U^{-2}-dependence of the relaxation rates.

To compare the influence of Λ, we added the case $\Lambda = 1.2$ as red stars, scaled by a factor of 10^4. Obviously, the relaxation rates generated for this small discretization parameter are significantly lower than those for $\Lambda = 2$. This can be explained by the fact, that the reservoir coupling is naturally weaker for small Λ. Additionally, the red stars reach their steady-state value significantly later than the green stars. In fact, in the range $U/D \in [8, 32]$ the curves exhibit the predicted U^{-2} behavior. A smaller Λ allows for a better resolution of large energies, which is to be preferred in the case $U \gg D$ and might explain the behavior of the red stars in comparison to the green ones. However, the slower convergence for smaller Λ is also in accordance with the slower convergence of the reservoirs to their steady-state (see Fig. 5.8).

Up to this point it is not clear, whether the parameters can be further aligned to the analytical predictions by varying the Wilson chain parameters. A larger Λ appears to be beneficial in the sense, that the relaxation rates approach the correct order of magnitude. However, a lowering of Λ, and consequently a slower relaxation, could possibly be compensated for by increasing the chain length. Thus we expect to improve the relaxation rates for $U \gg D$ by increasing the chain length and simultaneously choosing a relatively small Λ, which is better suited for the resolution of high energies. To attain longer Wilson chains, we proceed by introducing the truncation of high-energy system eigenstates to the IRLM.

In Fig. 7.5 we have plotted the impurity occupation $n_{\mathrm{d}}(t)$ for different values of U for relatively long Wilson chains of length $N_{\mathrm{C}} = 50$ with $N_{\mathrm{S}} = 10^3$ retained states at each NRG iteration. To extract the relaxation times τ, a fit with Eq. (7.1.1.3) has been performed. The success of this procedure is very susceptible to the correct choice of the initial value for the oscillation frequency Ω. One can either guess this value from the shape of the curves, or use the envelope function of the curves, which are obtained by artificially neglecting the CWC oscillations, i.e. setting $E_r^n - E_s^n \to 0$ in Eq. (6.1.5). The envelope function is obtained from Eq. (7.1.1.3) by setting $\Omega = 0$. Furthermore, the fitting process of the OWC curves can be simplified by choosing $\theta = \pi/2$ for all curves, as has been mentioned above. The fitting process with Eq. (7.1.1.3) confirms this choice of θ for $U \geq 4D$.

In Fig. 7.5 the fitted functions (dashed lines) deviate more from the original curves (solid lines) than in Fig. 7.3, where the differences are practically not existent. This stronger deviation can be attributed to the truncation of high-energy states in Fig. 7.5, as well as to the fact, that the OWC solution contains more different relevant relaxation rates, if the chain length is larger.

The parameters obtained from Fig. 7.5 are depicted in Fig. 7.6. The latter is an analog comparison to Fig. 7.4. In contrast, in Fig. 7.6 the relative deviation of the numerically calculated $\Gamma/\Gamma_{\text{eff}}$ is significantly reduced from approximately 650% to 13%. This is due to the higher accuracy of NRG equilibrium values for longer Wilson chains. A large value of U obviously increases the chain length N_{C}, which is necessary to reach a sufficient convergence here. The U-value at which all three parameters are effectively converged is not significantly changed. However, the most relevant difference lies in the relaxation rates τ^{-1}. In Fig. 7.4 the rates converge to a value, which is effectively constant in U for approximately $U \geq 16D$. In contrast, in Fig. 7.6 a U^{-2} dependence can be observed for $U \geq 96D$, which is the predicted physical behavior. According to

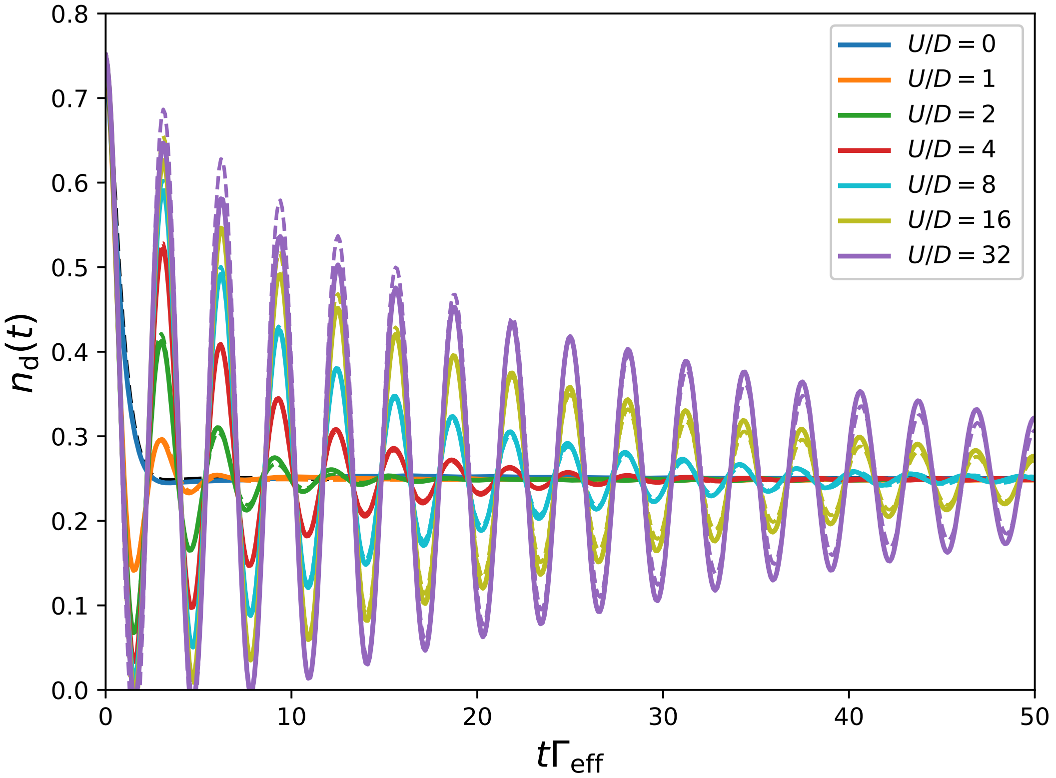

Figure 7.5.: Figure taken from Ref. [114]. Non-equilibrium impurity occupation versus dimensionless rescaled time $t\Gamma_{\text{eff}}$ for different values of U. $\Gamma/\Gamma_{\text{eff}}$ has been adapted to align the equilibrium values of the curves. The Wilson chain parameters are $\Lambda = 1.59, N_{\text{C}} = 50, D = 10^3\Gamma_{\text{eff}}$, which yields an effective temperature of $T = 0.01\Gamma_{\text{eff}}$. We retained $N_{\text{S}} = 10^3$ low-energy states at each iteration and averaged over $N_z = 4$ values of z. The Lamb-shift has been set to zero and the curves are artificially renormalized by the trace of the density matrix, since no coupling of iterations has been performed in the BRT. The non-interacting analytical solution is added as a black dashed line. The colored dashed lines are the fitted curves with Eq. (7.1.1.3).

the discussion above, we assume this is due to the longer Wilson chain in combination with a lowered Λ. We expect the relaxation rates to converge to a constant value, if U is chosen to be sufficiently large. The relaxation rates (green stars in Fig. 7.6) are too large in comparison to the analytical predictions (green dotted and dashed lines). We have shown in Fig. 7.4, that the choice of the discretization parameter impacts the steady-state, which is due to its influence on the quality of the BMA. Thus we expect a smaller Λ to better reproduce the correct steady-state of the relaxation rates.

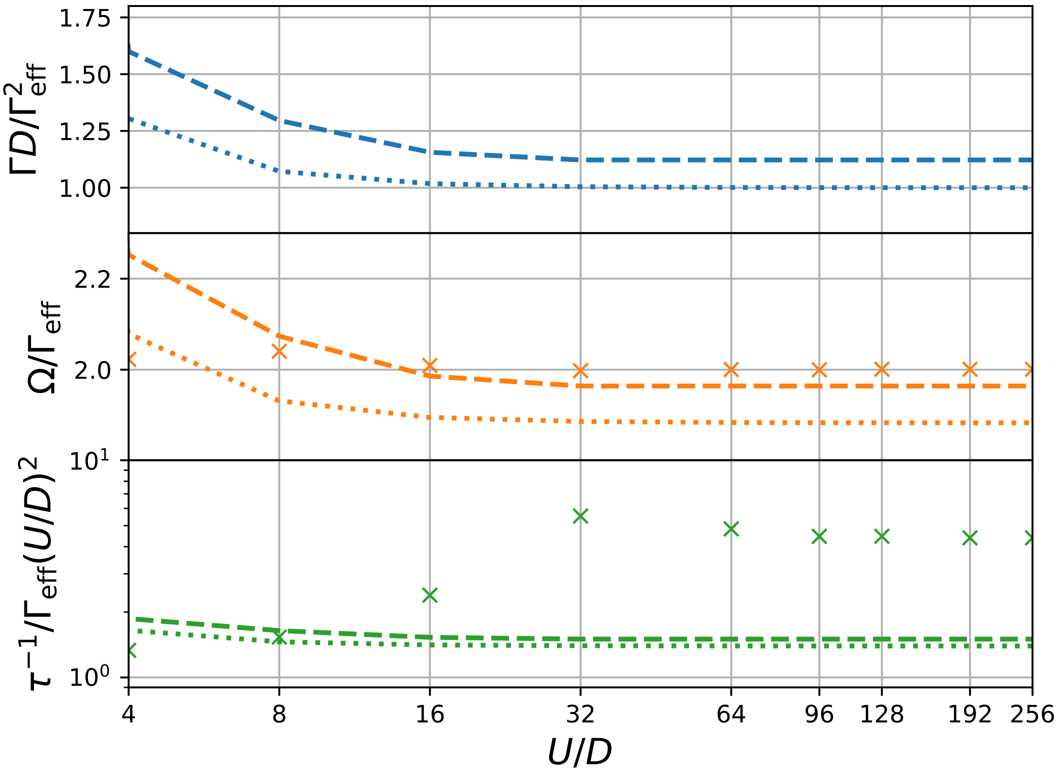

Figure 7.6.: Effective parameters $\Gamma/\Gamma_{\text{eff}}{\cdot}D/\Gamma_{\text{eff}}$, $\Omega/\Gamma_{\text{eff}}$ and $\tau_{\text{eff}}^{-1}/\Gamma_{\text{eff}}{\cdot}(U/D)^2$ for different U/D. The figure is to be understood analogly to Fig. 7.4. The dotted lines are the pure theoretical predictions via Eq. (7.1.1.8) and (7.1.1.7). The dashed lines are the parameters calculated via (7.1.1.7) for a numerically determined $\Gamma/\Gamma_{\text{eff}}$. The stars represent the fitted parameters of Fig. 7.3.

In the context of a BMA in second order, one might expect the relaxation rates of the OWC curves to lie below analytical predictions, instead of above. This might be the case for the BA, however the other approximations involved, especially the second MA, potentially falsely increase the components of the BRT. We know from calculations for the non-interacting case, that the influence of the second MA (which is basically expressed by an impairment of the short-time dynamics) is reduced by increasing the chain length (see Fig. 6.4). This is based on the fact, that the relaxation of the curves is mainly influenced by the DDM. However, the relaxation rates for large U/D are mainly given by the ODDM (see Fig. 9.2). Here, the influence of the second MA is still unknown.

To assess the effect of the single approximations for large U/D, one could calculate the OWC $N_C = 1$ curves for a non-Markovian reservoir, as has been done in Sec. 4.6.1

for the $N_\mathrm{C} = 0$ case. For a local Hilbertspace dimension of 4 one obtains a BRT of 4^4 components, which is the reason, why we do not attempt to calculate it in the non-Markovian case here. However, by separating the DDM and the ODDM as explained in Sec. 4.5, as well as restricting to the $\epsilon_\mathrm{d}^\mathrm{f} = 0$ case and exploiting all symmetries of the BRT, the calculation might be possible.

Let us summarize our findings regarding the suitability of the BMA for OWC TD-NEVs in the case $U \gg D$. For short chains the predicted U^{-2} behavior of the relaxation rates could not be reproduced, which is expected to be mainly based on the BA. A significant increase in the chain length is able to generate the correct U-dependence, which supports this hypothesis. Still, the absolute value of the rates is too large. This can be attributed mainly to the second MA by influencing the ODDM, which is most relevant to the local dynamics for large U/D. From calculations in the non-interacting case we know that a lowering of Λ improves short-time dynamics, which is connected to the second MA (not shown). The hypothesis, that a lowering of Λ improves the absolute value of the relaxation rates is supported by the short chain calculations in Fig. 7.4.

Additional calculations and figures for the OWC TD-NEV in the IRLM can be found in App. H.

7.1.2. Single Impurity Anderson Model

As the second non-trivial model investigated in this thesis, we turn to the SIAM. This model has been discussed in detail in Sec. 2.4, 3.6 and 4.6. Compared to the RLM, we add a spin DOF and a Hubbard-like local Coulomb repulsion U. In the IRLM the energy U favors the super-impurity (impurity plus zeroth chain site) to be singly occupied and by that induces local Rabi-like oscillations. The effect of U in the SIAM is similar, as it prohibits a doubly occupation of the impurity site. However, the dynamics is entirely different, as in the SIAM no direct hopping between the local spin-up and spin-down state is possible. In analogy to Sec. 4.6, we consider the impurity occupation $n_\mathrm{d}(t) = n_\uparrow(t) + n_\downarrow(t)$ and the impurity magnetization $S_z(t) = 0.5\Big(n_\uparrow(t) - n_\downarrow(t)\Big)$. Here $n_\sigma(t)$ denotes the time-dependent expectation value of the $|\sigma\rangle\langle\sigma| + |2\rangle\langle 2|$ operator.

In Fig. 7.7 we examine the impurity occupation and magnetization for a quench, which is inspired by Ref. [118] and [29]. Here we start with a spin-polarized state, i.e. the local energy levels are $E_0 = E_\uparrow = 0$ and $E_\downarrow = E_2 = \Gamma$, so that the empty and the spin-up state are thermally favored. We then quench at $t = 0$ to the particle-hole symmetric case by switching off the external magnetic field and adapting U and ϵ_d.

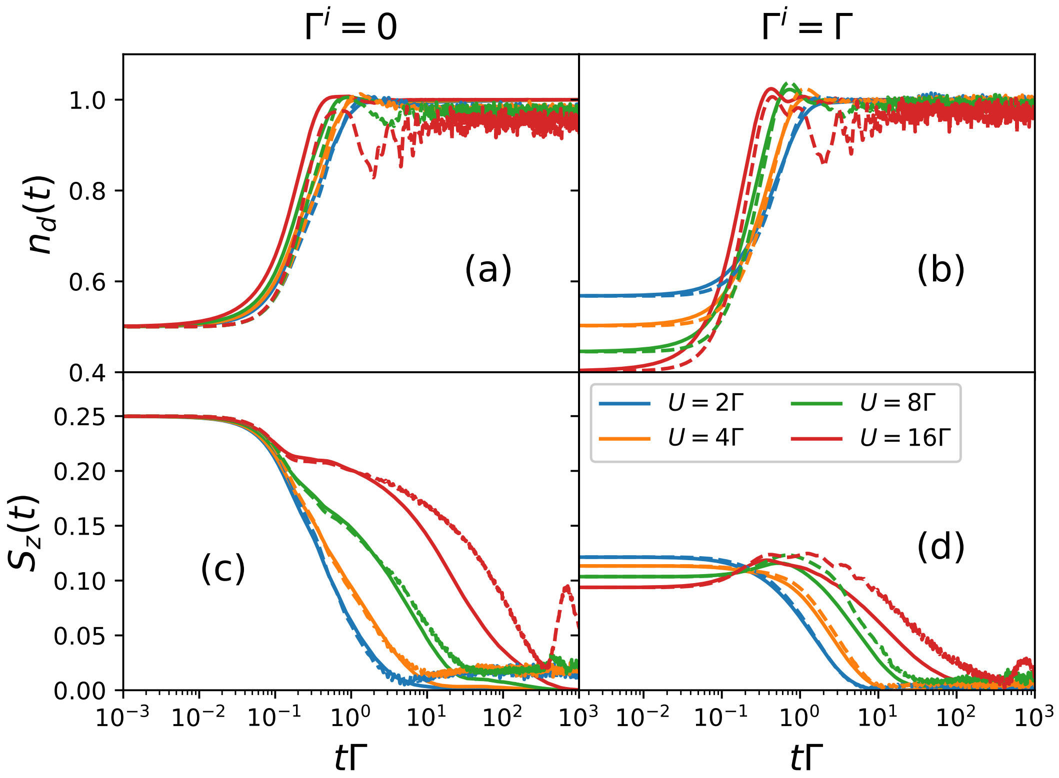

Figure 7.7.: Non-equilibrium impurity occupation $n_\mathrm{d}(t)$ (panels (a) and (b)) and magnetization $S_z(t)$ (panels (c) and (d)) for different values of the Coulomb repulsion U. We switch from $\epsilon_\mathrm{d}^\mathrm{i} = -0.5\Gamma, B^\mathrm{i} = \Gamma, U^\mathrm{i} = 0$ to $\epsilon_\mathrm{d}^\mathrm{f} = -U/2, B^\mathrm{f} = 0$ at $t = 0$. The initial hybridization is $\Gamma^\mathrm{i} = 0$ in panels (a) and (c) and $\Gamma^\mathrm{i} = \Gamma$ in panels (b) and (d). The final hybridization is $\Gamma^\mathrm{f} = \Gamma$ in both cases. The Wilson chain parameters are $N_\mathrm{C} = 30$, $\Lambda = 1.66$, $D = 20\Gamma$, so that a temperature of $T = 0.01\Gamma$ is reached. We have used $N_\mathrm{S} = 10^3$ states and $N_z = 4$. The CWC solution is added as dashed curves and the horizontal axes are chosen logarithmically.

Here the local eigenenergies are $E_0 = E_2 = 0, E_\uparrow = E_\downarrow = -U/2$, so the system is spin-degenerate and the singly occupied state is thermally favored. Consequently, the magnetization drops to zero for long times, while the occupation converges to 1, which is the equilibrium value of the SAM. We have chosen the temperature as the smallest energy scale and the bandwidth relatively small, to simulate the strong-coupling fixed point for $t \to \infty$. In the case $\Gamma^\mathrm{i} = 0$ we have the free-orbital fixed point for $t = 0$, since the impurity is decoupled from the Wilson chain. The case $\Gamma^\mathrm{i} = \Gamma$ corresponds to a valence-fluctuation fixed point. The impurity levels of those cases are depicted in Fig. 7.8, while Fig. 7.7 compares the OWC dynamics (solid lines) to those of the

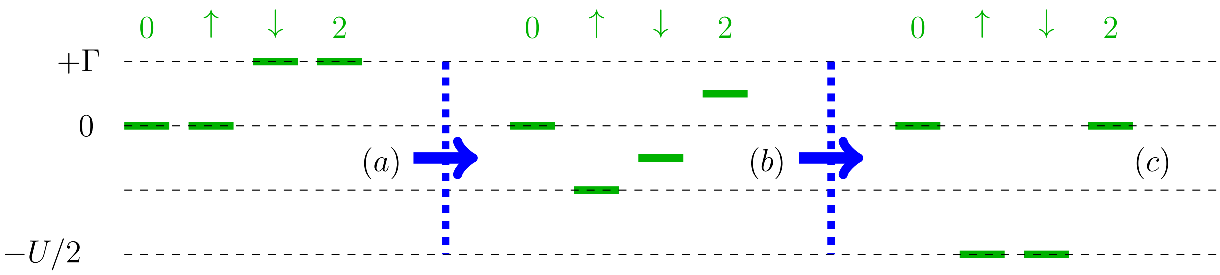

Figure 7.8.: Impurity level energies for the spin-polarized valence-fluctuation fixed point $\epsilon_\mathrm{d} = 0.5\Gamma, B = \Gamma, U = 0$ (panel (a)), the local-moment fixed point $\epsilon_\mathrm{d} = -U/2, B = 0$ (panel (c)) and a hypothetical transition state (b).

CWC (dashed lines). In contrast to Ref. [29], we have used a smaller number N_z in the z-averaging and no artificial damping of the ODDM. Thus the finite-size oscillations in the CWC solution are still visible, while the OWC curves thermalize to the correct steady-state value. For short-times the OWC version relaxates faster than the CWC, which is the well-known effect of the MA. Since the magnetic field is turned off, the magnetization drops to zero for $t \to \infty$. This behavior is well reflected by the OWC, while the CWC solution maintains a residue magnetization. Intuitively, one would expect the magnetization to steadily drop after the magnetic field has been turned off. Instead, we observe a bump around $t\Gamma \approx 10$, which is most pronounced in Fig. 7.7 (d), as here the magnetization is even increased on intermediate times.

To understand this behavior, consider Fig. 7.8. Recall that we have defined the magnetization as $\propto n_\uparrow - n_\downarrow$. At $t = 0$, the empty and the spin-up state are degenerate, meaning that the impurity is not fully occupied with the spin-up electron (see Fig. 7.8 (a)). By quenching to the symmetrical case, the levels of the singly occupied states are decreased (Fig. 7.8 (c)). Thus, the empty state is now thermally less accessible and the probability is effectively shifted to the spin-down state. However, the dynamics between the two steady-states is dominated by the fact, that at first this probability is shifted from the empty state and equally distributed between the two singly occupied states, leading to additional occupation of the spin-up state. This additional occupation then relaxates onto the spin-down state, until both spin states are degenerate, and is responsible for the bump of the impurity magnetization on intermediate time scales. Note, that this bump already partially shows in Fig. 4.5, where the most simple case of $N_\mathrm{C} = -1$ has been assumed (i.e. no Wilson chain). The transition between the two states can be depicted by the energy levels of Fig. 7.8 (b). This panel does not represent an actual physical state of the system, but merely serves to illustrate the

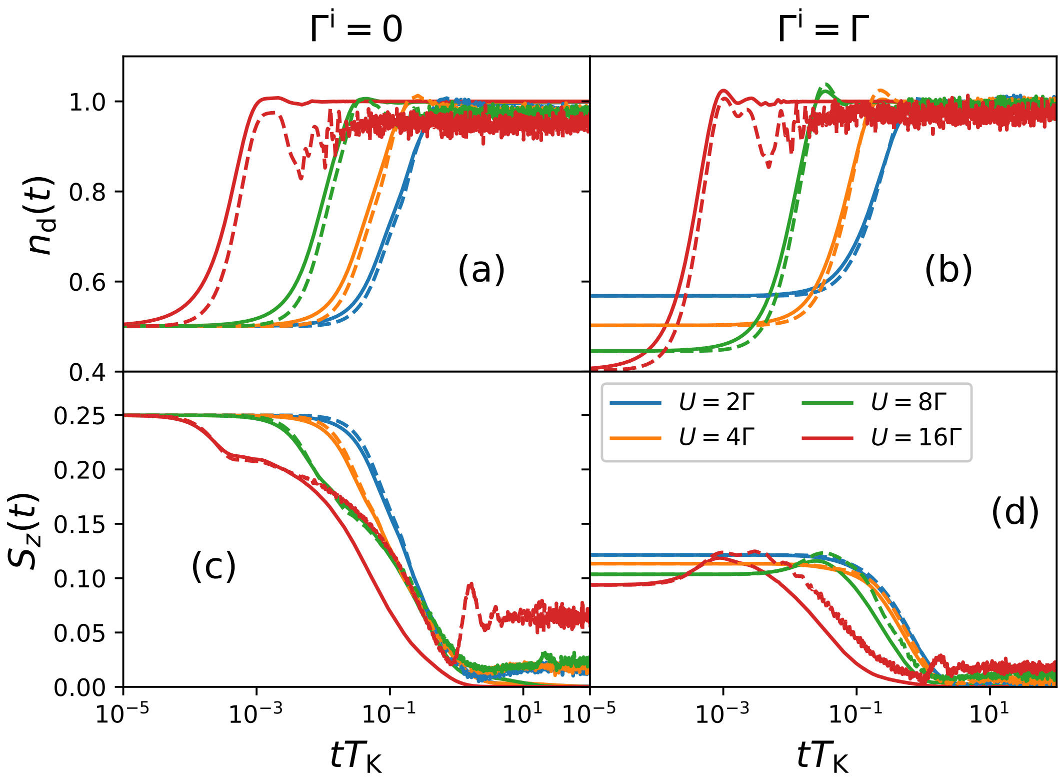

Figure 7.9.: Non-equilibrium impurity occupation $n_\mathrm{d}(t)$ and magnetization $S_z(t)$ for different values of the Coulomb repulsion U. The parameters are identical to Fig. 7.7. Here the horizontal axis is scaled by the respective Kondo temperature T_K, calculated from the impurity susceptibility via [14].

change in occupation probability right after the quench.

Another physically interesting feature is the relaxation time of the curves. For small U, all relaxation happens on the time scale of the hybridization Γ. In the context of the SIAM, the Kondo temperature T_K is an important energy scale as well. For that reason, we have scaled the curves of Fig. 7.7 by the Kondo temperature and replotted them in Fig. 7.9. In fact, the magnetization in Fig. 7.9 (c) reveals the expected relaxation behavior [119, 29], since the curves overlap at $tT_\mathrm{K} \approx 1$. The OWC curve for $U = 16\Gamma$ is an exception, since it relaxates too fast. Here the Kondo temperature is so low, that it is on the same magnitude as the system temperature. In other words, thermal processes overlap the Kondo effect. If the temperature would have been chosen lower by increasing N_C, we would expect the red solid curve to better match the dashed one. In fact, the deviation between the OWC and the CWC is increased in all curves if U is increased. This supports the assumption made in Sec. 7.1.1, that the MA is impaired for large U/D. In the red curves we have chosen $U \approx D$, which is why we expect the most impact of the BMA on the relaxation rates here.

Further figures for the TD-NEV in the SIAM can be found in App. I.

7.2. Equilibrium Spectral Function

In this section we investigate the TD-EGF and the ESF for the IRLM and the SIAM, respectively. The results are obtained analogly to Sec. 5.4.2, but for the interacting case. Note, that for the SIAM the χ-operator has a spin index. Consequently, two separate BRT are calculated and diagonalized, one for each spin value.

7.2.1. Interacting Resonant Level Model

As demonstrated in Fig. 7.2, a large local interaction U induces an effective separation of the zeroth chain site from the remaining Wilson chain. The local Hamiltonian of the super-impurity resembles the SAM with the one-particle energies $-\frac{U}{4}$ and the zero- and two-particle energies $+\frac{U}{4}$. The oscillations of $G_\mathrm{d}(t)$ are dominated by transitions from the one particle subspace to the zero- or two-particle subspaces, respectively, leading to frequencies $\frac{U}{4} - \left(-\frac{U}{4}\right) = \frac{U}{2}$.

In Fig. 7.10 we examine the TD-EGF for even and odd chain lengths and different values for U and D, respectively. The local oscillations with frequency $U/2$ are shown in Fig. 7.10 (a) and (c), where we have $G_\mathrm{d}(t) = \cos(\frac{U}{2}t)$ for large U and short times. In contrast to the non-equilibrium impurity occupation in Sec. 7.1.1, the oscillations are influenced by U and independent of any scaling Γ_eff.

For larger times, the relaxation rates, that are generated by the OWC, enter. In Fig. 7.10 (b) it is displayed, that for $U \gg D$ and $N_\mathrm{C} = 6$ the envelope function of the oscillations can be approximated by a single exponential decay rate α. This rate turns out to be proportional to the bandwidth D, which is plausible, since α is defined by the eigenvalues of the BRT, and the BRT is proportional to the correlation functions, which scale with the bandwidth. For odd chain length (Fig. 7.10 (d)) the relaxation rate is significantly smaller, which again matches with all observations made so far for the OWC. For higher chain length, the rates of even and odd chains are expected to coincide.

In Fig. 7.11 we investigate the OWC ESF for $U \geq D$ and an exact Wilson chain of length $N_\mathrm{C} = 6$. We observe Lorentzian-type excitations at $\omega = \pm(U/2 + \delta_\mathrm{shift})$, which

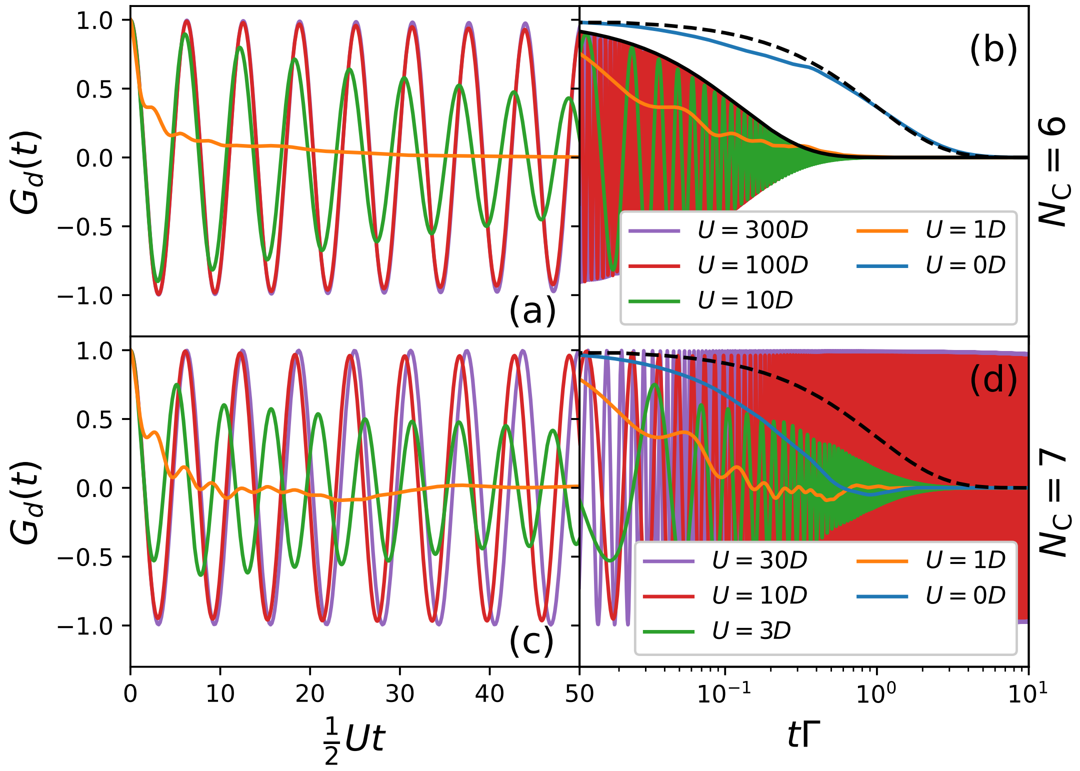

Figure 7.10.: The TD-EGF $G_\mathrm{d}(t)$, calculated via Eq. (5.4.2.62) in the IRLM, versus dimensionless time $\frac{1}{2}Ut$ and $t\Gamma$, respectively. The $U = 0$ curves are unscaled with respect to the horizontal axis. The analytical solution for $U = 0$ is added as black dashed lines for comparison. The black solid line in panel (b) represents $\exp(-\alpha t)$ with $\alpha = 0.08D$. The panels (a) and (c) are a zoom for short times, while panels (b) and (d) are plotted semi-logarithmically to reveal the relaxation behavior. The NRG parameters are chosen as in Fig. 5.19 with a chain length of $N_\mathrm{C} = 6$ (panels (a) and (b)) and $N_\mathrm{C} = 7$ (panels (c) and (d)), respectively. The bandwidth is $D = 100\Gamma$.

translate to the local transitions mentioned above. In the low-energy regime, the RLM excitation at $\omega = \epsilon_\mathrm{d} = 0$ is displayed, which is suppressed, if U is increased. To evaluate the IRLM curves, we need to recall Eq. (5.4.2.63) and (5.4.2.64), respectively. The weight and the position of the excitations in the OWC ESF are defined by the CWC, while their broadening and a small shift are generated by the real- and the imaginary-part of the eigenvalues of the BRT, respectively. In Fig. 7.11, all peaks are broadened proportionally to the bandwidth D, which originates from the influence of the reservoirs in the BRT, similar to the decay rates mentioned above. The only

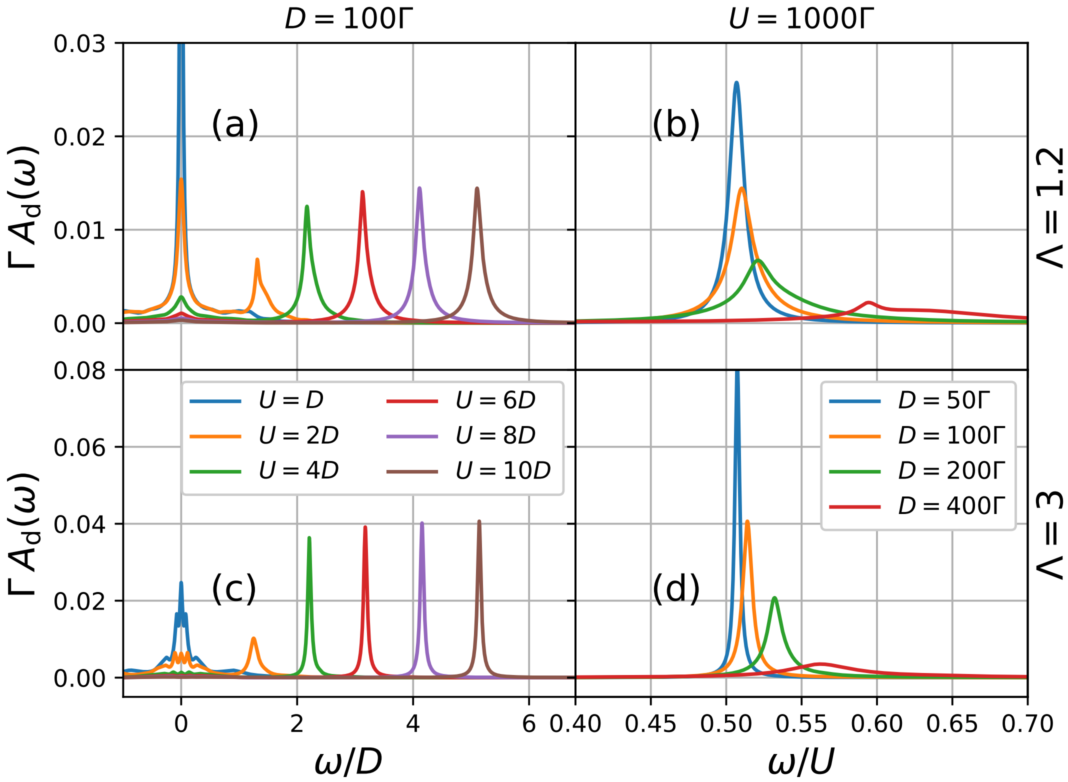

Figure 7.11.: The OWC ESF $\Gamma A_\mathrm{d}(\omega)$ for the IRLM with $\epsilon_\mathrm{d} = 0$, versus dimensionless energies ω/D and ω/U, respectively. A discretization with $\Lambda = 1.2$ is plotted in panels (a) and (b) and $\Lambda = 3$ in (b) and (d). We choose a chain length $N_\mathrm{C} = 6$ and adapt $\overline{\beta}$ to obtain $T = \Gamma$. In panels (a) and (c) the bandwidth $D = 100\Gamma$ is maintained and U is varied. In contrast, $U = 1000\Gamma$ is fixed in panels (b) and (d) and D is varied.

dependence of U is expressed by the position of the high-energy peaks, as well as by the weight of the low-energy excitations, which are solely defined by the influence of the CWC.

The U-independence with respect to the broadening has already been observed in the SAM for large $U \gg D$ in Sec. 4.6.2. Here we have coupled the bath directly to the impurity and the influence of the single approximations was illustrated. The MA cuts off the high-energy peaks, that lie outside the band. In contrast, Fig. 7.11 illustrates, that a Wilson chain of length $N_\mathrm{C} = 6$ is sufficient to improve the MA in such a way, that those high-energy excitations are recovered. On the other hand, the same scaling behavior of the peaks with respect to U and D is observed, i.e. the width of the peaks is still independent of U and only depends on D. In contrast, the width of the peaks is expected to be proportional to U^{-2} [109]. To obtain an analytical estimate of the precise behavior of $G_\mathrm{d}(t)$ in the case $U \gg D$, one could perform a perturbative calculation similar to App. E. Here we expect oscillations with a frequency of $U/2$ and a dominant decay rate $\propto U^{-2}$. Broadening parameters, which are constant in U for large U/D correspond to the relaxations rates found for TD-NEVs (see Fig. 7.4) and for TD-EGFs (see Fig. 7.10). The fact, that the broadening is converged for significantly smaller U ($U = 6D$ in Fig. 7.11 versus $U = 50D$ in Fig. 7.4) might be attributed to the different chain length and the even-odd effect. A slower convergence for smaller Λ, as seen for TD-NEVs, cannot clearly be observed.

The findings of Fig. 7.11 suggest, that the BRF is not suitable to reproduce a direct dependence of local parameters for the broadening of ESFs, if $U \gg D$. We assume, that this can be attributed to the BA, since here the local and the bath density matrix are separated, leading to the case, in which the BRT is scaled by the reservoirs, i.e. bath quantities, only. This is a systematic problem of the BA in second order, wherefore we propose a BRF in fourth order (see Sec. 4.7.1) or a transition to a different QIM (see Sec. 4.7.2) for $U \gg D$.

However, the relaxation rates plotted in Fig. 7.4 for TD-NEVs might inspire one to an alternative approach. By increasing the chain length and simultaneously lowering the discretization parameter, we obtain an OWC with a large number of site, where the reservoir coupling functions have not converged to their steady-state yet. We expect this regime to resonate with a slower convergence of the eigenvalues of the BRT (i.e. the relaxation rates and the broadening parameters generated by the BRF) with respect to U, meaning that the relevant eigenvalues will be in the regime $\propto U^{-2}$ for higher values of U, as found in Sec. 7.1.1. In any case, we expect the OWC solutions to converge to a constant value for $U \to \infty$, implying that the BRF in second order is not suitable for arbitrary large U.

7.2.2. Single Impurity Anderson Model

We conclude our investigations with the OWC ESF in the SIAM. We choose $N_\mathrm{C} = 5$, to match an IRLM of length $N_\mathrm{C} = 6$. The impurity of the SIAM then resembles the super-impurity of the IRLM, which in turn includes the zeroth Wilson chain site.

In Fig. 7.12 the OWC ESF is plotted in a similar manner as in Fig. 7.11. Again, U influences the position of the high-energy peaks (here called Hubbard peaks), but not their widths. Additionally, the shift δ_shift observed in all cases discussed above, effectively vanishes. Only for large bandwidths, a small $\delta_\mathrm{shift} < 0$ from the $\omega = \pm U/2$

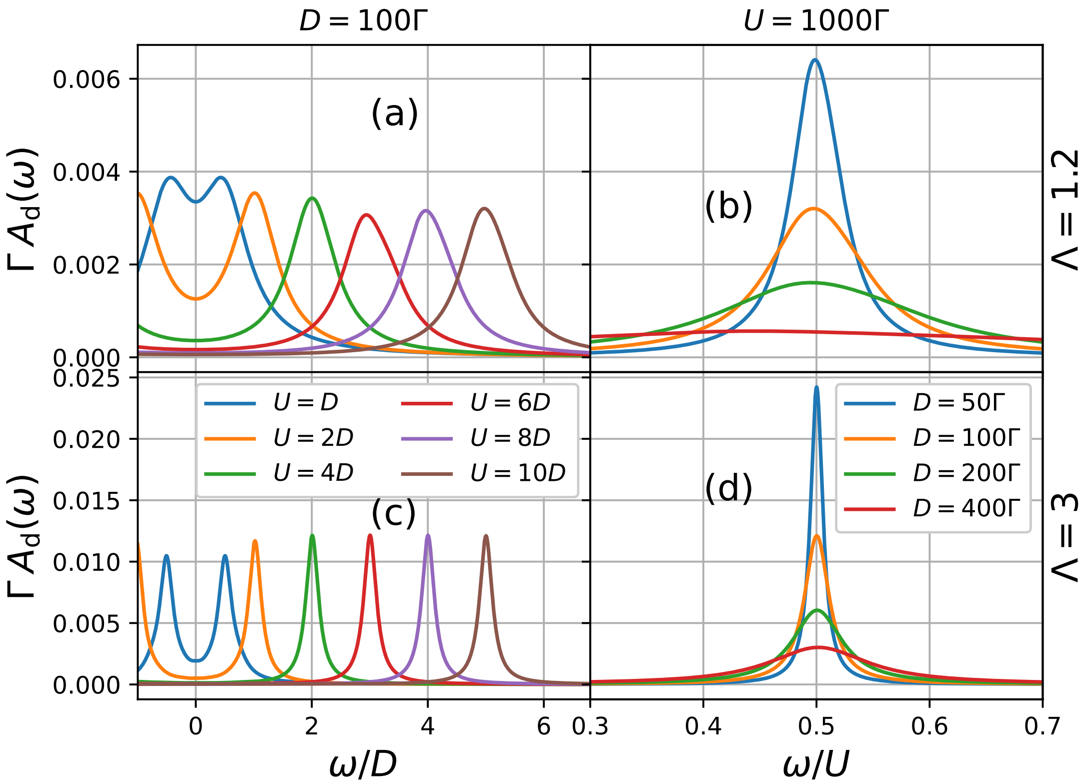

Figure 7.12.: The OWC ESF $\Gamma A_{\mathrm{d}}(\omega)$ for the symmetric Anderson model, versus dimensionless energies ω/D and ω/U, respectively. A discretization with $\Lambda = 1.2$ is plotted in panels (a) and (b) and $\Lambda = 3$ in (b) and (d). We choose a chain length $N_{\mathrm{C}} = 5$ and adapt $\overline{\beta}$ to obtain $T = \Gamma$. In panels (a) and (c) the bandwidth $D = 100\Gamma$ is maintained and U is varied. In contrast, $U = 1000\Gamma$ is fixed in panels panel (b) and (d) and D is varied.

points can be observed (Fig. 7.12 (b)), which is induced by the Lamb-shift and is not reproduced in the CWC solution (not shown). Also, increasing Λ reduces the Lamb-shift effect (Fig. 7.12 (d)) and thus makes the curves more symmetric around $\omega = \pm U/2$.

In contrast to the solution in Sec. 4.6.2, there is a smooth crossover of the OWC SIAM curves between the $U < 2D$ and the $U > 2D$ case. This suggests, that the discontinuity of the transition of the curves in Sec. 4.6.2 is induced by the BMA and that the OWC well compensates for that. In fact, even the sole addition of the zeroth Wilson chain site to the OQS is sufficient to restore the Hubbard peaks, which are cut off for $U > 2D$ by the MA. However, in short OWCs of even chain length, the spectrum is effectively cut off for $|\omega| > D$ and the Hubbard peaks appear as narrow delta-peaks.

With increasing chain length, these peaks are broadened until they converge to the odd chain curves. This is another example for the even-odd effect of short OWCs. In the IRLM this effect occurs in a similar manner. However, as mentioned above, the super-impurity needs to be interpreted as the local system here, meaning that even chains generate physical curves and odd chains display the delta-peaks for large U/D.

In 2004, Raas *et al* [109] used DMRG calculations, i.e. a linear bath discretization, to investigate ESF for a SAM in the $U > D$ regime. They found $\delta_{\text{shift}} \propto J$ and the width of the Hubbard peaks $\propto J^2$, with $J \propto V^2/U$, which is in accordance with Fermi's golden rule considerations. Figure 7.12 is constructed to be comparable to the results of the paper. Since a smaller Λ should be more suited to recover the DMRG results, we have plotted the ESF for two different values of Λ. However, the discretization seems to have no effect on the U-dependence of the high-energy peaks. This suggests, that the deviations cannot be attributed to the logarithmic discretization of the Wilson chain. Also, numerical inaccuracy can be excluded here, as argued above. For that reason, the cause of the deviations of Fig. 7.12 from the DMRG results has to lie in the BMA. Comparable to Fig. 4.8, the OWC results show the same independence of U with respect to the width of the Hubbard peaks in the $U \gg D$ regime, which suggests that the BA has the most relevant contribution to the deviations.

To investigate the low-energy spectrum of the SIAM, a longer chain length, and thus truncation of high-energy states, is required.

In Fig. 7.13 the ESF is plotted for the SAM. The Hubbard peak is clearly visible at $\omega \approx U/2 = 10\Gamma$. The Kondo resonance at $\omega \approx 0$ has a width, which corresponds to the Kondo temperature. The CWC curves (dashed lines) do not reproduce the exact solution here due to a limited chain length. The OWC curves (solid lines) basically resemble the dashed lines, but oscillate around them. This is a typical indicator of a finite-size effect (see Fig. 6.6), which can be compensated for by z-averaging. Figure 7.13 reveals, that the BRF is able to reproduce the small energy scale of the Kondo temperature. Thus we conclude that, in contrast to the $U \gg D$ regime, the BMA is well suited to treat the $U \ll D$ interacting case.

7.3. Summary

The BRF provides a thermalization on the correct time scale for the non-interacting RLM and for interacting models as well, if the local Coulomb repulsion U is small compared to the bandwidth. In the case $U \gg D$ the CWC reproduces the correct

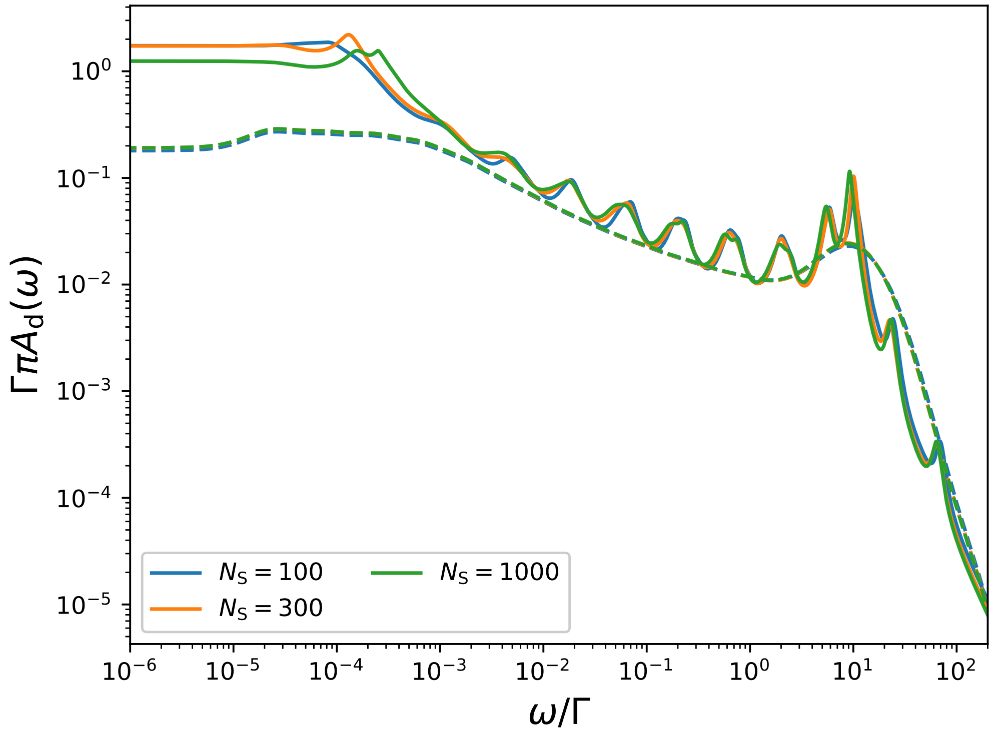

Figure 7.13.: Equilibrium impurity spectral function $A_\mathrm{d}(t)$ for the SAM with $\epsilon_\mathrm{d} = -U/2 = -10\Gamma, D = 100\Gamma, N_\mathrm{C} = 30, \Lambda = 3, T = 10^{-5}\Gamma$. The number N_S of kept states is varied. The CWC is depicted as dashed lines and the respective OWC as solid lines of the same color. The axes are chosen logarithmically and we restrict to the positive half of the spectrum.

oscillation frequency of local Rabi-like oscillations in TD-NEVs. Perturbative considerations predict a quadratic increase of the relaxation times τ in U. For short Wilson chains ($N_\mathrm{C} = 7$ in our example), we observe a quadratic behavior in a small region around $U = 10D$ and then τ converges to a value, which is constant in U. We were able to show, that an increase of the chain length to $N_\mathrm{C} = 50$ yields the correct U dependence for $64D < U < 256D$. At this point, it is not clear, whether τ approaches the constant regime for larger U, i.e. it is not clear, whether an increase of the chain length simply delays the convergence of τ to a constant value. Furthermore, the steady-state of τ and τ/U^2, respectively, exceeds the analytical predictions. Again, an increase in the chain length significantly reduces this deviation. Here the discretization parameter Λ has an influence as well, as it decreases the steady-state when Λ is decreased. We thus propose to choose the OWC to be as long as possible with an adequately small $\Lambda \to 1^+$

to optimally reproduce interacting models in the $U > D$ regime. However, the truncation scheme of the NRG is not adapted to small Λ, since here the separation of adjacent energy scales is too small. For large U a tight-binding chain treated with DMRG or an open NRG+DMRG might represent a fruitful approach here. Also the extension of the BRF to fourth order or the modification of the model via a Schrieffer-Wolff transform are worth considering here. Both approaches include a coupling of fourth order system operators to the reservoirs. These couplings are relevant for $U > D$, since here an effective local moment is formed, and so spin-flip processes are the dominant local interaction.

For IRLM ESFs we do not possess an analytical approximation, that aids in estimating the quality of the OWC solutions. In the symmetrical case $\epsilon_{\mathrm{d}} = 0$, the model converges to the SAM for large U/D, which we can use to benchmark the solutions. Aside from the Kondo resonance, the SAM exhibits its main excitations at $\omega = \pm(U/2 + \delta_{\mathrm{shift}})$, called Hubbard peaks. Fermi's golden rule considerations suggest that δ_{shift} is proportional to the spin-coupling $J \propto V^2/U$ and that the width of the peaks is proportional to J^2. In contrast, we find the width of the Hubbard peaks to be constant in U in the limit of large U/D, for each the IRLM and the SIAM respectively. This is the identical behavior observed for the short chain TD-NEVs, since the broadening parameters, as well as the relaxation rates, both stem from the eigenvalues of the BRT. Due to finite-size oscillations, we were not able to evaluate ESFs for longer Wilson chains at this point. However, from the parallelism of the relaxation rates and the broadening parameters we assume, that the broadening of the Hubbard peaks will be proportional to U^{-2}, if the Wilson chain is sufficiently long. Also, we apply the same argumentation as above for a possible improvement of the formalism with respect to the $U > D$ case.

8. Conclusion

We have implemented an OQS approach for QIMs. For this purpose, we extended the NRG formalism by reservoirs that are coupled to each Wilson chain site via a BRF. In contrast to closed system approaches, this allows for true dissipation of quantities in local TD-NEVs, as well as a finite lifetime of excitations in local ESFs. The OQS character of the approach is mediated by a time-dependent density matrix, which is defined by a von-Neumann equation. In the context of the BRF, this equation can be turned into a simple master equation, which is then solved by diagonalizing the so-called BRT. Here the BMA is necessary, which assumes a large bath and a weak coupling to the system.

We have investigated the BRF in the most simple case of a direct coupling of the impurity to the bath, where the effect of the single approximations included in the BMA can be examined in detail. It has been shown, that the BA impairs equilibrium values, while the MA mainly influences the short-time behavior of time-dependent quantities. However, in this simple approach, a relaxation on the correct time-scale, as well as the correct broadening of local excitations are already included for the non-interacting RLM.

The main component of this thesis is the improvement of the BMA by the construction of an OWC. Here discrete excitations are extracted from the bath and are included in the system Hamiltonian in the canonical manner of the NRG. The remaining bath parts are collected as reservoirs and coupled to the Wilson chain to restore the continuum. We were able to explain, how the BMA is improved by iteratively enlarging the system Hamiltonian, while simultaneously decreasing the effective hybridization to the remaining rest-bath. Due to the logarithmic discretization of the bath, discretization errors occur in the OWC solutions, that are already well-known from NRG calculations. These errors are expressed as unphysical oscillations in TD-NEVs and ESFs, and can be compensated for by a standard z-averaging. We have proofed that fact for TD-NEVs, while it is still left to show for ESFs.

When increasing the Wilson chain length, a truncation of certain system eigenstates is required to keep the Fockspace dimension manageable. When calculating dynamical properties with the NRG, all truncated iterations need to be included to avoid a violation of the sum-rule. For the OWC, we analogly need to include a coupling of all truncated iterations in the master equation, due to the application of an ASB. This coupling imposes infeasible demands with respect to CPU time and memory to modern workstations, which is the reason why we discussed and implemented several approximations to the BRT. In the SSA, the coupling between different NRG iterations is neglected. This significantly affects the Lamb-shift, which is yielded by the imaginary part of the BRT. We discussed a possible way to correct the Lamb-shift, however we decided to simply neglect it, since its influence on the solutions is exponentially small, if the discretization parameter is small. In TD-NEVs the SSA yields an unphysical loss of the trace over time. Here we discussed a coupling of all NRG iterations for the DDM, as well as efficient alternative approaches. In ESFs the coupling of different iterations is relevant for the dissipative part of the BRT. We have no practical way of including the iteration coupling here, however, in the limit of low temperatures, the dissipative part has no influence on the ESF and can safely be neglected. In that case the BRT is diagonal, which significantly simplifies calculations.

Since the purpose of this thesis is of methodological nature, all points above have been investigated for the simple RLM, where analytical solutions are available as benchmarks for the OCF. To proof that our formalism is also applicable to non-trivial models, we have included a local Coulomb interaction to investigate the IRLM and an additional spin DOF for the SIAM.

If the local Coulomb interaction is relatively small, i.e. within the bath bandwidth, it can be treated as an effective correction to the RLM in the context of the BRF. In TD-NEVs the relaxation rates generated by the BRT are modified by the local interaction and in the case of the IRLM, additional local Rabi-like oscillations are induced, which are solely defined by the CWC. In the SIAM a scaling of the magnetization with the Kondo temperature has been found for the OWC solutions, which is in accordance with TD-NRG calculations. For ESFs the OCF is capable of reproducing the Hubbard-peaks of a width of 2Γ and, within the limits of the discretization error, the Kondo resonance is of the width of the Kondo temperature. The secular approximation can lead to a discontinuous transition, if the interaction is turned on, however, this transition can be smoothed, by increasing the Wilson chain length. We conclude, that the BRF is well applicable to interacting QIMs, if the interaction energy lies within the range of the bandwidth.

If the local interaction exceeds the bandwidth, the BRF faces two major problems. Firstly, the MA prohibits transitions between the impurity and the band, which can easily be corrected by increasing the chain length. Secondly, the BRT, and consequently its eigenvalues, is independent of the interaction energy due to the BA, which leads to a corruption of the relaxation rates in TD-NEVs, as well as the broadening parameters in ESFs, respectively. We have shown, that this error can also be corrected by increasing the chain length, however, a significantly larger increase is required here compared to the correction of the MA. Furthermore, the relaxation rates obtained from the OCF are significantly larger than analytical predictions suggest, which can be compensated for by decreasing the discretization parameter. Considering these facts, the BMA in second order appears to be systematically maladapted to relatively large local interactions. The OCF is capable of compensating for that to a certain degree by increasing the system size, however, we propose to try different approaches, such as a BMA in fourth order or a Schrieffer-Wolff transform of the QIM, to more efficiently treat interacting models.

Due to its logarithmic discretization of the bath, the OCF is confined to QIMs. However, in this wide range of applications, the approach is versatile. The construction of the reservoirs is independent of the precise form of the impurity and so, e.g. multi-impurity models can be investigated as well. In the BRF we have included the spin in the SIAM as a DOF. Here we could add arbitrary DOF, e.g. different channels and by that extend the OCF to multi-channel models. By manipulating channel chemical potentials, local transport processes can be investigated. Our work was confined to a constant bath DOS, but the BRF can easily be adapted to, e.g. gapped systems. Bosonic systems are considerable as well. Furthermore, we have restricted ourselves to a single quench in non-equilibrium dynamics. Multiple quenches would be possible as well to simulate pulses for QDs. To better adapt our formalism to high-temperature calculations, one would need to extend the density matrix by a FDM approach. However, caution is advised when truncating high-energy states in ESFs in the regime of high temperatures for the reasons mentioned above.

In principle, the OCF can be applied to all problems the NRG is suitable for. This is due to the fact, that the BRF is independent of the impurity Hamiltonian and adaptable to different chain geometries. Solely the hybridization term has a major effect on the BRF. Here we have restricted ourselves to the canonical bilinear Hamiltonian, while it is, in principle, possible to adapt the formalism to higher order terms, as they appear e.g. in the Kondo model.

9. Appendix

A. Analytical Calculations for the Resonant Level Model

In the following analytic calculations we restrict to the RLM, i.e. a QIS comprising a local two-level system hybridized with a bath of non-interacting fermions (cf. Eq. (5.1.1)).

A.1. Equilibrium Spectral Function

We begin by calculating the equilibrium GF $G_{d,d^\dagger}(z)$ of the local impurity level using an equation of motion

$$zG_{A,B}(z) = \langle\{A,B\}\rangle + G_{\{A,H\},B}(z), \tag{A.1.1}$$

with the complex energy $z = \omega + i\delta$. For a decoupled impurity, i.e. $V = 0$, we obtain

$$G_{d,d^\dagger}(z) = \frac{1}{z - \epsilon_d} \tag{A.1.2}$$

for the retarded GF, yielding a spectral function of a simple delta-peak

$$A_{d,d^\dagger}(\omega) = -\frac{1}{\pi} \lim_{\delta \to 0^+} \mathfrak{Im} G_{d,d^\dagger}(z) = \delta(\omega - \epsilon_d), \tag{A.1.3}$$

which translates to an infinite lifetime of the impurity level due to a missing dissipation mechanism into the bath. The DOS of the bath

$$\rho(\omega) = \sum_k A_{c_k,c_k^\dagger}(\omega) = \sum_k \delta(\omega - \epsilon_k) \tag{A.1.4}$$

follows analogly.

For the coupled problem $V \neq 0$ the GF reads

$$G_{d,d^\dagger}(z) = \frac{1}{z - \epsilon_\mathrm{d} - \Sigma(z)} \tag{A.1.5}$$

containing the self-energy

$$\Sigma(z) = \sum_k |V_k|^2 G_{c_k,c_k^\dagger}(z) = \sum_k \frac{|V_k|^2}{z - \epsilon_k}. \tag{A.1.6}$$

By assuming a constant DOS

$$\rho(\omega) = \frac{1}{2D}\Theta(D - |\omega|), \tag{A.1.7}$$

where D is the bandwidth, the imaginary part of the self-energy becomes

$$\mathfrak{Im}\Sigma(\omega) = \lim_{\delta\to 0^+} \mathfrak{Im}\Sigma(z) = -\Gamma\Theta(D - |\omega|) \tag{A.1.8}$$

with $\Gamma = \frac{\pi V^2}{2D}$ (see Sec. 5.1), while the real part

$$\mathfrak{Re}\Sigma(\omega) = \frac{1}{\pi}\int_{-\infty}^{\infty} d\omega' \frac{\mathfrak{Im}\Sigma(\omega')}{\omega' - \omega} = -\frac{\Gamma}{\pi}\ln\left|\frac{D-\omega}{D+\omega}\right| \tag{A.1.9}$$

can be obtained by a Kramers-Kronig relation.

This result can now be inserted into Eq. (A.1.5) to calculate the spectral function

$$A_{d,d^\dagger}(\omega) = \frac{1}{\pi}\frac{\Gamma}{(\omega - \epsilon_\mathrm{d} - \mathfrak{Re}\Sigma(\omega))^2 + \Gamma^2} \tag{A.1.10}$$

of the impurity site. In the wideband limit $\omega \ll D$ (which coincides with a constant DOS) $\mathfrak{Re}\Sigma(\omega)$ vanishes, so we are left with a simple Lorentzian

$$A_{d,d^\dagger}(\omega) = \frac{1}{\pi}\frac{\Gamma}{(\omega - \epsilon_\mathrm{d})^2 + \Gamma^2}, \tag{A.1.11}$$

with a broadening of Γ, resulting in a finite lifespan of the impurity level. The curve is centered around $\omega = \epsilon_\mathrm{d}$, supplemented by a potential additional shift for a non-vanishing real part of the self energy.

From the spectral function the equilibrium occupation

$$\langle n_{\mathrm{d}} \rangle = \int_{-\infty}^{\infty} d\omega f_\beta(\omega) A_{d,d^\dagger}(\omega) \tag{A.1.12}$$

of the local level can be calculated with $f_\beta(\omega) = \left(1 + e^{\beta\omega}\right)^{-1}$ being the Fermi function for the inverse temperature β. In the limit of $T \to 0$ we obtain

$$\langle n_{\mathrm{d}} \rangle = \frac{1}{2} - \frac{1}{\pi} \arctan\left(\frac{\epsilon_{\mathrm{d}}}{\Gamma}\right). \tag{A.1.13}$$

For $\Gamma \to 0$ the impurity decouples from the bath, which is the $V = 0$ case discussed above. The spectral function consequently turns into a delta-peak leading to $\langle n_{\mathrm{d}} \rangle = f_\beta(\omega)$, i.e. the impurity occupation is solely defined by the Fermi-function.

A.2. Non-Equilibrium Occupation Number

The calculations of this section are based upon Ref. [29, 23]. We investigate exact non-equilibrium dynamics of the impurity occupation in the RLM by using a Keldysh formalism [120]. The considerations partially rely on the wideband limit $D \gg \Gamma$ and the occuring integrals can be evaluated analytically for vanishing temperature T. The non-equilibrium case is provided by a time-dependent impurity level $\epsilon_{\mathrm{d}}(t)$ and hybridization $V(t)$ in the Hamiltonian.

To begin with, we identify the impurity occupation

$$n_{\mathrm{d}}(t) = \langle d^\dagger(t) d(t) \rangle \tag{A.2.14}$$

as the equal-time version of the lesser GF

$$G^<_{d,d^\dagger}(t,t') = \int_{-\infty}^{\infty} d\tau \int_{-\infty}^{\infty} d\tau' G^r_{d,d^\dagger}(t,\tau) \Sigma^<(\tau,\tau') G^a_{d,d^\dagger}(\tau',t'), \tag{A.2.15}$$

where $\Sigma^<$ is the lesser self-energy. $G^{r/a}_{d,d^\dagger}$ is the retarded/advanced GF, which obeys the equation of motion

$$\left(i\partial_t - \epsilon_{\mathrm{d}}(t)\right) G^{r/a}_{d,d^\dagger}(t,t') = \delta(t-t') + \int_{-\infty}^{\infty} d\tau \Sigma^{r/a}(t,\tau) G^{r/a}_{d,d^\dagger}(\tau,t'). \tag{A.2.16}$$

Here enters the retarded/advanced self-energy

$$\Sigma^{r/a}(t,t') = \mp i\Theta(\pm(t-t'))V(t)V(t')\int_{-\infty}^{\infty} d\epsilon\rho(\epsilon)e^{-i\epsilon(t-t')}. \tag{A.2.17}$$

To simplify the integral we now assume the wideband limit which leads to a constant fermionic DOS $\rho(\epsilon) = \rho_F$. Together with Eq. (A.2.16) we obtain

$$G^{r/a}_{d,d^\dagger}(t,t') = \mp i\Theta(\pm(t-t'))\exp\left(-\int_{t'}^{t} d\theta i\epsilon_d(\theta) \pm \Gamma(\theta)\right), \tag{A.2.18}$$

where we have introduced the definition $\Gamma(t) = \pi\rho_{\mathrm{F}}V^2(t)$. Analogly to Eq. (A.2.17) the lesser self-energy is given by

$$\Sigma^{<}(t,t') = V(t)V(t')\int_{-\infty}^{\infty} d\epsilon\rho(\epsilon)e^{-i\epsilon(t-t')}f_\beta(\epsilon). \tag{A.2.19}$$

Plugging the derived equations into Eq. (A.2.15) yields

$$n_{\mathrm{d}}(t) = G^{<}_{d,d^\dagger}(t,t) = \int_{-\infty}^{\infty} d\epsilon\rho(\epsilon)f_\beta(\epsilon)\left|A(\epsilon,t)\right|^2, \tag{A.2.20}$$

with

$$\begin{aligned} A(\epsilon,t) &= \int_{-\infty}^{t} d\tau V(\tau)\exp\left(-i\epsilon\tau - \int_{\tau}^{t} d\theta i\epsilon_{\mathrm{d}}(\theta) + \Gamma(\theta)\right) \\ &= \left[\frac{V^{\mathrm{i}}}{\Gamma^{\mathrm{i}} + i(\epsilon^{\mathrm{i}}_{\mathrm{d}} - \epsilon)} - \frac{V^{\mathrm{f}}}{\Gamma^{\mathrm{f}} + i(\epsilon^{\mathrm{f}}_{\mathrm{d}} - \epsilon)}\right] e^{-(i\epsilon^{\mathrm{f}}_{\mathrm{d}} + \Gamma^{\mathrm{f}})t} + \frac{V^{\mathrm{f}}}{\Gamma^{\mathrm{f}} + i(\epsilon^{\mathrm{f}}_{\mathrm{d}} - \epsilon)} e^{-i\epsilon t}. \end{aligned} \tag{A.2.21}$$

In the last step we have restricted ourselves to a discontinuous parameter quench from the initial values $\epsilon^{\mathrm{i}}_d, V^{\mathrm{i}}, \Gamma^{\mathrm{i}}$ to the final ones $\epsilon^{\mathrm{f}}_d, V^{\mathrm{f}}, \Gamma^{\mathrm{f}}$ at $t = 0$. Note that in Eq. (A.2.19) and (A.2.20) a general $\rho(\epsilon)$ can be maintained even though previously a constant DOS has been proposed. This allows for approximate corrections of the DOS in cases that deviate from the wideband limit. In the case of $T \to 0$ a closed analytical form can be found. For details, see Ref. [23].

In the equilibrium cases, $t = 0$ and $t \to \infty$, Eq. (A.2.20) yields the expression of Eq. (A.1.12). If one recalls that here also the wideband limit has been considered by neglecting the real part (A.1.9) of the self-energy, it seems reasonable to substitute it back into the GF-like terms of Eq. (A.2.21). This makes up for the approximation done in Eq. (A.2.17), at least with respect to the equilibrium values.

If $A(\epsilon, t)$ is plugged into Eq. (A.2.20), one obtains a function of the type

$$n_d(t) = (n_d^{\mathrm{i}} - n_d^{\mathrm{f}})e^{-2\Gamma^{\mathrm{f}}t} + n_d^{\mathrm{f}} + e^{-2\Gamma^{\mathrm{f}}t}I_1 + e^{-\Gamma^{\mathrm{f}}t}I_2(t), \tag{A.2.22}$$

with $n_{\mathrm{d}}^{\mathrm{i}}, n_{\mathrm{d}}^{\mathrm{f}}$ being the equilibrium values. The first two terms on the r.h.s. of Eq. (A.2.22) resemble the simple 2Γ-decay of the BRF solution Eq. (4.6.1.67), while $I_2(t)$ adds an oscillation that decays with Γ and fulfills $I_2(0) = -I_1$.

B. Different Spectral Coupling Functions

The BRF can easily be adapted to more general spectral coupling functions $\Gamma(\omega)$. In Sec. 4.3 and 4.6 all $\Gamma(\omega)$ can be replaced, which does not require any additional calculations, if the BMA is applied.

Introducing a power-law spectral coupling function [85]

$$\Gamma(\omega) = \Gamma(1+r)D^{-r}|\omega|^{r}\Theta(D-|\omega|), \tag{B.23}$$

we can recognize the case of a constant function by setting $r=0$. For $r=1$, we can replace all spectral coupling functions in the BMA by

$$\Gamma(\omega) = \frac{2\Gamma}{D}|\omega|\Theta(D-|\omega|), \tag{B.24}$$

which simply rescales the relaxation rates generated by the BRT by $\frac{2|\omega|}{D} \leq 2$. The Lamb-shift $\gamma(\omega)$ (see Eq. (4.6.2.86)) is replaced by

$$\gamma(\omega) = \frac{1}{\pi}\int_{-\infty}^{\infty} d\epsilon \frac{\Gamma(\epsilon)}{\epsilon-\omega} = \frac{2}{\pi D}\omega \ln|\frac{D^2-\omega^2}{\omega^2}|, \tag{B.25}$$

and vanishes in the wideband limit $D \gg |\omega|$.

C. Higher Order Terms in the Von-Neumann Equation

We discuss a perturbative solution to the von-Neumann equation

$$\dot{\rho}^{\mathrm{I}}(t) = i\left[\rho^{\mathrm{I}}(t), H^{\mathrm{I}}_{\mathrm{SB}}(t)\right] \tag{C.26}$$

(see Eq. (4.2.4)) and the evaluation of the thermal expectation value of a local operator

$$\langle \hat{O}_{\mathrm{S}}(t)\rangle = \mathrm{Tr}_{\mathrm{S}}\Big\{e^{iH_{\mathrm{S}}t}\hat{O}_{\mathrm{S}}e^{-iH_{\mathrm{S}}t}\mathrm{Tr}_{\mathrm{B}}\Big[\rho^{\mathrm{I}}(t)\Big]\Big\}. \tag{C.27}$$

Here we concentrate on the impurity occupation operator $O_{\mathrm{S}} = n_{\mathrm{d}} = d^{\dagger}d$ and the RLM. Other choices for the local operator and the QIM are possible as well but the calculations would require appropriate adjustment.

The local system Hamiltonian in the RLM is simply given by

$$H_{\mathrm{S}} = \epsilon_{\mathrm{d}} d^{\dagger} d, \tag{C.28}$$

while the hybridization to the non-interacting fermionic bath is in the interaction picture defined as

$$V(t) \equiv H^{\mathrm{I}}_{\mathrm{SB}}(t) = \sum_{k} V_k \left[d^{\dagger}(t) c_k(t) + d(t) c^{\dagger}_k(t) \right]. \tag{C.29}$$

By defining the local eigenbasis $\{|0\rangle, |1\rangle\}$ and considering a bath of non-interacting particles, we can rewrite these Hamiltonians as

$$H_{\mathrm{S}} = \epsilon_{\mathrm{d}} |1\rangle \langle 1| \tag{C.30}$$

and

$$V(t) = \sum_{k} V_k \left[|0\rangle \langle 1| c^{\dagger}_k e^{i(\epsilon_k - \epsilon_d)t} + |1\rangle \langle 0| c_k e^{-i(\epsilon_k - \epsilon_d)t} \right] \tag{C.31}$$

respectively. If we define the non-equilibrium case by a quench

$$\epsilon_{\mathrm{d}}(t) = \epsilon^{\mathrm{i}}_{\mathrm{d}} \Theta(-t) + \epsilon_{\mathrm{d}} \Theta(t) \tag{C.32}$$

of the local impurity energy and assume the impurity and the bath to be separated for $t \leq 0$, the initial reduced density matrix is given by

$$\rho_{\mathrm{S}}(t=0) = f_{\beta}(-\epsilon^{\mathrm{i}}_{\mathrm{d}}) |0\rangle \langle 0| + f_{\beta}(\epsilon^{\mathrm{i}}_{\mathrm{d}}) |1\rangle \langle 1|, \tag{C.33}$$

with $f_{\beta}(\epsilon)$ being the Fermi-function for the inverse temperature β.

The local impurity occupation can now be written as

$$n_{\mathrm{d}}(t) = \mathrm{Tr}_{\mathrm{S}} \Big\{ n_{\mathrm{d}} \mathrm{Tr}_{\mathrm{B}} \Big[\rho^{\mathrm{I}}(t) \Big] \Big\} = \mathrm{Tr}_{\mathrm{S}} \Big\{ \rho_{\mathrm{S}}(t=0) \mathrm{Tr}_{\mathrm{B}} \Big[\sum_{n=0}^{\infty} R_{2n}(t) \Big] \Big\} \tag{C.34}$$

with

$$\begin{aligned} R_{n+2}(t) &= -\int_0^t dt_{n+1} \int_0^{t_{n+1}} dt_{n+2} \Big[V(t_{n+2}), [V(t_{n+1}), R_n(t)] \Big] \\ R_0(t) &= n_{\mathrm{d}}. \end{aligned} \tag{C.35}$$

The first order term

$$\begin{aligned} \Big[V(t_2), [V(t_1), n_{\mathrm{d}}] \Big] = {} & 2n_d \sum_k V_k^2 \cos\left((\epsilon_k - \epsilon_d)(t_2 - t_1) \right) \\ & - \sum_{k_1 k_2} V_{k_1} V_{k_2} c_{k_1}^\dagger c_{k_2} \left(e^{i(\epsilon_{k_1} - \epsilon_d)t_1 - i(\epsilon_{k_2} - \epsilon_d)t_2} + e^{i(\epsilon_{k_1} - \epsilon_d)t_2 - i(\epsilon_{k_2} - \epsilon_d)t_1} \right) \end{aligned} \tag{C.36}$$

can be obtained by switching the indices $k_1 \leftrightarrow k_2$ in two terms and exploiting

$$|1\rangle \langle 1| \, c_{k_2} c_{k_1}^\dagger - |0\rangle \langle 0| \, c_{k_1}^\dagger c_{k_2} = |1\rangle \langle 1| \, \delta_{k_1, k_2} - c_{k_1}^\dagger c_{k_2}. \tag{C.37}$$

To incorporate (C.36) into (C.34) one needs to calculate the trace over all impurity and bath DOF, which simply yields

$$\begin{aligned} & \mathrm{Tr}_{\mathrm{S}} \Big\{ \rho_{\mathrm{S}}(t = 0) \mathrm{Tr}_{\mathrm{B}} \Big[V(t_{n+2}), [V(t_{n+1}), n_{\mathrm{d}}] \Big] \Big\} \\ & = \frac{2}{\pi} \int_{-\infty}^{\infty} d\epsilon \Gamma(\epsilon) \left(f_\beta(\epsilon_d^{\mathrm{i}}) - f_\beta(\epsilon) \right) \cos\left((\epsilon - \epsilon_d)(t_2 - t_1) \right). \end{aligned} \tag{C.38}$$

Here we have turned the discrete sum over k into an integral over ϵ by defining the spectral coupling function as in Eq. (4.3.23).

The true challenge now lies in the calculation of higher order terms of $R_{2n}(t)$ with $n > 1$. Deriving higher order terms from the first branch of (C.36) is fairly simple, since no bath operators are involved and so the sums over the bath DOF will never be entangled. The second branch contains the operators $c_{k_1}^\dagger c_{k_2}$ and for that reason the evaluation in higher orders is not as apparent. Let us calculate

$$\begin{aligned}\Big[V(t_2), \Big[V(t_1), c^\dagger_{k_1} c_{k_2}\Big]\Big] &= \sum_{k\neq k_2} V_{k_1} V_k c^\dagger_k c_{k_2} e^{i(\epsilon_k-\epsilon_d)t_2 - i(\epsilon_{k_1}-\epsilon_d)t_1} \\ &+ \sum_{k\neq k_1} V_k V_{k_2} c^\dagger_{k_1} c_k e^{i(\epsilon_{k_2}-\epsilon_d)t_1 - i(\epsilon_k-\epsilon_d)t_2} \\ &+ V_{k_1} V_{k_2} (c^\dagger_{k_2} c_{k_2} - n_d) e^{i(\epsilon_{k_2}-\epsilon_d)t_2 - i(\epsilon_{k_1}-\epsilon_d)t_1} \\ &+ V_{k_1} V_{k_2} (c^\dagger_{k_1} c_{k_1} - n_d) e^{i(\epsilon_{k_2}-\epsilon_d)t_1 - i(\epsilon_{k_1}-\epsilon_d)t_2}. \end{aligned} \tag{C.39}$$

Interestingly, no bath correlations higher than second order emerge. With (C.36) and (C.39), $n_\mathrm{d}(t)$ can straightforwardly be calculated up to fourth order, since the first two terms of (C.39) vanish in the final expression. With each order of n, these terms add one summation over the bath DOF. A neglection of those terms would only affect third order contributions in k and then have an increasing effect on higher order terms. If we assume a weak coupling between the impurity and the bath, this approximation appears to be legitimate.

In any case, one is left with the integration of increasingly nested exponential functions. We do not want to proceed on this path, since this thesis is intended to restrict to the BMA. However, we want to point out, that the above discussed method is basically adaptable to arbitrary QIMs, since local and bath operators are entirely decoupled. Also, the calculation of a TD-EGF is possible as well by replacing (C.34) by

$$G_\mathrm{d}(t) = -i\Theta(t) e^{-i\epsilon_\mathrm{d} t} \mathrm{Tr}_\mathrm{S}\Big\{ d\,\mathrm{Tr}_\mathrm{B}\Big[\chi^\mathrm{I}(t)\Big]\Big\}, \tag{C.40}$$

where $\chi = d^\dagger \rho + \rho d^\dagger$.

D. Numerical Determination of the Cut-Off Frequencies

The cut-off frequencies ω_n^C are defined by

$$t_n^2 = \frac{1}{\pi} \int d\omega F_n(\omega) \Gamma_n(\omega) \tag{D.41}$$

with $F_n(\omega) = e^{-(\omega/\omega_n^{\mathrm{C}})^4}$. The problem is equivalent to finding the root of

$$f(x) = \pi t_n^2 - \int_{-\infty}^{+\infty} d\omega e^{-\omega^4/x^4} \Gamma_n(\omega). \tag{D.42}$$

To find a starting point x_0, we approximate $e^{-\omega^4/x^4} \approx 1 - \omega^4/x^4$ and set $f(x_0) = 0$. The constant term yields $\pi(V_n')^2$ by integration over ω. We end up with

$$x_0^4 = \int_{-\infty}^{+\infty} d\omega \frac{\omega^4 \Gamma_n(\omega)}{\pi (t_n')^2} \tag{D.43}$$

with $(t_n')^2 = (V_n')^2 - t_n^2$.

Now Newton's method is implemented as

$$\begin{aligned} x_{m+1} &= x_m - \frac{f(x_m)}{f'(x_m)} \\ &= \frac{4h(x_m) + \pi t_n^2 - g(x_m)}{4h(x_m)} x_m \end{aligned} \tag{D.44}$$

with

$$\begin{aligned} g(x) &= \int_{-\infty}^{+\infty} d\omega e^{-\omega^4/x^4} \Gamma_n(\omega) \\ h(x) &= \int_{-\infty}^{+\infty} d\omega \frac{\omega^4}{x^4} e^{-\omega^4/x^4} \Gamma_n(\omega). \end{aligned} \tag{D.45}$$

The radius of convergence is defined as $r = 1 - x_m/x_{m+1}$. The algorithm is iterated until $|r| \leq 10^{-7}$ is reached.

E. Interacting Resonant Level Model in the Strong Coupling Limit

Here we derive an analytical investigation of the IRLM in the limit of large $U \gg D, T$. The calculations basically follow the thoughts of Avi Schiller, presented in the thesis of Fabian Güttge [19], Appendix D, and in Ref. [36].

We start with the IRLM Hamiltonian (see Sec. 2.5), cast into the shape of a semi-infinite Wilson chain (see Sec. 3.1). The impurity part of the Hamiltonian is given by

$$H_{\text{imp}} = \epsilon_{\text{d}} d^\dagger d + U \left(d^\dagger d - \frac{1}{2} \right) \left(c_0^\dagger c_0 - \frac{1}{2} \right) . \tag{E.46}$$

A diagonalization of H_{imp} yields the eigenvalues

$$\begin{aligned} E_0 &= U/4 \\ E_\pm &= \epsilon_{\text{d}}/2 - U/4 \pm \Omega/2 \\ E_2 &= \epsilon_{\text{d}} + U/4 \end{aligned} \tag{E.47}$$

with $\Omega^2 = \epsilon_{\text{d}}^2 + 4V^2$. The eigenstates are given by

$$\begin{aligned} |0\rangle &= |0,0\rangle \\ |\pm\rangle &= \pm\alpha_\pm \, |1,0\rangle + \alpha_\mp \, |0,1\rangle \\ |2\rangle &= |1,1\rangle \end{aligned} \tag{E.48}$$

and $\alpha_\pm^2 = (\Omega \pm \epsilon_{\text{d}})/(2\Omega)$. For large U the one-particle eigenstates $|\pm\rangle$ become a low-energy subspace and so for temperatures well below U the higher energy states $|0\rangle$ and $|2\rangle$ are thermally inaccessible with respect to the rest of the system. This motivates a Schrieffer-Wolff-type transformation [16]

$$H_{\text{eff}} = e^{S-S^\dagger} H e^{S^\dagger - S} \tag{E.49}$$

that decouples the high-energy sector from the rest of the system up to a certain order in t_0. Here t_0 is the Wilson chain coupling parameter between the zeroth and the first chain site. As a perturbation part of the Hamiltonian we choose

$$H_1 = t_0 \left(f_1^\dagger f_0 + f_0^\dagger f_1 \right) , \tag{E.50}$$

while $H_0 = H - H_1$ resembles the unperturbed part. Note, that H_1 is the only part of the total Hamiltonian H that changes the particle number of the local "super-impurity". To ensure that in (E.49) no terms appear, that are linear in t_0, S needs to be chosen to be proportional to t_0 and

$$H_1 + [S, H_0] - [S^\dagger, H_0] \overset{!}{=} 0 \tag{E.51}$$

needs to be fulfilled. In that case we obtain

$$H_{\text{eff}} = H_0 + [S - S^\dagger, H_1] + \mathbf{O}(t_0^3). \tag{E.52}$$

For a large U we can approximate $H_0 \to H_{\text{imp}}$ in the commutator and so the requirement of (E.51) can be turned into

$$[S, H_{\text{imp}}] \overset{!}{=} -t_0 f_0^\dagger f_1. \tag{E.53}$$

By expanding the zeroth chain site creator $f_0^\dagger$ in the local eigenbasis (E.48) one arrives at

$$S = t_0 \left[\frac{\alpha_+}{E_2 - E_+} |2\rangle \langle +| - \frac{\alpha_-}{E_2 - E_-} |2\rangle \langle -| + \frac{\alpha_-}{E_+ - E_0} |+\rangle \langle 0| - \frac{\alpha_+}{E_- - E_0} |-\rangle \langle 0| \right] f_1. \tag{E.54}$$

Since U is considered to be the largest local energy, we can substitute the four denominators of (E.54) by $\pm U/2$.

For infinite U, charge on the impurity is expected to oscillate between the two low-energy states $|\pm\rangle$ with the frequency $\Omega = E_+ - E_-$. If U is finite, the charge relaxates from $|+\rangle$ to $|-\rangle$. According to Fermi's golden rule the transition rate is then, in first order, given by

$$\tau^{-1} = 2\pi |\langle +| H_{\text{eff}} |-\rangle|^2 \rho_1^2 \Omega. \tag{E.55}$$

Here, $\langle +| H_{\text{eff}} |-\rangle = \frac{4Vt_0^2}{\Omega U}$ follows from the Schrieffer-Wolff transform (E.52). ρ_1 is the local DOS at the first chain site. In the spirit of Sec. 5.1 we can connect the GF of the zeroth and first chain site operators by

$$G_0(z) = \frac{1}{z - \epsilon_0 - t_0^2 G_1(z)} \tag{E.56}$$

(see Sec. 5.1). In the particle-hole symmetric case we have $\epsilon_0 = 0$ and $\mathfrak{Re} G_i(0) = 0$. This gives an equation for the DOS $\rho_i(0) = -\frac{1}{\pi} \mathfrak{Im} G_i(0)$ at $\omega = 0$. For a constant DOS we set $\rho_0 \equiv 1/(2D)$ and obtain $t_0^2 \rho_1 = 2D/\pi^2$. One ends up with

$$\tau = \frac{\pi^4}{256} \frac{\Omega}{D\Gamma} \left(\frac{U}{D} \right)^2. \tag{E.57}$$

With the considerations made above the local observables can now be calculated in the limit of large U. We start with a time-dependent system state

$$|\Psi(t)\rangle = \sum_{p=\pm} c_p(t) e^{-iE_p t} |p\rangle \otimes |\Psi_p(t)\rangle \,. \tag{E.58}$$

Here, the local part and the bath part $|\Psi_p(t)\rangle$ are factorized in the spirit of a BA for a weak coupling t_0. For the impurity occupation number it follows

$$\begin{aligned} n_\mathrm{d}(t) &= \langle\Psi(t)|\, d^\dagger d \,|\Psi(t)\rangle \\ &= \alpha_+^2 c_+^2(t) + \alpha_-^2 c_-^2(t) - 2\alpha_+\alpha_- c_+(t) c_-(t) \mathfrak{Re}\Big\{ e^{-i\Omega t} \langle\Psi_-(t)|\Psi_+(t)\rangle \Big\}. \end{aligned} \tag{E.59}$$

According to Fermi's golden rule the state $|+\rangle$ decays with a rate τ^{-1}, meaning that $|+\rangle\langle+|(t) = |\langle+|\Psi(t)\rangle|^2 \propto e^{-t/\tau}$. Combined with the fact that the states (E.58) are normalized to 1, we obtain the time-dependent coefficients

$$\begin{aligned} c_+(t) &= c_+(0) e^{-t/(2\tau)} \\ c_-(t) &= \sqrt{1 - c_+^2(0) e^{-t/\tau}}. \end{aligned} \tag{E.60}$$

Equation (E.59) can be written as

$$\begin{aligned} n_\mathrm{d}(t) =& (n_\mathrm{d}^\mathrm{i} - n_\mathrm{d}^\mathrm{f}) e^{-t/\tau} + n_\mathrm{d}^\mathrm{f} \\ &+ A \left(\cos(\Omega t) \sqrt{1 - \cos^2(\theta) e^{-t/\tau}} e^{-t/(2\tau)} - \sin(\theta) e^{-t/\tau} \right), \end{aligned} \tag{E.61}$$

where the quantities A and θ are undefined and need to be determined numerically by a fitting procedure. Equation (E.61) resembles a decay of the impurity on the timescale τ with damped Rabi-oscillations with a frequency of Ω.

F. Algorithm for the Biorthogonal Lanczos Method

In the following we explicitly describe the Lanczos algorithm we have used to diagonalize the BRT R (cf. Eq. (6.1.7.50)). All elements of the algorithm are considered complex. Vectors are written with a bold font and the scalar product " $\cdot$ " implies, that the first vector is conjugated complexly.

As a first step we declare the matrices $\underline{\underline{\phi}}, \underline{\underline{\varphi}}$ to store the left and right Lanczos vectors

$\boldsymbol{\phi}_i$ and $\boldsymbol{\varphi}_i$, respectively, and choose the starting vectors

$$\boldsymbol{\phi}_0 = \boldsymbol{\varphi}_0 = \frac{\boldsymbol{\rho}(t=0)}{||\boldsymbol{\rho}(t=0)||}. \tag{F.62}$$

We define the temporary vectors

$$\begin{aligned} \boldsymbol{r} &= R\boldsymbol{\varphi}_0, \\ \boldsymbol{s} &= R^\dagger \boldsymbol{\phi}_0, \end{aligned} \tag{F.63}$$

declare the values $\alpha, \beta, \gamma, \omega$ and set

$$\alpha = \boldsymbol{\phi}_0 \cdot \boldsymbol{r}. \tag{F.64}$$

Furthermore, we declare the matrix T, which is initialized as a zero-matrix of dimension $m_{\mathrm{Lan}} \times m_{\mathrm{Lan}}$ and set

$$T[0,0] = \alpha. \tag{F.65}$$

The following steps are performed in a loop for $i \in [0, m_{\mathrm{Lan}} - 1]$.

We start with

$$\begin{aligned} &\boldsymbol{r} \to \boldsymbol{r} - \alpha\boldsymbol{\varphi}_i \\ &\boldsymbol{s} \to \boldsymbol{s} - \alpha^*\boldsymbol{\phi}_i \\ &\omega = \boldsymbol{r} \cdot \boldsymbol{s} \\ &\beta = \sqrt{|\omega|} \\ &\gamma = \omega^*/\beta \end{aligned} \tag{F.66}$$

and compute the new Lanczos vectors:

$$\begin{aligned} \boldsymbol{\varphi}_{i+1} &= \boldsymbol{r}/\beta \\ \boldsymbol{\phi}_{i+1} &= \boldsymbol{s}/\gamma^*. \end{aligned} \tag{F.67}$$

We may re-biorthogonalize the new Lanczos vectors with respect to all vectors $j \leq i$:

$$\begin{aligned} \boldsymbol{\varphi}_{i+1} &\to \boldsymbol{\varphi}_{i+1} - \sum_{j=0}^{i} \left(\boldsymbol{\phi}_j \cdot \boldsymbol{\varphi}_{i+1} \right) \boldsymbol{\varphi}_j \\ \boldsymbol{\phi}_{i+1} &\to \boldsymbol{\phi}_{i+1} - \sum_{j=0}^{i} \left(\boldsymbol{\varphi}_j \cdot \boldsymbol{\phi}_{i+1} \right) \boldsymbol{\phi}_j. \end{aligned} \tag{F.68}$$

This process can be repeated until the vectors are sufficiently converged. We continue by setting

$$\begin{aligned} \boldsymbol{r} &= R\boldsymbol{\varphi}_{i+1} - \gamma\boldsymbol{\varphi}_i, \\ \boldsymbol{s} &= R^\dagger \boldsymbol{\phi}_{i+1} - \beta^* \boldsymbol{\phi}_{i+1} && \text{(F.69)} \\ & && \text{(F.70)} \end{aligned}$$

and

$$\alpha = \boldsymbol{\phi}_{i+1} \cdot \boldsymbol{r}.$$

Now the parameters are stored in the T matrix:

$$\begin{aligned} T[i+1, i+1] &= \alpha, \\ T[i, i+1] &= \gamma, \\ T[i+1, i] &= \beta, \end{aligned} \tag{F.71}$$

which concludes the loop iteration.

As a measure for the numerical accuracy of the algorithm

$$\det \underline{\underline{\phi}}^\dagger \underline{\underline{\varphi}} = 1 \tag{F.72}$$

has to be fulfilled.

The matrix T is now diagonalized to obtain the Ritz values. The right eigenvectors of T are stored in a matrix U. We calculate the left and right Ritz vector matrices

W, V by using the Lanczos vectors

$$\begin{aligned} V &= \underline{\underline{\varphi}} U, \\ W &= \underline{\underline{\phi}} \left(U^{-1}\right)^{\mathrm{T}}. \end{aligned} \tag{F.73}$$

The bottleneck of the algorithm regarding program complexity is the matrix-vector multiplication (F.70). Here it is important to exploit the sparsity of the matrix R.

A typical criterion for the numerical break-down of the algorithm is that any of the values $||r||, ||s||, |\omega| \approx 0$. In that case, one has to choose new starting vectors and restart the algorithm. The data computed up to this point, however, is valid to calculate the first Ritz values and vectors. In our program, a break-down of that kind has never occurred. In some cases, α might diverge. Here the algorithm has to be interrupted early enough, but still all calculated values are valid, since an eigenvalue $E \to \infty$ has no contribution in the final result. To combat this divergence, one might repeat the re-biorthogonalization (F.68) or simply choose a slightly different set of system parameters.

G. Sinc-Broadening for the RLM Equilibrium Spectral Function

In closed systems the TD-EGF $G_{\mathrm{d}}(t)$ is given as a sum of oscillating terms (see Eq. (6.2.3.57) for the CWC). Consequently, the respective ESF resembles a sum of delta-peaks. We investigate a simple broadening scheme for closed systems, that provides a natural, non-arbitrary broadening for the spectrum. This sinc-broadening procedure is based on the assumption, that $G_{\mathrm{d}}(t)$ thermalizes due to decoherence and that finite-size oscillations do not occur up to times $t = T$. By assuming that $G_{\mathrm{d}}(t)$ is zero for $t > T$, the function can be Fourier transformed to obtain an ESF with a natural broadening $\gamma = 1/T$.

Let us investigate this procedure for the simple RLM with the local energy level $\epsilon_{\mathrm{d}} = 0$ and a constant bath DOS. Here the exact GF

$$G_{\mathrm{d}}(t) = -i\Theta(t)e^{-\Gamma t} \tag{G.74}$$

is known. In Fig. 9.1 (a) we have Fourier transformed (G.74) over the interval $t \in [0, T]$ and plotted the resulting ESF. We can see, that the curves quickly converge to the

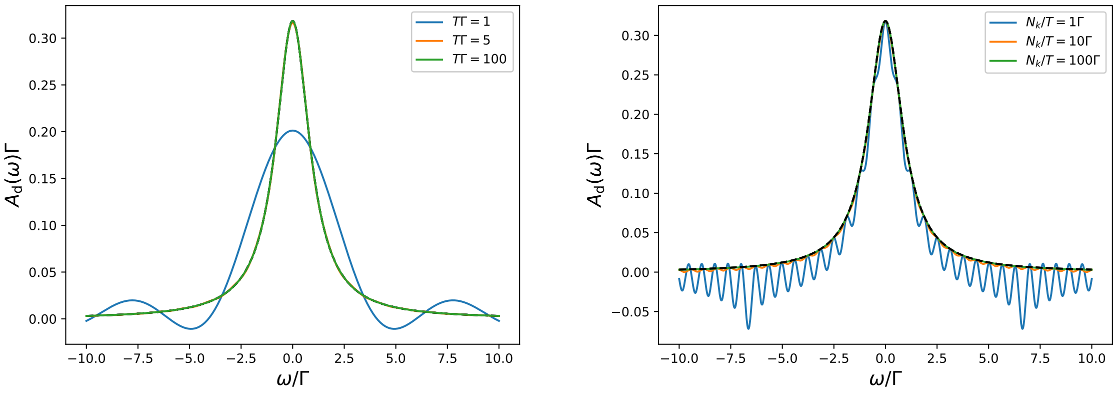

(a) (b)

Figure 9.1.: Spectral function calculated by (a) integrating (G.74) over the interval $t \in [0, T]$ for different values of T and (b) applying (G.77) for different ratios N_k/T.

exact solution of a Lorentzian of width Γ, if T is increased. In this trivial example, T can be chosen arbitrarily large. However, in a closed system, the maximum value of T depends on the size of the system. If T is chosen too large, finite-size oscillations are included in the ESF.

Let us proceed to a more complex problem, in which we express an arbitrary function $G_\mathrm{d}(t)$ on the interval $t \in [0, T]$ as a sum of oscillating terms, which resembles the CWC expression of Eq. (6.2.3.57). We obtain a Fourier series

$$G_{\mathrm{d,CWC}}(t) = -i\Theta(t) \sum_{k=-N_\mathrm{F}}^{N_\mathrm{F}} a_k e^{i\omega_k t}, \tag{G.75}$$

with frequencies $\omega_k = 2\pi k/T$. This function can resemble an arbitrary analytical function for $t < T$ and is periodic with T. The number N_F of terms in the expression defines the numerical accuracy of the series and needs to be increased, if T is increased. The periodicity of the Fourier series on the interval $[t, t+T)$ is an analogue to the finite-size nature of the CWC. The ratio N_F/T can be chosen in such a way, that the maximum energy ω_{N_F} equals the bandwidth D of the system. From a numerical standpoint, N_F loosely corresponds to the chain length N_C and should be chosen as large as possible.

For the GF (G.74) the coefficients of (G.75) are given as

$$a_k = \frac{1}{T}\int_0^T dt G_{\mathrm{d,CWC}}(t) e^{i\omega_k t} = \frac{e^{-\Gamma T} - 1}{\Gamma T + 2\pi k i} \tag{G.76}$$

and we obtain an energy-dependent GF of

$$G_{\mathrm{d,CWC}}(\omega) = \int_0^T dt G_{\mathrm{d,CWC}}(t) e^{i\omega t} = \sum_{k=-N_{\mathrm{F}}}^{N_{\mathrm{F}}} a_k \frac{e^{i\omega T} - 1}{\omega + \omega_k} \tag{G.77}$$

after a Fourier transform up to $t = T$. For $T \to \infty$ the ω-dependent part of the functions approaches delta-peaks. However, the coefficients a_k are affected by T as well and compensate this effect, if N_{F} is chosen large enough.

In Fig. 9.1 (b) we display the convergence of the ESF calculated from (G.77) with the ration N_k/T. For $N_k = T\Gamma$ oscillations close to the exact solution are visible, which resemble the finite-size effect of the OWC solution. By increasing the numerical resolution N_k per considered interval T, the curves quickly approach the physical solution. This behavior is similar to the OWC solution of Fig. 6.9 (c), where the energy resolution can be increased by increasing the Wilson chain length and simultaneously decreasing the discretization parameter. We have shown, that the resulting ESF curves are independent of the broadening $\gamma = 1/T$, given that T is chosen large enough for the TD-EGF to have sufficiently decayed and that the numerical accuracy (in our case N_k) can be adapted to adequately suppress finite-size oscillations on the respective interval $t \in [0, T]$.

H. Additional Calculations for the IRLM

In the following we present additional figures for TD-NEVs in the IRLM, calculated with the OCF. Consequently, this section is a continuation of Sec. 7.1.1.

In Fig. 9.2 we compare the non-equilibrium dynamics of the IRLM to the RLM. As in the previous sections, N_{C} is chosen relatively low to allow for a comparison to the exact OWC (that is the OWC without truncation of high-energy states) and Λ is chosen large at the same time to exaggerate the effects of the Lamb-shift and of truncation at the same time. In Fig. 9.2 (a) and (b) we investigate the curves for their particular parts. The green dashed lines only include the DDM and represent a simple relaxation with rates almost independent of U on the effective scale $1/\Gamma_{\mathrm{eff}}$. For

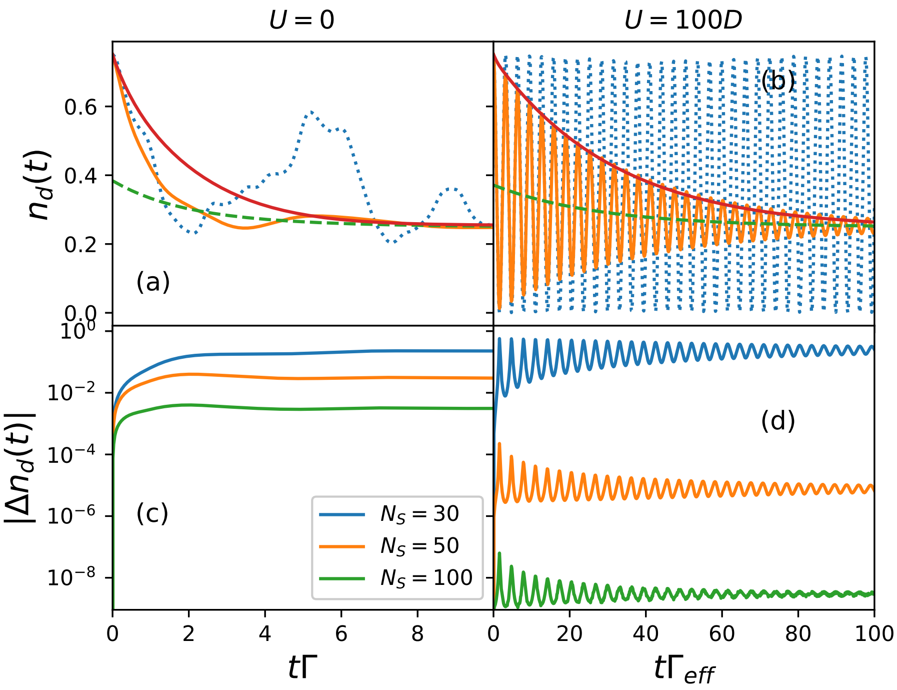

Figure 9.2.: Non-equilibrium impurity occupation for $N_\mathrm{C} = 10, \Lambda = 10, D = 100\Gamma, T = 0.01\Gamma$. On the l.h.s. we plot the RLM and on the r.h.s. the IRLM with $U = 100D$. We have chosen $\Gamma = 8.289 \cdot 10^{-3}\Gamma_\mathrm{eff}$ for the $U = 100D$ curves. Panels (a) and (b) show $n_\mathrm{d}(t)$ in the untruncated case for the CWC (blue, dotted), OWC (orange), DDM only (green, dashed) and without the CWC oscillations (red). Panels (c) and (d) show the relative difference $|\Delta n_\mathrm{d}(t)|$ of the untruncated OWC solution and a truncated one with $N_\mathrm{S} = 30$ (blue), $N_\mathrm{S} = 50$ (orange) and $N_\mathrm{S} = 100$ (green) kept states without Lamb-shift.

the red lines we have artificially set the oscillatory terms $e^{i(E_r^n - E_s^n)t}$ in Eq. (6.1.5) to zero. Thus the dynamical behavior is here solely generated by the OWC. Similar to the green curves, the red curves in (a) and (b) are almost identical and differ by a maximum relative difference of around 13% on intermediate time-scales. Consequently, the major influence of the interaction U is to induce Rabi-like oscillations between the impurity and the zeroth Wilson chain site, which are included in the CWC. The contributions of the BRF to the result are expressed as certain relaxation rates for the DDM and the ODDM, which appear to be independent of U, at least if the temperature is sufficiently low.

To further investigate this point, we need to increase N_C to reach low temperatures without choosing a large Λ and thus generating large discretization errors. Longer OWCs require a truncation of the high-energy states. For that reason, we investigate

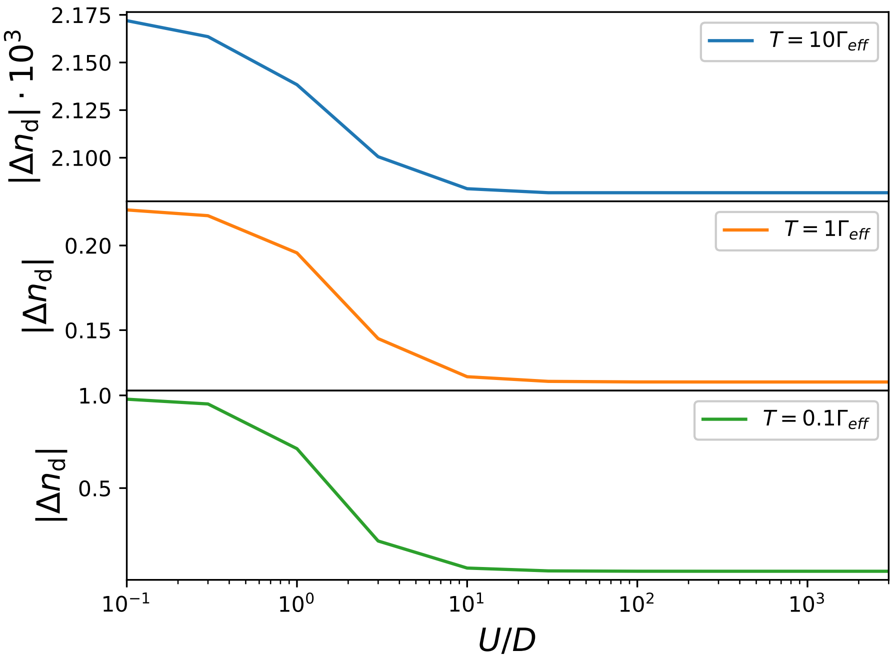

Figure 9.3.: Relative difference $|\Delta n_\mathrm{d}|$ between the equilibrium impurity occupation of $U = 0$ and $U > 0$. In the case of finite U, a scaling of the parameters with $\Gamma/\Gamma_\mathrm{eff} = \Gamma_\mathrm{eff}/D$ has been applied. We have chosen $\Lambda = 2, D = 100\Gamma_\mathrm{eff}, \epsilon_\mathrm{d} = \Gamma_\mathrm{eff}, N_\mathrm{S} = 300$ for all curves. The chain length N_C has been varied to reach the indicated temperatures and fine adjustments have been made by tuning $\overline{\beta}$.

the influence of truncation on the OWC in Fig. 9.2 (c) and (d). Here we show the relative difference between the truncated and the untruncated eigenbasis for different numbers of kept states N_S without Lamb-shift. Obviously, a value of $N_\mathrm{S} = 100$ already yields a good match with the untruncated case. Note that the total number of states is $d^{2+N_\mathrm{C}} = 2048$ in our case, so keeping $N_\mathrm{S} = 100$ per NRG-iteration is a significant reduction of this number. The effect of the Lamb-shift for $U > 0$ is a small increase of the oscillation frequency Ω. This deviation grows if N_S is reduced, which means that the Lamb-shift is more susceptible to a reduction of the eigenbasis.

In Fig. 7.4 we have seen that the IRLM values $\Gamma/\Gamma_\mathrm{eff}, \Omega$ and τ deviate from theoretical predictions, especially in the limit $U \to \infty$. To investigate this observation further, let us first concentrate on the equilibrium case and $\Gamma/\Gamma_\mathrm{eff}$.

In Fig. 9.3 we depict the relative difference $|\Delta n_\mathrm{d}|$ of the equilibrium NRG values $n_\mathrm{d}(U = 0)$ and $n_\mathrm{d}(U > 0)$. The finite U value is plotted on the horizontal axis in dimension of the bandwidth and in the $U > 0$ cases the parameters are scaled by $\Gamma/\Gamma_{\text{eff}} = \Gamma_{\text{eff}}/D$, which is the theoretical prediction for the limit of $U \to \infty$ according to Eq. (7.1.1.8). The temperature has been varied, since the equilibrium values coincide for all values of U in the case $T \to \infty$ and start to increasingly deviate, if the temperature is lowered. Independently of the temperature, the NRG values are practically converged for $U > 10D$ and the convergence scale is almost identical for all investigated chain lengths. We expect this scale to change depending on the choice of Λ, analogly to Fig. 7.4.

The impact of U on the equilibrium value is highly dependent on the temperature. As for other local quantities, such as ϵ_{d}, the relative and absolute influence of U on the equilibrium value is increased, if the temperature is lowered. This is due to the fact, that a small inverse temperature β in the Boltzmann factor strongly damps variations in the local parameters. By decreasing the temperature, i.e. increasing β, the influence of these variations on the total NRG equilibrium value is enhanced. Here $T = 0.1\Gamma_{\text{eff}}$ can be seen as an effective low-temperature limit, since a further lowering of T does not significantly impact the U-dependence.

We proceed to the frequency Ω of the Rabi-like oscillations, defined via Eqs. (7.1.1.2) and (7.1.1.3). This frequency is a dynamical quantity in the sense, that it only occurs in non-equilibrium quench dynamics. In Fig. 9.2 it has been shown, that these oscillations are solely generated by system Hamiltonian eigenenergies, i.e. by the CWC. For that reason, the pure TD-NRG without an OQS extension is the most simple system to study the effect of T and U on the frequency Ω.

In Fig. 9.4 we plot $n_{\text{d}}(t)$ in the CWC case for increasing U. The Coulomb-interaction favors the "super-impurity" site, consisting of the impurity and the zeroth Wilson chain site, to be half filled. Consequently, any relaxation into the chain is suppressed for large U. The theoretically predicted oscillation period $2\pi\Gamma_{\text{eff}}/\Omega = 2\pi/\sqrt{1+8/\pi} \approx 3.336$ (black dashed line) is met within 1% for $U \geq 100D$. Note, that we choose $\Gamma/\Gamma_{\text{eff}} = \Gamma_{\text{eff}}/D$ according to Eq. (7.1.1.8), so the equilibrium values do not exactly align. For lower temperatures, the influence of U is most pronounced, as it induces the local Rabi-like oscillations. For higher temperatures, thermal fluctuations hinder this effect and consequently, a larger U is required to obtain comparable local oscillations.

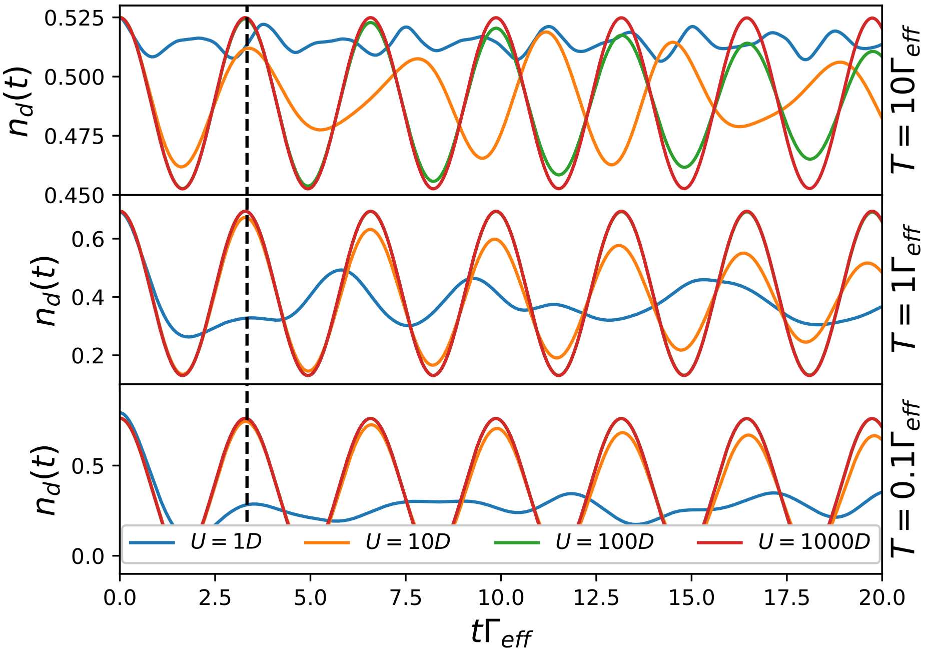

Figure 9.4.: Non-equilibrium impurity occupation of the CWC. The parameters are $\Lambda = 2, D = 100\Gamma_{\text{eff}}, \epsilon_{\text{d}} = \Gamma_{\text{eff}}, N_{\text{S}} = 100$ for all curves. The chain length N_{C} and $\overline{\beta}$ have been varied to reach the indicated temperatures. $\Gamma/\Gamma_{\text{eff}} = \Gamma_{\text{eff}}/D$ has been chosen according to Eq. (7.1.1.8). The theoretical prediction for Ω in the limit $U \to \infty$ has been added as a black dashed line.

I. Additional Calculations for the SIAM

In the following we present additional figures for TD-NEVs in the SIAM, calculated with the OCF. Consequently, this section is a continuation of Sec. 7.1.2.

Both spin states of the SIAM can be discriminated by an external magnetic field B. For that reason, we start by a quench $B^{\text{i}} = -B$ to $B^{\text{f}} = B$, where the local parameters ϵ_{d} and U are set to zero for all times. The occupation number is constant over time and the magnetization dynamics is entirely driven by the switch of the external magnetic field.

In Fig. 9.5 $S_z(t)$ is depicted in the limit $T \to 0$. For $t\Gamma > 10$ in panel (a) the CWC curve oscillates around the steady-state value defined by the DDM for $t = 0$ (for details see Fig. 3.4 for the artificially damped CWC curves). The OWC solution, on the other hand, thermalizes to the correct equilibrium value defined by the Boltzmann distribution (i.e. ± 0.5 for $B \to \infty$) with a deviation of under 1%. The z-averaging

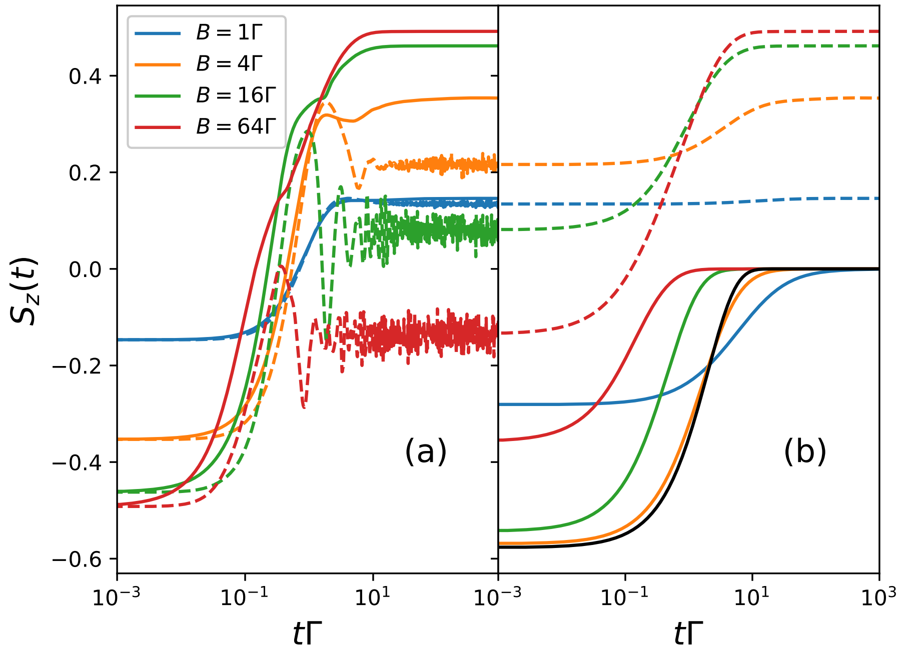

Figure 9.5.: Non-equilibrium impurity magnetization $S_z(t)$ for different values of the external magnetic field B. We switch $B^{\mathrm{i}} = -B$ to $B^{\mathrm{f}} = B$ at $t = 0$ and keep $\epsilon_{\mathrm{d}} = U = 0$. The NRG parameters are $N_{\mathrm{C}} = 50$, $\Lambda = 2$, $D = 100\Gamma$, so that a temperature of $T \approx 10^{-6}\Gamma$ is reached. We have used $N_{\mathrm{S}} = 300$ states and $N_z = 12$. In panel (a) we compare the CWC (dashed lines) and the OWC (solid lines). The Lamb-shift is set to zero. In panel (b) we artificially exclude the CWC oscillations and plot the ODDM (solid lines) separated from the DDM contribution (dashed lines). The time axes are plotted logarithmically.

performed only smooths the unphysical oscillations induced by the discretization for intermediate times. Apart from some small oscillations that occur around $t\Gamma \approx 1$ the magnetization performs a simple quench, which is (on a logarithmic scale) symmetrical around a point $(\tilde{t}, 0)$. Interestingly, $\tilde{t}$ decreases with increasing B, which implies that the relaxation is accelerated when the difference between the initial and the final state is increased. We know, that for sufficiently long chains the CWC solution converges to the exact solution for short times, i.e. quadratic dynamics in t. The OWC solution experiences an over-exaggerated relaxation due to the MA (see Sec. 4.6). Consequently, the OWC curves are shifted to the left in the figure. The influence of B is here a stretching of both axes in the sense that this shift grows with B, as does the difference between the equilibrium values. The Lamb-shift is set to zero in the figure, since it

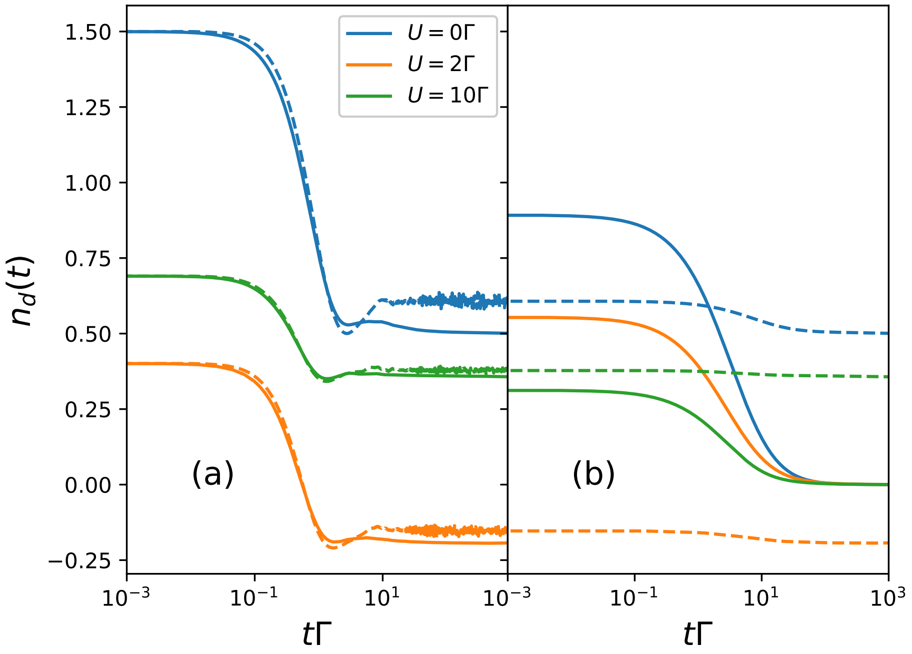

Figure 9.6.: Non-equilibrium impurity occupation $n_\mathrm{d}(t)$ for different values of the Coulomb repulsion U. We switch $\epsilon_\mathrm{d}^\mathrm{i} = -\Gamma$ to $\epsilon_\mathrm{d}^\mathrm{f} = \Gamma$ at $t = 0$ and keep U and $B = 0$ constant. All other properties of the plot are identical to Fig. 9.5.

only has a small contribution that vanishes for larger B in the exact case and induces a large error, when truncating high-energy states. In Fig. 9.5 (b) the contribution of the reservoirs to the dynamics is examined by artificially neglecting the CWC oscillations (see Fig. 9.2, red curves). For small B the dynamics is almost entirely carried by the ODDM, while for increasing B the DDM dominates.

In Fig. 9.6, we quench the impurity energy ϵ_d for different $U \geq 0$ without an external magnetic field. This way, the magnetization is zero, and we obtain the pure effect of a variation in U. Obviously, an increase of U decreases the equilibrium values $n_\mathrm{d}(t = 0)$, since a large local Coulomb repulsion depopulates the $|2\rangle$ state. However, the relaxation rate is not influenced by a variation of U. This holds for the CWC solution (see Fig. 9.6 (a), dashed lines), as well as the OWC solution (Fig. 9.6 (b), solid lines). Consequently, in this case U only impacts the equilibrium values and has no influence on non-equilibrium dynamics. This especially means that the eigenvalues of the BRT are independent of U, which can be attributed to the small temperature chosen for the curves of the figure and the small $U \ll D$. The CWC solution shows the same independence of U with respect to the relaxation rate. Thus we can conclude that this effect is not caused by the BMA, but that it is of physical origin.

Note, that the choice of parameters in Fig. 9.6 is similar to the quench investigated for the IRLM in Fig. 9.2. However, the resulting dynamics is fundamentally different. In the IRLM, the hybridization V mediates a hopping between the two local states. Charge can only dissipate via the zeroth Wilson chain site. This leads to damped oscillations of the impurity occupation number. In the SIAM, no hopping between the two local singly occupied states is possible and charge can dissipate directly from both sites. Thus we observe a simple relaxation process, with U only influencing the equilibrium values. Furthermore, we chose $U > D$ in the IRLM case to obtain the damped oscillations. In the case $U < D$, almost no oscillations occur.

Bibliography

[1] J. Bardeen, L. N. Cooper, and J. R. Schrieffer. “Theory of Superconductivity”. In: *Physical Review* 108.5 (Dec. 1957), pp. 1175–1204. DOI: `10.1103/physrev.108.1175`.

[2] Dirk van Delft and Peter Kes. “The discovery of superconductivity”. In: *Physics Today* 63.9 (Sept. 2010), pp. 38–43. DOI: `10.1063/1.3490499`.

[3] N F Mott. “The Basis of the Electron Theory of Metals, with Special Reference to the Transition Metals”. In: *Proceedings of the Physical Society. Section A* 62.7 (July 1949), pp. 416–422. DOI: `10.1088/0370-1298/62/7/303`.

[4] Philip Phillips. “Mottness”. In: *Annals of Physics* 321.7 (July 2006), pp. 1634–1650. DOI: `10.1016/j.aop.2006.04.003`.

[5] K. Andres, J. E. Graebner, and H. R. Ott. “$4f$-Virtual-Bound-State Formation in CeAl_3 at Low Temperatures”. In: *Physical Review Letters* 35.26 (Dec. 1975), pp. 1779–1782. DOI: `10.1103/physrevlett.35.1779`.

[6] Alexander Cyril Hewson. *The Kondo Problem to Heavy Fermions.* Cambridge University Press, Jan. 1993. DOI: `10.1017/cbo9780511470752`.

[7] W.J. de Haas, J. de Boer, and G.J. van dën Berg. “The electrical resistance of gold, copper and lead at low temperatures”. In: *Physica* 1.7-12 (May 1934), pp. 1115–1124. DOI: `10.1016/s0031-8914(34)80310-2`.

[8] J. Kondo. “Resistance Minimum in Dilute Magnetic Alloys”. In: *Progress of Theoretical Physics* 32.1 (July 1964), pp. 37–49. DOI: `10.1143/ptp.32.37`.

[9] M. Reed et al. “Observation of discrete electronic states in a zero-dimensional semiconductor nanostructure”. In: *Physical Review Letters* 60.6 (Feb. 1988), pp. 535–537. DOI: `10.1103/physrevlett.60.535`.

[10] R. Hanson et al. “Spins in few-electron quantum dots”. In: *Reviews of Modern Physics* 79.4 (Oct. 2007), pp. 1217–1265. DOI: `10.1103/revmodphys.79.1217`.

[11] Ren-Bao Liu, Wang Yao, and L.J. Sham. "Quantum computing by optical control of electron spins". In: *Advances in Physics* 59.5 (Sept. 2010), pp. 703–802. DOI: `10.1080/00018732.2010.505452`.

[12] T. D. Ladd et al. "Quantum computers". In: *Nature* 464.7285 (Mar. 2010), pp. 45–53. DOI: `10.1038/nature08812`.

[13] P. W. Anderson. "Localized Magnetic States in Metals". In: *Physical Review* 124.1 (Oct. 1961), pp. 41–53. DOI: `10.1103/physrev.124.41`.

[14] H. Krishna-murthy, J. Wilkins, and K. Wilson. "Renormalization-group approach to the Anderson model of dilute magnetic alloys. I. Static properties for the symmetric case". In: *Physical Review B* 21.3 (Feb. 1980), pp. 1003–1043. DOI: `10.1103/physrevb.21.1003`.

[15] H. Krishna-murthy, J. Wilkins, and K. Wilson. "Renormalization-group approach to the Anderson model of dilute magnetic alloys. II. Static properties for the asymmetric case". In: *Physical Review B* 21.3 (Feb. 1980), pp. 1044–1083. DOI: `10.1103/physrevb.21.1044`.

[16] J. R. Schrieffer and P. A. Wolff. "Relation between the Anderson and Kondo Hamiltonians". In: *Physical Review* 149.2 (Sept. 1966), pp. 491–492. DOI: `10.1103/physrev.149.491`.

[17] V.M. Filyov and P. Wiegmann. "A method for solving the Kondo problem". In: *Physics Letters A* 76.3-4 (Mar. 1980), pp. 283–286. DOI: `10.1016/0375-9601(80)90494-6`.

[18] P. Schlottmann. "Simple spinless mixed-valence model. II. Solution of the isolated f-level problem". In: *Physical Review B* 22.2 (July 1980), pp. 622–631. DOI: `10.1103/physrevb.22.622`.

[19] Fabian Güttge. "Real-Time Dynamics and Critical Phenomena of Quantum Impurity Systems, A Hybrid Numerical Renormalization Group Approach". PhD thesis. Technische Universität Dortmund, Chair of theoretical physics II, 2012.

[20] Kenneth G. Wilson. "Renormalization Group and Critical Phenomena. I. Renormalization Group and the Kadanoff Scaling Picture". In: *Physical Review B* 4.9 (Nov. 1971), pp. 3174–3183. DOI: `10.1103/physrevb.4.3174`.

[21] Uwe C. Täuber. "Renormalization Methods: A Guide for Beginners". In: *Physics Today* 58.6 (June 2005), pp. 62–63. DOI: `10.1063/1.1996480`.

[22] Kenneth G. Wilson. “The renormalization group: Critical phenomena and the Kondo problem”. In: *Reviews of Modern Physics* 47.4 (Oct. 1975), pp. 773–840. DOI: `10.1103/revmodphys.47.773`.

[23] Frithjof B. Anders and Avraham Schiller. “Spin precession and real-time dynamics in the Kondo model: Time-dependent numerical renormalization-group study”. In: *Physical Review B* 74.24 (Dec. 2006), p. 245113. DOI: `10.1103/physrevb.74.245113`.

[24] Robert Peters, Thomas Pruschke, and Frithjof B. Anders. “Numerical renormalization group approach to Green’s functions for quantum impurity models”. In: *Physical Review B* 74.24 (Dec. 2006), p. 245114. DOI: `10.1103/physrevb.74.245114`.

[25] Ralf Bulla, Theo A. Costi, and Thomas Pruschke. “Numerical renormalization group method for quantum impurity systems”. In: *Reviews of Modern Physics* 80.2 (Apr. 2008), pp. 395–450. DOI: `10.1103/revmodphys.80.395`.

[26] Wanda C. Oliveira and Luiz N. Oliveira. “Generalized numerical renormalization-group method to calculate the thermodynamical properties of impurities in metals”. In: *Physical Review B* 49.17 (May 1994), pp. 11986–11994. DOI: `10.1103/physrevb.49.11986`.

[27] Vivaldo L. Campo and Luiz N. Oliveira. “Alternative discretization in the numerical renormalization-group method”. In: *Physical Review B* 72.10 (Sept. 2005), p. 104432. DOI: `10.1103/physrevb.72.104432`.

[28] Rok Žitko and Thomas Pruschke. “Energy resolution and discretization artifacts in the numerical renormalization group”. In: *Physical Review B* 79.8 (Feb. 2009), p. 085106. DOI: `10.1103/physrevb.79.085106`.

[29] Frithjof B. Anders and Avraham Schiller. “Real-Time Dynamics in Quantum-Impurity Systems: A Time-Dependent Numerical Renormalization-Group Approach”. In: *Physical Review Letters* 95.19 (Oct. 2005), p. 196801. DOI: `10.1103/physrevlett.95.196801`.

[30] Eitan Eidelstein et al. “Coherent control of correlated nanodevices: A hybrid time-dependent numerical renormalization-group approach to periodic switching”. In: *Physical Review B* 85.7 (Feb. 2012), p. 075118. DOI: `10.1103/physrevb.85.075118`.

[31] A. Rosch. "Wilson chains are not thermal reservoirs". In: *The European Physical Journal B* 85.1 (Jan. 2012). DOI: `10.1140/epjb/e2011-20880-7`.

[32] R. Bulla, T. A. Costi, and D. Vollhardt. "Finite-temperature numerical renormalization group study of the Mott transition". In: *Physical Review B* 64.4 (June 2001), p. 045103. DOI: `10.1103/physrevb.64.045103`.

[33] M. Yoshida, M. A. Whitaker, and L. N. Oliveira. "Renormalization-group calculation of excitation properties for impurity models". In: *Physical Review B* 41.13 (May 1990), pp. 9403–9414. DOI: `10.1103/physrevb.41.9403`.

[34] Osamu Sakai, Yukihiro Shimizu, and Tadao Kasuya. "Single-Particle and Magnetic Excitation Spectra of Degenerate Anderson Model with Finite $f-f$ Coulomb Interaction". In: *Journal of the Physical Society of Japan* 58.10 (Oct. 1989), pp. 3666–3678. DOI: `10.1143/jpsj.58.3666`.

[35] R Bulla, A C Hewson, and Th Pruschke. "Numerical renormalization group calculations for the self-energy of the impurity Anderson model". In: *Journal of Physics: Condensed Matter* 10.37 (Sept. 1998), pp. 8365–8380. DOI: `10.1088/0953-8984/10/37/021`.

[36] Fabian Güttge et al. "Hybrid NRG-DMRG approach to real-time dynamics of quantum impurity systems". In: *Physical Review B* 87.11 (Mar. 2013), p. 115115. DOI: `10.1103/physrevb.87.115115`.

[37] Steven R. White. "Density matrix formulation for quantum renormalization groups". In: *Physical Review Letters* 69.19 (Nov. 1992), pp. 2863–2866. DOI: `10.1103/physrevlett.69.2863`.

[38] A.G. REDFIELD. "The Theory of Relaxation Processes". In: *Advances in Magnetic Resonance*. Elsevier, 1965, pp. 1–32. DOI: `10.1016/b978-1-4832-3114-3.50007-6`.

[39] Fritz Haake. "On a non-Markoffian master equation, I. Derivation and General Discussion". In: *Zeitschrift für Physik A Hadrons and nuclei* 223.4 (Aug. 1969), pp. 353–363. DOI: `10.1007/bf01392865`.

[40] Howard J. Carmichael. *Statistical Methods in Quantum Optics 1*. Springer Berlin Heidelberg, 1999. DOI: `10.1007/978-3-662-03875-8`.

[41] Michał Karski, Carsten Raas, and Götz S. Uhrig. "Single-particle dynamics in the vicinity of the Mott-Hubbard metal-to-insulator transition". In: *Physical Review B* 77.7 (Feb. 2008), p. 075116. DOI: `10.1103/physrevb.77.075116`.

[42] Alan A. Dzhioev and D. S. Kosov. “Stability analysis of multiple nonequilibrium fixed points in self-consistent electron transport calculations”. In: *The Journal of Chemical Physics* 135.17 (Nov. 2011), p. 174111. DOI: `10.1063/1.3658736`.

[43] Alan A. Dzhioev and D. S. Kosov. “Super-fermion representation of quantum kinetic equations for the electron transport problem”. In: *The Journal of Chemical Physics* 134.4 (Jan. 2011), p. 044121. DOI: `10.1063/1.3548065`.

[44] Shigeru Ajisaka et al. “Nonequlibrium particle and energy currents in quantum chains connected to mesoscopic Fermi reservoirs”. In: *Physical Review B* 86.12 (Sept. 2012), p. 125111. DOI: `10.1103/physrevb.86.125111`.

[45] Antonius Dorda et al. “Auxiliary master equation approach to nonequilibrium correlated impurities”. In: *Physical Review B* 89.16 (Apr. 2014), p. 165105. DOI: `10.1103/physrevb.89.165105`.

[46] A. Dorda et al. “Optimized auxiliary representation of non-Markovian impurity problems by a Lindblad equation”. In: *New Journal of Physics* 19.6 (June 2017), p. 063005. DOI: `10.1088/1367-2630/aa6ccc`.

[47] Heinz-Peter Breuer and Francesco Petruccione. *The Theory of Open Quantum Systems*. Oxford University Press, Jan. 2007. DOI: `10.1093/acprof:oso/9780199213900.001.0001`.

[48] Gernot Schaller. *Open Quantum Systems Far from Equilibrium*. Springer International Publishing, 2014. DOI: `10.1007/978-3-319-03877-3`.

[49] Unknown. “Still irresistible”. In: *Nature Physics* 10.5 (Apr. 2014), pp. 329–329. DOI: `10.1038/nphys2972`.

[50] P. Nozires. “A ”fermi-liquid” description of the Kondo problem at low temperatures”. In: *Journal of Low Temperature Physics* 17.1-2 (Oct. 1974), pp. 31–42. DOI: `10.1007/bf00654541`.

[51] M. P. Sarachik, E. Corenzwit, and L. D. Longinotti. “Resistivity of Mo-Nb and Mo-Re Alloys Containing 1% Fe”. In: *Physical Review* 135.4A (Aug. 1964), A1041–A1045. DOI: `10.1103/physrev.135.a1041`.

[52] A. A. Abrikosov. “Electron scattering on magnetic impurities in metals and anomalous resistivity effects”. In: *Physics Physique Fizika* 2.1 (Sept. 1965), pp. 5–20. DOI: `10.1103/physicsphysiquefizika.2.5`.

[53] P W Anderson. “A poor man’s derivation of scaling laws for the Kondo problem”. In: *Journal of Physics C: Solid State Physics* 3.12 (Dec. 1970), pp. 2436–2441. DOI: `10.1088/0022-3719/3/12/008`.

[54] N. Andrei. “Diagonalization of the Kondo Hamiltonian”. In: *Physical Review Letters* 45.5 (Aug. 1980), pp. 379–382. DOI: `10.1103/physrevlett.45.379`.

[55] P B Wiegmann. “Exact solution of the s-d exchange model (Kondo problem)”. In: *Journal of Physics C: Solid State Physics* 14.10 (Apr. 1981), pp. 1463–1478. DOI: `10.1088/0022-3719/14/10/014`.

[56] H. Bethe. “Zur Theorie der Metalle”. In: *Zeitschrift für Physik* 71.3-4 (Mar. 1931), pp. 205–226. DOI: `10.1007/bf01341708`.

[57] J. Hubbard. “Electron correlations in narrow energy bands”. In: *Proceedings of the Royal Society of London. Series A. Mathematical and Physical Sciences* 276.1365 (Nov. 1963), pp. 238–257. DOI: `10.1098/rspa.1963.0204`.

[58] J. F. Herbst, R. E. Watson, and J. W. Wilkins. “Relativistic calculations of4fexcitation energies in the rare-earth metals: Further results”. In: *Physical Review B* 17.8 (Apr. 1978), pp. 3089–3098. DOI: `10.1103/physrevb.17.3089`.

[59] F. D. M. Haldane. “Scaling Theory of the Asymmetric Anderson Model”. In: *Physical Review Letters* 40.6 (Feb. 1978), pp. 416–419. DOI: `10.1103/physrevlett.40.416`.

[60] B. Coqblin and J. R. Schrieffer. “Exchange Interaction in Alloys with Cerium Impurities”. In: *Physical Review* 185.2 (Sept. 1969), pp. 847–853. DOI: `10.1103/physrev.185.847`.

[61] K. M. Stadler et al. “Dynamical Mean-Field Theory Plus Numerical Renormalization-Group Study of Spin-Orbital Separation in a Three-Band Hund Metal”. In: *Physical Review Letters* 115.13 (Sept. 2015), p. 136401. DOI: `10.1103/physrevlett.115.136401`.

[62] K.M. Stadler et al. “Hundness versus Mottness in a three-band Hubbard–Hund model: On the origin of strong correlations in Hund metals”. In: *Annals of Physics* 405 (June 2019), pp. 365–409. DOI: `10.1016/j.aop.2018.10.017`.

[63] Fabian Eickhoff and Frithjof B. Anders. “Strongly correlated multi-impurity models: The crossover from a single-impurity problem to lattice models”. In: *Physical Review B* 102.20 (Nov. 2020), p. 205132. DOI: `10.1103/physrevb.102.205132`.

[64] G. Yuval and P. W. Anderson. “Exact Results for the Kondo Problem: One-Body Theory and Extension to Finite Temperature”. In: *Physical Review B* 1.4 (Feb. 1970), pp. 1522–1528. DOI: `10.1103/physrevb.1.1522`.

[65] A.M. Finkel’Shtein P B Wiegmann. “Resonant-level model in the Kondo problem”. In: *Journal of Experimental and Theoretical Physics* 48 (July 1978), p. 102.

[66] L. Borda, A. Schiller, and A. Zawadowski. “Applicability of bosonization and the Anderson-Yuval methods at the strong-coupling limit of quantum impurity problems”. In: *Physical Review B* 78.20 (Nov. 2008), p. 201301. DOI: `10.1103/physrevb.78.201301`.

[67] P. Schlottmann. “The Kondo problem. I. Transformation of the model and its renormalization”. In: *Physical Review B* 25.7 (Apr. 1982), pp. 4815–4827. DOI: `10.1103/physrevb.25.4815`.

[68] P. Schlottmann. “Simple spinless mixed-valence model. I. Coherent-hybridization states versus virtual-bound states”. In: *Physical Review B* 22.2 (July 1980), pp. 613–621. DOI: `10.1103/physrevb.22.613`.

[69] Gonzalo Camacho, Peter Schmitteckert, and Sam T. Carr. “Exact equilibrium results in the interacting resonant level model”. In: *Physical Review B* 99.8 (Feb. 2019), p. 085122. DOI: `10.1103/physrevb.99.085122`.

[70] H. T. M. Nghiem et al. “Ohmic two-state system from the perspective of the interacting resonant level model: Thermodynamics and transient dynamics”. In: *Physical Review B* 93.16 (Apr. 2016), p. 165130. DOI: `10.1103/physrevb.93.165130`.

[71] Pankaj Mehta and Natan Andrei. “Nonequilibrium Transport in Quantum Impurity Models: The Bethe Ansatz for Open Systems”. In: *Physical Review Letters* 96.21 (June 2006), p. 216802. DOI: `10.1103/physrevlett.96.216802`.

[72] E. Boulat, H. Saleur, and P. Schmitteckert. “Twofold Advance in the Theoretical Understanding of Far-From-Equilibrium Properties of Interacting Nanostructures”. In: *Physical Review Letters* 101.14 (Sept. 2008), p. 140601. DOI: `10.1103/physrevlett.101.140601`.

[73] Mikhail Pletyukhov, Dirk Schuricht, and Herbert Schoeller. “Relaxation versus Decoherence: Spin and Current Dynamics in the Anisotropic Kondo Model at Finite Bias and Magnetic Field”. In: *Physical Review Letters* 104.10 (Mar. 2010), p. 106801. DOI: `10.1103/physrevlett.104.106801`.

[74] D. M. Kennes et al. “Renormalization group approach to time-dependent transport through correlated quantum dots”. In: *Physical Review B* 85.8 (Feb. 2012), p. 085113. DOI: `10.1103/physrevb.85.085113`.

[75] Yuval Vinkler-Aviv, Avraham Schiller, and Frithjof B. Anders. “From thermal equilibrium to nonequilibrium quench dynamics: A conserving approximation for the interacting resonant level”. In: *Physical Review B* 90.15 (Oct. 2014), p. 155110. DOI: `10.1103/physrevb.90.155110`.

[76] Tim Child et al. “An Introduction to the Kondo Effect”. In: (Nov. 2018).

[77] M. A. Kastner. “The single-electron transistor”. In: *Reviews of Modern Physics* 64.3 (July 1992), pp. 849–858. DOI: `10.1103/revmodphys.64.849`.

[78] Sara Marie Cronenwett. “Coherence, charging, and spin effects in quantum dots and point contacts”. In: (Aug. 2002).

[79] D. Goldhaber-Gordon et al. “From the Kondo Regime to the Mixed-Valence Regime in a Single-Electron Transistor”. In: *Physical Review Letters* 81.23 (Dec. 1998), pp. 5225–5228. DOI: `10.1103/physrevlett.81.5225`.

[80] V. Madhavan. “Tunneling into a Single Magnetic Atom: Spectroscopic Evidence of the Kondo Resonance”. In: *Science* 280.5363 (Apr. 1998), pp. 567–569. DOI: `10.1126/science.280.5363.567`.

[81] Jiutao Li et al. “Kondo Scattering Observed at a Single Magnetic Impurity”. In: *Physical Review Letters* 80.13 (Mar. 1998), pp. 2893–2896. DOI: `10.1103/physrevlett.80.2893`.

[82] H. C. Manoharan, C. P. Lutz, and D. M. Eigler. “Quantum mirages formed by coherent projection of electronic structure”. In: *Nature* 403.6769 (Feb. 2000), pp. 512–515. DOI: `10.1038/35000508`.

[83] Ralf Bulla et al. “Numerical renormalization group for quantum impurities in a bosonic bath”. In: *Physical Review B* 71.4 (Jan. 2005), p. 045122. DOI: `10.1103/physrevb.71.045122`.

[84] Matthew T. Glossop and Kevin Ingersent. “Numerical Renormalization-Group Study of the Bose-Fermi Kondo Model”. In: *Physical Review Letters* 95.6 (Aug. 2005), p. 067202. DOI: `10.1103/physrevlett.95.067202`.

[85] R. Bulla, T. Pruschke, and A. C. Hewson. “Anderson impurity in pseudo-gap Fermi systems”. In: *Journal of Physics: Condensed Matter* 9.47 (Nov. 1997), pp. 10463–10474. DOI: `10.1088/0953-8984/9/47/014`.

[86] Ralf Bulla, Ning-Hua Tong, and Matthias Vojta. “Numerical Renormalization Group for Bosonic Systems and Application to the Sub-Ohmic Spin-Boson Model”. In: *Physical Review Letters* 91.17 (Oct. 2003), p. 170601. DOI: `10.1103/physrevlett.91.170601`.

[87] Frithjof B. Anders. *Lecture notes: Introduction to the Renormalization Group.* Technische Universität Dortmund, Feb. 2018.

[88] Andreas Weichselbaum and Jan von Delft. “Sum-Rule Conserving Spectral Functions from the Numerical Renormalization Group”. In: *Physical Review Letters* 99.7 (Aug. 2007), p. 076402. DOI: `10.1103/physrevlett.99.076402`.

[89] H. T. M. Nghiem, H. T. Dang, and T. A. Costi. “Time-dependent spectral functions of the Anderson impurity model in response to a quench with application to time-resolved photoemission spectroscopy”. In: *Physical Review B* 101.11 (Mar. 2020), p. 115117. DOI: `10.1103/physrevb.101.115117`.

[90] H. T. M. Nghiem and T. A. Costi. “Generalization of the time-dependent numerical renormalization group method to finite temperatures and general pulses”. In: *Physical Review B* 89.7 (Feb. 2014), p. 075118. DOI: `10.1103/physrevb.89.075118`.

[91] Amy C. Cassidy, Charles W. Clark, and Marcos Rigol. “Generalized Thermalization in an Integrable Lattice System”. In: *Physical Review Letters* 106.14 (Apr. 2011), p. 140405. DOI: `10.1103/physrevlett.106.140405`.

[92] J. B. Silva et al. “Particle-Hole Asymmetry in the Two-Impurity Kondo Model”. In: *Physical Review Letters* 76.2 (Jan. 1996), pp. 275–278. DOI: `10.1103/physrevlett.76.275`.

[93] S. C. Costa et al. “Numerical renormalization-group computation of specific heats”. In: *Physical Review B* 55.1 (Jan. 1997), pp. 30–33. DOI: `10.1103/physrevb.55.30`.

[94] Tomaž Prosen. “Open XXZ Spin Chain: Nonequilibrium Steady State and a Strict Bound on Ballistic Transport”. In: *Physical Review Letters* 106.21 (May 2011), p. 217206. DOI: `10.1103/physrevlett.106.217206`.

[95] Daniel Manzano and Elica Kyoseva. “An atomic symmetry-controlled thermal switch”. In: *Scientific Reports* 6.1 (Aug. 2016). DOI: `10.1038/srep31161`.

[96] B. Kraus et al. “Preparation of entangled states by quantum Markov processes”. In: *Physical Review A* 78.4 (Oct. 2008), p. 042307. DOI: `10.1103/physreva.78.042307`.

[97] Todd A. Brun. “Continuous measurements, quantum trajectories and decoherent histories”. In: *Physical Review A* 61.4 (Mar. 2000), p. 042107. DOI: `10.1103/physreva.61.042107`.

[98] F. Schwarz et al. “Lindblad-driven discretized leads for nonequilibrium steady-state transport in quantum impurity models: Recovering the continuum limit”. In: *Physical Review B* 94.15 (Oct. 2016), p. 155142. DOI: `10.1103/physrevb.94.155142`.

[99] Jan Jeske et al. “Bloch-Redfield equations for modeling light-harvesting complexes”. In: *The Journal of Chemical Physics* 142.6 (Feb. 2015), p. 064104. DOI: `10.1063/1.4907370`.

[100] Archak Purkayastha, Abhishek Dhar, and Manas Kulkarni. “Out-of-equilibrium open quantum systems: A comparison of approximate quantum master equation approaches with exact results”. In: *Physical Review A* 93.6 (June 2016), p. 062114. DOI: `10.1103/physreva.93.062114`.

[101] Philip Pearle. “Simple derivation of the Lindblad equation”. In: *European Journal of Physics* 33.4 (Apr. 2012), pp. 805–822. DOI: `10.1088/0143-0807/33/4/805`.

[102] Matthias Bauer. “Lindblad driving for nonequilibrium steady-state transport for noninteracting quantum impurity models”. Fakultät Physik. PhD thesis. Ludwig–Maximilians–Universität München, 2011.

[103] Fritz Haake. “On a non-Markoffian master equation, II. Application to the Damped Oscillator”. In: *Zeitschrift für Physik A Hadrons and nuclei* 223.4 (Aug. 1969), pp. 364–377. DOI: `10.1007/bf01392866`.

[104] David E. Evans. “Irreducible quantum dynamical semigroups”. In: *Communications in Mathematical Physics* 54.3 (Oct. 1977), pp. 293–297. DOI: `10.1007/bf01614091`.

[105] David E Evans and Harald Hanche-Olsen. “The generators of positive semigroups”. In: *Journal of Functional Analysis* 32.2 (May 1979), pp. 207–212. DOI: `10.1016/0022-1236(79)90054-5`.

[106] Juzar Thingna, Daniel Manzano, and Jianshu Cao. "Dynamical signatures of molecular symmetries in nonequilibrium quantum transport". In: *Scientific Reports* 6.1 (June 2016). DOI: `10.1038/srep28027`.

[107] Victor V. Albert and Liang Jiang. "Symmetries and conserved quantities in Lindblad master equations". In: *Physical Review A* 89.2 (Feb. 2014), p. 022118. DOI: `10.1103/physreva.89.022118`.

[108] N. Grewe. "Perturbation expansions for systems with strong local correlation". In: *Zeitschrift für Physik B Condensed Matter* 52.3 (Sept. 1983), pp. 193–210. DOI: `10.1007/bf01307369`.

[109] Carsten Raas, Götz S. Uhrig, and Frithjof B. Anders. "High-energy dynamics of the single-impurity Anderson model". In: *Physical Review B* 69.4 (Jan. 2004), p. 041102. DOI: `10.1103/physrevb.69.041102`.

[110] E. R. Gagliano and C. A. Balseiro. "Dynamical Properties of Quantum Many-Body Systems at Zero Temperature". In: *Physical Review Letters* 59.26 (Dec. 1987), pp. 2999–3002. DOI: `10.1103/physrevlett.59.2999`.

[111] Qimiao Si et al. "Correlation induced insulator to metal transitions". In: *Physical Review Letters* 72.17 (Apr. 1994), pp. 2761–2764. DOI: `10.1103/physrevlett.72.2761`.

[112] Karen A. Hallberg. "Density-matrix algorithm for the calculation of dynamical properties of low-dimensional systems". In: *Physical Review B* 52.14 (Oct. 1995), R9827–R9830. DOI: `10.1103/physrevb.52.r9827`.

[113] B. Bruognolo et al. "Open Wilson chains for quantum impurity models: Keeping track of all bath modes". In: *Physical Review B* 95.12 (Mar. 2017), p. 121115. DOI: `10.1103/physrevb.95.121115`.

[114] Jan Böker and Frithjof B. Anders. "Restoring the continuum limit in the time-dependent numerical renormalization group approach". In: *Physical Review B* 102.7 (Aug. 2020), p. 075149. DOI: `10.1103/physrevb.102.075149`.

[115] V. S. Viswanath and Gerhard Müller. *The Recursion Method.* Springer Berlin Heidelberg, 1994. DOI: `10.1007/978-3-540-48651-0`.

[116] Yousef Saad. *Iterative Methods for Sparse Linear Systems.* Society for Industrial and Applied Mathematics, Jan. 2003. DOI: `10.1137/1.9780898718003`.

[117] Jack J. Dongarra. *Biorthogonal Lanczos Method*. `http://www.netlib.org/utk/people/JackDongarra/etemplates/node245.html`. Accessed: 2021-09-27. 2000.

[118] J. M. Elzerman et al. “Single-shot read-out of an individual electron spin in a quantum dot”. In: *Nature* 430.6998 (July 2004), pp. 431–435. DOI: `10.1038/nature02693`.

[119] Dmitry Lobaskin and Stefan Kehrein. “Crossover from nonequilibrium to equilibrium behavior in the time-dependent Kondo model”. In: *Physical Review B* 71.19 (May 2005), p. 193303. DOI: `10.1103/physrevb.71.193303`.

[120] Leonid V. Keldysh. “SUPERCONDUCTIVITY IN NONMETALLIC SYSTEMS”. In: *Soviet Physics Uspekhi* 8.3 (Mar. 1965), pp. 496–500.

Danksagung

Zu guter Letzt möchte ich allen meine Dankbarkeit aussprechen, die mich unterstützt haben. Spezieller Dank geht an:

- Frithjof Anders als Betreuer und Erstgutachter dieser Arbeit. Er war immer mit motiviertem und hilfreichem Rat zur Stelle, wenn es einmal nicht weiter ging.
- Jan von Delft, der die Aufgabe des Zweitgutachters übernimmt.
- Adrian Schratt für viele angeregte Diskussionen zum Thema der Arbeit und darüber hinaus.
- Carsten Nase, der sich um die Computer kümmert und bei technischen Fragen immer zur Verfügung steht.
- die Mitglieder von T2 für unterhaltsame Stunden in der Mensa und vor allem an Fabian Eickhoff für seine Hilfe beim Kampf mit dem NRG-Ordner.
- meine Eltern, weil sie immer für mich da waren und sind, wenn ich Unterstützung in jeglicher Hinsicht brauche. Besonders möchte ich ihnen dafür danken, dass sie mich immer wieder motiviert haben, diese Arbeit zu vollenden.
- meinen Bruder dafür, dass er schon lange ein wichtiger Teil meines Lebens ist und es hoffentlich immer bleiben wird.
- meine engen Freunde aus Breckerfeld, Dortmund und Bochum dafür, dass sie jederzeit für einen feucht-fröhlichen Abend bereit stehen, wenn ich einmal Ablenkungen brauche.
- meine Freundin Theresa, weil sie an meiner Seite ist und mir während dieser Arbeit immer so gut es ging den Rücken freigehalten hat.
- und schließlich an meinen Sohn Linus dafür, dass er jeden unserer Tage mit seinem Lachen versüßt.